

NEVADA GEOTHERMAL FAVORABILITY MAPPING, WEIGHTS OF EVIDENCE
SMOOTHED FUNCTIONS AND REFINED METHODOLOGY

AS

36

2019

ERTH

.D43

A Thesis submitted to the faculty of
San Francisco State University

In partial fulfillment of
the requirements for
the Degree

Master of Science

In

Geoscience

by

Jacob DeAngelo

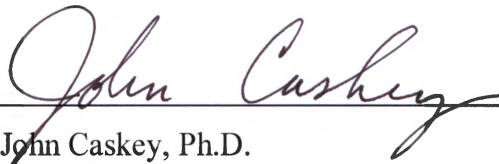
San Francisco, California

May 2019

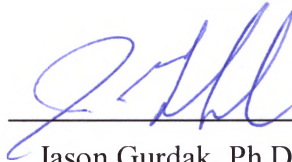
Copyright by
Jacob DeAngelo
2019

CERTIFICATION OF APPROVAL

I certify that I have read Nevada Geothermal Favorability Mapping, Weights of Evidence Smoothed Functions and Refined Methodology by Jacob DeAngelo, and that in my opinion this work meets the criteria for approving a thesis submitted in partial fulfillment of the requirement for the degree Master of Science in Geoscience at San Francisco State University.



John Caskey, Ph.D.
Associate Professor



Jason Gurdak, Ph.D.
Associate Professor



Mark Coolbaugh, Ph.D.
Geologist



Jonathan Glen, Ph.D.
Geophysicist

NEVADA GEOTHERMAL FAVORABILITY MAPPING, WEIGHTS OF EVIDENCE
SMOOTHED FUNCTIONS AND REFINED METHODOLOGY

Jacob DeAngelo
San Francisco, California
2019

Geothermal energy provides clean renewable electrical power in the United States and around the world. It is most efficiently harnessed from active hydrothermal systems, which only occur in very specific tectonic environments with naturally occurring permeability. Most known systems have surface manifestations such as hot springs or fumaroles that led to their discovery, however a significant resource potential resides in blind systems that are not expressed at the surface. One of the largest barriers to successful exploration for blind systems stems from uncertainty in characterizing resource potential. This study develops new methodology and applies it to arrive at a new geothermal favorability assessment to predict where best to explore for active hydrothermal systems. While drilling is ultimately necessary to verify a resource, regional assessment tools can help reduce uncertainties, refine the identification of prospective areas, and significantly reduce costs associated with drilling and other exploration efforts.

The approximately 286, 000 km² study area covered the entire state of Nevada, which has high potential for containing undiscovered geothermal resources. Nevada has relatively comprehensive regional coverage of publicly available geological and geophysical data directly related to processes that control hydrothermal systems including: Quaternary faults, crustal heat flow, crustal strain rates, and seismicity. These data, known as evidence data were compiled and assessed to determine which were the

most useful for predicting resource occurrence and to determine which processing techniques best transform raw geologic data into forms useful for statistical analysis. Locations of fifty-five moderate and high temperature geothermal systems served as training data, the benchmarks used to calculate weights for evidence data.

The general framework of this study was adopted directly from prior geothermal assessments that used Weights of Evidence (WofE), a Bayesian data-driven technique to quantify spatial relationships between training and evidence data. This study sought to apply the best practices seen in prior assessments and to further refine those approaches when possible by developing and applying new techniques. New exploratory techniques were assisted by the development and application of customized Python-based tools that automated different data processing approaches and subsequent visualization of the resulting WofE statistics. Additionally, a technique was developed and applied in this study to calculate “smoothed” weights by fitting mathematical functions to weights generated using the traditional WofE approach. Generating smoothed weights eliminates a geologically artificial relic of the modeling process, the abrupt changes in favorability at category boundaries seen in prior WofE-based assessment maps. Smoothing may also provide greater accuracy in some parts of the map. Weight functions calculated in this study could potentially be applied to future studies using identical evidence in analogous tectonic environments.

Ultimately, data-driven geothermal favorability maps were produced that could be used to guide future exploration for undiscovered geothermal resources, and several prospective target areas were identified. Three evidence layers were used to create final predictive surfaces, resulting in a conservative view of favorability driven by layers with relatively strong correlations and consistent distribution across the study area.

Approaches and results from this study were compared with the most relevant prior assessments to contextualize decisions made and results discovered. Techniques developed in this project could be applied in other geographic regions or applied to investigations of other types of natural resources.

I certify that the Abstract is a correct representation of the content of this thesis.

John Cashey
Chair, Thesis Committee

5/21/19
Date

ACKNOWLEDGEMENTS

I am deeply grateful to my advisor Dr. John Caskey for guiding, teaching, and trusting me throughout my graduate school experience. He welcomed me into his program despite my untraditional background and helped me gain invaluable knowledge about the field I work in. I would like to thank him for his contributions, his patience with me, his kindness, and his genuine desire for me to arrive a good result without cutting corners.

I would also like to thank Dr. Mark Coolbaugh for his extensive and selfless help with my thesis. I relied heavily on his advice to keep me on track while planning this study. He provided extremely detailed and helpful reviews throughout my writing process. We exchanged many emails and met for hours online. I appreciate his help tremendously, I hope I can help him back someday soon. My door is open to anyone seeking help I can provide on topics pioneered by Coolbaugh, Raines, Bonham-Carter and others.

Dr. Jonathan Glen helped inspire me to pursue graduate school and he's been helping me every step of the way, he's an honored colleague and a valued friend. Dr. Jason Gurdak also showed me great patience, support, and kindness in my experience at SFSU.

I would like to thank Dr. Colin Williams, my supervisor at USGS, no person has been more influential on my professional development. I would also like to thank Dr. Erick Burns, Dr. Drew Siler, and Dr. Tom Parsons from the USGS for their guidance, kindness, and contributions to this project. Thanks also to Dr. Patrick Dobson from LBL for contributions and guidance. I would also like to thank the entire faculty of the SFSU Geosciences Department, particularly Russell McArthur and Dr. Yadira Ibarra.

All my love and thanks to my wife Yiman and daughter Mila for doing everything it took to make it through such busy times. I'm happily looking forward to having more time to enjoy life together. I'd also like to thank my mom and dad, Joe and Linda for everything.

TABLE OF CONTENTS

List of Table.....	xiii
List of Figures.....	xiv
List of Appendices.....	xix
1.0 Introduction.....	1
1.1 Geologic Setting.....	6
1.2 Undiscovered Geothermal Systems.....	8
1.3 Training and Evidence Data.....	9
1.3.1 Training Data: Known Geothermal Systems.....	9
1.3.2 Evidence Data: Quaternary Faults.....	10
1.3.3 Evidence Data: Crustal Strain Rate.....	13
1.3.4 Evidence Data: Crustal Heat Flow.....	16
1.3.5 Evidence Data: Earthquakes.....	19
1.4 Weights of Evidence.....	19
1.4.1 Weights of Evidence Technique.....	19
1.4.2 Cumulative Weight Test.....	23
1.4.3 Categorical Weight Test.....	26
1.4.4 Posterior Probability Calculation.....	30
1.5 Prior Works.....	31
1.5.1 Coolbaugh et al., 2005.....	31
1.5.2 Williams and DeAngelo, 2008.....	33

1.5.3	Faulds et al., 2015	35
1.5.4	Coolbaugh and Bedell, 2006.....	39
1.6	Summary	42
2.0	Methodology	43
2.1	Geoprocessing Tools.....	44
2.1.1	Distance Function	44
2.1.2	Density Functions	45
2.1.3	Interpolators	45
2.2	Python Tools	46
2.2.1	Processing Toolset	46
2.2.1.1	Subset-Distance Cumulative Weight Test Tool.....	47
2.2.1.2	Density Function and Cumulative Weight Tool	47
2.2.1.3	Continuous Layer Reclassify and Cumulative Weight Test Tool.....	47
2.2.1.4	Categorical Weight Test Tool.....	48
2.2.2	Plotting Toolset.....	48
2.2.2.1	Cumulative Weight Plotter	48
2.2.2.2	Categorical Weight Plotter.....	49
2.3	Evidence Layer Creation and Selection	49
2.3.1	Strain Rate.....	49
2.3.2	Quaternary Faults.....	50
2.3.2.1	Distance Function on Fault Subsets	51
2.3.2.2	Other Approaches Not Used on Faults	56
2.3.3	Heat Flow	59

2.3.4	Earthquakes.....	62
2.4	Generating Categorical Weights.....	70
2.4.1	Quaternary Faults.....	70
2.4.2	Strain Rate.....	73
2.4.3	Heat Flow.....	79
2.5	Generating Smoothed Weights from Categorical Weights.....	87
2.5.1	Heat Flow.....	88
2.5.2	Strain Rate.....	93
2.5.3	Quaternary Faults.....	96
	2.5.3.1 Fault Subset 2.4 ('Latest Quaternary' and younger of all slip rates).....	96
	2.5.3.2 Fault Subset 5.3 ('Undifferentiated Quaternary' and younger with slip rates equal to or greater than 0.2 mm/yr).....	102
2.6	Posterior Probability Calculations.....	104
3.0	Results.....	105
3.1	Review of Evidence Data.....	105
3.2	Categorical Weight Results.....	107
3.3	Functions Fit by Area.....	111
3.3.1	Heat Flow.....	111
3.3.2	Strain Rate.....	112
3.3.3	Fault Subset 2.4 ('Latest Quaternary' and Younger of All Slip Rates).....	113
3.3.4	Fault Subset 5.3 ('Undifferentiated Quaternary' and Younger with Slip Rates Equal to or Greater Than 0.2 mm/yr).....	114
3.4	Review of Fitting Individual Layers by Area.....	115
3.5	Multilayer Analysis Conditional Independence Testing.....	116

3.5.1	Conditional Independence Using Different Fault Layers	122
3.5.2	Conditional Independence Between Layer Pairs	122
3.5.3	Conditional Independence Between Categorical & Smooth Models	122
3.6	Maps.....	123
4.0	Discussion.....	138
4.1	Comparing Approach with Prior Works.....	138
4.1.1	Coolbaugh et al., 2005	141
4.1.2	Williams and DeAngelo, 2008.....	142
4.1.3	Faulds et al., 2015	145
4.1.4	Coolbaugh and Bedell, 2006.....	146
4.2	Geothermal Favorability Maps	147
4.2.1	Best Favorability Maps	147
4.2.2	Areas of High Favorability	151
4.3	Comparing Results with Prior Works.....	154
4.3.1	Williams and DeAngelo, 2008.....	154
4.3.2	Faulds et al., 2015	160
4.4	Additional Findings	165
4.4.1	Fit by Area Approach.....	165
4.4.2	Geographic Processing Techniques	166
4.4.3	Evidence Data	167
4.4.4	Cell Size	169
4.4.5	Two Layer Models	169
4.4.6	Strain Rate Weighting.....	169

4.5	Future Work	171
4.5.1	Additional Evidence Layers.....	171
4.5.2	Other Possible Uses of Dilation and Slip Tendency.....	171
4.5.3	Other Possible Uses of Earthquake Data	172
4.5.4	Using Density Functions on Fault Subsets	172
5.0	Conclusions.....	174
	References Cited.....	177
	Appendices.....	185
	Appendix 1: Temperature at Depth Map	183
	Appendix 2: EBK Statistics	185
	Appendix 3: Python Code.....	188
	Processing Tools	189
	Cumulative Plotting Tool.....	202
	Categorical Plotting Tool.....	210
	Appendix 4: Other Possible Future Work Topics.....	221

LIST OF TABLES

Table	Page
1. Table 2.1: Bin ranges tested for 2.4 fault subset	71
2. Table 2.2: Bin ranges tested for 5.3 fault subset	72
3. Table 3.1: Evidence layer approach table	106
4. Table 3.2: Heat flow categorical weights	108
5. Table 3.3: Strain rate categorical weights	108
6. Table 3.4: Faults 2.4 ('latest Quaternary' and younger, all slip rates) categorical weights	109
7. Table 3.5: Faults 5.3 ('undifferentiated Quaternary' and younger, slip rates ≥ 0.2 mm/yr) categorical weights	110
8. Table 3.6: Conditional independence overprediction results table	117
9. Table 3.7: Conditional independence ratio table	119
10. Table 3.8: Agterberg-Cheng Conditional Independence Test results table	121
11. Table 4.1: Prior works evidence layer table	140

LIST OF FIGURES

Figures	Page
1. Figure 1.1: Overview map of study area (the state of Nevada) and data layers	2
2. Figure 1.2: Tectonic overview figure from Pérouse and Wernicke (2017)	7
3. Figure 1.3: Normal faults in Nevada by recency	11
4. Figure 1.4: Normal faults in Nevada by slip rate	12
5. Figure 1.5: Estimated strain rate within the Nevada study area	15
6. Figure 1.6: Estimated crustal heat flow in Nevada	18
7. Figure 1.7: Ascending weight plot for normal fault subset 2.4	24
8. Figure 1.8: Categorical weight plot of strain rate categories by category	27
9. Figure 1.9: Categorical weight plot of strain rate categories by native unit	29
10. Figure 1.10: Geothermal potential map from Coolbaugh et al., 2005b	32
11. Figure 1.11: Amagmatic geothermal potential map from Williams and DeAngelo, 2008.....	34
12. Figure 1.12: Overview map from Faulds et al., 2015	36
13. Figure 1.13: ‘The Fairway’ map from Faulds et al., 2015	37
14. Figure 1.14: Evidence data diagram from Faulds et al., 2015.....	38
15. Figure 1.15: Weight table and geothermal potential maps from Coolbaugh and Bedell, 2006	40

16. Figure 1.16: Example of weight functions from Coolbaugh and Bedell, 2006	41
17. Figure 2.1: Cumulative weight tables from fault subsets of all slip senses	52
18. Figure 2.2. Cumulative weight tables from fault subsets of normal faults	54
19. Figure 2.3: Cumulative weight test results of faults weighted by dilation or slip tendency using simple and kernel density functions with multiple search radii	57
20. Figure 2.4: Cumulative weight test results of heat flow and temperature at 3 km depth surfaces generated using two interpolators	61
21. Figure 2.5: Cumulative weight test results examining earthquakes using density functions weighed by seismic moment	63
22. Figure 2.6: Categorical weight test results examining earthquakes	65
23. Figure 2.7: Earthquake density function map weighted by moment magnitude	66
24. Figure 2.8: Cumulative weight test results examining earthquakes using density functions with no weighting	68
25. Figure 2.9: Earthquake density function map using no weighting	69
26. Figure 2.10: Cumulative weight plot of strain rate	74
27. Figure 2.11: Map of strain rate categories	76
28. Figure 2.12: Categorical strain rate exploratory plots	78
29. Figure 2.13: Ascending weight plot of heat flow data	80
30. Figure 2.14: Categorical heat flow exploratory plots	83
31. Figure 2.15: Categorical weight plot of heat flow rate categories	85
32. Figure 2.16: Map of heat flow categories	86
33. Figure 2.17: Plot showing weight functions calculated for heat flow, displayed using native units as a linear independent variable	90
34. Figure 2.18: Plot showing weight functions calculated for heat flow, displayed using cumulative area as the x-axis independent variable	92

35. Figure 2.19: Plot showing weight functions calculated for strain rate, displayed using native units as independent variable	94
36. Figure 2.20: Plot showing weight functions calculated for strain rate, displayed using cumulative area as independent variable	95
37. Figure 2.21: Plot showing weight functions calculated for Quaternary faults 2.4 subset (Age equal to or younger than ‘Latest Quaternary’, all slip rates), displayed using native units as independent variable with x-axis values increasing linearly	98
38. Figure 2.22: Plot showing weight functions calculated for Quaternary faults 2.4 subset (Age equal to or younger than ‘Latest Quaternary’, all slip rates), displayed using native units as independent variable with x-axis values increasing logarithmically	99
39. Figure 2.23: Plot showing weight functions calculated for Quaternary faults 2.4 subset (Age equal to or younger than ‘Latest Quaternary’, all slip rates), displayed using cumulative area as independent variable with x-axis values increasing logarithmically	101
40. Figure 2.24: Plot showing weight functions calculated for Quaternary faults 5.3 subset (Age equal to or younger than ‘undifferentiated Quaternary’ and slip rate equal to or younger than 1.0 mm/yr), displayed using cumulative area as independent variable with x-axis values increasing logarithmically	103
41. Figure 3.1: Geothermal favorability map using categorical weights for heat flow, strain rate, and a binary 250-meter buffer on the 2.4 fault subset (Age equal to or younger than ‘Latest Quaternary’, all slip rates	124
42. Figure 3.2: Geothermal favorability map using categorical weights for heat flow, strain rate, and a binary 1-km buffer on the 2.4 fault subset (Age equal to or younger than ‘Latest Quaternary’, all slip rates)	125
43. Figure 3.3: Geothermal favorability map using categorical weights for heat flow, strain rate, and ternary buffers on the 2.4 fault subset (Age equal to or younger than ‘Latest Quaternary’, all slip rates	126

44. Figure 3.4: Geothermal favorability map using weights fit ‘by area’ for heat flow, strain rate, and a binary 250-meter buffer on the 2.4 fault subset (Age equal to or younger than ‘Latest Quaternary’, all slip rates)	127
45. Figure 3.5: Geothermal favorability map using weights fit ‘by area’ for heat flow, strain rate, and a binary 1-km buffer on the 2.4 fault subset (Age equal to or younger than ‘Latest Quaternary’, all slip rates)	128
46. Figure 3.6: Geothermal favorability map using weights fit ‘by area’ for heat flow, strain rate, and ternary buffers on the 2.4 fault subset (Age equal to or younger than ‘Latest Quaternary’, all slip rates)	129
47. Figure 3.7: Geothermal favorability map using weights fit ‘by area’ for heat flow, strain rate, the 2.4 fault subset (Age equal to or younger than ‘Latest Quaternary’, all slip rates)	130
48. Figure 3.8: Geothermal favorability map using categorical weights for heat flow, strain rate, and a binary 250-meter buffer on the 5.3 fault subset (Age equal to or younger than ‘undifferentiated Quaternary’ and slip rate equal to or younger than 1.0 mm/yr)	131
49. Figure 3.9: Geothermal favorability map using categorical weights for heat flow, strain rate, and a binary 1-km buffer on the 5.3 fault subset (Age equal to or younger than ‘undifferentiated Quaternary’ and slip rate equal to or younger than 1.0 mm/yr)	132
50. Figure 3.10: Geothermal favorability map using categorical weights for heat flow, strain rate, and ternary buffers on the 5.3 fault subset (Age equal to or younger than ‘undifferentiated Quaternary’ and slip rate equal to or younger than 1.0 mm/yr)	133
51. Figure 3.11: Geothermal favorability map using weights fit ‘by area’ for heat flow, strain rate, and a binary 250-meter buffer on the 5.3 fault subset (Age equal to or younger than ‘undifferentiated Quaternary’ and slip rate equal to or younger than 1.0 mm/yr)	134

52. Figure 3.12: Geothermal favorability map using weights fit ‘by area’ for heat flow, strain rate, and a binary 1-km buffer on the 5.3 fault subset (Age equal to or younger than ‘undifferentiated Quaternary’ and slip rate equal to or younger than 1.0 mm/yr)	135
53. Figure 3.13: Geothermal favorability map using weights fit ‘by area’ for heat flow, strain rate, and ternary buffers on the 5.3 fault subset (Age equal to or younger than ‘undifferentiated Quaternary’ and slip rate equal to or younger than 1.0 mm/yr)	136
54. Figure 3.14: Geothermal favorability map using weights fit ‘by area’ for heat flow, strain rate, the 5.3 fault subset (Age equal to or younger than ‘undifferentiated Quaternary’ and slip rate equal to or younger than 1.0 mm/yr)	137
55. Figure 4.1: Comparison of best performing models	150
56. Figure 4.2: Identification of high favorability regions	152
57. Figure 4.3: Comparison maps with Williams and DeAngelo, 2008	156
58. Figure 4.4: Comparison maps with Williams and DeAngelo, 2008 showing faults and heat flow wells	158
59. Figure 4.5: Favorability maps compared with those of Faulds et al., 2015	161
60. Figure 4.6: Favorability maps compared with those of Faulds et al. (2015) Fairway map	163

LIST OF APPENDICES

Appendix	Page
1. Appendix 1: Temperature at Depth Map	184
2. Appendix 2: EBK Statistics	185
3. Appendix 3: Python Code	188
4. Appendix 4: Other Possible Future Work Topics	221

1.0 Introduction

Geothermal power plants produce electricity by mining heat from permeable rock in the subsurface, using water as the transport medium. Geothermal energy produces very low levels of pollution compared to conventional hydrocarbons and can generate continuous (baseload) electricity unlike solar and wind that fluctuate daily and seasonally. The greatest barrier to additional development of this industry is the uncertainty and cost associated with exploration. Assessing where conditions favor geothermal development helps to reduce uncertainty for the geothermal industry and may help to promote the development of a domestic renewable energy resource. The present study uses data-driven techniques to conduct a geothermal favorability assessment, an analysis of where favorable conditions exist for future exploration.

Geothermal power plants depend on the presence of a hydrothermal system in the subsurface at a depth that can be reached economically by drilling. Hydrothermal systems are underground circulation systems where hot, low-density, buoyant and pressurized fluids rise from depth through fractures in rocks before reaching a maximum proximity to the surface and often circulating back down due to gravity.

The entire state of Nevada was examined in the present study because it sits largely within the Great Basin physiographic province, a large region characterized mostly by extensional tectonics and high heat flow (Figure 1.1). Limiting the analysis to Nevada served as a convenient way of enabling compilation of relatively uniform high-resolution data sets and Nevada contained many known hydrothermal systems that could be used as training sites or benchmarks to make predictions about resource potential.

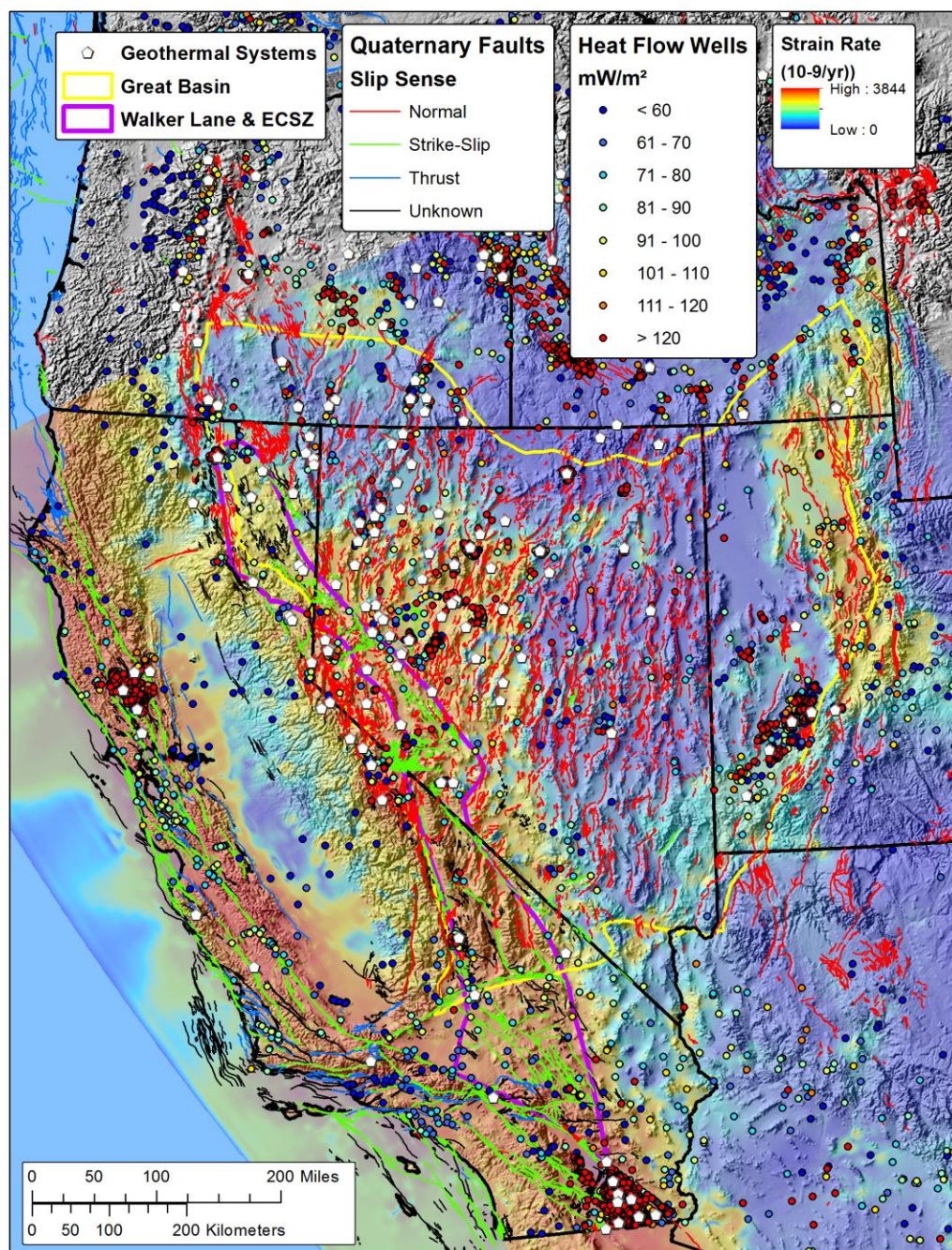


Figure 1.1: Overview map of study area (the state of Nevada) and data layers. An outline of the Great Basin is depicted in yellow. An outline of the Walker Lane and Eastern California Shear Zone is depicted in purple (Faulds et al., 2012). Identified moderate and high temperature geothermal systems used as training sites are depicted as white pentagons. Normal faults are depicted in red, strike-slip faults in green, thrust or reverse faults in blue. Geothermal wells with calculated heat flow values are depicted as dots with colors denoting their heat flow in mW/m^2 . The colored map overlying the topography depicts the estimated strain rate, or the rate of deformation as measured by the second invariant strain rate tensor in units of ($10^{-9}/yr$) (Kreemer, 2012).

Weights-of-Evidence (WofE), a Bayesian data-driven statistical technique, was employed to calculate associations between ‘training data,’ locations of known geothermal systems, and ‘evidence data,’ data related to the geologic conditions believed to control or influence the formation of hydrothermal systems in Nevada. Statistically derived weightings can then be applied to evidence data, which can be combined to produce geothermal favorability maps. Prior studies have used WofE to assess geothermal favorability in the western United States (Williams & DeAngelo, 2008; Williams et al., 2007), the Great Basin (Coolbaugh et al., 2005; Coolbaugh et al., 2005b), Nevada (Coolbaugh et al., 2006), and portions of Nevada (Faulds et al., 2015). The present study was informed by previous geothermal assessments and sought to refine certain techniques while examining new evidence data where available.

The WofE technique is based on comparing two factors: the size of an area containing a specific type of evidence data, and how many training sites fall within that area. Each weight applies to the entire area used to generate it. This results in a map with distinct weighted categories that have abrupt changes in weight at category boundaries, as seen in prior WofE studies. The abrupt changes at boundaries have no real geologic basis and are simply artifacts of the modeling process. The present study puts forward an approach to generate maps comprised of layers that change gradually across space by ‘smoothing’ the weights calculated in categories in a way that minimizes bias and inaccuracies. Smoothing functions relating evidence layer values to weights are reported so they can be applied to similar conditions elsewhere in future studies.

The present study also puts forward recommendations on how to best transform raw geologic information into a setting that can be analyzed mathematically. Different data processing approaches and evidence data were explored, including the use of different interpolators and density function parameters. Simple techniques were developed to isolate the highest correlating subsets of evidence data, apply different processing tools

and parameter variations, and to automate common processing and analysis techniques. The evidence data used in the present study reflect the two major geologic conditions believed to be driving geothermal occurrence in Nevada, permeability and elevated heat flow.

Permeability is the measure of the ability of a medium, such as rock, to permit fluid flow through it. Some rocks have intrinsic primary permeability, but secondary fracture permeability, provided by a system of connected fractures that allows fluid to pass through rock layers, is required to permit the high flow rates necessary to generate and sustain commercial electricity production at most hydrothermal systems (Williams, 2004; Williams et al., 2007).

Hydrothermal systems will eventually seal closed if there are no active or recent tectonic forces such as hydraulic fracturing or earthquakes to generate new permeability at a rate greater than the loss from mineral sealing and other forces (Gleeson and Ingebritsen, 2016). Hydrothermal fluids contain high concentrations of dissolved minerals in the form of ions in suspension. Many of these dissolved ions are only soluble at high temperatures and pressures. As fluids rise and lose temperature and pressure, minerals precipitate out, sealing the fracture pathways that have been providing permeability. Permeability in hydrothermal systems is therefore a dynamic property and requires active tectonics in long lived hydrothermal systems to generate new permeability faster than the system seals (Gleeson and Ingebritsen, 2016).

Sustained hydrothermal systems are typically associated with areas where natural fracture permeability is actively being generated. Locations of normal Quaternary faults were therefore used as evidence data in the present study to represent known discrete locations that may have elevated permeability. Only Quaternary faults were examined because older structures are more likely to be impermeable from chemical sealing. A map

depicting on-going crustal strain rates, or the rate of crustal deformation, was also used to represent permeability by depicting broad areas where elevated strain rates are likely to be expressed as higher slip rates along faults, which in turn promotes secondary permeability.

The resource potential, or energy extraction capacity of a hydrothermal system is dependent in part on the enthalpy (heat content) of the geothermal reservoir, which for liquid-dominated systems is largely a function of temperature. Most Great Basin geothermal systems are thought to be amagmatic, meaning that the thermal anomalies associated with the hydrothermal system are not believed to be derived from upper crustal magma chambers, but instead are believed to originate from elevated heat flow associated with a thin and extending crust. Heat flow is the measure of the rate of heat transfer from the Earth's interior to the surface. Understanding geographic variations in heat flow is the other main condition, along with permeability, used in the present study to model geothermal favorability. A map estimating rates of crustal heat flow across the study area was therefore used as an evidence layer to help estimate the potential magnitude of a possible system.

Four data sets were examined, three of which were ultimately chosen for generating geothermal potential maps for the present study. Locations of normal Quaternary faults were examined to represent known discrete locations that could have elevated permeability. A map depicting estimated crustal strain rates was used to represent areas where structures may have more active permeability generation and where potentially unknown permeable structures may exist. A map estimating variations in the rate of crustal heat flow was also used. Seismicity was examined but no significant correlations with training sites were discovered. Alternate approaches to characterize contributions from heat and Quaternary faults were explored before finding a best practice for each.

1.1 Geologic Setting

The Great Basin subprovince of the Basin and Range province consists an alternating series of elongate, roughly north-trending valleys and mountain ranges that extend east-west across the width of Nevada and the western part of Utah (Figure 1.1, Figure 1.2). This physiography results from active WNW-ESE-directed crustal extension accomplished by movement on NNE-striking normal faults oriented perpendicular to the direction of extension. Normal faults and associated systems of brittle fractures provide permeable pathways and reservoirs for naturally circulating upper-crustal geothermal fluids.

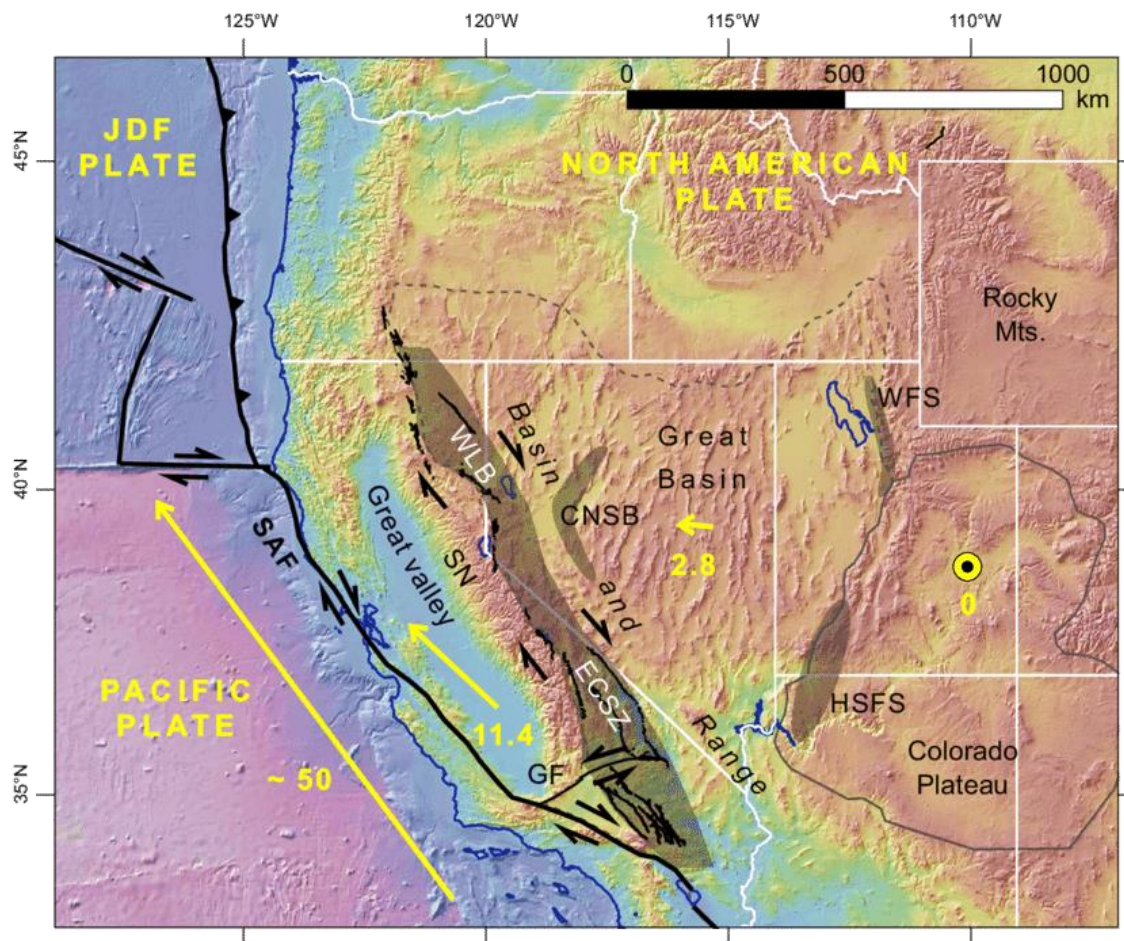


Figure 1.2: Tectonic overview figure from Pérouse and Wernicke (2017): Author's original caption included: 'Tectonic map of the western U.S., showing location of major plate boundaries and geographic features discussed in text. CNSB—central Nevada seismic belt; ECSZ—Eastern California shear zone; GF—Garlock fault; HSFS—Hurricane Sevier fault system; JDF—Juan de Fuca plate; SAF—San Andreas fault; SN—Sierra Nevada; WLB—Walker Lane belt; WFS—Wasatch fault system. Yellow arrows indicate geodetic velocities in a fixed Colorado Plateau reference frame, values in mm/yr (Bennett et al., 2003).'

Recent investigations have suggested that the complicated tectonics that characterize the western US, resulting from the collision of the North American and Pacific plates (Figure 1.2) has led to elevated permeability in parts of Nevada by transferring strain from strike-slip faults in western Nevada to the normal faults in north-central Nevada (Faulds et al., 2012). It is estimated that the Walker Lane (also known as the Walker Lane Belt) and Eastern California Shear Zone (Figure 1.1, Figure 1.2), overlapping systems of northwest-striking right-lateral strike-slip faults along the western edge of the Great Basin, accommodate up to 20% of the dextral motion between the Pacific and North American Plates (Bennett et al., 2003, Hammond et al., 2004, Kreemer et al., 2009) (Figure 1.1, Figure 1.2). A northward decrease in the geodetic velocity in the northern Walker Lane together with observations of high strain rates northeast of the Walker Lane appears to indicate that the termination of the Walker Lane is causing a transfer of dextral shear in the Walker Lane to transtensional and extensional strain in the normal faults northeast of the Walker Lane that developed coevally with Walker Lane faults (Faulds et al., 2012). The elevated rates of transtensional and extensional strain in the normal faults northeast of the Walker Lane are believed to be contributing to the high geothermal capacity of this region (Faulds et al., 2012).

1.2 Undiscovered Geothermal Systems

Surface manifestations of hydrothermal activity, such as hot springs, fumaroles, and hydrothermal alteration and mineral deposition, have been used to identify hydrothermal systems. Many of the known geothermal systems in the region however, do not display any expressions at the surface and are therefore deemed ‘blind.’ Blind systems account for approximately 39% of the known geothermal systems in the Great Basin (Faulds and Hinz, 2015). They were discovered either during regional geothermal drilling programs, or accidentally while drilling mineral exploration boreholes or agricultural wells (Faulds et al., 2015). This suggests that more systems exist which have yet to be discovered

throughout the Great Basin. Prior studies estimate that approximately 75% of all geothermal systems in the Great Basin are blind (Coolbaugh et al., 2007) and that the total electric power generation potential of undiscovered geothermal systems in Nevada is more than three times the current generation capacity from geothermal power plants (Williams et al., 2008).

Blind geothermal systems can be challenging to detect, thus justifying a systematic statistical approach to identifying the most favorable locations to explore. Blind geothermal systems are known to be similar to conventional identified hydrothermal systems in the sense that both types possess a permeable reservoir allowing hydrothermal fluids to circulate at depth (Dobson, 2016). Several conditions can prevent hydrothermal systems from being expressed at the earth's surface (Koenig and McNitt, 1983; Coolbaugh et al., 2007; Dobson, 2016) including: the presence of a thick geologic seal, involvement of fault or fracture systems that do not penetrate to the earth's surface due to being sealed or being buried, having a depressed water table or overlying cold-water aquifer, being smaller than other geothermal systems in the same geologic setting, or simply being too deep to have fluid pathways that reach the surface (Dobson, 2016).

1.3 Training and Evidence Data

1.3.1 Training Data: Known Geothermal Systems

Locations of 55 known geothermal systems were obtained from a United States Geological Survey (USGS) report detailing identified geothermal systems with temperatures estimated at or above 90° C in Nevada (Williams et al., 2008). These locations were used as training sites, the data which serve as benchmarks to measure how strongly the evidence data correlated with locations of known hydrothermal activity.

1.3.2 Evidence Data: Quaternary Faults

Locations and attributes of Quaternary faults were obtained from the USGS Quaternary Fault and Fold Database (QFFDB) of the United States (USGS et al., 2006). In the current version of this database, every fault has attribute information relating to its slip sense (Figure 1.1), age of most recent movement (recency) (Figure 1.3), and slip rate (Figure 1.4). These attributes were examined to assess which subsets of the database associated most strongly with training sites. The identification of higher correlating subsets has two advantages; 1) improved understanding of the controls on geothermal activity and 2) more focused targeting.

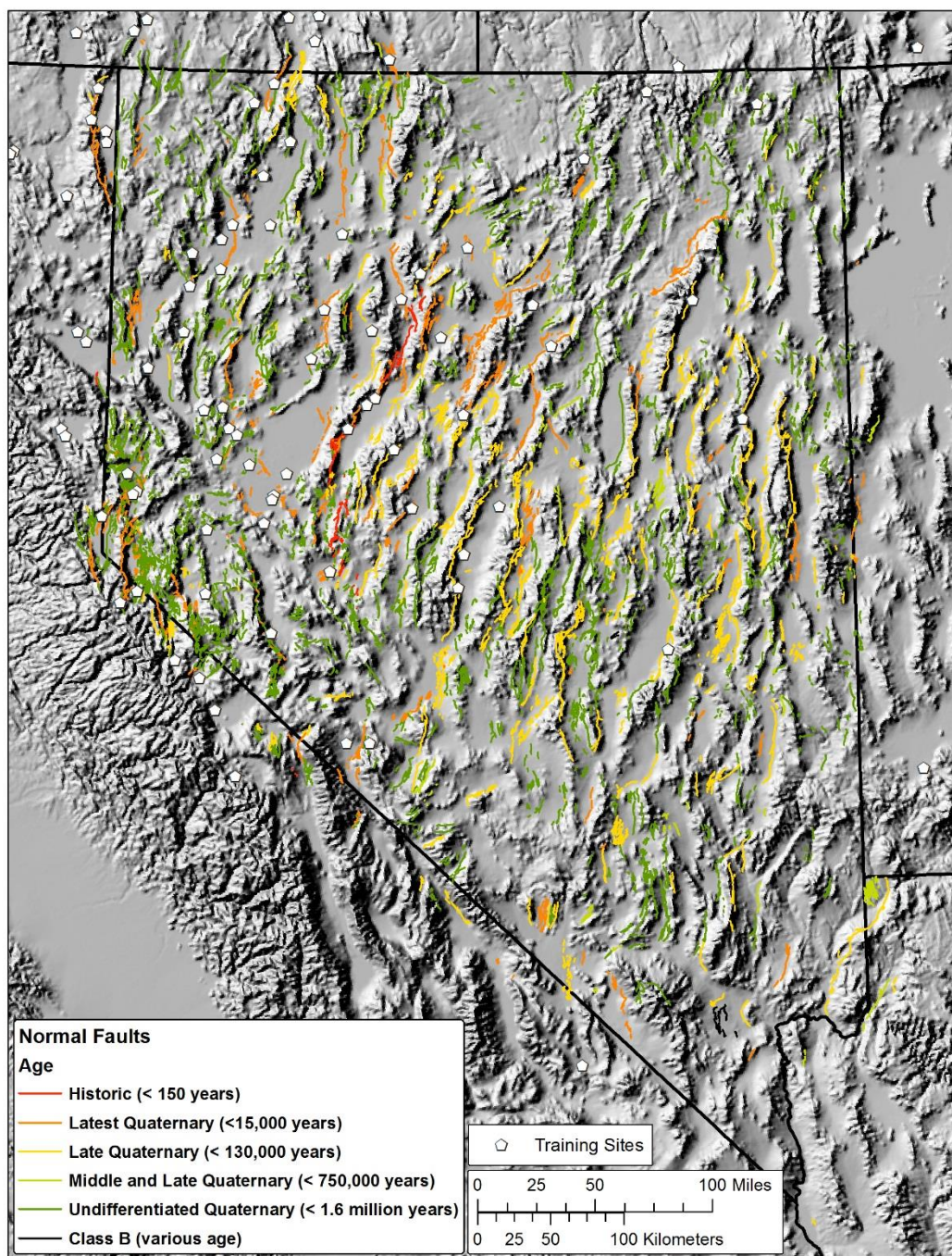


Figure 1.3: Normal faults in Nevada by recency. Normal faults are depicted as lines colored by their recency with warmer colors representing younger faults and cooler colors representing older faults. Identified moderate and high temperature geothermal systems used as training sites are depicted white pentagons.

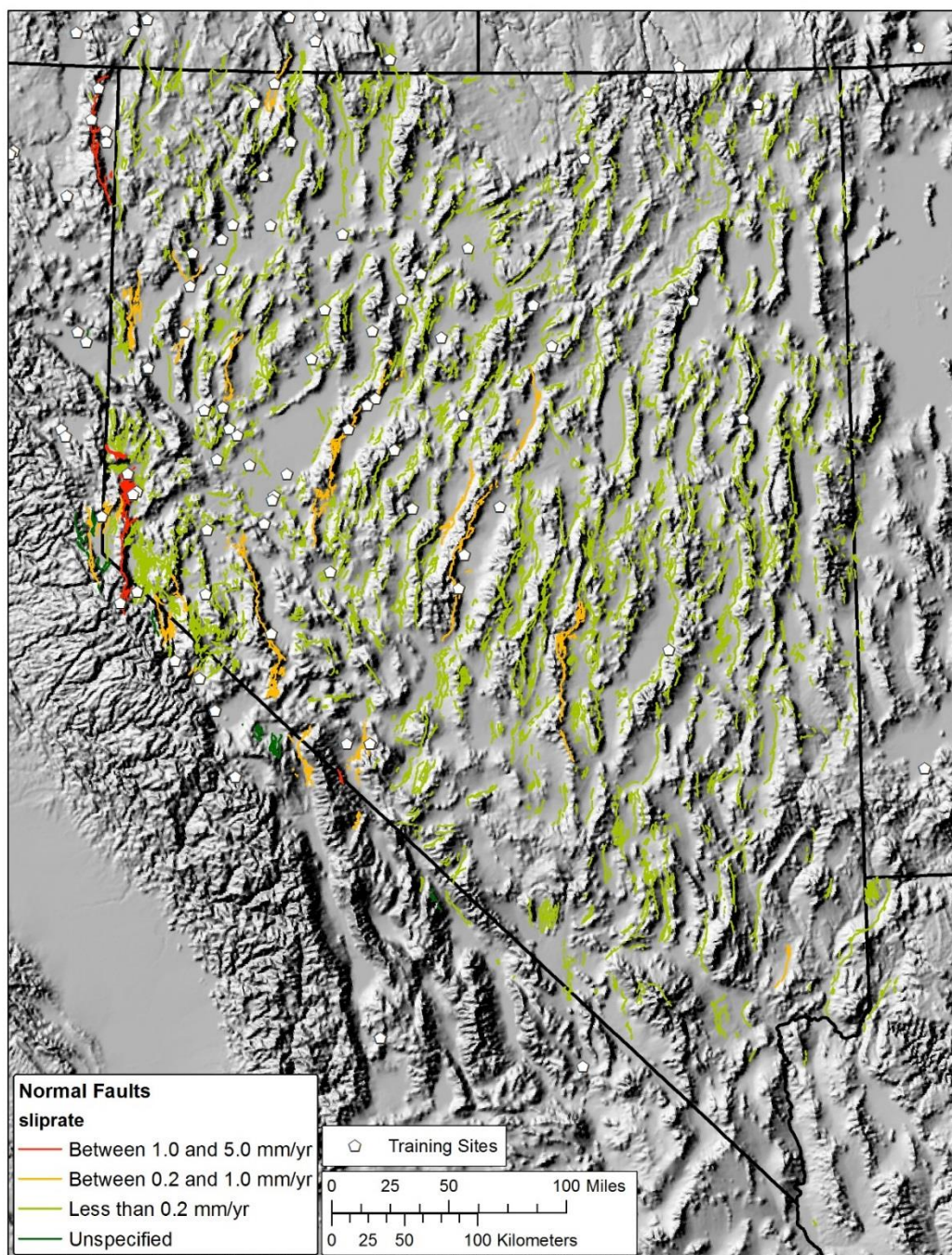


Figure 1.4: Normal faults in Nevada by slip rate. Normal faults are depicted as lines colored by their slip rate with warmer colors representing faults with higher slip rates and cooler colors representing faults with lower slip rates. Identified moderate and high temperature geothermal systems used as training sites are depicted as white pentagons.

Initial examination revealed that 86% of Nevada lies within 10km of a Quaternary fault, and 54% lies within 4km. This can be visualized in Figure 1.1, which shows the distribution of faults in Nevada colored by their slip sense. Applying positive weights to such a large portion of the state would risk diluting predictions by weighting favorable areas too low and unfavorable areas too high. It was therefore considered important to evaluate subsets of the QFFDB based on their slip sense, recency, and slip rate to see if proximity to certain types of faults associated more strongly with geothermal activity than others and to identify optimal buffer distances.

A completely different approach was also explored that examined a fault's estimated likelihood to dilate or slip. Dilation tendency (TD) and slip tendency (TS) are parameters calculated for faults based on their attitude relative to the local direction of the stress field. Values for this parameter were calculated by Dr. Drew Siler, USGS using techniques he and others developed for geothermal assessments (Siler et al., 2016, Siler et al., 2017, Faulds et al., 2015). Dr. Siler was provided with the QFFDB faults used in the present study. For every segment of every fault, Dr. Siler calculated a value for TD and TS. In a personal communication with Dr. Siler, he defined the parameters as follows:

'Dilation tendency (TD) is the ratio of all the components of the stress tensor that are normal to the plane [Ferrill et al., 1999]. Slip tendency (TS) is the ratio between the shear components of the stress tensor and the normal components of the tensor [Morris et al., 1996].' – Dr. Drew Siler, USGS

1.3.3 Evidence Data: Crustal Strain Rates

A digital map depicting crustal strain rates was obtained from a Nevada Bureau of Mines and Geology study that interpreted geodetic horizontal velocities of Global Positioning System station locations (Kreemer et al., 2012). This map estimated the rate of

deformation expressed as the second invariant strain rate tensor by interpolating measurements from geodetic stations. Values ranged throughout the study area from a minimum of 0.021×10^{-9} /yr in eastern Nevada to a maximum of 231.634×10^{-9} /yr in the west (Figure 1.5, Figure 1.1). These data were used directly in the analysis.

The second invariant was calculated by taking the *'square root of the sum of squares of the four tensor components'*, thereby depicting overall deformation with *'no indication of orientation, or style of strain.'* (Blewitt et al., 2002). The second invariant was chosen instead of other components, such as dilatational or shear strain, or strain style. This decision was based on findings from Faulds et al. (2015) and earlier studies by Coolbaugh and others (Coolbaugh, verbal communication, 2018) at the Nevada Bureau of Mines and Geology and Nevada Geodetic Laboratory, in which maps depicting each component of strain were compared to known benchmarks to assess correlations. Faulds et al. (2015) state, 'Based on the statistical correlations and map patterns, the 2nd invariant of strain was chosen as the most stable and representative measure of strain rate with which to predict geothermal potential... although many of the other parameters performed nearly as well.' One might expect a map depicting dilatational strain to be a more useful indicator than overall deformation, but this was not the case. This may be explained by the fact that separating the individual components increases uncertainties, especially in areas with a limited number of measuring locations, making local variation more difficult to accurately characterize.

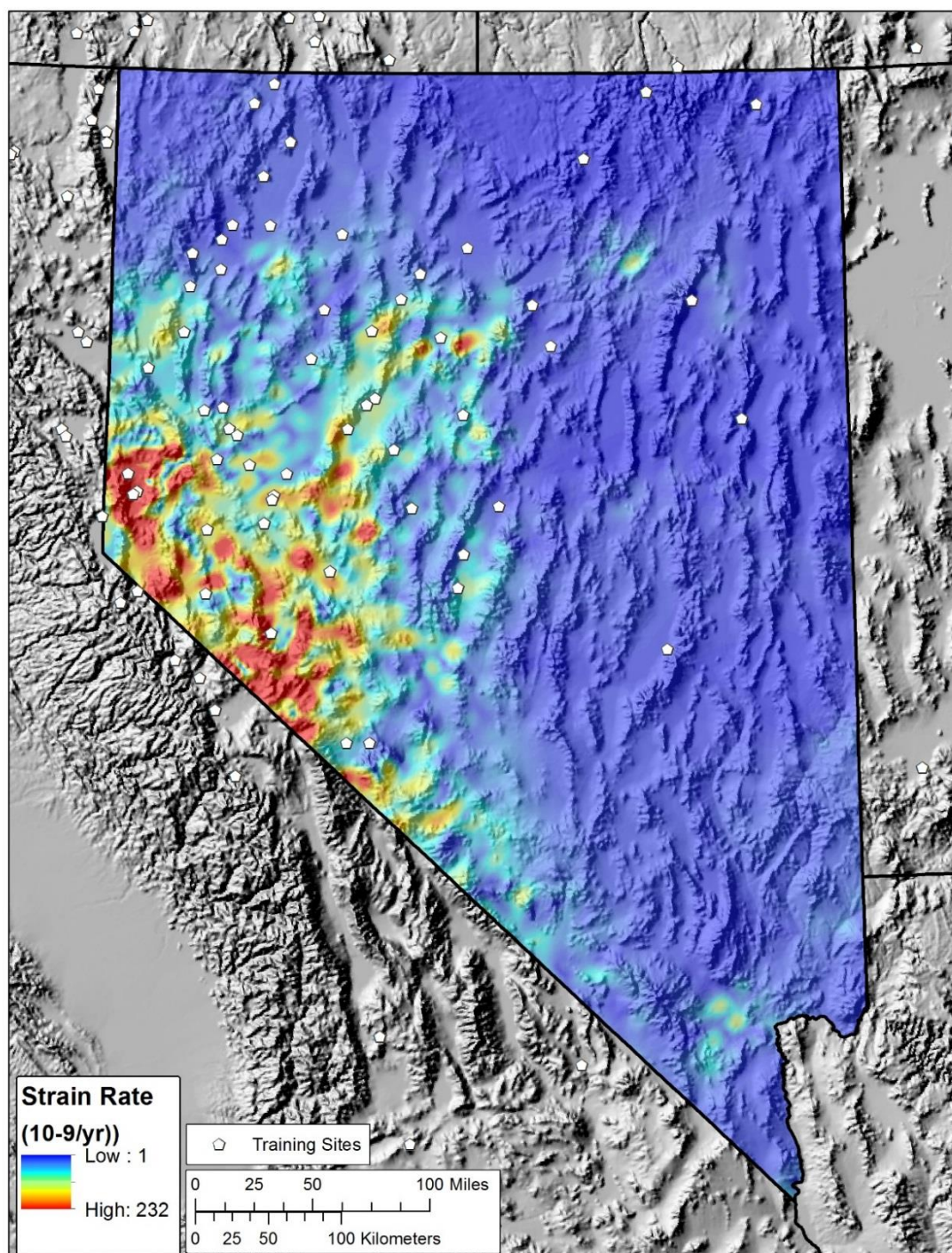


Figure 1.5: Estimated strain rate within the Nevada study area. Warmer colors depict higher rates, cooler colors depict lower rates. Rate values represent the second invariant strain rate tensor in units of 10^{-9} /yr. Identified moderate and high temperature geothermal systems used as training sites are depicted as white pentagons.

1.3.4 Evidence Data: Crustal Heat Flow

Estimated crustal heat flow values and locations were obtained from USGS and Southern Methodist University Geothermal Lab databases (Williams and DeAngelo, 2008, Williams and DeAngelo 2011, Blackwell et al., 1989, Blackwell and Richards, 2004). The rate of heat flow is calculated for a well by multiplying its vertical temperature gradient by the thermal conductivity of the rock. A well's temperature gradient was calculated by measuring the rate of increase in temperature with increasing depth over a portion of the depth profile identified by authors as representing affects from background crustal heat flow only. Thermal conductivity is measured in lab tests on rock samples obtained during drilling. Williams and DeAngelo (2011) provides the following description of uncertainties associated with these data:

'The thermal conductivity of rocks can be measured in the laboratory to an accuracy of better than 5% (e.g., Sass et al., 1971), and the uncertainty in the measured temperature gradient can be significantly less than 1 %, which suggests that individual heat flow measurements uncertainties can be reduced to less than $\pm 5\%$. However, these uncertainties reflect the performance of the laboratory and borehole logging equipment, not the epistemic uncertainty associated with the question of whether these measurements accurately represent background crustal heat flow and can be used to estimate temperature at depth. Even in the best of circumstances, with high precision equilibrium temperature logs and numerous samples for thermal conductivity measurements, heat flow determinations have to account for a large number of potential disturbances, such as thermal refraction, topography, sedimentation or erosion, conductive transients, and shallow groundwater flow. Although accurate corrections can be applied when these effects are recognized and quantifiable, in many cases the relevant information is unavailable or only sufficient to place approximate bounds on the magnitude of the

disturbances... For most of the western US, uncertainties in heat flow are probably on the order of 10 to 15 %.'

Heat flow data were used to interpolate estimated background heat flow rates across the study area (Figure 1.6). Two different interpolation techniques were used to see which correlated more strongly with training sites.

Sediments in basins, which have relatively low thermal conductivities, can act as thermal blankets, thereby decreasing heat flow rates and increasing temperature gradients in parts of basins with thicker sediments. Maps were produced to estimate the temperature at 3 km depth considering affects from sediment thickness to test whether estimated temperature at depth correlated more strongly with training sites than heat flow. Heat flow maps generated by the two interpolators were transformed to estimate the temperature at 3 km using a 'depth to basement' map (Saltus and Jachens, 1995) to quantify the thickness of sediments in basins. This was done using techniques and equations applied in Williams and DeAngelo (2011). This approach accounted for changes in thermal conductivity with temperature and incorporated influences from radiogenic heat production. For each cell in the study area, the estimated value of heat flow was transformed to an estimate of temperature at 3 km depth using the equation and parameters reported in Williams and DeAngelo (2011). The analysis and subsequent weighting tests were performed using the native study area and tessellation of the depth to basement map. One of the maps estimating temperature at 3 km depth was included as an appendix (Appendix 1); it shows the study area and cell sized used in the analysis. This map was generated as a potential evidence layer for this analysis, but it may also be of interest as a stand-alone product. In total, four maps derived from heat flow data were examined: for each of two interpolators, maps were created depicting heat flow and estimated temperature at 3 km depth.

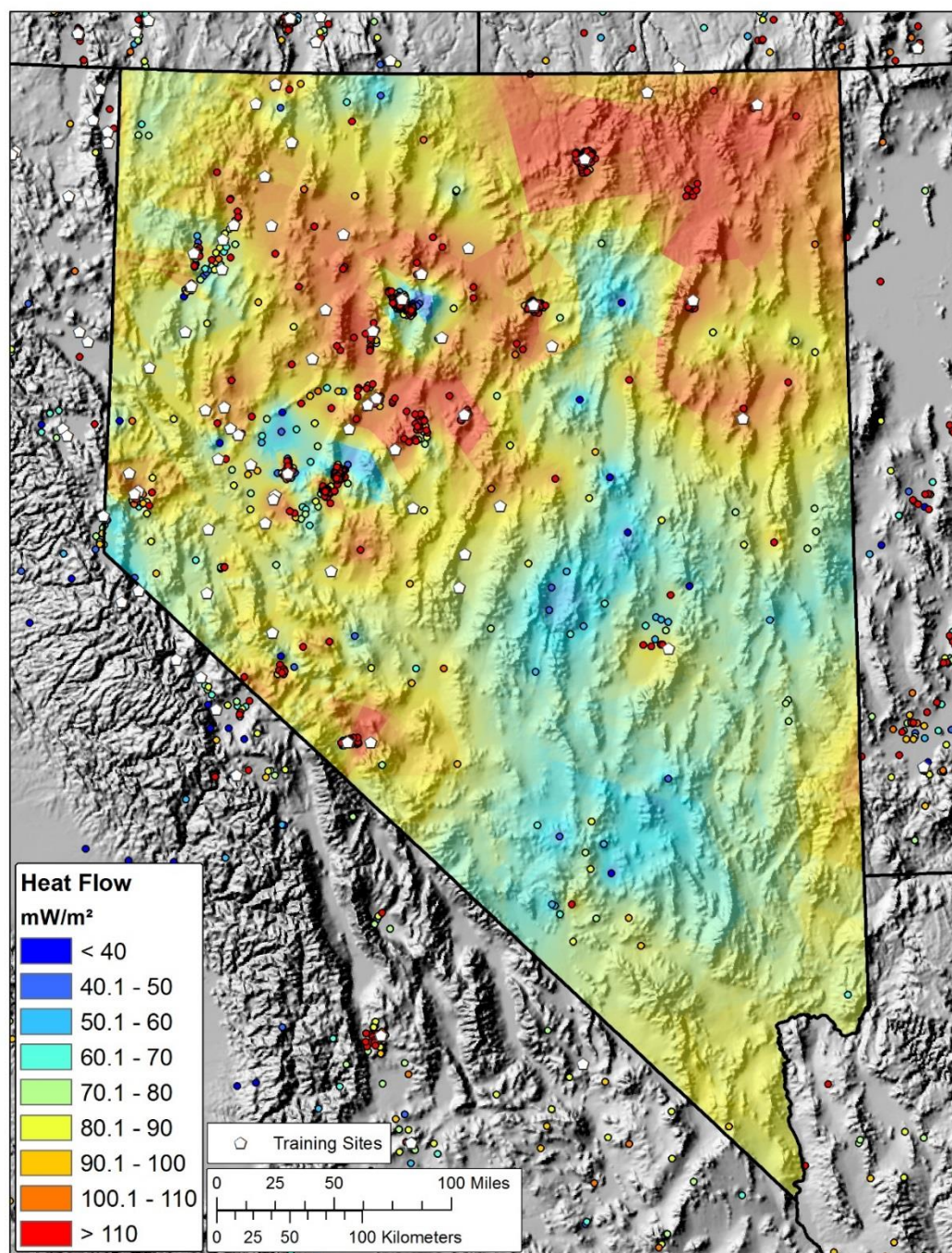


Figure 1.6: Estimated crustal heat flow in Nevada. The surface was interpolated from heat flow wells, depicted as small circles colored by their heat flow value in units of mW/m^2 . Warmer colors depict higher rates, cooler colors depict lower rates for both the points and the surface. Identified moderate and high temperature geothermal systems used as training sites are depicted as the larger white pentagons. Estimated crustal heat flow rate values and locations were obtained from USGS and Southern Methodist University Geothermal Lab Databases (Williams and DeAngelo, 2008, Williams and DeAngelo 2011, Blackwell et al., 1989, Blackwell and Richards, 2004).

1.3.5 Evidence Data: Earthquakes

An earthquake catalog was obtained with the full record of every known earthquake in Nevada (NCEDC, 2016). Earthquakes were filtered out to remove events that are too weak to have been correctly measured given the accuracy of the seismic network during different historical periods of time using the same parameters detailed in ‘Table P-2’ in Faulds et al., 2015 to reduce errors associated with unreliable data. The filtered catalog was investigated using different spatial techniques, tool parameters, and weightings.

1.4 Weights of Evidence

1.4.1 Weights of Evidence Technique

The WofE technique uses Bayesian statistics to measure how strongly an evidence layer correlates with known locations of the phenomenon being modeled. The present study used the WofE tools in the ArcSDM tool package (Raines et al., 2000; Geological Survey of Finland, 2018) in a Geographic Information Systems (GIS) setting using ArcGIS software (ESRI 2017). The toolset requires that users convert evidence data into raster layers with integer codes that represent ranges of the native evidence data.

A central concept in Bayesian statistics involves the use of ‘prior’ and ‘posterior’ probabilities. The prior probability is simply the likelihood of encountering a phenomenon, in our case a geothermal system, at any given location due solely to chance. If one had no prior knowledge of where a geothermal system would be likely to exist, the chances of correctly predicting the location of a geothermal system would be the prior probability, the number of training sites divided by the number of area ‘unit cells’ being examined.

The WofE technique bases calculations on the assumption that each training site occupies one ‘unit cell.’ The unit cell therefore represents the size of each training site and is the counting unit for WofE calculations. The present study used a 1 km² unit cell as a conservative estimate of the spatial area covered by a typical geothermal system in Nevada. Unit cells containing training sites therefore account for 55 km² of the total study area because each of the 55 training sites fell within different 1 km² unit cell.

The posterior probability of a location is the estimated probability of encountering the phenomenon at any given location after considering the evidence data. Values of posterior probability greater than the prior probability indicate a relatively favorable area, while values less than the prior probability indicate a less favorable area. Evidence data in this case includes the geological and geophysical indicators for geothermal favorability.

Weights are calculated by comparing the portion of cells with training points contained within a spatial pattern to the portion of the total unit cells represented by the spatial pattern not containing training sites. The following equations (Bonham-Carter, 1994) show how weights are calculated for a spatial pattern where P is the probability of object occurrence. B refers to the favorable area of the evidence layer (pattern 1). \bar{B} refers to the non-favorable area of the evidence layer (pattern 2). D refers to the presence of deposits, \bar{D} refers to the absence of deposits. W_+ is the positive weight of evidence and is an expression of the level of positive correlation between the presence of the evidential (controlling) theme and the training points.

$$W_+ = \ln \left(\frac{P(B|D)}{P(B|\bar{D})} \right) \quad (1 - 1)$$

$$W- = \ln \left(\frac{P(\bar{B}|D)}{P(\bar{B}|\bar{D})} \right) \quad (1 - 2)$$

Equations 1-1 and 1-2 can be expressed alternatively as:

$$W+ = \ln \left(\frac{\frac{\# \text{ Cells With Training Points}_{\text{Inside Pattern}}}{\# \text{ Cells With Training Points}_{\text{Total}}}}{\frac{\# \text{ Cells}_{\text{Inside Pattern}} - \# \text{ Cells With Training Points}_{\text{Inside Pattern}}}{\# \text{ Cells}_{\text{Total}} - \# \text{ Cells With Training Points}_{\text{Total}}}} \right) \quad (1 - 3)$$

$$W- = \ln \left(\frac{\frac{\# \text{ Cells With Training Points}_{\text{Outside Pattern}}}{\# \text{ Cells With Training Points}_{\text{Total}}}}{\frac{\# \text{ Cells}_{\text{Outside Pattern}} - \# \text{ Cells With Training Points}_{\text{Outside Pattern}}}{\# \text{ Cells}_{\text{Total}} - \# \text{ Cells With Training Points}_{\text{Total}}}} \right) \quad (1 - 4)$$

Each spatial pattern for which a weight can be calculated reflects a range of the evidence data. A classic example involves a binary weighting of a distance raster. In this scenario, one would create a raster that shows the distance (for each cell in the raster) from a feature of interest such as a Quaternary fault. Every cell in the study area would then be categorized with an integer code denoting how far it is from a Quaternary fault. Weight statistics would then be calculated for each increasingly large category. A binary distance threshold would then be determined by identifying the distance with either the highest correlation or the lowest error. This threshold acts as the boundary between places with positive correlation within the threshold distance and negative correlation beyond the threshold distance.

This example would result in two weight values. The $W+$ is applied to the area within the threshold distance and the $W-$ is applied to the area outside the threshold. $W-$ is calculated using the same equation reported for $W+$ but examines spatial patterns outside the threshold. The following excerpt from Bonham-Carter (1996) conveys the meaning of

the weight values in an example where there is a positive correlation measured between the binary evidence pattern and the training sites:

“... W_+ is positive, and W_- is negative, due to the positive correlation between the points and the binary pattern. Conversely W_+ would be negative and W_- positive for the case where fewer points occur on the pattern than would be expected due to chance. If the deposits are independent of whether the pattern is present or not, then $W_+ = W_- = 0$, and the posterior = the prior.” (Bonham-Carter, 1994)

Positive weights indicate a positive correlation where more training sites fall within an evidence pattern than would be expected due to chance. Conversely, negative weights indicate a negative correlation where fewer training sites than would have been expected by chance fall within the pattern. For binary evidence patterns, values for W_+ and W_- will always have an opposite sign unless they both equal zero.

When multiple evidence layers are used to predict occurrences, and if those evidence layers are not conditionally independent in terms of predicting training sites, the WofE technique will typically over-predict the number of systems in the posterior probability map generally (Bonham-Carter, 1994), particularly where conditionally dependent map patterns coincide. It can be standard practice to discard models that do not meet conditional independence standards, though Coolbaugh et al. (2005) notes that these models can still be used to show relative favorability. Agterberg-Cheng Conditional Independence (ACCI) tests (Agterberg and Cheng, 2002) were used from the ArcSDM tool package to assess conditional independence for all posterior probability maps created for the present study.

Two basic types of tests were used to calculate weights for evidence layers. An iterative binary weight test using cumulative statistics was typically run first to explore the data

and identify optimal thresholds before reclassifying the evidence layer for use in a multi-class ‘categorical’ weight test.

1.4.2 Cumulative Weight Test

An iterative binary weight test was the first step in the WofE analysis used for understanding the correlation between non-categorical evidence and training data and functions as an exploratory tool. The test works by comparing the number of training sites to the measured area of progressively increasing bin ranges of the evidence data. Using the example of a binary reclassification of Quaternary faults, the test calculates W_+ and W_- for the first class (for example, areas inside and outside a fault distance buffer of 250 m) by comparing the training site counts and area measurements for the zones on either side of the distance threshold. For the next class, the test calculates W_+ and W_- of the areas represented by the combined first two classes (for example, areas inside and outside a fault distance buffer of 500 m). W_+ and W_- for the third group are calculated based on the cumulative area of the first three groups, and so on. For each calculated weight, a corresponding standard deviation is also reported.

This process results in a table of values that can be plotted graphically to more easily grasp the patterns (Figure 1.7). In Figure 1.7, the x-axis relates to class number. In this case the class value labels have been replaced with the distance to a fault values they represent. The y-axis on the left relates to W_+ , the red points and red line represent the W_+ value at each cumulative class bin, the blue shading around the red line indicates the standard deviation of the weight. The y-axis on the right shows training point count; the number of training points in each cumulative bin is represented by blue points. When a positive correlation exists, W_+ will typically rise to a maximum value quickly before declining and plateauing farther along the x-axis, as seen in Figure 1.7. In such a

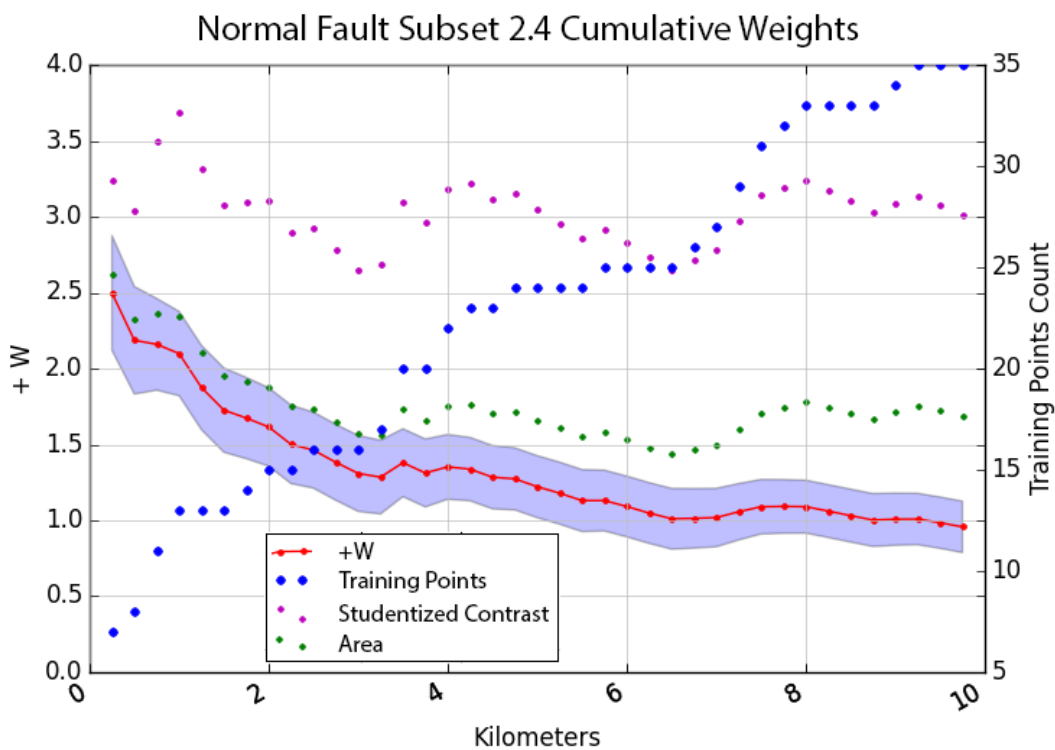


Figure 1.7: Ascending weight plot for normal fault subset 2.4. Contains faults equal to or younger than 'latest Quaternary' (the plot numbering sequence is explained in Figure 2.2). The x-axis depicts distance from faults in km. The red points and line represent W_+ and use the left axis. The green points represent contrast ($W_+ - W_-$) and use the left axis. The blue points represent training point count and use the right axis. The purple points represent half the value of the studentized contrast and use the left axis.

situation, it is also typical to see the count of training points quickly increase before plateauing. The green points represent the 'contrast', simply the absolute value of the $W+$ minus the $W-$; a higher contrast indicates a higher overall association of the training data with the evidence layer. Purple points represent 'studentized contrast,' which is the contrast divided by its standard deviation and is thus a measure of the confidence in the contrast; in this plot these points use the left y-axis but only half of their value was plotted so they could be viewed in the same scale range, because their values tended to be higher than $W+$ values. A value of 2 or greater implies high confidence that the reported contrast is greater than zero (Bonham-Carter, 1994) and could therefore provide reliable predictive information. The decision of where to place the binary threshold can either be determined by choosing the class with the highest statistically significant positive weight, the highest contrast, or the highest studentized contrast (Bonham-Carter, 1994). Once the threshold is determined, the evidence layer can be reclassified into two patterns to produce a simple binary predictive layer. However, more predictive value can commonly be obtained from an evidence layer by dividing it into multiple (> 2) patterns. In such a case, as applied in the present study, the information obtained from the initial binary weight plot was used to design a multi-class evidence layer using categorical statistics as described below.

1.4.3 Categorical Weight Test

The categorical weight test is not cumulative. Each category is weighted based only on the number of training sites in the spatial area it encompasses.

Evidence layers that depict phenomena that vary gradationally across space like strain rate or heat flow can be split into a series of independently weighted categories that each depict a subset of the full range. A cumulative test can be used to guide where to define these bin ranges, but ultimately the process of finding ideal categorical bin ranges involves trial and error. There are no hard rules for how to do this, but the process can be guided by some basic principles.

If the evidence is positively correlated with the training sites for a continuous phenomenon like strain rate, one would expect higher strain rates to correlate more strongly with training sites than lower strain rates. This can be modeled by breaking the strain rate map into categories or bins that represent ranges of strain rate values. A weight can be calculated for each category independently of the other categories (not cumulative). It is important that these categories do not cover vastly different amounts of area to avoid creating biased categories. Each of these categories should contain a similar number of training sites for the same reason. It is also important to choose bin ranges that result in a weight pattern from category to category that decreases or increases in a statistically significant manner.

Figure 1.8 shows the seven categories that were ultimately settled upon for the strain data. Category 1 contains the highest range of strain values; each subsequent category contains lower ranges. The weight (red line/points) decreases from each category to the next as one would expect to see when a positive correlation is present between training

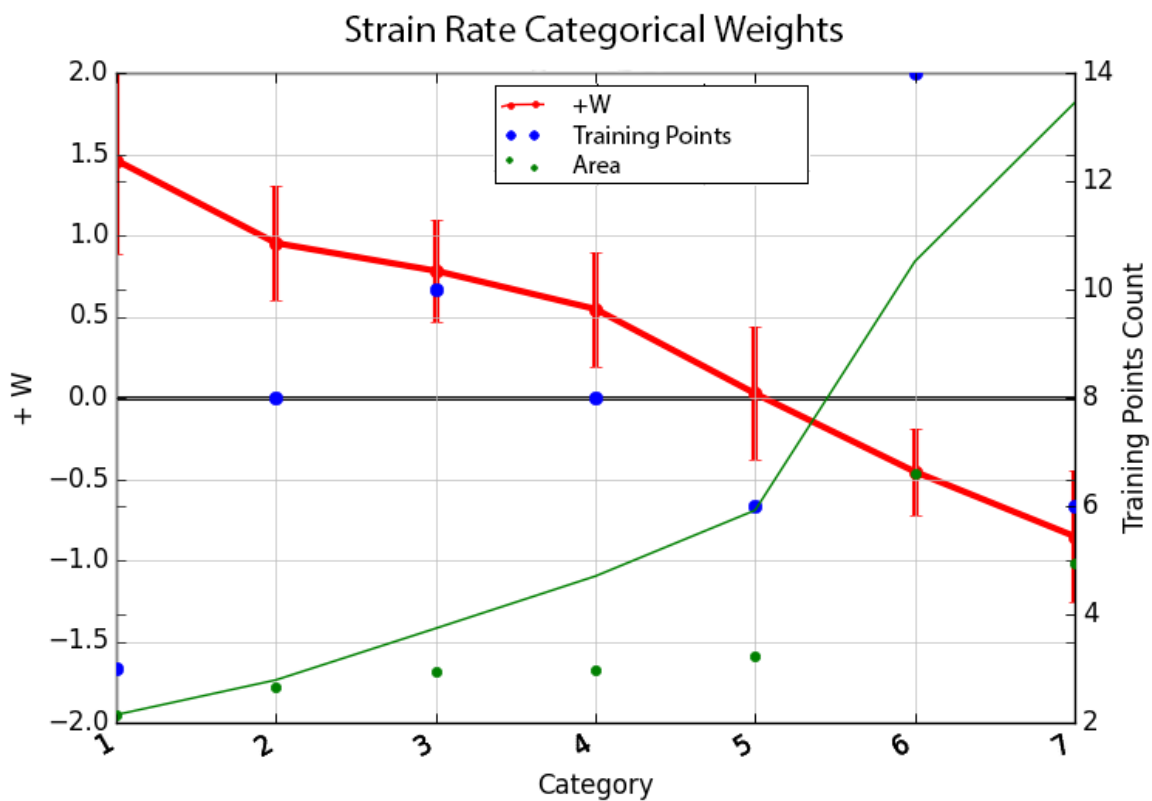


Figure 1.8: Categorical weight plot of strain rate categories by category. The x-axis depicts category numbers, not native units (strain rate). All x-axis values of all points on this figure are plotted at their native unit midpoint. The red points and line represent W_+ and use the left axis. Error bars around weight values indicate standard deviation of the weight. The blue points represent training point count and use the right axis. The green points represent percent area associated with each bin, on an axis of 0 (bottom of graph) to 100% (top of graph). The green line represents cumulative percent area, also plotted with 0 at the bottom of y-axis and 100% at top of y-axis.

and evidence data. The standard deviation of each weight is depicted with red error bars. The relative area covered by each category is depicted by a green dot, for which there is no y-axis scale shown. The green line represents cumulative area from 0 – 100%. Many bin ranges were attempted before this scenario was settled upon. Of the binning scenarios attempted, this scenario best allowed for the steady decline of W_+ while maintaining similar area sizes per bin (green dot height). Confidence in categorical weights can be assessed by confirming that each weight value is significantly different from adjacent weight values. This can be visualized on plots using error bars to represent the standard deviation of each weight. Ideally, weight values should fall outside the error-bar range of adjacent weight values, but in practice, overlap is seen in some cases where all other considerations were well-met (steadily decreasing weights, similar sized area and training point count).

Figure 1.9 shows the same data as Figure 1.8, but the x-axis was transformed to show the actual strain rate values represented by the categories. Viewing the data in this manner provides a more representative way of viewing the data and will become important for later attempts to model the weights at any point along the curve.

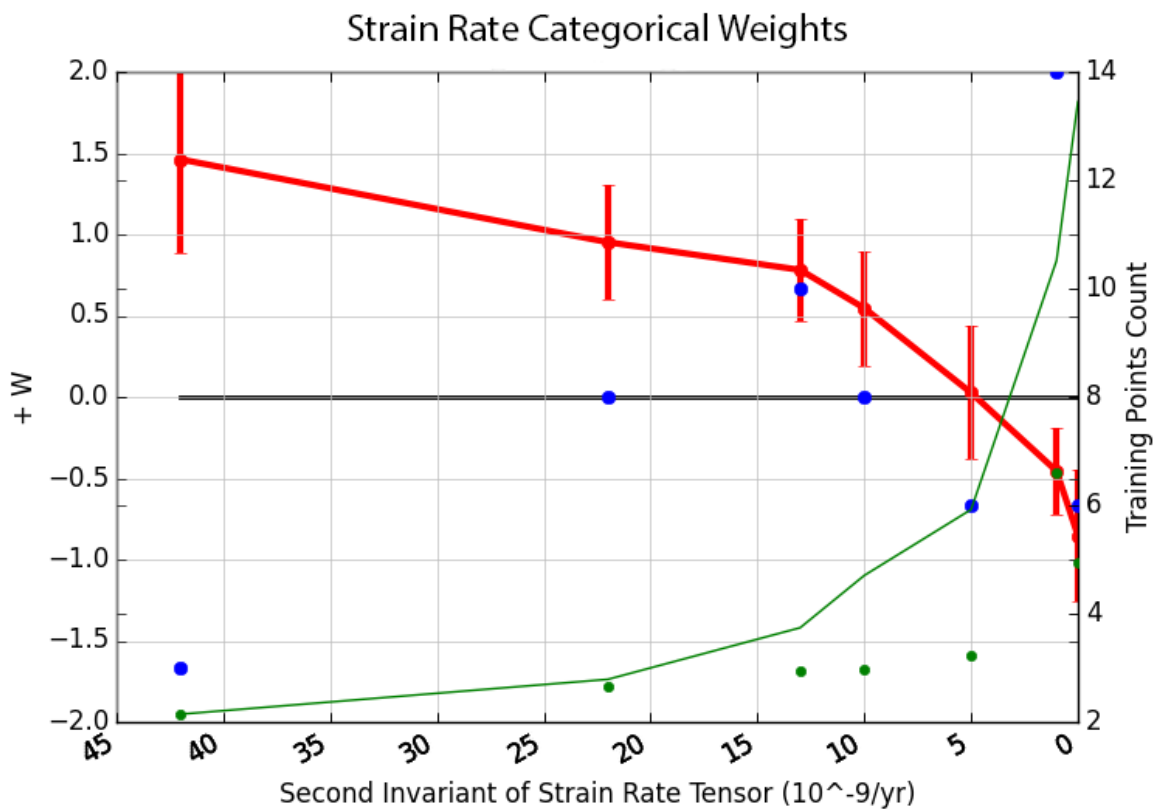


Figure 1.9: Categorical weight plot of strain rate categories by native unit. The X-axis depicts the native units (strain rate). X-axis values of all points on this figure are plotted at their native unit midpoint. The red points and line represent $W+$ and use the left axis. Error bars around weight values indicate standard deviation of the weight. The blue points represent training point count and use the right axis. The green points represent percent area associated with each bin, on an axis of 0 (bottom of graph) to 100% (top of graph). The green line represents cumulative percent area, also plotted with 0% at the bottom of y-axis and 100% at top of y-axis.

1.4.4 Posterior Probability Calculation

In a traditional WofE analysis, posterior probability maps can be calculated once weights for each pattern (category) of each evidence layer have been generated. Posterior probability is calculated by using weight values to modify the prior probability. The following equation (Bonham-Carter, 1994) shows how the posterior logit is calculated, the exponent of which equals posterior odds.

$$\text{posterior logit } (D|B_1 \cap B_2 \dots \cap B_n) = \text{prior logit}(D) + \sum_{i=1}^n W^+_i \quad (1 - 5)$$

Equation 1-5 uses the same nomenclature as equations 1-1 and 1-2. W^+ is W^- when the favorable i 'th map pattern is absent. The prior logit is the natural log of the prior odds. The prior odds are equal to the prior probability divided by 1 minus the prior probability. Similarly, the posterior logit can be converted to posterior probability by first taking the exponent of the posterior logit (which equals the posterior odds), then dividing by 1 plus the posterior odds.

Distance based features, such as the distance to the nearest fault, are traditionally depicted as a binary raster, with a positive weight within a threshold distance and a negative weight beyond the threshold. Continuous data types, such as heat flow and strain rate, are traditionally binned into several categories, each with an independently measured weight. The 'Calculate Response' tool in ArcSDM was used to calculate posterior probability maps by inputting recategorized rasters and categorical weight tables. The tool also generates an error surface that depicts standard deviation of the posterior probability map.

1.5 Prior Works

Prior geothermal assessments provide the basis for decisions made in the present study regarding which geologic and geophysical data to investigate as potential evidence data and which processing techniques to apply when interpreting raw geologic data into products that can be used in a WofE analysis. This section introduces the prior works that informed decision making in the present study but a comparison of modeling results and technique effectiveness with prior studies will be detailed in the Discussion section.

1.5.1 Coolbaugh et al., 2005

Coolbaugh et al. (2005) assessed geothermal favorability across the Great Basin and surrounding areas using logistic regression with a 1 km² grid cell size (Figure 1.10 and Coolbaugh et al., 2005b). For evidence data, Coolbaugh et al. (2005) used data representing combined gravity and topographic gradients, combined crustal dilation derived from geodetic motion measurements and Quaternary fault slip rates, estimated temperature gradient in the first kilometer of the crust, and a weighted sum of earthquake magnitudes. The evidence layers used in Coolbaugh et al. (2005) represented proxies for the same processes being modeled in the present study. The present study was able to take advantage of newer and in some cases more robust data sets than were available for prior assessments. Many of the geographic and data-manipulation techniques used in Coolbaugh et al. (2005) were used in subsequent geothermal assessments and were adopted for use in this study. Examples include the methodology for interpreting seismicity, and for handling of non-binary evidence data in WofE testing.

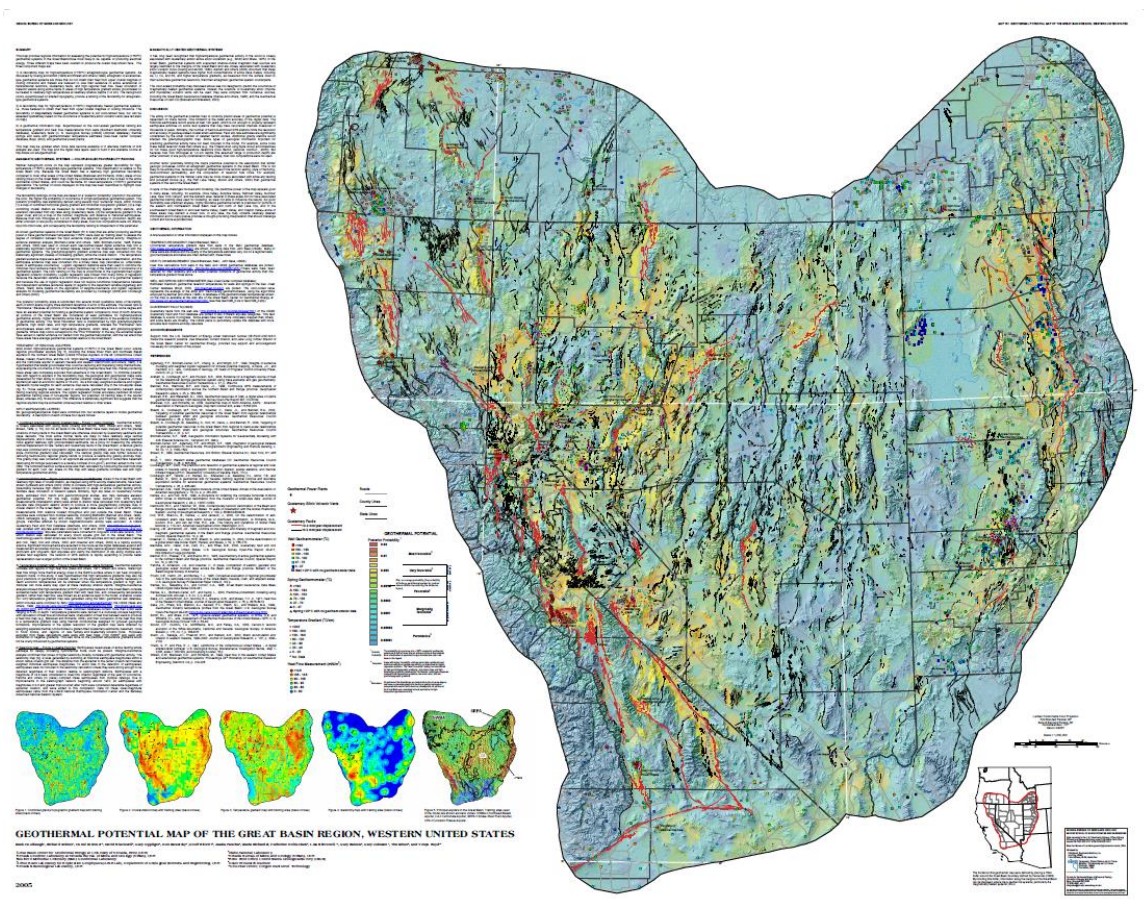


Figure 1.10: Geothermal potential map from Coolbaugh et al., 2005b: This study combined data representing combined gravity and topographic gradient, combined GPS-derived crustal dilation and fault dilation, seismicity, thermal gradient, and aquifers to predict geothermal favorability in the Great Basin using logistic regression.

1.5.2 Williams and DeAngelo, 2008

Williams and DeAngelo (2008) assessed geothermal favorability across the western United States using WofE with a 2 km x 2 km grid cell size (Figure 1.11). Williams and DeAngelo (2008) used data representing heat flow, Quaternary magmatism, Quaternary faulting, seismicity, and tectonic stress as evidence data. Many decisions about which evidence data to investigate and what techniques to use in Williams and DeAngelo (2008) were informed by Coolbaugh et al. (2005), Coolbaugh et al., (2005b), as well as other works (Williams and DeAngelo, 2008). The present study used similar techniques to Williams and DeAngelo (2008) with regards to interpretation of data representing heat flow, Quaternary faults, and seismicity.

Model 13 Weights of Evidence Surface

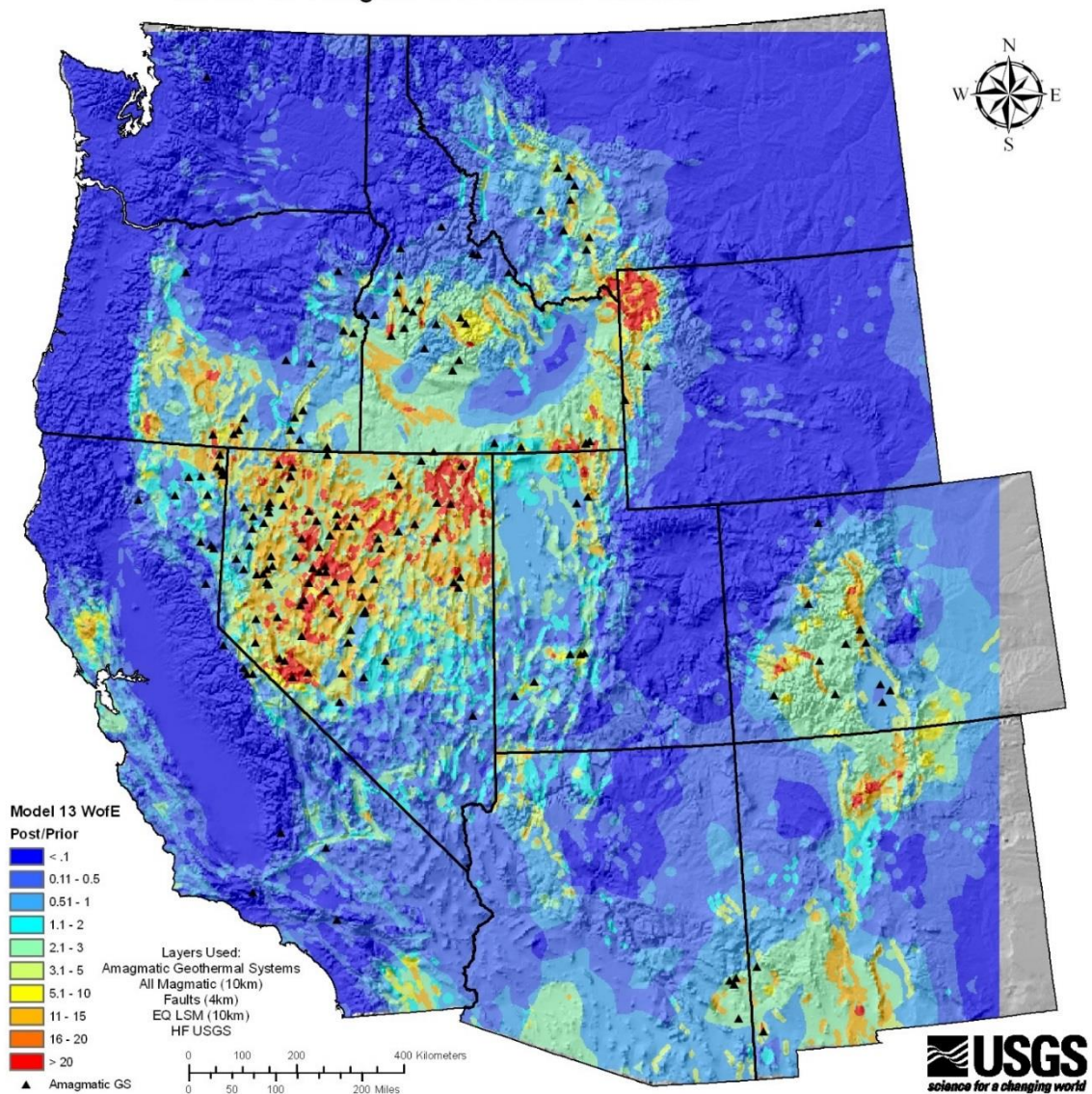


Figure 1.11: Amagmatic geothermal potential map from Williams and DeAngelo, 2008: This study combined data representing tectonic stress, Quaternary faults, seismicity, and heat flow to predict geothermal favorability in the western United States using WofE.

1.5.3 Faulds et al., 2015

Faulds et al. (2015) assessed geothermal favorability across a portion of Nevada (Figure 1.12) using weights determined by experts guided by WofE and logistic regression correlations with a 250 x 250 m minimum grid cell size (Figure 1.13). Faulds et al. (2015) used data representing estimated temperature at 3 km depth, favorable structural settings, horizontal gravity gradient, geodetic strain rate, seismicity, as well Quaternary faults and information regarding their recency, slip & dilation tendency, and slip rate as evidence data (Figure 1.14). The present study did not adopt any new techniques from Faulds et al. (2015) but it was informed by their use of fault recency information, slip and dilation tendency, and strain rate.

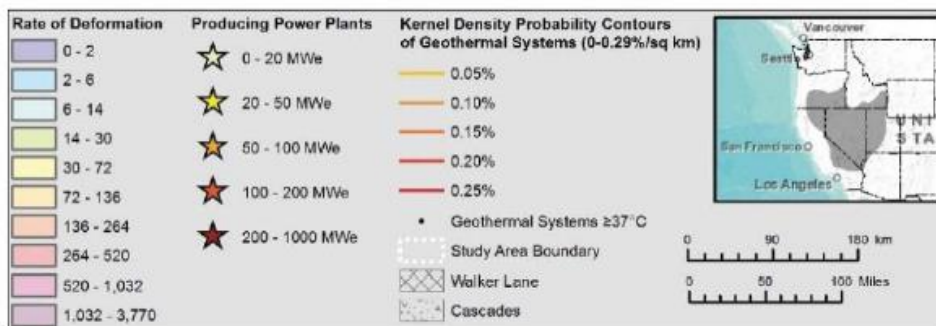
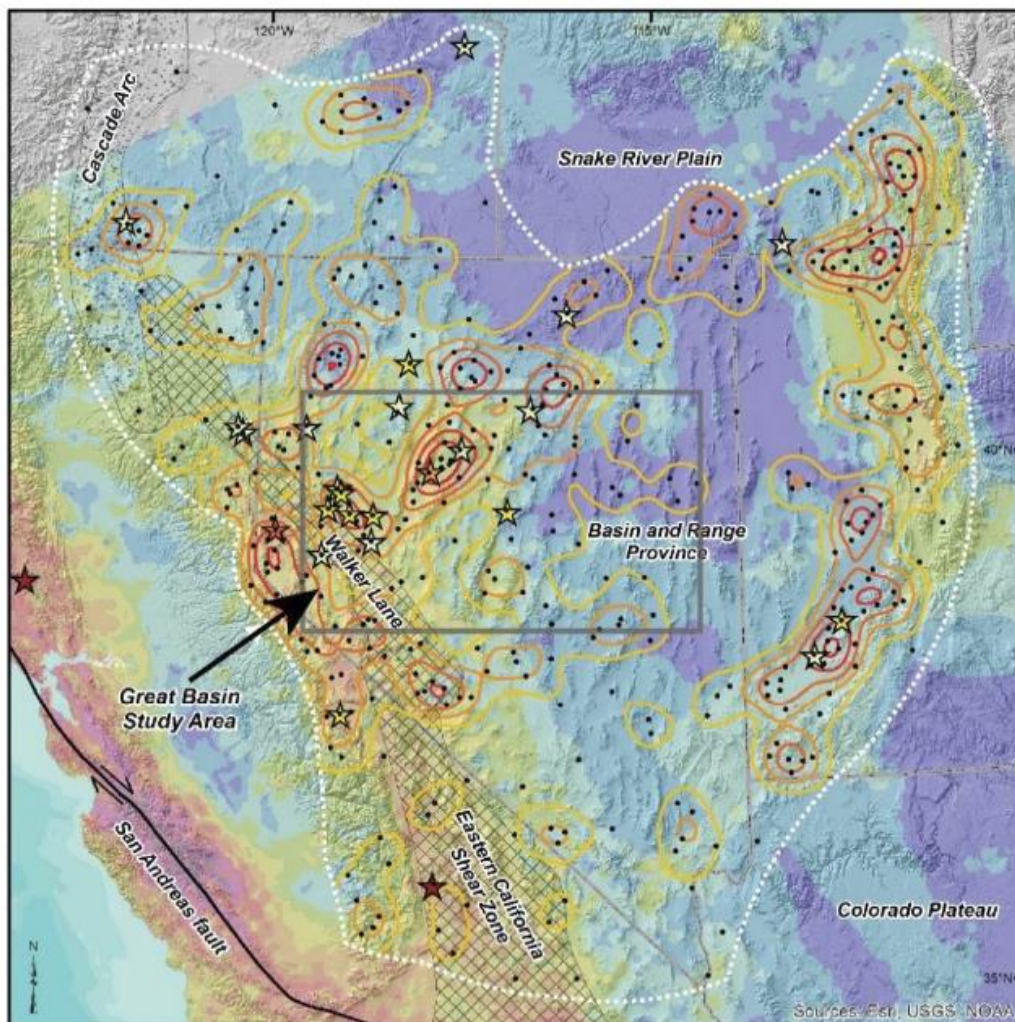
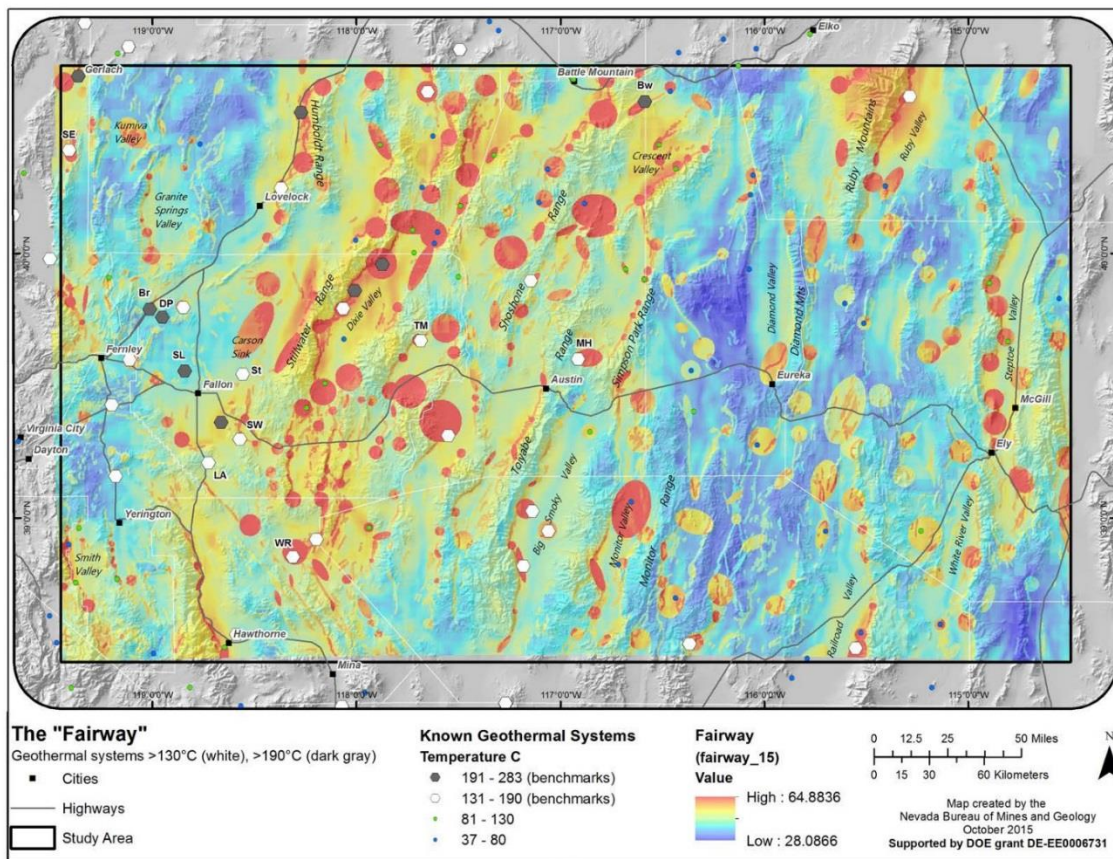


Figure 1.12: Overview map from Faulds et al., 2015: This figure shows the study area rectangle (grey) those authors used to predict geothermal favorability in their Play Fairway Analysis. The shading on the topography denotes the rate of deformation. Locations of geothermal powerplants and systems are depicted as stars and circles, respectively. The Walker Lane and Eastern California Shear Zone are depicted in a hatch pattern. Geothermal system densities are depicted using colored iso lines.



E-54

Figure 1.13: ‘The Fairway’ map from Faulds et al., 2015: This figure shows geothermal favorability within their study area based on multiple evidence layers grouped together to represent permeability and heat.

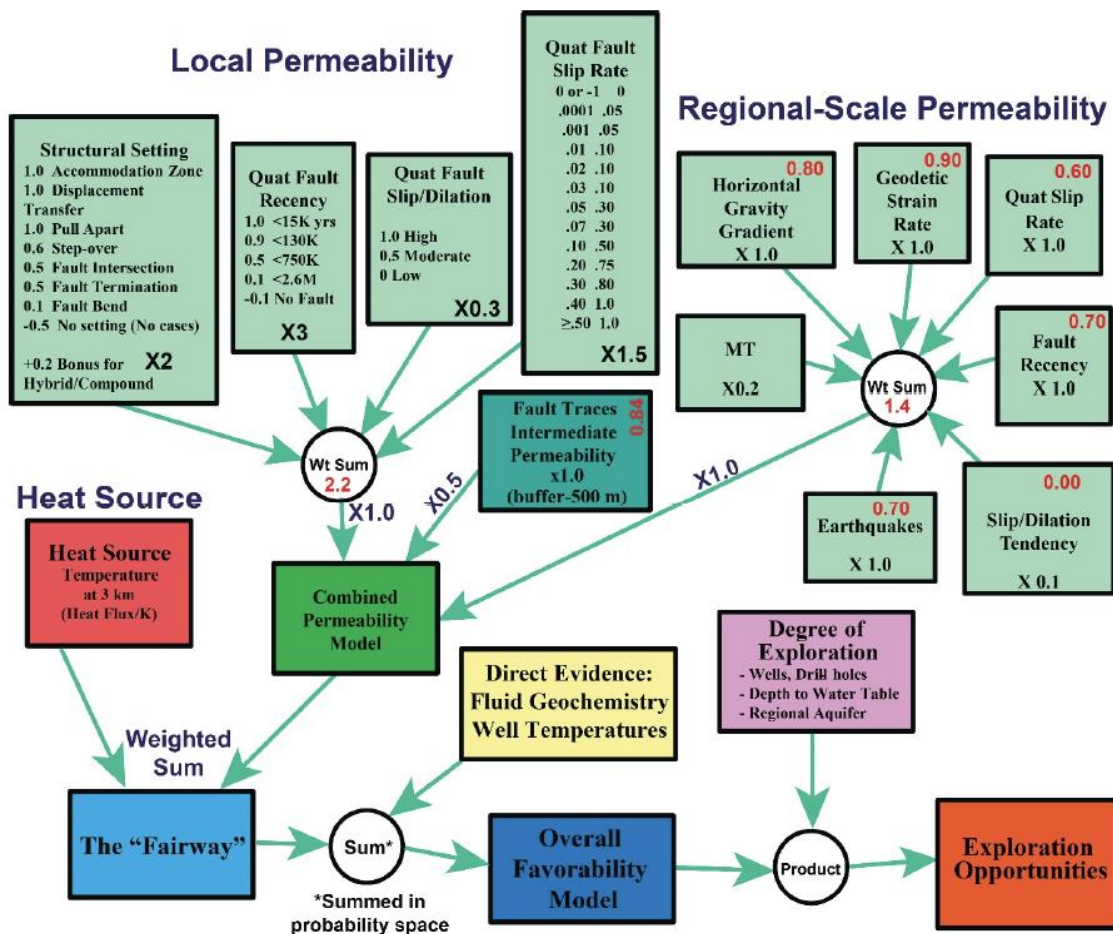


Figure 1.14: Evidence data diagram from Faulds et al., 2015: This figure illustrates how evidence data were combined using a play fairway analysis approach to produce geothermal favorability maps.

1.5.4 Coolbaugh and Bedell, 2006

Coolbaugh and Bedell (2006) assessed geothermal favorability in Nevada and used mathematical functions to generate gradational changes in evidence layer weights. This technique resulted in maps that did not have the abrupt changes in favorability seen in other assessments when artificial thresholds were passed (Figure 1.15, Figure 1.16). Coolbaugh and Bedell (2006) used data representing estimated regional heat flux, young faults, depth to water table, groundwater chemistry (represented by boron concentrations), young volcanics, earthquakes, and Paleozoic carbonates. Coolbaugh and Bedell (2006) served as a model for many of the ideas used to fit smooth functions in the present study.

Evidence Layer	Positive Weight	Negative Weight	Contrast	Student Contrast	Standard Deviation of Contrast	Additional Classes (z score = 2)	Additional Classes (z score = 1)
Young Volcanics	2.48	-0.05	2.52	4.22	0.5989	1.1	3.2
Water Table Depth	0.19	-2.22	2.41	2.39	1.0108	0.2	1.4
Regional Heat Flux	0.14	-2.12	2.26	2.24	1.0087	0.1	1.2
Paleozoic Carbonates	0.34	-1.42	1.77	3.78	0.4676	0.9	2.8
NE-trending Young Faults	1.41	-0.11	1.52	3.99	0.3816	1.0	3.0
Boron in Groundwater	0.75	-0.48	1.23	4.40	0.2787	1.2	3.4
Earthquakes	0.22	-0.32	0.54	1.97	0.2753	0.0	1.0
				Sum:		4.5	16.0

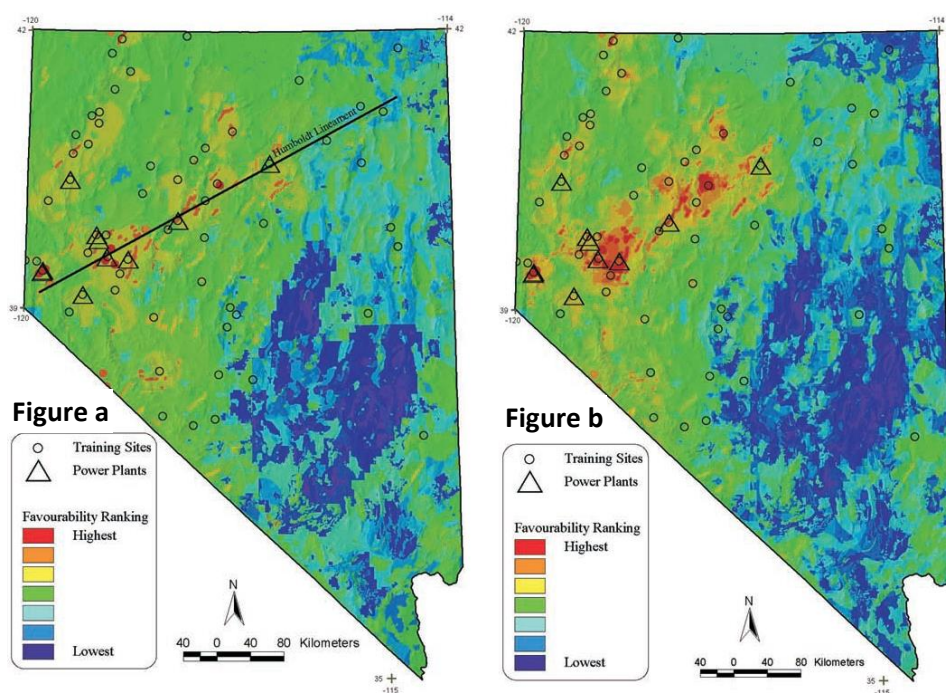


Figure 1.15: Weight table and geothermal potential maps from Coolbaugh and Bedell, 2006: This study fit smooth functions to a proxy for WofE weights to produce smoothly varying favorability maps. Table 1 shows WofE statistics calculated for layers. Figure a shows favorability using the traditional binary WofE approach. Figure b shows favorability calculated using a multiclass density function to show more gradations in favorability.

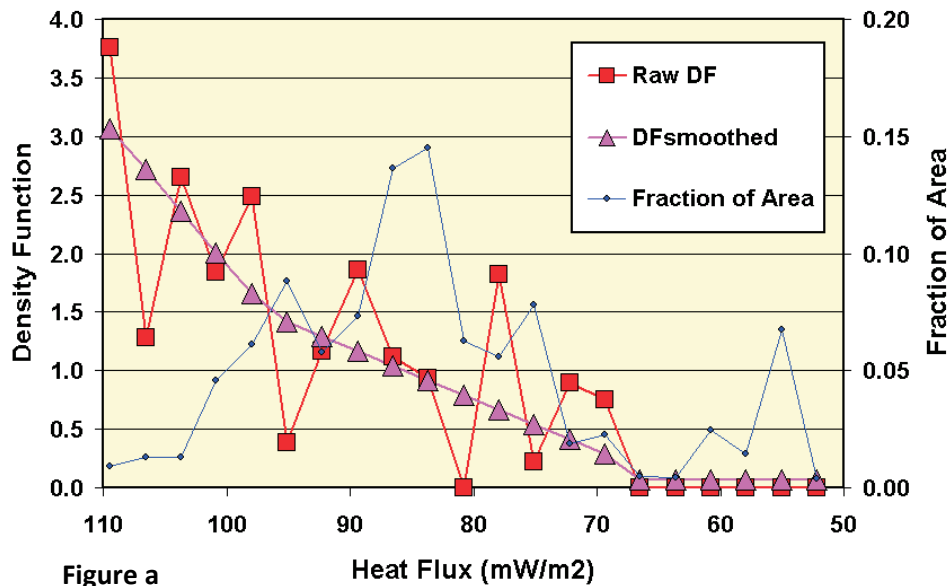


Figure a

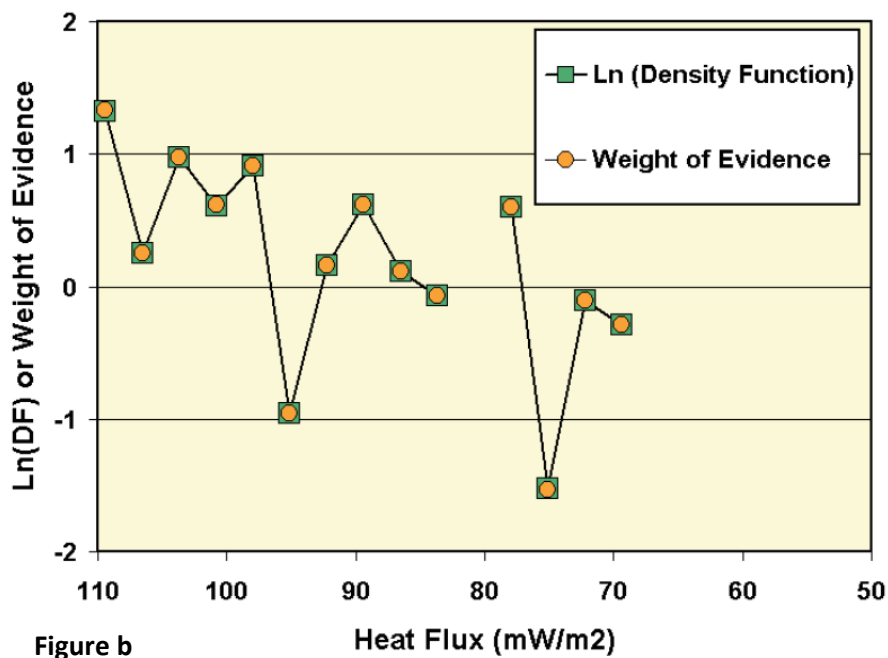


Figure b

Figure 1.16: Example of weight functions from Coolbaugh and Bedell, 2006: Figure a shows density function values (a simplified proxy for WofE weight values) fit with a smooth function modeling heat flux. Figure b shows the similarity between density function and calculated WofE weights.

1.6 Summary

This study sought to evaluate evidence data and modeling techniques used in prior geothermal assessments, and to adopt techniques and evidence layers best suited for a regional analysis while incorporating new approaches. New approaches included creating automated techniques to quickly apply geographic, statistical, and visualization tools to allow for testing of different evidence data and their derivative layers to see which display strong significant correlations with training sites and what other lessons could be learned. A new approach was used to accurately generate ‘smoothed’ weights that vary gradationally across space derived from categorical weights. Predictive maps were produced depicting favorability of geothermal system occurrence in Nevada and compared with prior assessment results. Weight statistics calculated for evidence layers were reported so they might be applied to similar conditions elsewhere in future studies. Topics for potential future research discovered during the present study were also reported.

2.0 Methodology

Evidence data were examined to see whether meaningful statistical relationships could be measured against locations of identified geothermal systems. The following sections describe the processes that each evidence source underwent to go from raw data to final interpretations. Each evidence data set needed to first be transformed in a way that optimized its relevance to geothermal exploration. For some evidence sources this involved significant preparation and interpretation to go from raw data to a usable data input for a WofE analysis. Next, a systematic series of weighting tests were run to understand the nature of the statistical relationship. Finally, a best practice was settled upon for each data set based on the unique characteristics discovered during examination before being used as inputs for creating posterior probability maps or discarded.

Some aspects of data handling were common to all evidence types. All evidence layers were produced to cover the study area, the entire state of Nevada. All evidence layers were produced on the same raster grid using 250-meter grid cells. All evidence layers used North American Datum 1983 (NAD 1983) Universal Transverse Mercator (UTM) zone 11N projection.

The geological and geophysical data that were examined for potential inclusion as evidence data include the following: Heat flow, Quaternary faults, strain rate, and earthquakes. Some of these layers or derivative variations of them did not show significant correlations with locations of known geothermal systems and were not used in this analysis to produce predictive maps.

Generating an evidence layer from raw data involved different approaches for different data sets to optimize relevance for geothermal exploration. For some layers, raw data in the form of points (heat flow measurements, earthquakes) or lines (faults) used

processing tools to generate a two-dimensional grid. These tools included ArcGIS distance functions, density functions, and interpolators.

The only requirement for an evidence layer was that the two-dimensional grid generated must use the common study area and grid spacing, and be labeled with integer codes representing classes, or intervals, that rank the magnitude of the phenomena being modeled. After application of integer codes, WofE weighting tests could begin.

This section describes the entire process of data handling by first describing geoprocessing tools and the customized Python tools developed to automate production. Then, the processes used to generate evidence layers are described for each layer along with a description of how an optimal transformation approach was selected. Next are sections describing how categorical weights were calculated and fit to generate smoothed weights. The final section describes how the evidence layers were used to create the posterior probability map depicting geothermal favorability.

2.1 Geoprocessing Tools

2.1.1 Distance Function

A distance function generates a two-dimensional surface where each cell reports the distance to the closest feature (such as a fault). The present study used the ArcMap ‘Euclidian Distance’ tool in the Spatial Analyst Tools toolset. In the present study, all distance surfaces were transformed to integer codes where the smallest integer codes corresponded to the cells with the shortest distance to a feature in increments equal to the cell size (250 m) using the ‘Reclassify’ tool in the ArcMap Spatial Analyst Tools toolset.

2.1.2 Density Functions

Geographic density functions were used to calculate the spatial density of lines (faults). In a simple density function, the tool draws a buffer of a user-specified distance from the grid cell being calculated to every feature (fault segment). The length of each fault segment falling within the radius is summed and divided by the area of the search radius to calculate a fault density. These densities can be weighted by the attributes of the input faults. A kernel density function adds the ability to inversely weight the density function by the distance between the fault and the grid cell being calculated. The distance weighting function in ArcMap is based on a Gaussian distribution. This can be useful for weighting faults more when they are closer to the grid cell being calculated. The search distance a user chooses can be a very important consideration because it requires one to place it within a geologic context (up to what distance does the user think the feature is relevant?) as well as a mathematical context (which distances produce the highest and strongest correlations?). A range of search distances can be tested on layers. The present study used the ‘Density’ tools in the ArcMap Spatial Analyst Tools toolset. All density layers were converted into integer codes representing an equal portion of the range of the density values for use in WofE testing.

2.1.3 Interpolators

Interpolators use points to generate two-dimensional surfaces that estimate the magnitude of a phenomena that gradationally across space. The present study used the Empirical Bayesian Kriging (EBK) tool (Krivoruchko and Gribov, 2014) as well as the Radial Basis Function (RBF) tool in ArcGIS. Heat flow rates calculated for individual well locations were used to create interpolated map surfaces that estimated the rate of heat flow across all of Nevada. RBF is a simple deterministic spline function used in a previous geothermal assessment of the western United States (Williams & DeAngelo, 2008). EBK

is a recently developed geostatistical tool that models by fitting semivariogram distributions (Krivoruchko and Gribov, 2014). EBK differs from ordinary kriging because it uses many semivariogram models (ordinary kriging uses one) to account for errors in the modeling process, generating many local-scale interpolated surfaces that are not influenced by distant factors and combining them into a single surface. This leads to an interpolated map with more local-scale definition than ordinary kriging.

The EBK tool was developed by geostatistical engineers at ESRI, the company that makes ArcMap software. An unpublished tool was obtained from one of these engineers in 2016 that calculates cross-validation error statistics from EBK models generated with many different combinations of key EBK modeling parameters. This tool was used to find optimal EBK parameters, this will be illustrated in the next section describing the optimization of the heat flow evidence layer.

2.2 Python Tools

Two Python toolsets were developed while undertaking the present study to facilitate comprehensive evaluation of evidence data. One toolset performed analysis and generated weight tables (Processing Toolset), the other plotted the results (Plotting Toolset). Example code is included in Appendix 3. Nearly all functional steps were performed using these toolsets, greatly enhancing the ability to test different techniques and to quickly visualize in a way that greatly aided simple interpretation. The programming was written in Python code, the language used in ArcGIS for customized and batch-mode operations.

2.2.1 Processing Toolset

2.2.1.1 Subset-Distance Cumulative Weight Test Tool

This tool uses two attributes of a layer to generate a subset for each unique combination of the two attributes for cumulatively larger groups. To use this tool, a user must tag input data with codes representing important ordinal characteristics, such as rankings of fault recency or slip rate categories in the case of the Quaternary fault data. For example, in a case with six recency categories and three slip categories, $(3 \times 6 =)$ 18 subsets would be generated. Each subset is cumulative in the sense that lower ranked categories contain all higher-ranked categories. For example, the youngest faults comprise the first recency ranking but the second recency ranking contains the two youngest groups, and so on.

For each subset, a distance function is applied, a new surface is generated with integer codes representing recategorized distances, and a cumulative weight test is run generating tables that can be used directly in the Plotting Toolset. This toolset can take either line or point features as inputs. These processes can be run for each set in a list of different training sites.

2.2.1.2 Density Function and Cumulative Weight Tool

This tool generates either a simple or kernel density function from line or point features and can optionally generate a layer calculating the log of the density surface. The tool recategorizes the surface into integer codes representing equal intervals and calculates cumulative weights. This process can be run for each value in a list of different search radii. These processes can be run for each set in a list of different training sites. Results of the cumulative weights test can be used directly in the Plotting Toolset.

2.2.1.3 Continuous Layer Reclassify and Cumulative Weight Test Tool

This tool reclassifies a continuous data layer (such as heat flow or strain rate) into integer codes representing equal intervals and calculates cumulative weights. These processes can be run for each set in a list of different training sites. Results of the cumulative weights test can be used directly in the Plotting Toolset.

2.2.1.4 Categorical Weight Test Tool

This tool calculates categorical weights for a series of input files. These processes can be run for each set in a list of different training sites. Results of the cumulative weights test can be used directly in the Plotting Toolset.

2.2.2 Plotting Toolset

The Plotting Toolset consists of two individual tools, one that plots cumulative weights and one that plots categorical weights. This toolset reads the weight tables generated by ArcSDM weight tests. This toolset creates an individual plot for each weight table and also creates summary tables by arranging plots in a single table for side-by-side-examination. Both plotting tools use the same symbology to represent weight values and training point count but use different symbology to show information specific to each type. Both tools have options to show native units, and to invert the x-axis.

2.2.2.1 Cumulative Weight Plotter

This tool generates plots that display weight values and their standard deviations, training point counts, contrast, and studentized contrast. Summary statistics are reported in the title of each plot to allow for easy comparison of important statistics across different subsets. This tool offers an option to show plot distance on the x-axis, and an option to display high studentized contrast values at half their actual value.

2.2.2.2 Categorical Weight Plotter

This tool generates plots that display weight values and their standard deviations, training point counts, relative area, and cumulative area. This tool offers an option to show plot by native units but requires a user provide bin thresholds.

2.3 Evidence Layer Creation and Selection

This section describes how for each evidence data source, raw data were ultimately transformed into integer codes representing the magnitude of the phenomena being modeled for use in WofE testing. Three of the four evidence sources were examined to see whether there were ways to optimize relevance for geothermal exploration. Strain rate data were directly sampled. Fault, heat flow, and earthquake data, however, were examined using different techniques relating to data processing, subset selection data, and transformation, to identify an approach that generated the strongest weights when compared with training sites to calculate WofE statistics.

2.3.1 Strain Rate

The simplest example in the present study is the use of the strain rate data because the only processing step was to resample the strain rate data from Kreemer et al. (2012) to fit the study area raster grid. The original data came at a spatial resolution of 0.01 degrees by 0.01 degrees (approximately 850 meters (x) by 1100 meters (y)); this grid was resampled to the current 250-meter grid spacing. Original data were sampled to a point file representing the centroid of each study area grid cell using the ArcGIS 'Extract Values to Points' tool in the 'Spatial Analyst Tools' toolset. This point file was converted into a raster grid using the 'Point to Raster' tool in the ArcMap 'Conversion Tools' toolset.

Next, the data were categorized into 232 bins, with each increasing bin value representing, from highest to lowest strain rates, a decreasing 1 strain unit portion of the total domain. For example, raster cells with a value of 1 represented locations with a strain rate greater than $231 \cdot 10^{-9}$ /yr, a value of 2 represented locations ranging from $230 - 231 \cdot 10^{-9}$ /yr, etc. Increasing values in the evidence layer integer codes corresponded to decreasing values in strain rate. This recategorization was done using the 'Reclassify' tool in the 'Spatial Analyst Tools' toolset.

2.3.2 Quaternary Faults

The final predictive maps in the present study used surfaces generated by using Quaternary fault subsets in a distance function to generate surfaces showing the distance from the nearest fault. These surfaces were reclassified into integer codes where the smallest integer codes corresponded to the cells with the shortest distance to a feature in increments equal to the cell size (250 m). For example, Class 1 encompassed places 0 – 250 m from a fault, class 2 encompassed areas 250 – 500 m from a fault, etc.

Three other techniques for generating two-dimensional surfaces representing fault characteristics were explored, but ultimately not used because the approach examining subsets with distance functions generated stronger associations with the benchmark geothermal systems. Two of the three techniques used density functions; one simple density function and one kernel density function. Density functions were explored because unlike distance functions, they highlight areas with more faults and they can be weighted by a quantitative measure, such as TD and TS. The third approach examined TD using the same distance-based subset approach to see whether subsets with higher TD values showed stronger associations with the benchmark geothermal systems. In the

following subsections, the distance function-based approach will first be presented, followed by presentation of approaches that were not ultimately used.

2.3.2.1 Distance Function on Fault Subsets

Quaternary faults were examined based on their slip sense (Figure 1.1), recency (Figure 1.3), and slip rate (Figure 1.4). Cumulative weight tests were run on recategorized distance rasters generated from a series of fault subsets with different attributes to see which fault subsets produced the highest weights. Finding higher correlating subsets has two advantages, a stronger correlation and less of the map area will be positively weighted. Processing was done using the ‘Distance Subset Toolset’ and results were plotted using the ‘Plotting Toolset.’

In Figure 2.1, each plot represents the result of a cumulative weight test run on a subset of faults with no consideration for their slip sense. Each plot uses the same symbology seen in Figure 1.7. Plots vary from left (younger) to right (older) by their recency; up (faster) to down (slower) by their slip rate. The plots furthest to the left only contain the youngest faults (Historic), the plots furthest to the right contain faults of all Quaternary ages. The groups are cumulative in the sense that each older group also contains the younger groups. The vertical groups are also cumulative with the top row representing faults with the highest strain rate and the bottom row representing faults with all strain rates. The bottom-right plot therefore contains all faults in the QFFDB for Nevada, containing Quaternary faults of all ages and all slip rates.

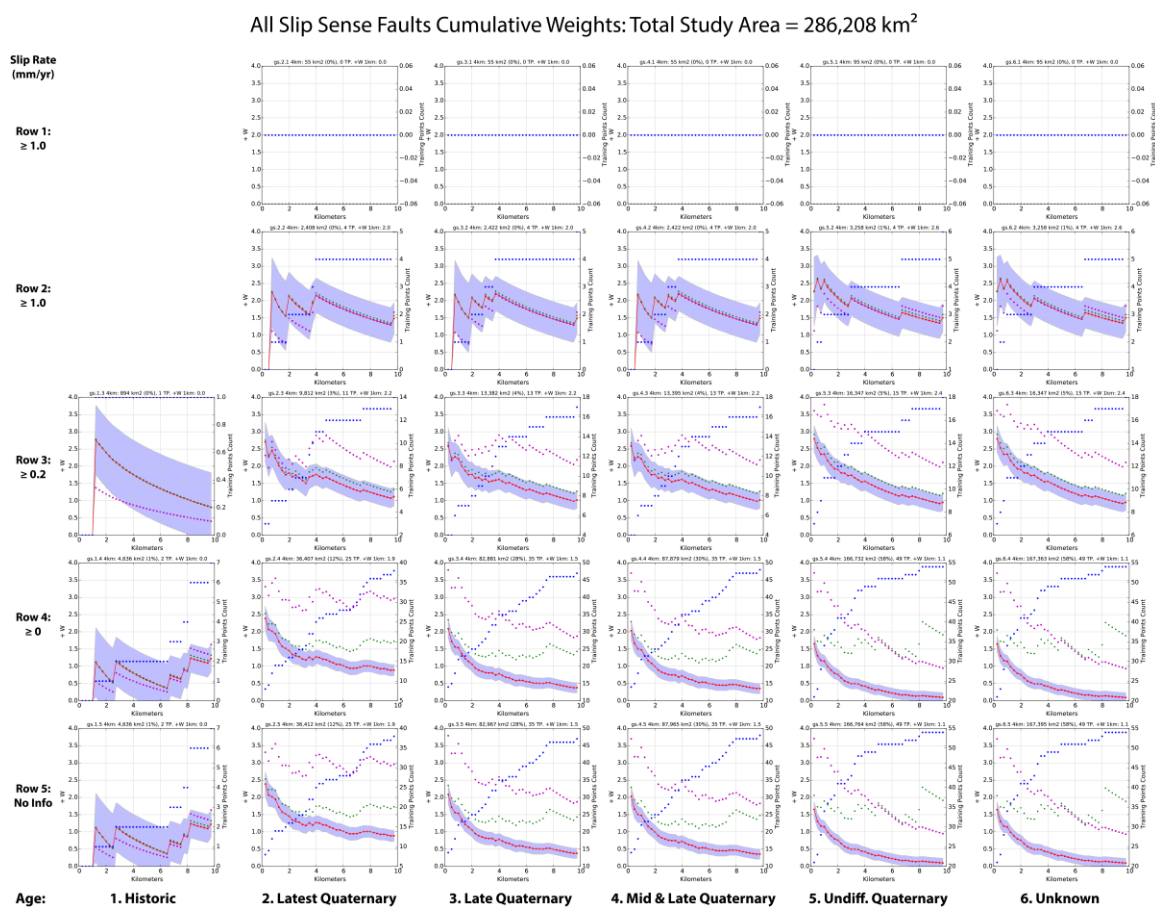


Figure 2.1: Cumulative weight tables from fault subsets of all slip senses. Each plot represents the result of a cumulative weight test run on a subset of faults with no consideration for their slip sense. The x-axis depicts distance from faults in km. The red points and line represent W_+ and use the left axis. The green points represent contrast ($W_+ - W_-$) and use the left axis. The blue points represent training point count and use the right axis. The purple points represent half the value of the studentized contrast and use the left axis. Plots vary from left (younger) to right (older) by their recency; up (faster) to down (slower) by their slip rate. The plots furthest to the left only contain the youngest faults (Historic), the plots furthest to the right contain faults of all ages. The groups are cumulative, each older group also contains the younger groups. The vertical groups are also cumulative with the top row representing faults with the highest slip rate and the bottom row representing faults with all slip rates. Above each plot, titles provide descriptive statistics to more easily compare important parameters. In order, plot titles provide recency and slip rate designations, followed by percent of total area, and training point count within an arbitrary threshold distance of 4 km. Finally, W_+ is reported at the arbitrary distance of 1km.

Some plots in Figure 2.1 show unreliable results. For example, the entire top row was generated from fault subsets that had no training sites within 10 km. Several plots, including the plots on the second row from the top have weights that exhibit a jagged pattern within the first few kilometers from faults, indicating unreliable weights generated from too few training sites, as confirmed by large standard deviation values (blue shading). This pattern is often indicative of the use of too small a bin size, but in this case the pattern is observed occurring over significant distances from faults. Reliable results generally produce plots that can be seen rising to a maximum and gradually declining.

Above each plot, descriptive statistics were noted to more easily compare important parameters. Plots each list their name, which indicates their recency and slip rate designations. Then the area, percent of total area, and training point count within an arbitrary threshold distance are reported. In the case of Figure 2.1, these parameters are listed using a distance threshold of 4 km. Finally, W_+ is reported at the arbitrary distance of 1 km. Though these thresholds are arbitrary, they provide a consistent way to see how important parameters change as older and slower faults are shed from consideration. They are also useful when looking at whether normal faults correlate more strongly with training sites than the full QFFDB for Nevada.

Figure 2.2 shows results when only examining normal faults and uses the same symbology used in Figure 2.1. W_+ at 1 km is higher in Figure 2.2 (normal faults) in every reliable looking fault subset plot than in Figure 2.1 (all faults). It was therefore decided to only use normal faults in the investigation.

Normal Fault Subset Cumulative Weights: Total Study Area = 286,208 km²

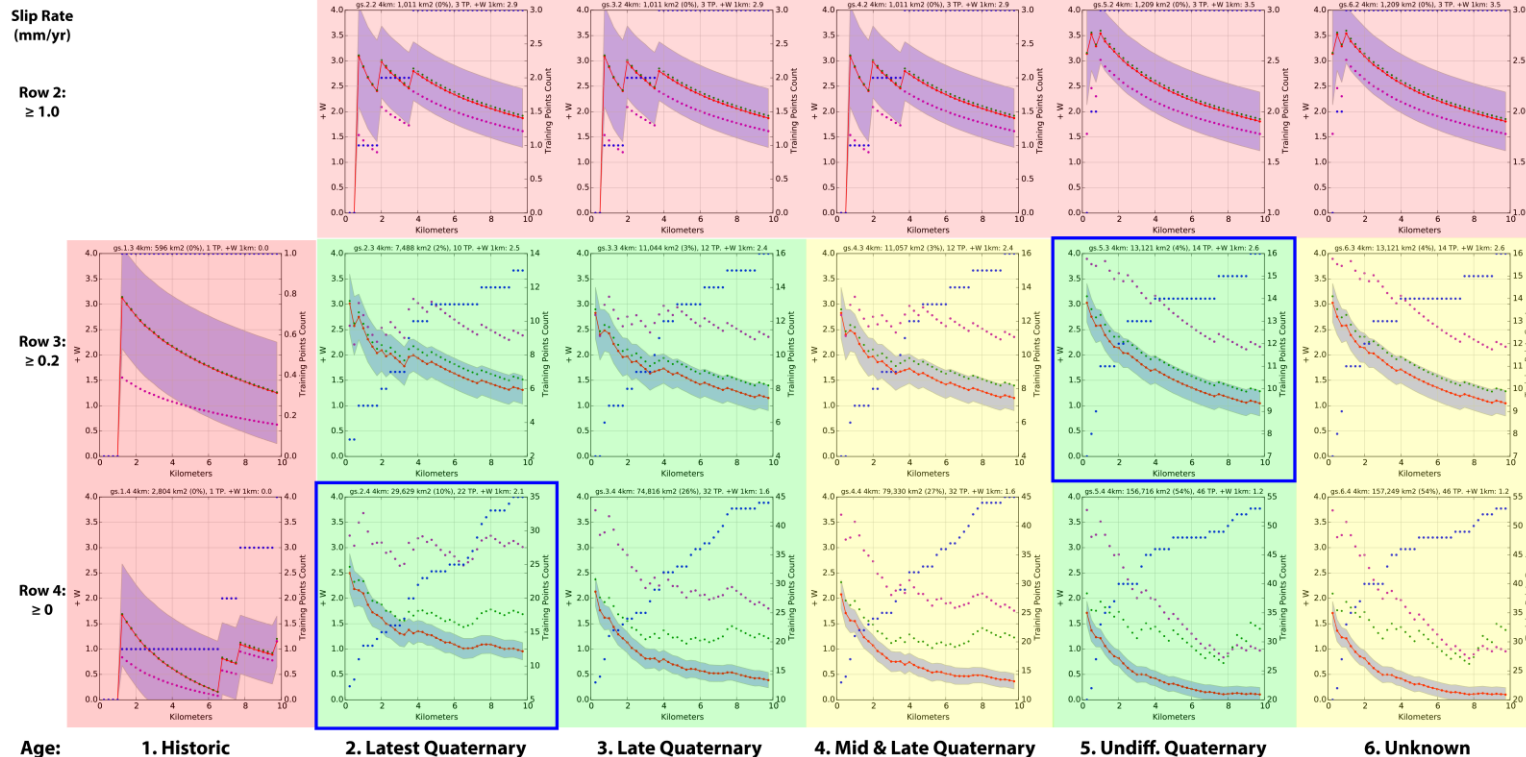


Figure 2.2. Cumulative weight tables from fault subsets of normal faults. Each plot represents the result of a cumulative weight test run on a subset of normal faults. The X-axis depicts distance from faults in km. The red points and line represent W+ and use the left axis. The green points represent contrast (W+ - W-) and use the left axis. The blue points represent training point count and use the right axis. The purple points represent half the value of the studentized contrast and use the left axis. Plots vary from left (younger) to right (older) by their recency; up (faster) to down (slower) by their slip rate. The plots furthest to the left only contain the youngest faults (Historic), the plots furthest to the right contain faults of all ages. The groups are cumulative, each older group also contains the younger groups. The vertical groups are also cumulative with the top row representing faults with the highest slip rate and the bottom row representing faults with all slip rates. Above each plot, titles provide recency and slip rate designations, followed by percent of total area, and training point count within an arbitrary threshold distance of 4 km. Finally, W+ is reported at the arbitrary distance of 1km. Poorly performing tests were shaded red. Redundant weight tests (see text) were shaded yellow. Promising looking graphs with higher positive weights were shaded green. The best performing tests were outlined with a blue box.

To choose the best performing fault subset from Figure 2.2, poorly performing (shaded red) and redundant weight tests (shaded yellow) were first eliminated from consideration. Then promising looking weight tests with relatively high positive weights (shaded green) were compared to each other before settling on the best performer(s) (blue box).

Poorly performing fault subset weight plots (shaded red) include the top row of Figure 2.2 (strain rate between 1-5 mm/yr) and the first column (Column 1, Historic faults only). These plots had too few training sites to calculate reliable weights.

Some of the categories in the QFFDB did not contain many faults. For that reason, some of the categories are effectively redundant. To find redundant categories within the 'age' designations, one can look at the plots on the bottom row (to not consider slip rate) of Figure 2.2 and note the amount of area each subset covers at 4 km. Starting from the bottom right and moving left, each new plot sheds the oldest group. If adjacent plots cover approximately the same area at 4 km, they effectively show the same thing and one column can therefore be eliminated. Plots on the bottom row of the two oldest columns, columns 5 and 6, (bottom right, bottom second from right) both cover approximately 54% of the state. The oldest column, column 6 (right most column), can therefore be eliminated from consideration (yellow shading) because the adjacent column covers slightly less area while containing the same number of training sites. Similarly, Column 4 was eliminated from consideration (shaded yellow) because its plot covers a similar percentage of the total area to the plot in Column 3 while picking up the same number of training sites at 4 km. No such redundancies were seen when comparing slip rate graphs.

After eliminating many of the plots from consideration (red and yellow shading), the remaining six plots in Figure 2.2 were shaded green to denote their not being poorly performing or redundant and therefore worthwhile of consideration. Of the six plots shaded green, three are in 'row 3', faults with slip rate equal or greater than 0.2 and less

than 1.0 mm/yr. Three plots are in ‘row 4’ that include all categories of strain rate. On the bottom row, row 4, as older faults are shed, W_+ at 1 km rises as the associated area falls. This is exactly what one would hope to see, smaller areas being given higher weight. The green plot on the bottom left, plot ‘2.4’, shows the highest W_+ at 1 km ($W_+ = 2.15$) with the lowest amount of area covered. This makes it the best performing subset of the plots in row 4. Of the plots in row 3, the green plot on the top right, plot ‘5.3’, shows the highest W_+ at 1 km ($W_+ = 2.56$). It does not, however, cover the least area because it contains older faults. It was still chosen as the best performer in row 3 because it has higher W_+ while still covering a relatively small portion of the entire study area (4% at 4 km). Weights seen in both the 2.4 and the 5.3 subset both possess strong measures of studentized contrast, indicating weights are significantly larger than zero.

Ultimately multiple versions of the geothermal favorability maps were generated, some using the 2.4 subset, the others using the 5.3 subset, because they highlight different features and each version could be useful. In a traditional binary WofE analysis, either of these subsets would be converted into a binary categorical layer with a threshold determined by where the highest contrast (green dots) or studentized contrast (purple dots) exists.

2.3.2.2 Other Approaches Not Used on Faults

Figure 2.3 shows cumulative weight test results run on the entire fault dataset using simple and kernel density functions weighted by fault segment TD and TS using different search radii. Plot titles indicate which density function was used (‘ld’ = simple density, ‘kd’ = kernel density), which field was used for weighting (TD or TS), and the distance in meters.

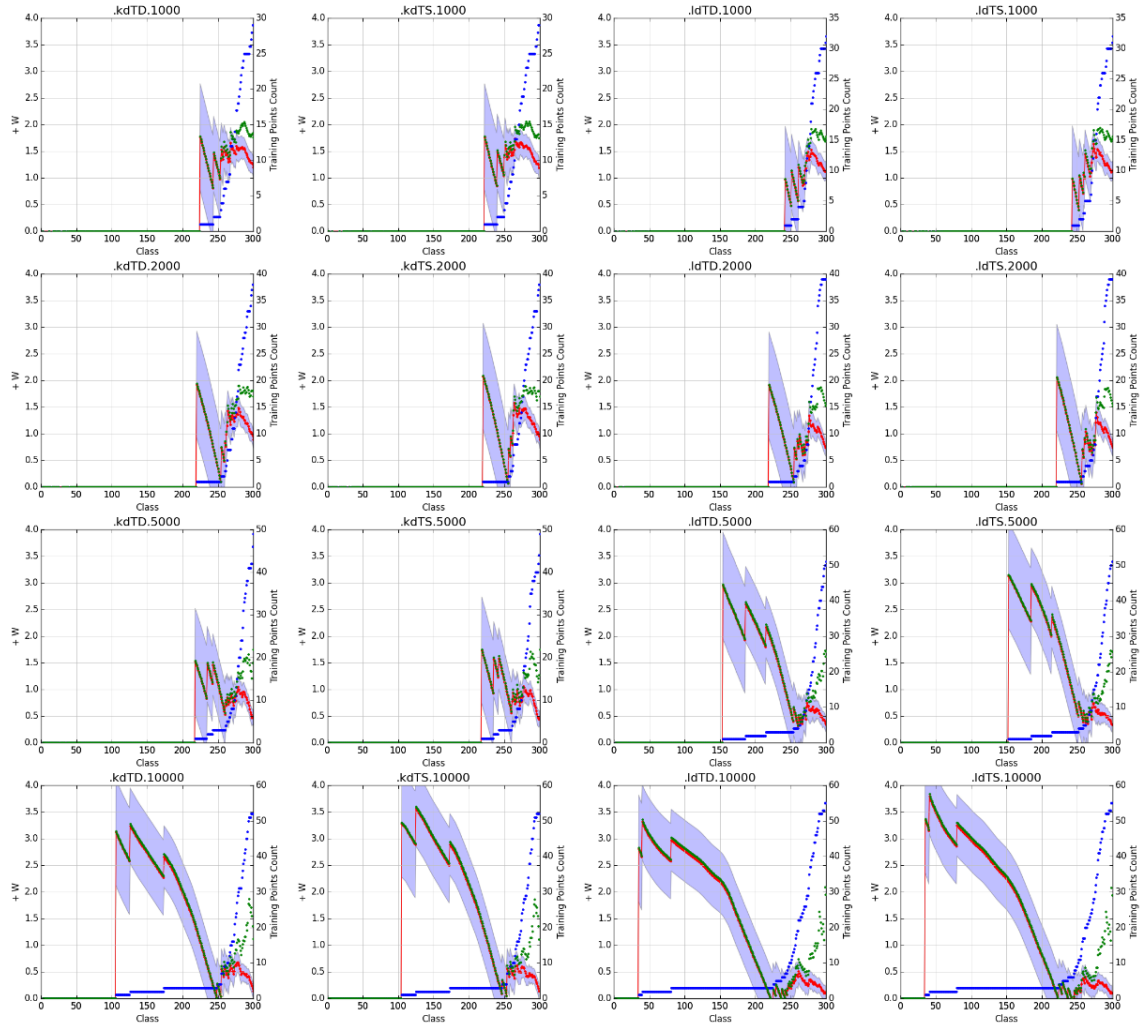


Figure 2.3: Cumulative weight test results of faults weighted by dilation or slip tendency using simple and kernel density functions with multiple search radii. Plot titles indicate which density function was used ('ld' = simple density, 'kd' = kernel density), which field was used for weighting (TD or TS), and the distance in meters. The x-axis shows class; each class is an equal interval bin of the full range of the density surface being examined with the highest density values being assigned the lowest class codes. The red points and line represent $W+$ and use the left axis. Blue shading around the red line indicates standard deviation of the weight. The blue points represent training point count and use the right axis. The purple points represent the studentized contrast and use the left axis. The green points represent contrast and use the left axis. Numbers in each plot's title (1000, 2000, and 5000, 10000) denote the search radius used in meters.

Most of these plots have weight values (red points and line, left y-axis) that spike as the first training sites (blue dots, right y-axis) fall within the cumulative class group being examined (x-axis). All of these plots show a distinct range on the x-axis where many training sites get picked up, seen where the blue dots suddenly go up. Weights calculated before this rise began were not considered reliable because they were generated from too few training sites. Weight values calculated after the rise in training point count were considered based on their maximum weight and whether weight values dropped off suddenly or not.

First, the 'TD' plots look nearly identical to their 'TS' counterparts. Second, it appears that kernel density functions performed better than their simple density counterparts by having higher maximum weight values that dropped off less suddenly. Third, the large search distances produce lower maximum weight values than the 1 km and 2 km plots, which exhibit similar features. This makes sense because a Quaternary fault's impact on permeability may not be expected to extend to distances as large as 5 or 10 km.

These trends highlight the kernel density plots as the best performers, weighted by either TD or TS using either a 1 km or 2 km search radius. Using the earlier stated criteria, the surface using kernel density, weighted by TS, using a 1 km radius (figure to the right of the top left-most figure) appears to offer the most justifiable choice; weight values exceed 1.5 and persist at high levels.

The range of density values represented by the approximate class range of 250-300 using a search distance near 1-2 km represents an opportunity for further exploration, especially because these results were tested on the entire QFFDB, but not the more highly correlating subsets. Applying this technique to fault subsets may reveal additional opportunities, as will be discussed in the 'Future Work' section.

TD and TS were also evaluated using the same approach applied to the distance raster subsets but instead of slip rate categories, categories representing equal intervals of the full range of TD values were used to see if the distance surfaces produced from subsets with high TD produced higher weights than from those produced using subsets with increasingly lower minimum TD. Very little change was seen between groups with a higher and lower minimum TD, so the technique was not pursued further.

2.3.3 Heat Flow

Crustal heat flow, like crustal strain rate, is a characteristic that changes gradationally across space. Heat flow was calculated for individual locations; values from these point locations were interpolated into raster surfaces that estimate heat flow in units of mW/m^2 across Nevada using the EBK and RBF interpolators in ArcGIS (Figure 1.6). Values of heat flow greater than $120 \text{ mW}/\text{m}^2$ were reduced to equal $120 \text{ mW}/\text{m}^2$ to minimize the impact of extremely high values measured at hydrothermal systems concealing the background rates of crustal heat flow regionally as in Williams and DeAngelo (2011). Default RBF model parameters were used (Completely regularized spline, one sector).

An optimal kriging model was settled upon for the EBK by varying the transformation and semivariogram models to run 82 unique variations and identify the model with lowest errors using a tool provided by geostatistical engineers developing ArcGIS geostatistical tools. Appendix 2 shows the error statistics from 82 EBK models in the second and third columns, the Root Mean Square Error (RMSE) and the Root Mean Square Error (rmsStd), respectively. RMSE indicates how closely a model predicts measured values. Generally, the lower the RMSE, the better the fit. rmsStd is the average of the standardized errors. The closer rmsStd is to 1.0, the better the fit. Model number 2 was chosen because there was no model with lower RMSE besides model 1, which contained an error calculating rmsStd.

Heat flow maps generated using both interpolators were transformed to estimate temperature at 3 km, resulting in four maps that could be used to represent heat. A simple comparison of these approaches was performed by calculating cumulative weights on each layer. The upper plots in Figure 2.4 show results from the EBK, the lower plots show the results from the RBF. The heat flow map using EBK (upper-left plot) correlated more strongly with training data than the other approaches.

Plots on the left in Figure 2.4 show results from using heat flow, plots on the right show the results from using temperature at 3 km. In the temperature at 3 km plots, the highest temperatures do not intersect with locations of geothermal systems. Systems begin intersecting in the moderate temperature ranges and have low weight values compared with the heat flow plots. Both interpolation methods led to higher estimated temperatures closer to the center of basins, which may be a more realistic depiction of heat distribution. However, identified locations for geothermal systems tend to be located at the edges of basins near basin-bounding faults, making this technique ineffective for generating strong weights. These techniques of estimating temperature at depth was therefore not pursued further for modeling purposes. Results could, however, be useful as a standalone product (Appendix 1) or for use in future studies that could take dipping structures into account. All weight results seen in Figure 2.4 were generated using a modified study area (seen in Appendix 1), limited by the extent of the depth to basement map used to estimate temperature at depth.

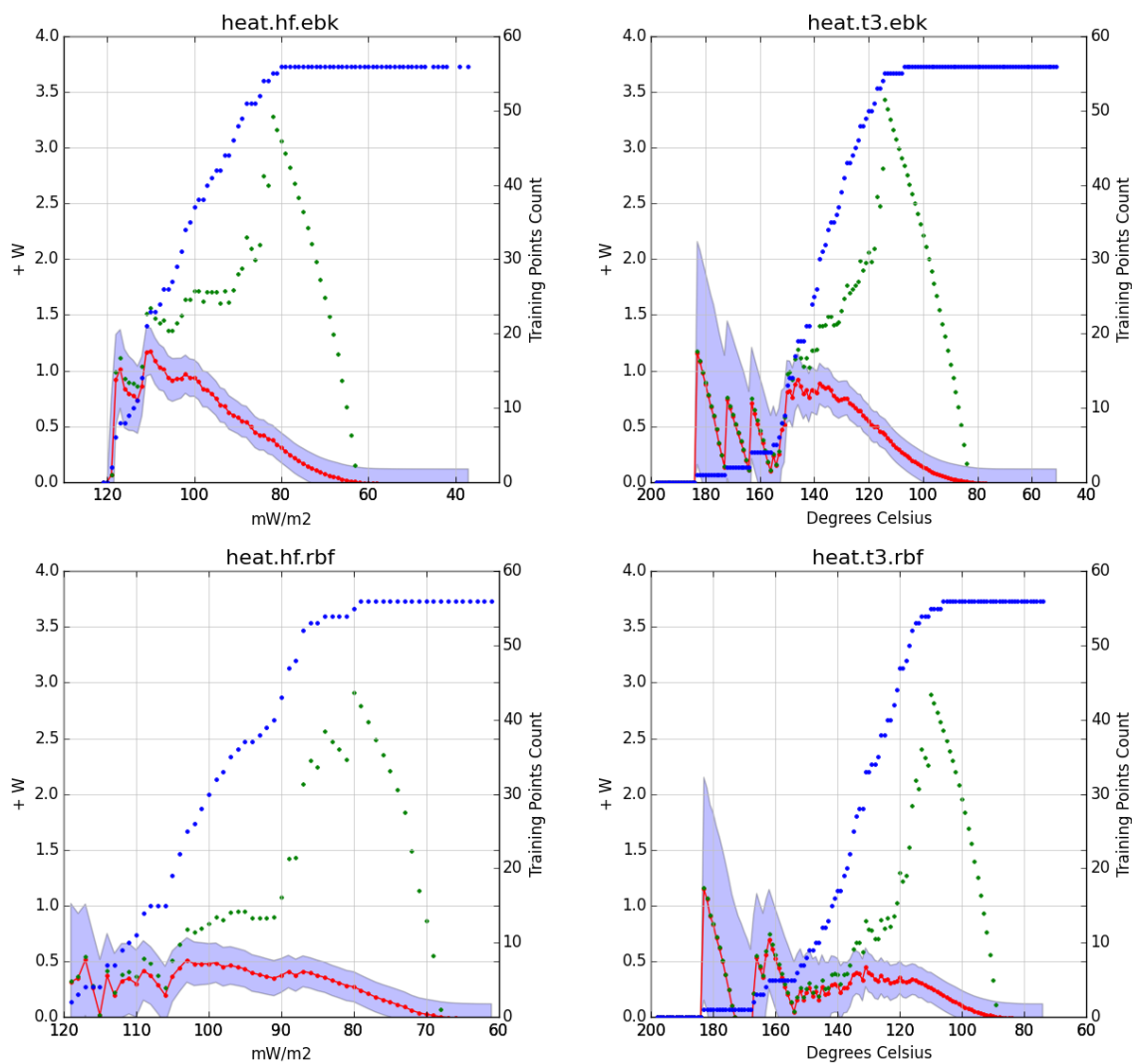


Figure 2.4: Cumulative weight test results of heat flow and temperature at 3 km depth surfaces generated using two interpolators. Plot titles indicate which density function was used ('hf' = heat flow, 't3' = temperature at 3 km (degrees C)), which interpolator was used (EBK or RBF). The x-axis shows native units. The red points and line represent W_+ and use the left axis. Blue shading around the red line indicates standard deviation of the weight. The blue points represent training point count and use the right axis. The green points represent contrast and use the left axis.

2.3.4 Earthquakes

The ‘log of the sum of the moment (LSM)’ technique used in Williams & DeAngelo, 2008 was used in the present study to characterize how earthquakes could quantitatively contribute to permeability. The LSM technique used a ‘neighborhood sum’ tool, which upon further inspection was identical to the simple density function. First, the seismic moment of each earthquake was calculated as follows:

$$Moment = 10^{(Mag*1.5)+9.1} \quad (2 - 1)$$

Moment values were very large, so they were divided by a constant (10^{14}) to allow for ArcGIS geoprocessing tools to work with them. These values were used to weight simple and kernel density functions, then the log of those surfaces was generated. The full ranges of these values were divided into many equally spaced categories and cumulative weight tests were run using multiple search distance values. Figure 2.5 shows the results of using search distances of 1, 2, 5, and 10 km for both simple and kernel density plots.

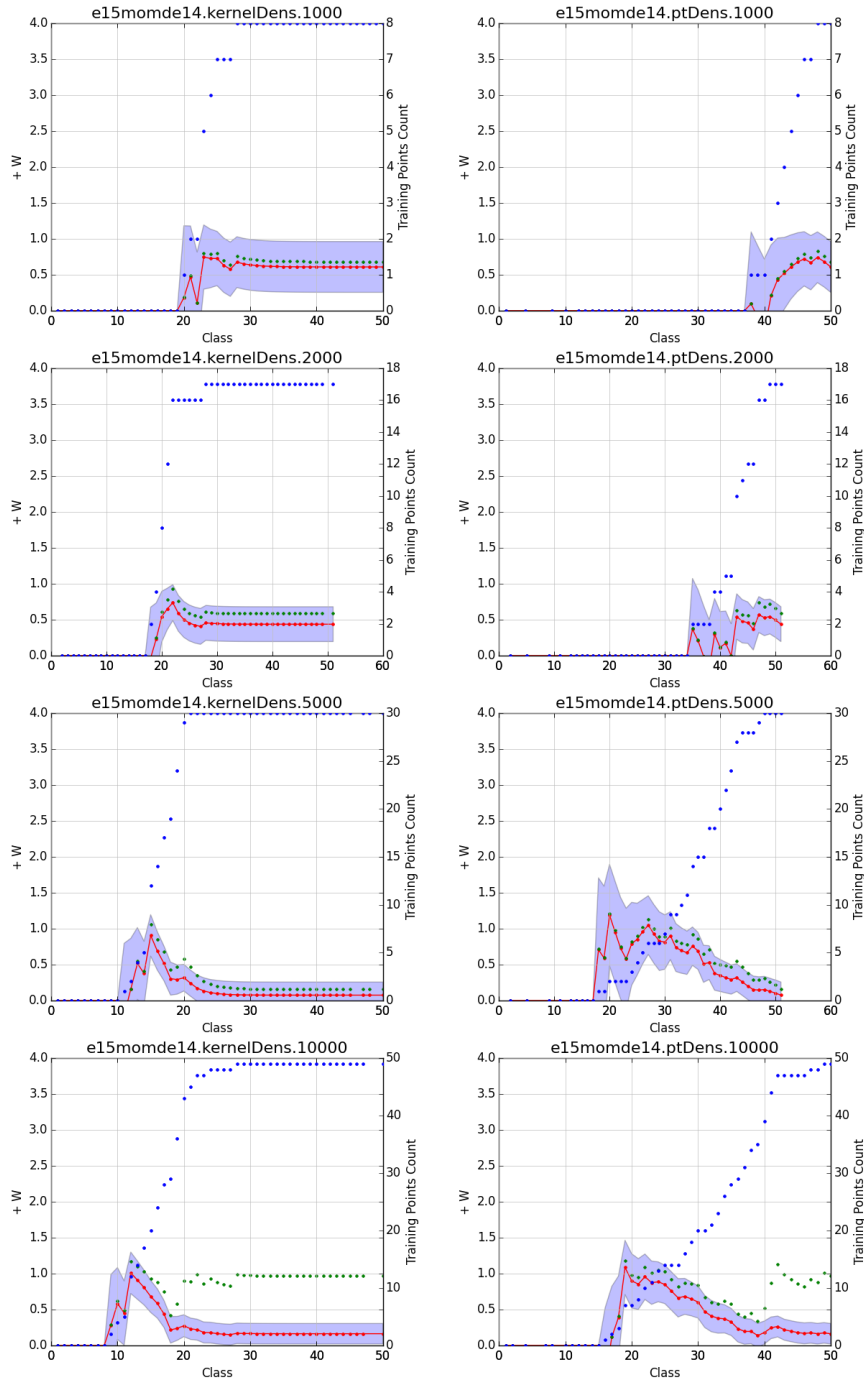


Figure 2.5: Cumulative weight test results examining earthquakes using density functions weighed by seismic moment. Plot titles indicate which density function was used ('kernelDens' = kernel density, 'ptDens' = simple or point density), numbers in each plot's title (1000, 2000, and 5000, 10000) denote the search radius used in meters. The x-axis shows class; each class is an equal interval bin of the full range of the density surface being examined with the highest density values being assigned the lowest class codes. The red points and line represent W^+ and use the left axis. Blue shading around the red line indicates standard deviation of the weight. The blue points represent training point count and use the right axis. The green points represent contrast and use the left axis.

In general, the simple density plots appeared to sustain slightly higher weights than the kernel density plots. The simple density plots using 5 and 10 km both perform well, but the simple density plot using a 10 km radius (bottom right figure) appears to perform best, reaching weight values around 1.0 with lower standard error while using more training sites.

Some experimenting revealed that multiple categorical weights could be generated using this layer that decline across categories, but the highest weights (weight ≥ 0.65 ,) only persist for a small portion (around 11%) of the total study area, represented by the first two categories in Figure 2.6. The map (Figure 2.7) shows the distribution of LSM values, high values appear to be driven by a small number of high magnitude events.

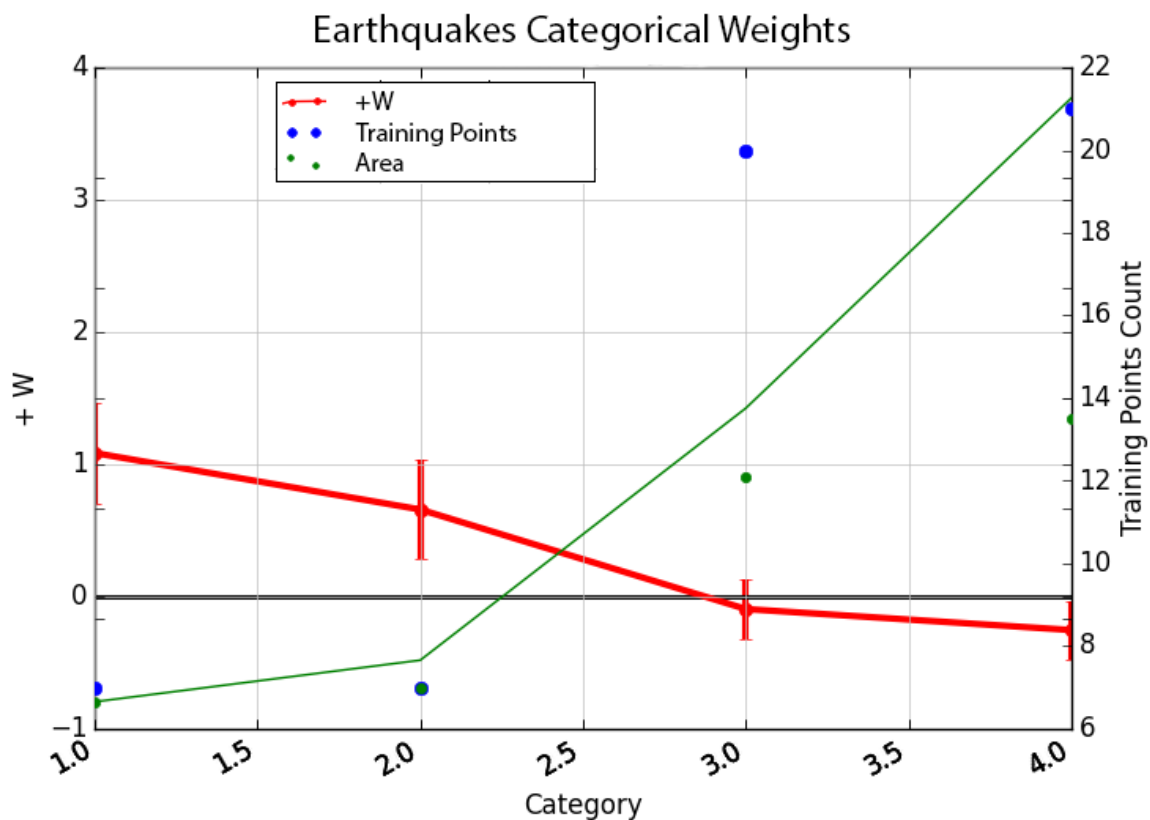


Figure 2.6: Categorical weight test results examining earthquakes. The recategorized surface was generated using a simple density function weighed by seismic moment using a 10 km search radius. All x-axis values of all points on this figure are plotted at their native unit midpoint. The x-axis shows categories. The red points and line represent W_+ and use the left axis. Error bars around weight values indicate standard deviation of the weight. The blue points represent training point count and use the right axis. The green points represent percent area associated with each bin, on an axis of 0 (bottom of graph) to 100% (top of graph). The green line represents cumulative percent area, also plotted with 0 at the bottom of y-axis and 100% at top of y-axis.

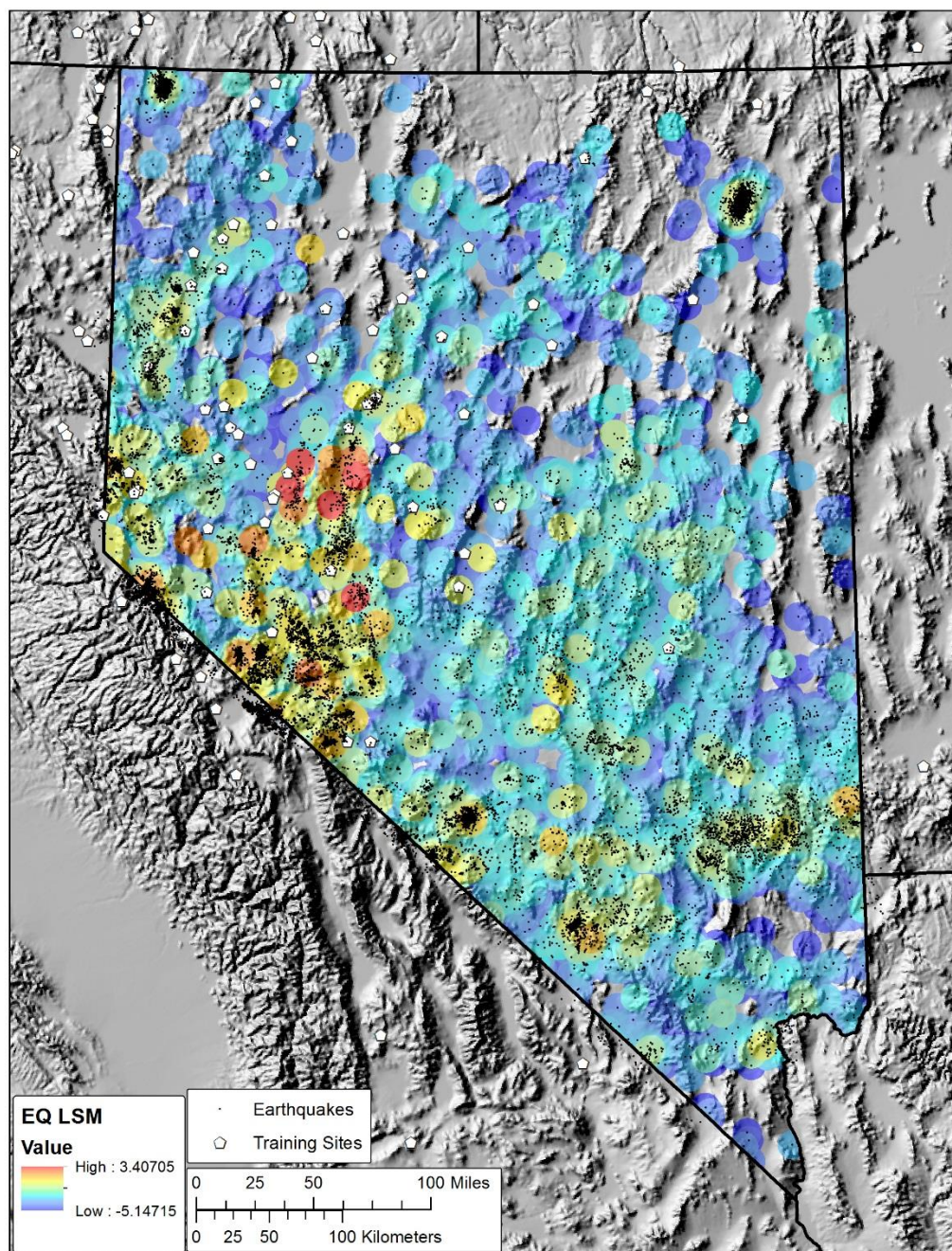


Figure 2.7: Earthquake density function map weighted by moment magnitude. Events were weighted by seismic moment using a 10 km search radius. Background colors show the log of a density function using earthquakes weighted in the LSM technique and a 10 km search radius. For each earthquake, magnitude was converted to estimate seismic moment. Seismic moment values were divided by a large constant and used in a simple density function with a 10 km search radius. The log of that density surface is depicted in this map. Earthquakes are plotted as small black circles; training sites are depicted as white pentagons.

Earthquake density maps were also prepared without weighting earthquakes by moment or magnitude (Figure 2.8). These maps yielded even lower weights than those weighted by moment (Figure 2.9). Because of the relatively low maximum weights obtained for all derivative maps, the use of earthquakes as an evidence layer was not pursued further.

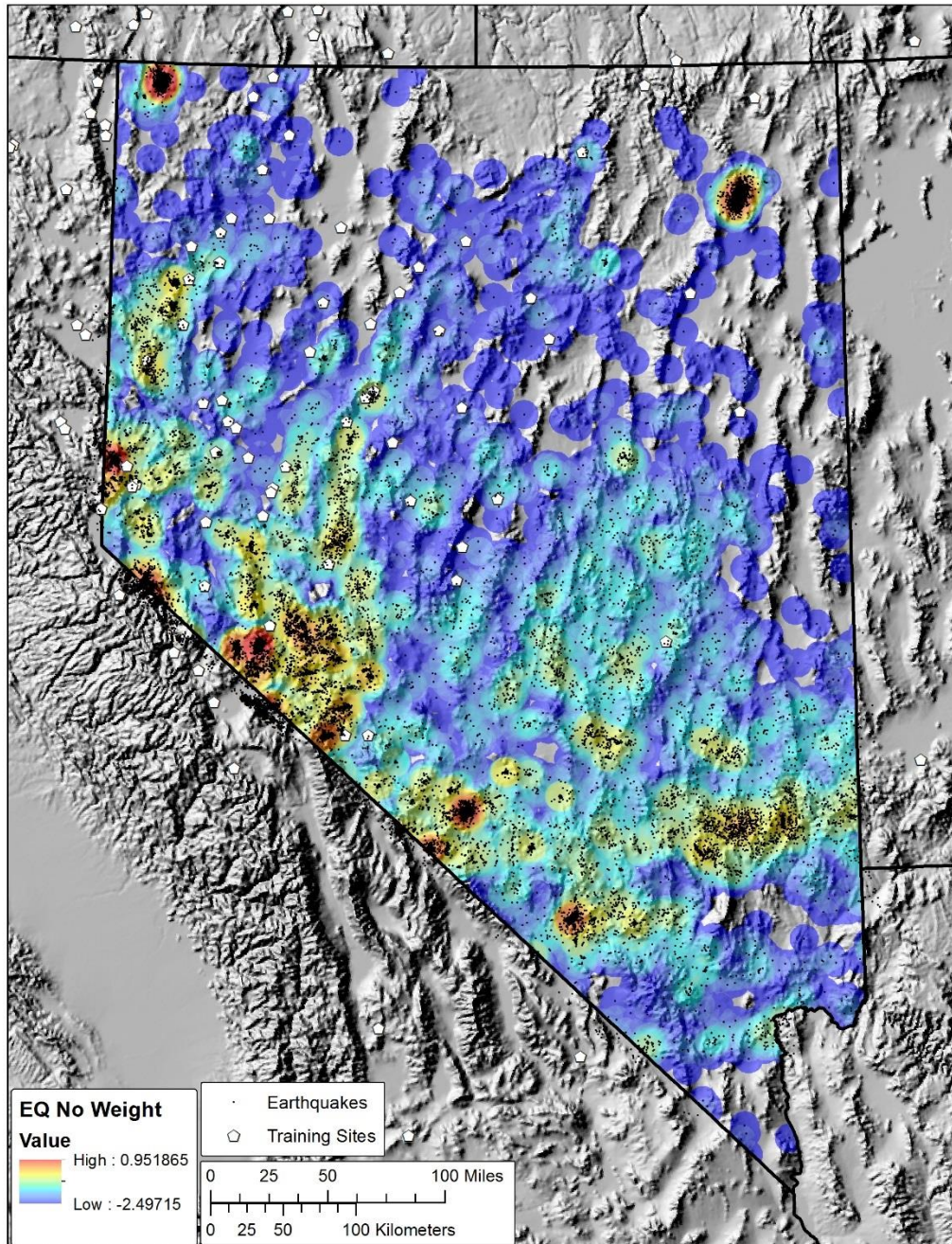


Figure 2.8: Earthquake density function map using no weighting. Background colors show the log of a density function using unweighted earthquakes and a 10 km search radius. Earthquakes are plotted as small black circles; training sites are depicted as white pentagons.

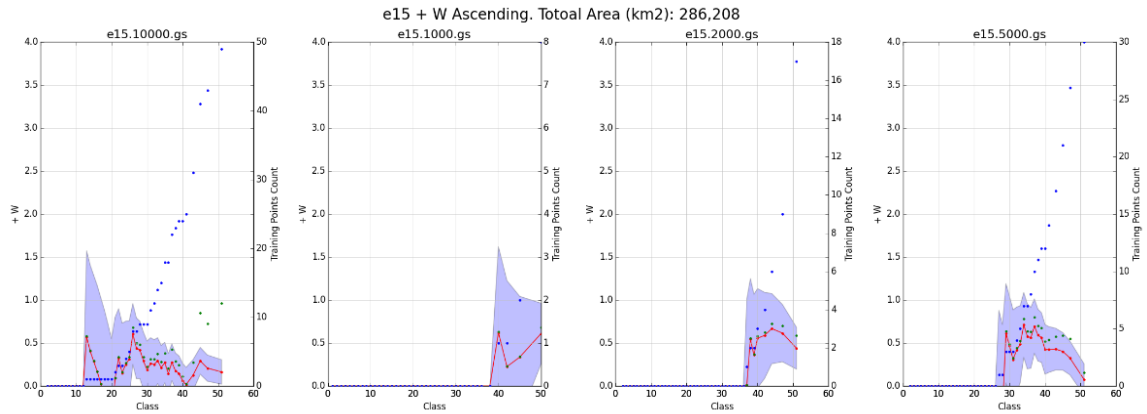


Figure 2.9: Cumulative weight test results examining earthquakes using density functions with no weighting. Numbers in each plot's title (1000, 2000, and 5000, 10000) denote the search radius used in meters. The x-axis shows class; each class is an equal interval bin of the full range of the density surface being examined with the highest density values being assigned the lowest class codes. The red points and line represent $W+$ and use the left axis. Blue shading around the red line indicates standard deviation of the weight. The blue points represent training point count and use the right axis. The green points represent contrast and use the left axis.

2.4 Generating Categorical Weights

2.4.1 Quaternary Faults

The process of selecting the 2.4 and 5.3 subsets of normal faults for use as possible evidence layers was described in a prior chapter. Two binary versions of each fault subset's weightings were chosen for further investigation, one using the threshold based on contrast, the other using the threshold based on studentized contrast. In addition, one set of ternary weights was chosen for each of the two fault subsets after examination of multiple possible bin thresholds. A fault's influence is local and would not contribute positively to geothermal potential beyond some unknown distance, almost certainly past 10 km and possibly beyond 5 km. Therefore, using a distance range that is too far from faults to calculate positive categorical weights does not appear to be a good idea. This limited the number of possible categorical weights to three (ternary binning), two of which had positive weights and the other a negative weight. Table 2.1 and Table 2.2 show the binary thresholds selected and ternary bin thresholds explored for fitting each subset; rows in bold were used in favorability maps.

Name	Class 1	Class 2	Class 3	W1	W2	W3
b5	0 km ≤ x ≤ 1 km	1 km < x		2.098	-0.240	
b6	0 km ≤ x ≤ 250 m	250m < x		2.497	-0.126	
t1	0 km ≤ x ≤ 750 m	750 m < x ≤ 3.5 km	3.5 km < x	2.159	0.872	-0.356
t2	0 km ≤ x ≤ 1 km	1 km < x ≤ 3.5 km	3.5 km < x	2.098	0.711	-0.356
t3	0 km ≤ x ≤ 750 m	750 m < x ≤ 2.5 km	2.5 km < x	2.159	0.719	-0.274
t4	0 km ≤ x ≤ 1 km	1km < x ≤ 2.5 km	2.5 km < x	2.098	0.351	-0.274
t5	0 km ≤ x ≤ 750 m	750 m < x ≤ 4 km	4 km < x	2.159	0.912	-0.402
t6	0 km ≤ x ≤ 1 km	1 km < x ≤ 4 km	4 km < x	2.098	0.787	-0.402
t7	0 km ≤ x ≤ 250 m	250 m < x ≤ 750 m	750 m < x	2.497	1.752	-0.200
t8	0 km ≤ x ≤ 250 m	250 m < x ≤ 1 km	1 km < x	2.497	1.773	-0.240
t9	0 km ≤ x ≤ 250 m	250 m < x ≤ 2 km	2 km < x	2.497	1.201	-0.263
t10	0 km ≤ x ≤ 250 m	250 m < x ≤ 2.5 km	2.5 km < x	2.497	1.056	-0.274

Table 2.1: Bin ranges tested for 2.4 fault subset. Name column shows model name, models beginning with ‘b’ are binary, models beginning with ‘t’ are ternary. Class 1 column shows the distance range used as the first bin threshold. Class 2 column shows the distance range used as the second bin threshold. Class 3 column shows the distance range used as the third bin threshold for ternary models. W1, W2, and W3 represent W+ for binned categories. Rows in bold were used to produce favorability maps.

Name	Class 1	Class 2	Class 3	W1	W2	W3
b1	0 km \leq x \leq 1 km	1 km $<$ x		2.58233	-0.2079	
b2	0 km \leq x \leq 250 m	250m $<$ x		3.02777	-0.13	
t1	0 km \leq x \leq 1 km	1 km $<$ x \leq 4 km	4 km $<$ x	2.58233	0.57518	-0.24687
t2	0 km \leq x \leq 750 m	750 m $<$ x \leq 4 km	4 km $<$ x	2.57584	1.00262	-0.24687
t3	0 km \leq x \leq 750 m	750 m $<$ x \leq 2.5 km	2.5 km $<$ x	2.57584	1.36502	-0.23815
t4	0 km \leq x \leq 500 m	500 m $<$ x \leq 2.5 km	2.5 km $<$ x	2.75601	1.42882	-0.23815
t5	0 km \leq x \leq 500 m	500 m $<$ x \leq 4 km	4 km $<$ x	2.75601	1.09311	-0.24687
t6	0 km \leq x \leq 500 m	500 m $<$ x \leq 2 km	2 km $<$ x	2.75601	1.48778	-0.22013
t7	0 km \leq x \leq 250 m	250 m $<$ x \leq 1 km	1 km $<$ x	3.02777	2.09434	-0.20791
t8	0 km \leq x \leq 250 m	250 m $<$ x \leq 2 km	2 km $<$ x	3.02777	1.53909	-0.22013
t9	0 km \leq x \leq 250 m	250 m $<$ x \leq 2.5 km	2.5 km $<$ x	3.02777	1.47888	-0.23815

Table 2.2: Bin ranges tested for 5.3 fault subset. Name column shows model name, models beginning with 'b' are binary, models beginning with 't' are ternary. Class 1 column shows the distance range used as the first bin threshold. Class 2 column shows the distance range used as the second bin threshold. Class 3 column shows the distance range used as the third bin threshold for ternary models. W1, W2, and W3 represent W+ for binned categories. Rows in bold were used to produce favorability maps.

In Table 2.1, the b5 model and b6 models represent binary thresholds with maximum values for studentized contrast and contrast respectively. Model b5 uses a 1 km buffer, model b6 uses a 0.25 km buffer. The ternary model t5 used distance bins of 0.75 and 4.0 km.

In Table 2.2, the b1 model and b2 models represent binary thresholds with maximum values for studentized contrast and contrast respectively. Model b1 uses a 1 km buffer, model b2 uses a 0.25 km buffer. The ternary model t6 used distance bins of 0.5 and 2.0 km.

2.4.2 Strain Rate

First, a cumulative weight test was run to get an idea of how the data correlate generally. Figure 2.10 shows a steady but jagged decrease in W_+ as represented by the red line with decreasing strain values. A jagged pattern is indicative of the very fine bin width, with the weight increasing significantly with each new training site. Weight values begin to behave less erratically once more training sites are covered by the pattern.

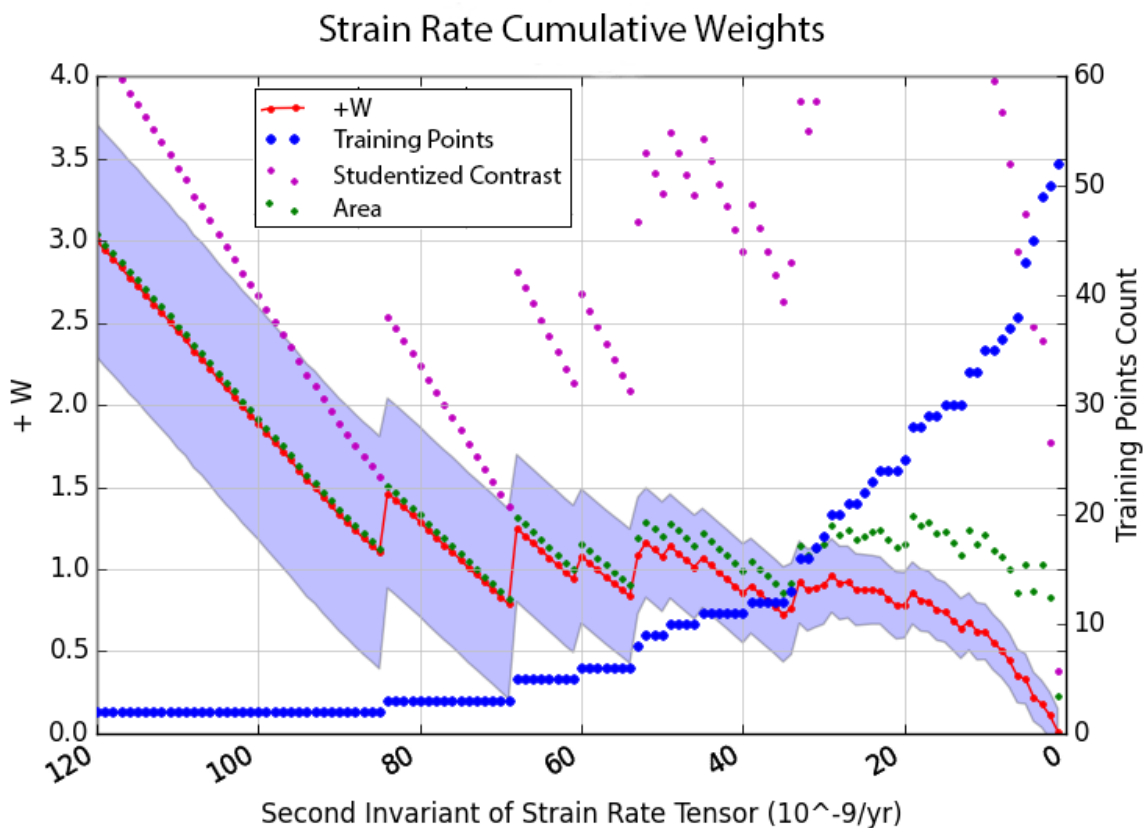


Figure 2.10: Cumulative weight plot of strain rate. The x-axis depicts native units (strain rate). Values for all parameters we calculated for 1-unit intervals of strain rate. The red points and line represent W_+ and use the left axis. Blue shading around the red line indicates standard deviation of the weight. The blue points represent training point count and use the right axis. The purple points represent the studentized contrast and use the left axis. The green points represent contrast ($W_+ - W_-$) and use the left axis.

About halfway along the x-axis of Figure 2.10, the strain rate categories begin picking up many more training sites quickly. The $W+$ decreases gradually and smoothly. This second half of the figure is the approximate range of the strain rate data that were used to create most of the individually weighted categories because enough training sites fell into significantly large portions of the study area. While this may appear like a small range of the total strain rate data, it represented a large proportion of the study area because most of Nevada had strain rates that varied within the low to moderate ranges of the total rate examined.

An iterative approach was then undertaken to characterize a trend between $W+$ and strain rate by binning the full range of the strain rate data into categories that each depict a subset of the full range. Each of these categories could then be weighted independently from one another by use of a categorical weight test. Then a process of guided trial and error was undertaken to find bin ranges that created categories that sequentially: had steady decreases in weight, steady increases in the spatial area encompassed, and contained enough training sites to calculate an accurate weight without containing more training sites than needed to allow for the creation of more robust subsequent categories.

Figure 1.8 and Figure 1.9 show results of the categorical weight test that used the best performing bin ranges. Though error bars around weight values show some overlap between categories, these bin ranges yielded a gradual decline in weight (red points & line, left axis) and similar bin geographic area (green dots show relative area, green line shows cumulative area; both are relative) across categories with a similar number of training sites (blue dots, right axis) in each bin (Figure 1.8 and Figure 1.9). These bin ranges were used to recategorize raw strain rate data (Figure 1.5) into the strain rate categories (Figure 2.11) used in generation of predictive maps.

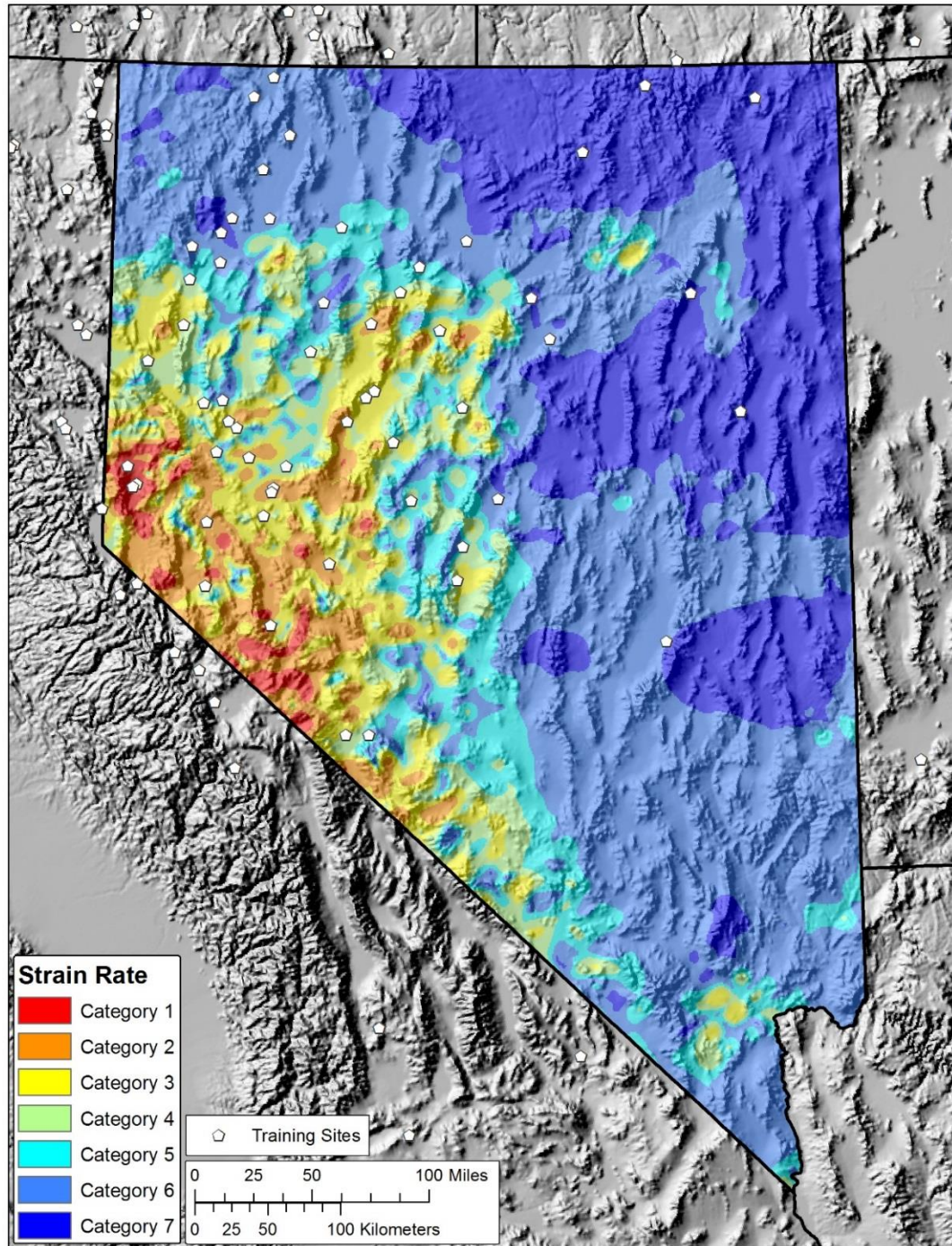


Figure 2.11: Map of strain rate categories. The map depicts the categories of estimated strain rate used for categorical and smoothed posterior probability calculations, clipped to the Nevada study area. Warmer colors depict higher rates, cooler colors depict lower rates. Each category represents a portion of the entire range of estimated strain rate, measured in units of 10^{-9} /yr. Identified moderate and high temperature geothermal systems used as training sites are depicted as white pentagons.

The process of arriving at the best performing bin thresholds involved first exploring, then refining bin ranges, as detailed in Figure 2.12. These charts are presented to illustrate the iterative processes undertaken to arrive at optimal bin ranges.

Figure 2.12a shows the result of three binning attempts that helped guide initial approaches. Each plot in Figure 2.12a uses a different number of categories of equal size (in native units). The first plot uses 10 equal sized categories, the next two plots use 11 and 12 respectively. The second two plots indicated there were too many small categories, causing some to pick up too few training sites to make useful measurements. The first plot shows that it might be possible to shift bin ranges to get weights to decline smoothly.

After some manual testing, another round with fewer bin ranges was attempted. Figure 2.12b shows some plots getting close to a steady decline in weights, some maintaining similar areas and training point counts between early groups. These guided the next round, seen in Figure 2.12c, which uses category code on the x-axis and in Figure 2.12d, which uses native units on the x-axis. Model 8c in Figure 2.12d appeared to meet all considerations well. A smooth-looking decline was achievable while maintaining considerations for area and training point count.

Because this iterative work was completed prior to considering ‘by area’ fitting (discussed in a later section), all exploratory fine tuning was done using native units on the x-axis. When fitting strain rate using the ‘by area’ method (see section ‘Generating Smoothed Weights From Categorical Weights’), several of the bin range scenarios seen in Figure 2.12d were tested and the model with the best r^2 (8c model) was used.

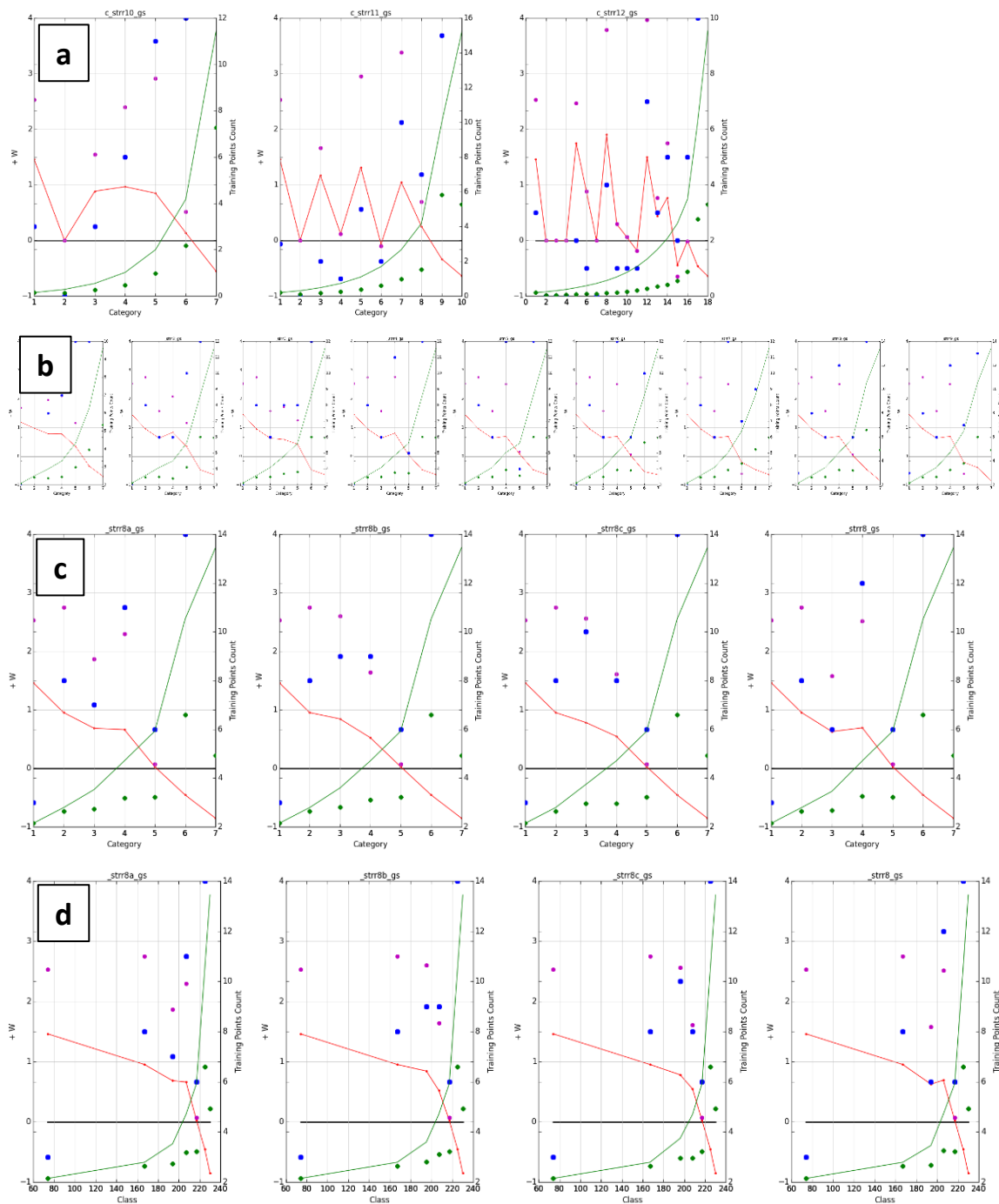


Figure 2.12: Categorical strain rate exploratory plots. Multiple charts are presented to illustrate the process of arriving at the best performing bin thresholds. This involved first exploring (subplot a), then refining bin ranges (subplots b, c, d). The x-axis on all plots is just an integer category code representing ranges of the data, except for subplot 'd' which uses a proxy for native units. W+ are the red points and lines (left axis), Blue points are number of training sites (right axis), green points are area, green line is cumulative area (no axis used, bottom represents 0%, top 100%). Purple is studentized contrast but is only relevant for the first category and should otherwise be ignored.

2.4.3 Heat Flow

The selection of the heat flow EBK surface to represent heat contributions was done using a modified study area based on the extent of the depth to basement map used to produce estimates of temperature at 3 km depth. The first step was therefore to run a cumulative weight test using the standard study area to get an initial idea of how the data were correlated, as seen in Figure 2.13.

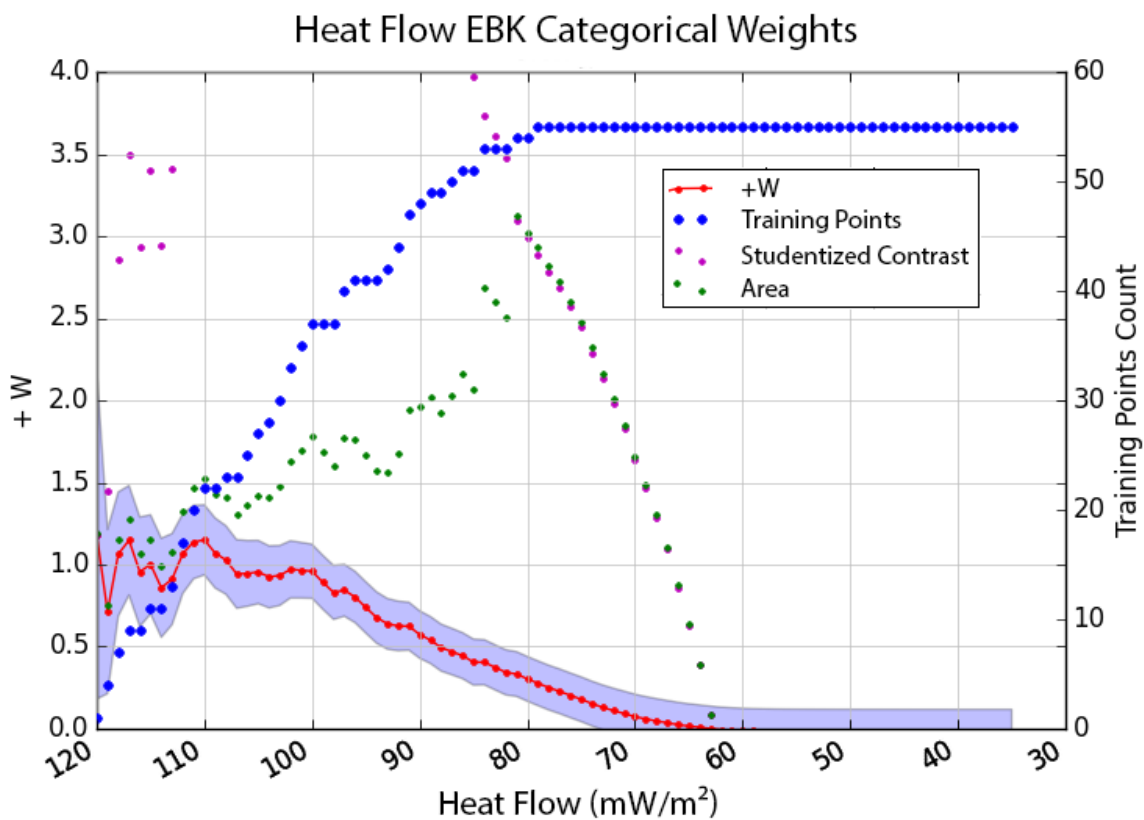


Figure 2.13: Ascending weight plot of heat flow data. The x-axis depicts heat flow in units of mW/m^2 . The red points and line represent W_+ and use the left axis. Blue shading around the red line indicates standard deviation of the weight. The blue points represent training point count and use the right axis. The purple points represent the studentized contrast and use the left axis. The green points represent contrast $(W_+ - W_-)$ and use the left axis.

The next step was to reclassify the full range of the heat flow data into categories that each represent a portion of the total range of heat flow values so that a weight could be independently measured for each category with the goal of defining a trend in the weights with changing rates of heat flow. A guided process of trial and error resulted in bin ranges for categories with weight values that declined gradually while maintaining steady increases in the spatial area encompassed and containing enough training sites.

Figure 2.14 shows the result of many binning attempts that used many different binning approaches. The x-axis on all these plots is the class value where smaller class numbers reflect ranges of higher heat flow values.

The first two plots in Figure 2.14a divided the heat flow map using an equal interval classification method (as was done in Coolbaugh and Bedell, 2006). Interval sizes of 10, and 15 mW/m^2 are shown. The next two plots divided the heat flow map up into categories using the natural breaks technique. Numbers of categories tested included 10 and 7. The next and final two plots divided the heat flow map up into categories by quantile. Numbers of categories tested included 6 and 8.

Some of these plots in Figure 2.14a have weights that decline steadily. Many of these plots appear to cross $W_+ = 0$ around class 30, which corresponds to a minimum heat flow of 92 mW/m^2 . These facts appear to indicate that categorical weights can decline steadily for this layer and when it does, it tends to have $W_+ = 0$ around class 30. Of plots that declined steadily, 'hf_n7_gs' did so while maintaining similar sized category areas. These bin values became the starting point for a new set of bin range attempts as seen in Figure 2.14b. Because this exploratory work was completed prior to considering 'by area' fitting (discussed in next chapter), the iterative work described here was done using a proxy for native units on the x-axis. When fitting heat flow by area in a later section titled "Generating Smoothed Weights from Categorical Weights", several bin range

classifications seen in Figure 2.14b were tested and the model with the best r^2 (model c2 in Figure 2.14b) was used.

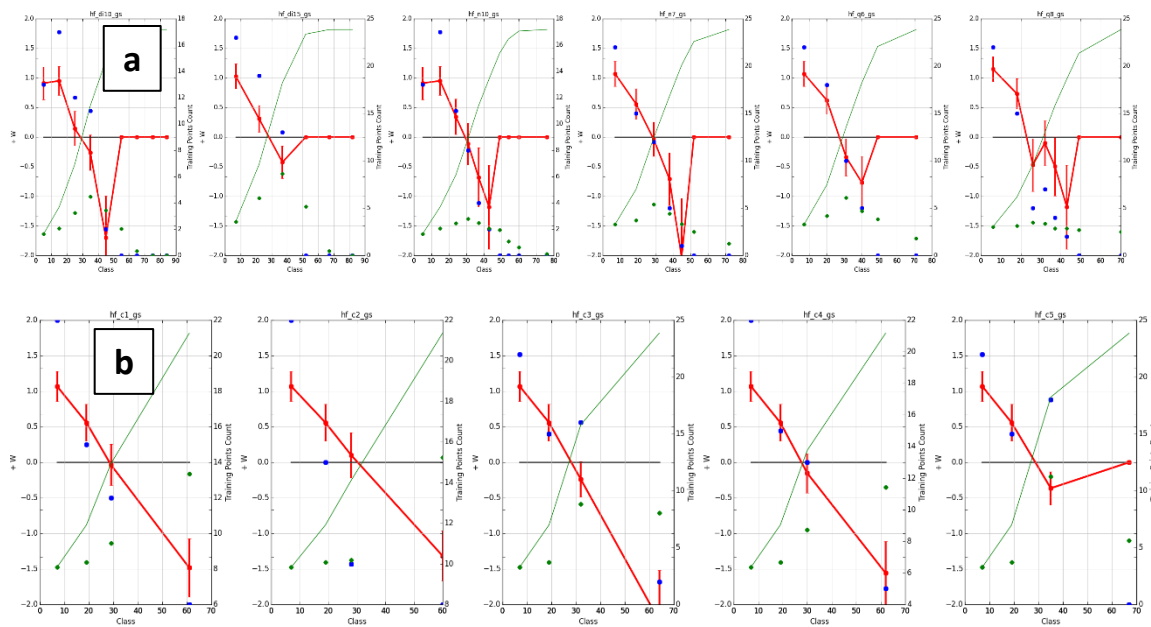


Figure 2.14: Categorical heat flow exploratory plots. Two charts are presented to illustrate the process of arriving at the best performing bin thresholds. This involved first exploring (subplot a), then refining bin ranges (subplot b). The x-axis on all uses a proxy for native units. $W+$ are the red points and lines (left axis), Blue points are number of training sites (right axis), green points are area, green line is cumulative area (no axis used, bottom represents 0%, top 100%).

Figure 2.15 shows the results of a categorical weight test performed on the best performing bin ranges, and Figure 2.16 shows how the recategorization looks spatially. In Figure 2.15, though error bars around weight values show some overlap between categories, weights (red dots & line, left axis) decline in a linear fashion, categories contain similar geographic area measurements (green dots, no scale, relative area depicted), and a similar number of training points in each category (blue dots, right axis).

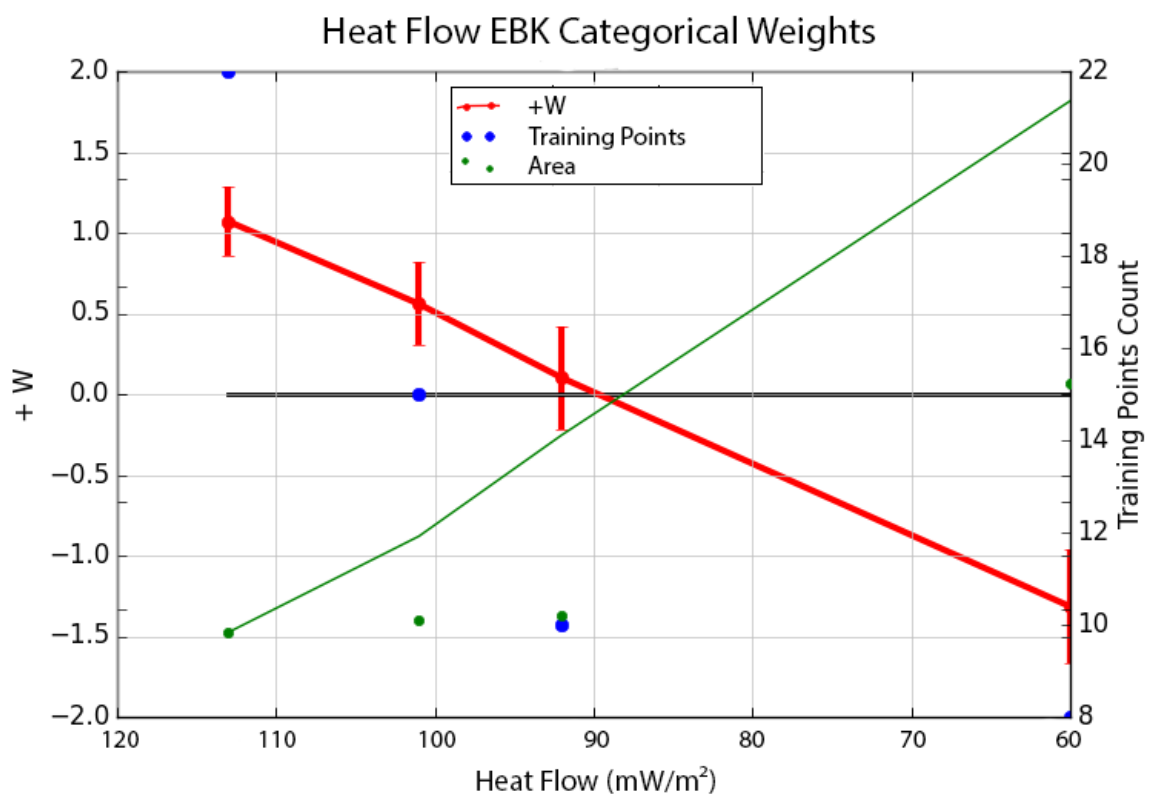


Figure 2.15: Categorical weight plot of heat flow rate categories. All x-axis values of all points on this figure are plotted at their native unit midpoint. The x-axis shows native units of heat flow (mW/m^2). The red points and line represent W_+ and use the left axis. Error bars around weight values indicate standard deviation of the weight. The blue points represent training point count and use the right axis. The green points represent percent area associated with each bin, on an axis of 0 (bottom of graph) to 100% (top of graph). The green line represents cumulative percent area, also plotted with 0 at the bottom of y-axis and 100% at top of y-axis.

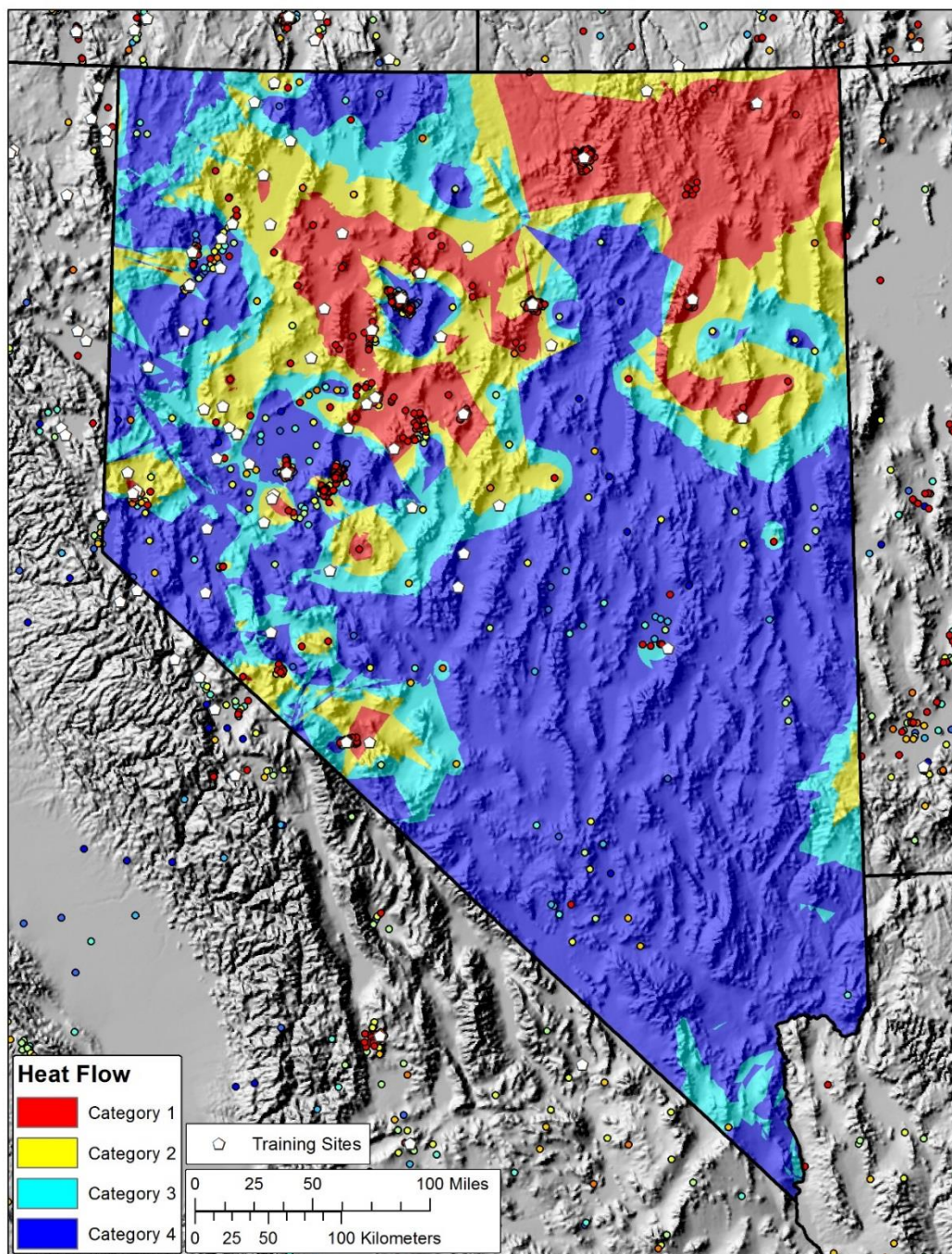


Figure 2.16: Map of heat flow categories. The map depicts the categories of estimated heat flow rate used for categorical and smoothed posterior probability calculations in units of mW/m^2 . The surface was interpolated from heat flow wells, depicted as small circles colored by their heat flow value. Warmer colors depict higher rates, cooler colors depict lower rates. Each category represents a portion of the entire range of estimated heat flow rate. Identified moderate and high temperature geothermal systems used as training sites are depicted as white pentagons.

2.5 Generating Smoothed Weights from Categorical Weights

The ACCI tool is typically used at the end of a WofE analysis to assess conditional independence of layers within a multilayer model. It was used in this step of the analysis instead primarily for its ability to calculate the number of training sites an individual layer predicts. If an evidence layer is broken into categories and has categorical weights generated for those categories, the ACCI tool will always predict the exact number of training sites because the weights were calculated specifically to predict the number of training sites used. When smoothed weights are interpolated from categorical weights, there is a risk that the weights could over- or under-predict the number of training sites. The ACCI tool was used to monitor the training site prediction, thus working as a constraint on the type of curve fitting employed. A curve-fitting approach was ultimately selected for each evidence layer that came the closest to predicting the correct number of training sites while accurately characterizing trends in the data.

To fit a function through categorical weights across the range of an evidence layer, the weights are the dependent variable and would be plotted on the y-axis of a figure. Initial attempts to fit a function using the native unit (heat flow, strain, or distance) as the independent variable as in Coolbaugh and Bedell (2006) consistently over-predicted the number of training sites. It was found that by using cumulative area as the independent variable instead of native units, it was easier to develop smoothing curves that closely approximated the correct number of training sites. An exact estimate of the number of training sites is unlikely because it is nearly impossible to fit a perfect function ($r^2 = 1.0$) to data derived through the means described earlier of finding optimal categorical weights. If individual layers over or under-predict, those discrepancies will propagate through a multi-layer model. For that reason, small artificial modifications were made to the function that would result in exact predictions.

The process of ‘fitting by area’ initially involves plotting each categorical weight using its ‘area midpoint’ as the independent variable, plotted using ‘cumulative area’ as the quantity on the x-axis. When categorical weights are calculated using the ArcSDM tool, a table is generated that notes the spatial area associated with each category or bin. The area midpoint for each category was calculated by dividing its area by two and adding that value to the sum of the areas of all preceding categories. For example, the area midpoint of the first category was calculated by dividing the first category’s area by two. The second category was calculated by dividing its area by two, then adding that value to the area of the first category. Once an area midpoint was calculated for each category, the values were plotted, and a function was fit using cumulative area as the independent variable. Where convenient for visualization purposes, as will be seen shortly, the x-axis of area can be converted back to native units by using the relationship between cumulative area and native units present in the original predictive layer (e.g. the map of heat flow).

These functions were used to modify the cumulative weight tables so they could be used to assign unique weights for every bin that was originally examined using the cumulative weight test. The heat flow data turned out to be the simplest example and will therefore be presented first, followed by strain rate and Quaternary faults.

2.5.1 Heat Flow

Of the four surfaces created to represent heat, the surface that estimated heat flow using the EBK interpolator performed best and was therefore used as the evidence layer representing heat. Figure 2.15 shows the categorical weights calculated for heat flow and shows native units on the x-axis, with categorical weights plotted at the midpoint for each bin. As heat flow declines, weights decline in a linear fashion. The red points in Figure 2.15 (weight plotted by native unit) are depicted by the yellow points in Figure 2.17.

Figure 2.17 plots the weights on two different scales, one scale by heat flow and the other by equivalent cumulative area. The blue line in Figure 2.17 is a linear trendline fit through the yellow points (native unit midpoint) and has a high r^2 value of 0.9994. The green points (area midpoint) plot the same weight values at their area midpoint, a different location on the x-axis than the yellow points (native unit midpoint). The grey vertical lines on the plot represent the bin boundaries. The yellow points always fall exactly between the grey lines and plot edges. The green and yellow points appear very close to one another in the first three bins, in the fourth bin they do not.

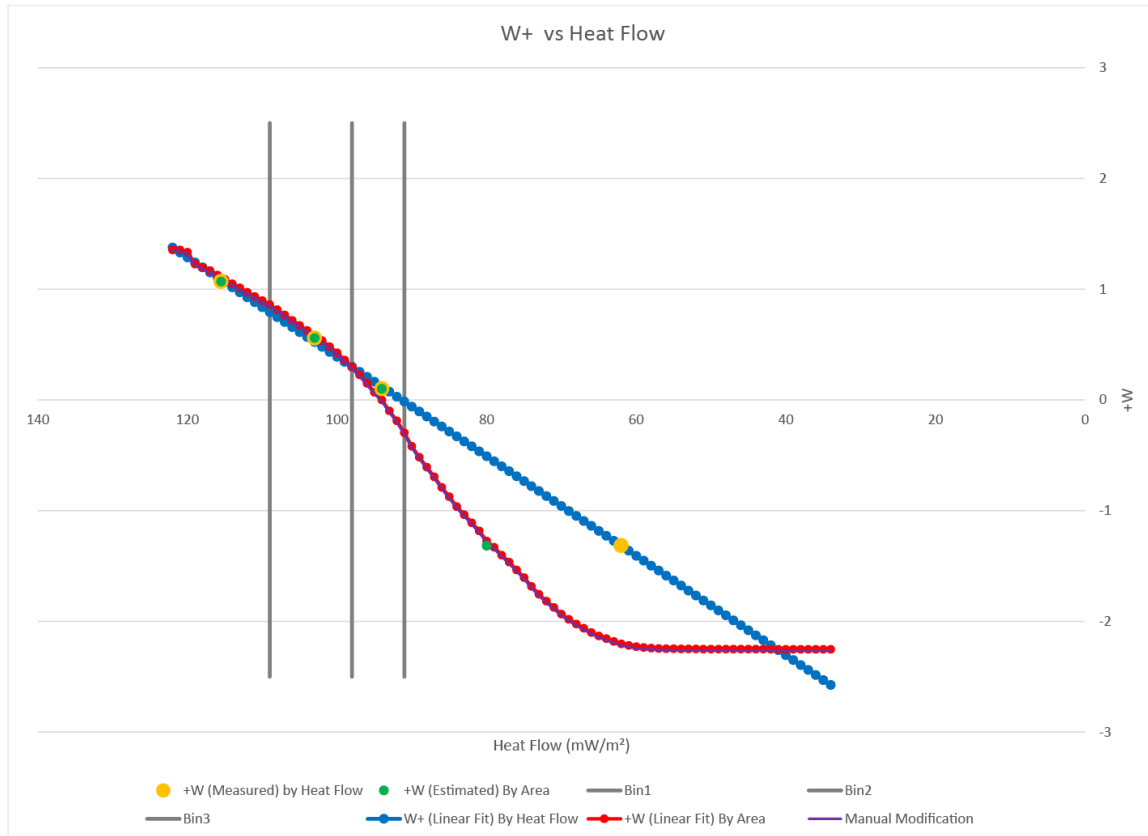


Figure 2.17: Plot showing weight functions calculated for heat flow, displayed using native units as a linear independent variable. The y-axis depicts the weight (either positive or negative), the x-axis shows native units of heat flow in mW/m^2 . The yellow points depict categorical weight values plotted at their native unit midpoint on the x-axis. The blue line is a linear trendline fit through the yellow points. The green points depict categorical weight values plotted at their area midpoint on the x-axis. The red line is a trendline through the green points which was fit 'by area' using the linear relationship shown on Figure 2.18. The grey vertical lines on the plot represent the bin boundaries. The purple line shows the modified fit that perfectly predicts the number of training sites.

The red line in Figure 2.17 depicts a trend in the green dots (area midpoint) fit by using area as the independent variable. This line does not appear linear when the x-axis is depicted in linear native units. However, plotting the green dots using linear cumulative area on the x-axis reveals a linear trend, as seen in Figure 2.18. Figure 2.18 shows how an equation was derived to 'fit by area.' The x-axis represents cumulative area. The figure shows the weights plotted by their area midpoint (green dots). A linear best-fit equation was applied to the green dots ($r^2 = 0.9957$), represented by the dotted red line. The dotted blue line depicts the smoothed weights derived from a linear fit with native units in Figure 2.17. When the linear trend derived 'by native unit' is plotted 'by area,' it appears curved.

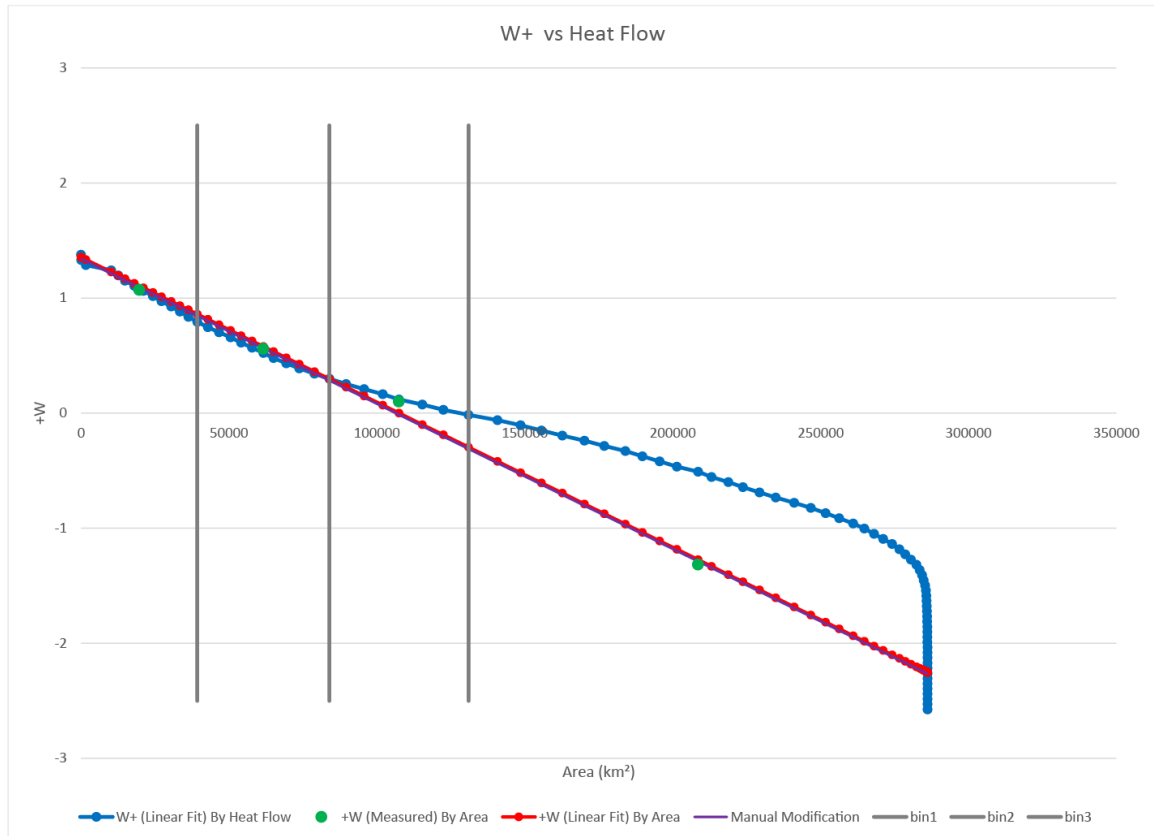


Figure 2.18: Plot showing weight functions calculated for heat flow, displayed using cumulative area as the x-axis independent variable. The y-axis depicts the weight (either positive or negative), the x-axis shows cumulative area. The green points depict categorical weight values plotted at their area midpoint on the x-axis. The red line is a linear trendline fit through the green points. The grey vertical lines on the plot represent the bin boundaries. The purple line shows the modified fit that perfectly predicts the number of training sites.

When the area-smoothed heat flow layer using weights from the red line in Figure 2.17 and Figure 2.18 was evaluated in the ACCI test, it performed well. 55 training sites were used in the analysis and the test predicted 55.7. By comparison, the linear fit derived using the native unit midpoints predicted 64.5 systems. The purple line in Figure 2.17 was artificially modified to predict exactly 55 systems. It was lowered by the same amount for each bin to artificially produce an exact estimate. The purple and red lines are virtually indistinguishable on this figure.

2.5.2 Strain Rate

Figure 1.9 shows the categorical weights calculated for strain rate using native units on the x-axis, with weights plotted at the native unit midpoint. As strain rate declines, the weights decline in a non-linear fashion. The red points in Figure 1.9 ($W+$ plotted by native unit) are depicted by the yellow points in Figure 2.19. The blue line in Figure 2.19 is a logarithmic trendline fit through the yellow points and has a high r^2 value of 0.9678. The logarithmic fit performed better than linear or polynomial approaches. The green points (area midpoint) depict the same weights plotted at their area midpoint, using the same procedure used above for heat flow. The grey vertical lines on the plot represent the bin boundaries. The yellow points always fall exactly halfway between the grey lines. The green and yellow points appear far apart in most bins, showing a significant disparity in approaches. The red line depicts a third-order polynomial trend in the green dots fit by using area as the independent variable. Figure 2.20 shows how an equation was derived to 'fit by area.' The x-axis represents linear cumulative area. The figure shows the weights plotted by their area midpoint (green dots). A third-order polynomial fit was applied to the green dots ($r^2 = 0.9824$), represented by the dotted red line. The dotted blue line depicts the same curve shown as Figure 2.19's blue line, the logarithmic fit by native unit.

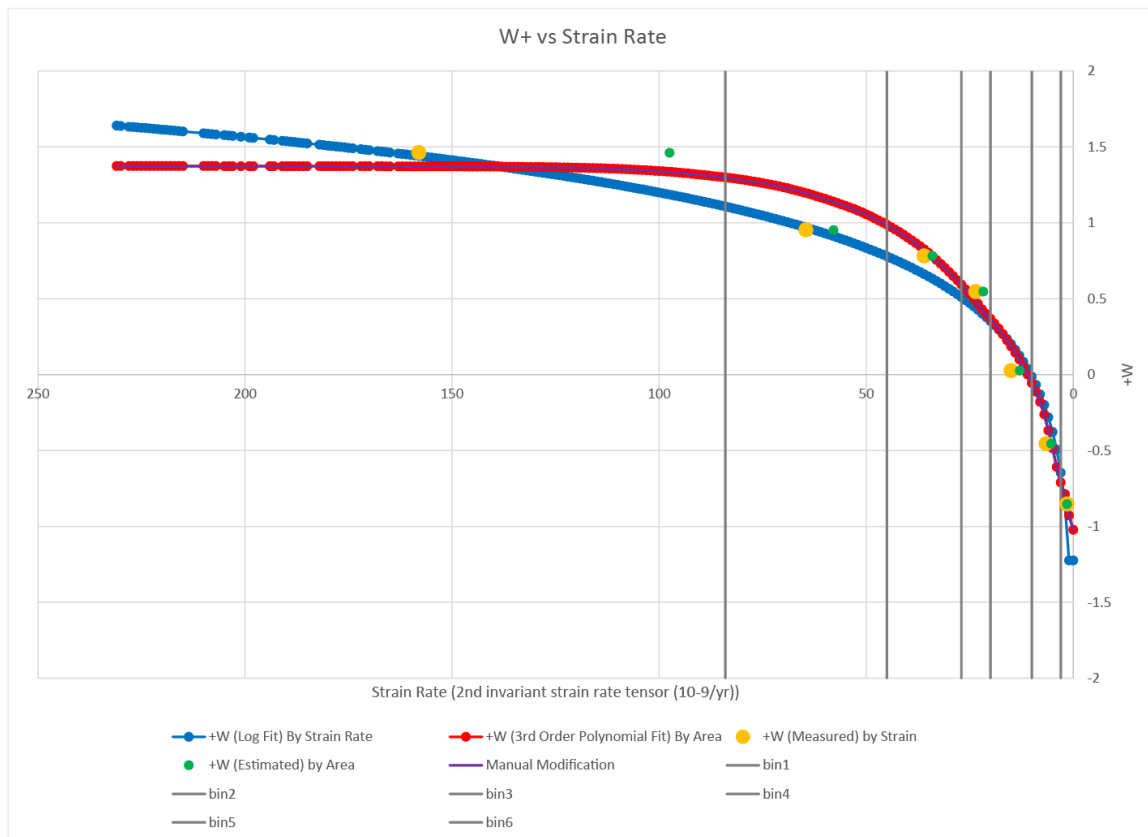


Figure 2.19: Plot showing weight functions calculated for strain rate, displayed using native units as independent variable. The y-axis depicts the weight (either positive or negative), the x-axis shows native units of the second invariant strain rate tensor in units of $10^{-9}/\text{yr}$. The yellow points depict categorical weight values plotted at their native unit midpoint on the x-axis. The blue line is a logarithmic trendline fit through the yellow points. The green points depict categorical weight values plotted at their area midpoint on the x-axis. The red line is a 3rd order polynomial fit through the green points (see Figure 2.20). The grey vertical lines on the plot represent the bin boundaries. The purple line shows the modified fit that perfectly predicts the number of training sites.

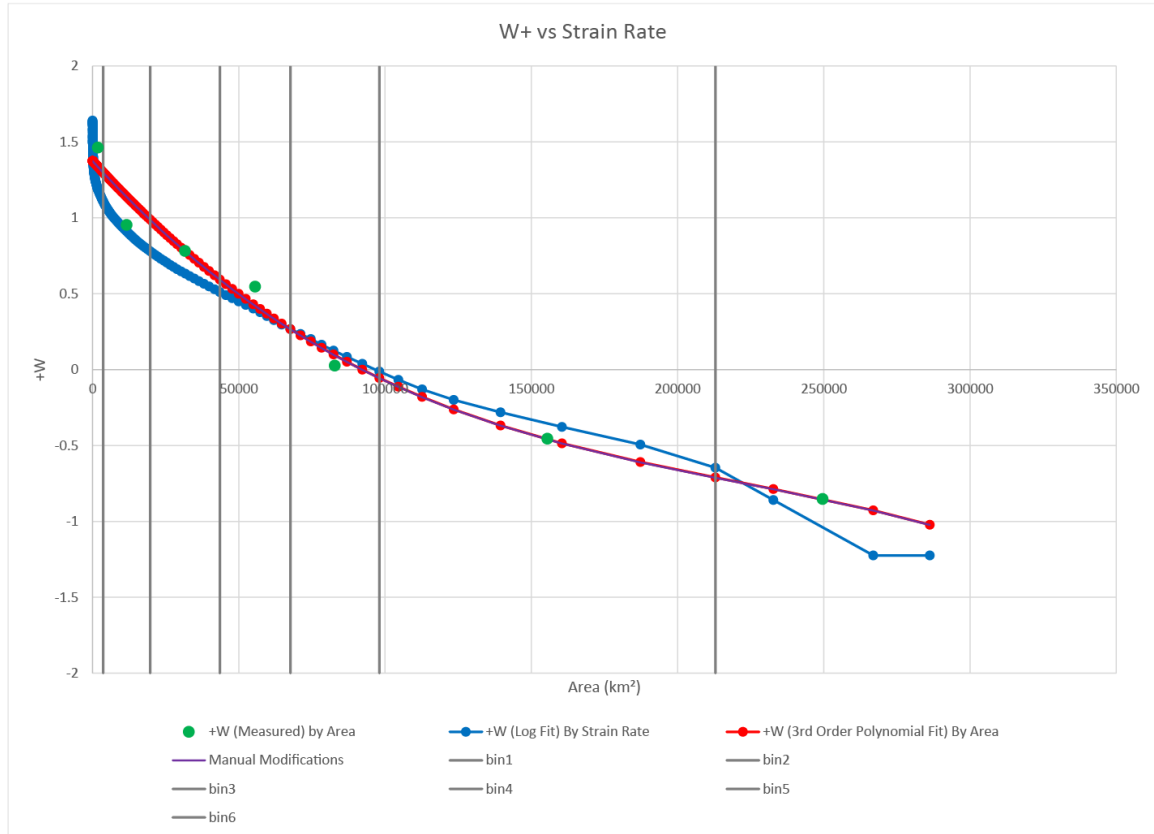


Figure 2.20: Plot showing weight functions calculated for strain rate, displayed using cumulative area as independent variable. The y-axis depicts the weight (either positive or negative), the x-axis shows linear cumulative area. The green points depict categorical weight values plotted at their area midpoint on the x-axis. The red line is a 3rd order polynomial trendline fit through the green points. The grey vertical lines on the plot represent the bin boundaries. The purple line shows the modified fit that perfectly predicts the number of training sites.

When the ‘fit by area’ curve (red line/points in Figure 2.19, Figure 2.20) was tested in the ACCI test, it performed very well. 55 training sites were used in the analysis and the test predicted 55.1. By comparison, the logarithmic fit derived using the native unit midpoint predicted 51.7 systems. The purple line in Figure 2.19 was artificially modified to predict exactly 55 systems. It was lowered by the same amount for each bin to artificially produce an exact estimate. The purple and red lines are virtually indistinguishable on this figure.

2.5.3 Quaternary Faults

Smoothing of fault data was more challenging than it was for the prior examples of heat flow and strain rate. As described in earlier sections, using a binary threshold to recategorize fault distances yielded two points with which to fit a weight function. Ternary binning yielded three categories, thereby improving the characterization of a gradational relationship. Ternary binning was used for smoothing the two subsets of normal faults identified in descriptions of Figure 2.2 as having the strongest measured weights, subset 2.4 (Faults ‘Latest Quaternary’ and younger of all slip rates), and subset 5.3 (Faults ‘Undifferentiated Quaternary’ and younger with slip rates equal to or greater than 0.2 mm/yr).

2.5.3.1 Fault Subset 2.4 (‘Latest Quaternary’ and younger of all slip rates)

Figure 2.21 shows weight values plotted by distance from faults (yellow dots) and weighted by area (green dots) using linear distance on the x-axis. The first bin used in the ternary classification was 0.75 km from a fault, the second bin was from 0.75 to 4.0 km from a fault. Figure 2.22 shows the same data but applies a log transformation to the x-axis. Here, the weights plotted by their native unit midpoint (yellow dots) can be used to

generate a fit (blue line) with a high r^2 value of 0.9785. This approach predicted 78 systems, a very large overprediction of the actual 55 systems.

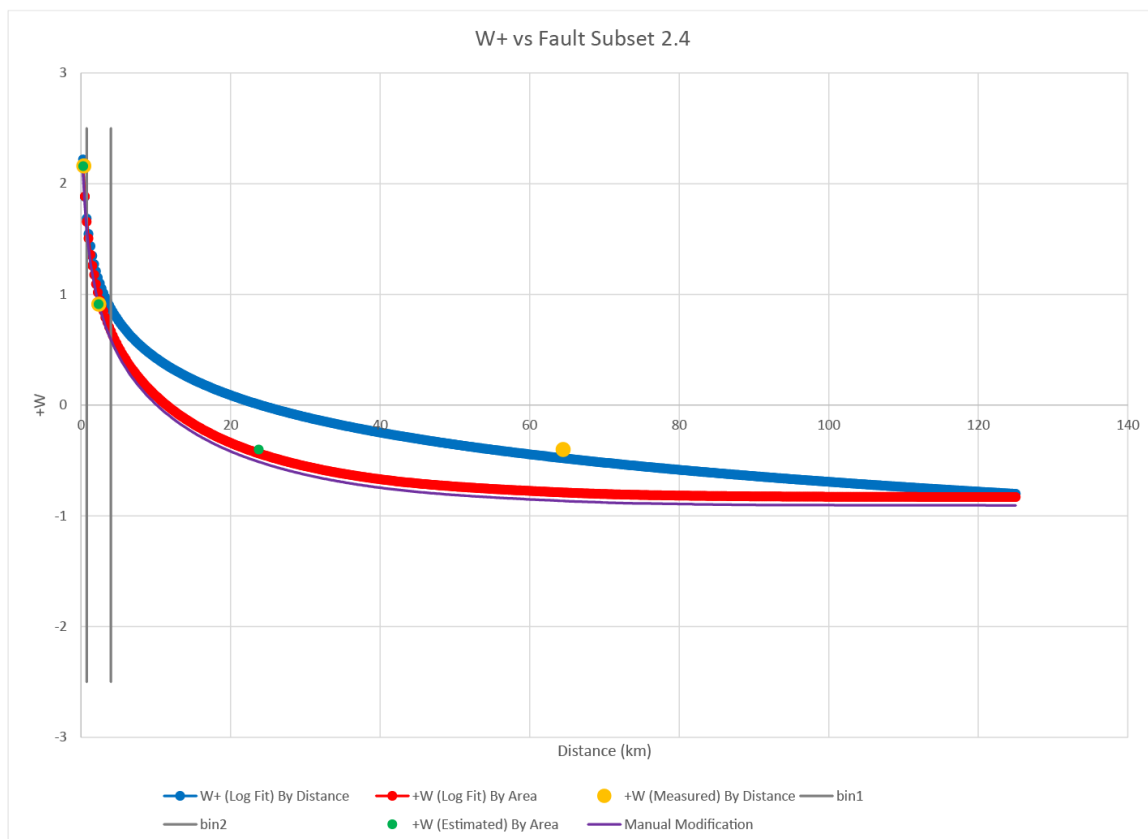


Figure 2.21: Plot showing weight functions calculated for Quaternary faults 2.4 subset (Age equal to or younger than ‘Latest Quaternary’, all slip rates), displayed using native units as independent variable with x-axis values increasing linearly. The y-axis depicts $W+$, the x-axis shows native units, distance in km. The yellow points depict categorical weight values plotted at their native unit midpoint on the x-axis. The blue line is a linear trendline fit through the yellow points. The green points depict categorical weight values plotted at their area midpoint on the x-axis. The red line is a linear trendline fit through the green points derived from an analysis presented in Figure 2.23. The grey vertical lines on the plot represent the bin boundaries. The purple line shows the modified fit that perfectly predicts the number of training sites.

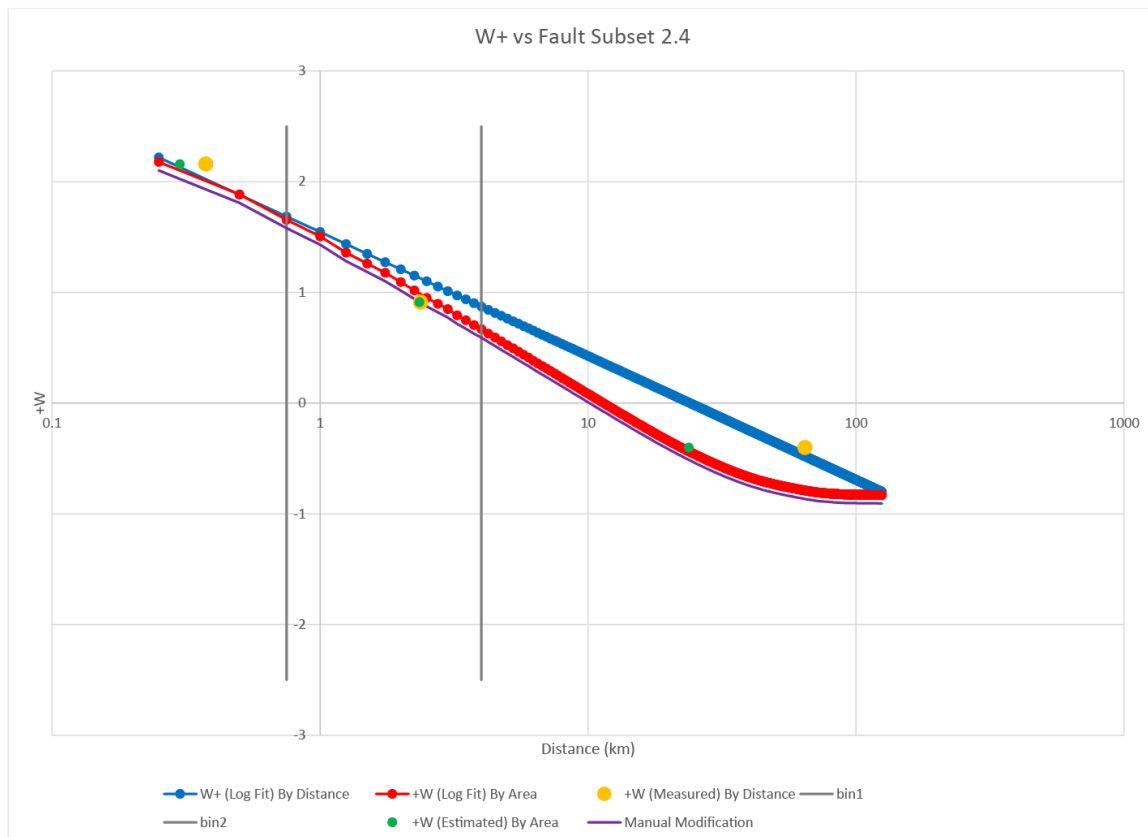


Figure 2.22: Plot showing weight functions calculated for Quaternary faults 2.4 subset (Age equal to or younger than ‘Latest Quaternary’, all slip rates), displayed using native units as independent variable with x-axis values increasing logarithmically. The y-axis depicts $W+$, the x-axis shows native units, distance in km which increases logarithmically. The yellow points depict categorical weight values plotted at their native unit midpoint on the x-axis. The blue line is a linear trendline fit through the yellow points. The green points depict categorical weight values plotted at their area midpoint on the x-axis. The red line is a linear trendline fit through the green points derived from an analysis presented in Figure 2.23. The grey vertical lines on the plot represent the bin boundaries. The purple line shows the modified fit that perfectly predicts the number of training sites.

Figure 2.23 shows how a function was fit by area. The red points and line represent the log function fit through the green points (weight plotted using area midpoint). It had a very high r^2 value of 0.997. It predicted 59.4 systems. This is a large overprediction, but it is much lower than the fit attempted using the native units (78 systems). The purple line shows results of lowering the function by a constant value to achieve a perfect prediction of 55 systems.

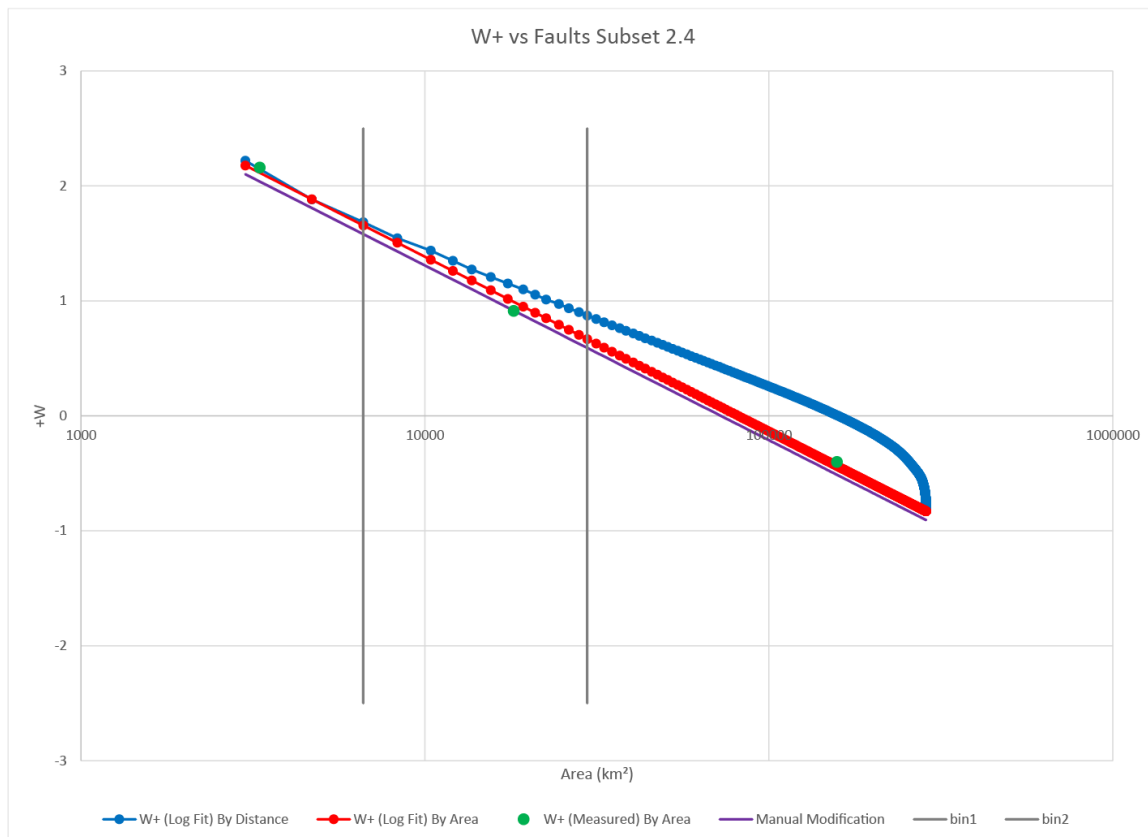


Figure 2.23: Plot showing weight functions calculated for Quaternary faults 2.4 subset (Age equal to or younger than ‘Latest Quaternary’, all slip rates), displayed using cumulative area as independent variable with x-axis values increasing logarithmically. The y-axis depicts $W+$, the x-axis shows cumulative area which increases logarithmically. The green points depict categorical weight values plotted at their area midpoint on the x-axis. The red line is a linear trendline fit through the green points. The grey vertical lines on the plot represent the bin boundaries. The purple line shows modified fit that perfectly predicts the number of training sites.

2.5.3.2 Fault Subset 5.3 ('Undifferentiated Quaternary' and younger with slip rates equal to or greater than 0.2 mm/yr)

Figure 2.24 shows how a function was fit by area for fault subset 5.3 (Quaternary faults with known age with slip rates ≥ 0.2 mm/yr). The first bin used in the ternary classification was 0.75 km from a fault, the second bin was from 0.75 to 2.5 km from a fault. The red points and line represent the log function fit through the green points (W+ by area midpoint). It had a high r^2 value of 0.9742. It predicted 63.3 systems. The purple line shows results of lowering the function by a constant value to achieve a perfect prediction of 55 systems. No estimates were calculated using native units, it would certainly have estimated more systems than the 'by area' approach. This can be seen in Figure 2.24; lowering the red line to the purple line resulted in $(63.3 - 55 =) 8.3$ fewer systems. The blue line is higher than the red line nearly everywhere, and therefore would predict many more systems than the 'by area' approach.

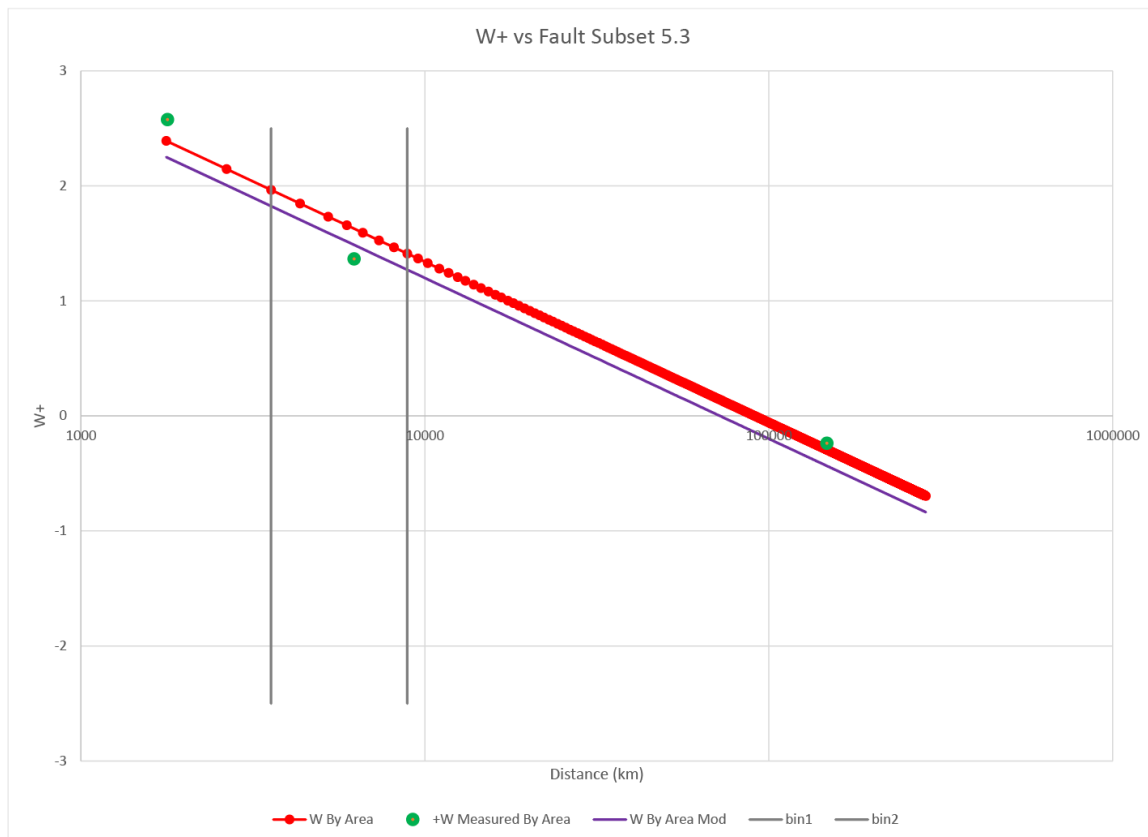


Figure 2.24: Plot showing weight functions calculated for Quaternary faults 5.3 subset (Age equal to or younger than ‘undifferentiated Quaternary’ and slip rate equal to or younger than 1.0 mm/yr), displayed using cumulative area as independent variable with x-axis values increasing logarithmically. The y-axis depicts $W+$, the x-axis shows cumulative area which increases logarithmically. The green points depict categorical weight values plotted at their area midpoint on the x-axis. The red line is a linear trendline fit through the green points. The grey vertical lines on the plot represent the bin boundaries. The purple line shows modified fit that perfectly predicts the number of training sites.

2.6 Posterior Probability Calculations

Posterior probability maps were generated using the “Calculate Response” tool in ArcSDM. Posterior probability maps depict the probability of occurrence of a geothermal system, based on the prior probability and on the weights calculated for each of the input evidence maps as per Equation 1-5.

A total of fourteen different posterior probability maps were generated that each used a unique combination of the three evidence layers with either measured categorical weights or the smoothed weights fit by area. Conditional independence tests were run on each scenario to see the degree to which they correctly predicted the number of training sites and to test whether each scenario’s layers were conditionally independent with respect to each other. By comparing similar scenarios, judgements could be made as to which layers are conditionally dependent with which others, and to compare the performance of smoothed weights relative to multiple categorical weights.

3.0 Results

This section first reports a summary of all the evidence layers that were explored in the process of selecting the three evidence layers chosen for use in the final favorability maps. Next, categorical weights and associated statistics are reported for the three evidence layers. The next section details the findings while calculating smoothed weights from categorical weights. Then results of tests that assessed the smoothing process were presented. Next, results of tests that assessed how accurately multilayer models predict were presented. Finally, a series of maps are presented to show the full variety of model combinations produced.

3.1 Review of Evidence Data

Data depicting distance from Quaternary faults, crustal heat flow, and geodetic strain rate were chosen as sources of evidence data for modeling posterior probability in the present study. These layers are summarized in Table 3.1, which shows all approaches attempted on all layers examined in the study.

Evidence Layer	Approach	Used
Strain Rate	Categorical, Smoothed	Yes
Heat Flow	Empirical Bayesian Kriging; Categorical, Smoothed	Yes
Heat Flow	Radial Basis Function; Categorical	No
Temperature at 3 km	Empirical Bayesian Kriging (heat flow); Categorical	No
Temperature at 3 km	Radial Basis Function (heat flow); Categorical	No
Faults	Normal Subsets By Distance; Categorical, Smoothed	Yes
Faults	All Sense Subsets of TD By Distance	No
Faults	Simple Density Dilation Tendency	No
Faults	Simple Density Slip Tendency	No
Faults	Kernel Density Dilation Tendency	No
Faults	Kernel Density Slip Tendency	No
Faults	Distance Dilation Tendency	No
Earthquakes	'Log of Sum of Moment' Simple Density	No
Earthquakes	'Log of Sum of Moment' Kernel Density	No

Table 3.1: Evidence layer approach table: The 'Evidence Layer' column refers to the data used to create each evidence layer/approach pair tested in WofE analysis. The 'Approach' column describes the geographic techniques applied to each evidence layer/approach pair. 'Used' shows if each evidence layer/approach pair was used in this analysis (Blue) or not used (Orange) to calculate posterior probability.

3.2 Categorical Weight Results

Categorical weight test results are reported in tables that list each weight's range of native units, area, training point count, weight, and standard deviation of the weight for heat flow (Table 3.2) and strain rate (Table 3.3). Similar tables for fault subset 2.4 (Table 3.4), and fault subset 5.3 (Table 3.5) also included columns indicating contrast and studentized contrast. These weights were used to calculate posterior probability using the traditional WofE approach.

Category	Heat Flow Range (mW/m ²)	Area (km ²)	# Training Points	Weight	SD Weight
1	$109 \leq x < 122$	39,285	22	1.07	0.21
2	$98 \leq x < 109$	44,662	15	0.56	0.26
3	$91 \leq x < 98$	47,062	10	0.10	0.32
4	$34 \leq x < 91$	155,200	8	-1.32	0.35

Table 3.2: Heat flow categorical weights: From left to right, columns represent for each category: a weight ID number, the range of native units represented, the area occupied in km², the number of training points, W_+ , standard deviation of W_+ , and studentized contrast.

Category	Strain Rate Range (10^{-9}) /yr	Area (km ²)	# Training Points	Weight	SD Weight
1	$84 \leq x < 233$	3,621	3	1.46	0.58
2	$45 \leq x < 84$	16,073	8	0.95	0.35
3	$27 \leq x < 45$	23,822	10	0.78	0.32
4	$20 \leq x < 27$	24,112	8	0.55	0.35
5	$10 \leq x < 20$	30,425	6	0.03	0.41
6	$3 \leq x < 10$	114,890	14	-0.46	0.27
7	$0 \leq x < 3$	73,265	6	-0.85	0.41

Table 3.3: Strain rate categorical weights: From left to right, columns represent for each category: a weight ID number, the range of native units represented, the area occupied in km², the number of training points, W_+ , standard deviation of W_+ , and studentized contrast.

Binary (Max Contrast)	Distance Range (km)	Area (km ²)	# Training Points	Weight	SD Weight	Stud. Contrast	Contrast
1	$0 < x \leq 0.25$	3,005	7	2.50	0.38	6.48	2.62
2	$0.25 < x \leq 125$	283,204	48	-0.13	0.14	-6.48	-2.62
Binary (Max Studentized)	Distance Range (km)	Area (km ²)	# Training Points	Weight	SD Weight	Stud. Contrast	Contrast
1	$0 < x \leq 1.0$	8,310	13	2.10	0.28	7.36	2.34
2	$1.0 < x \leq 125$	277,898	42	-0.24	0.15	-7.36	-2.34
Ternary	Distance Range (km)	Area (km ²)	# Training Points	Weight	SD Weight	Stud. Contrast	Contrast
1	$0 < x \leq 0.75$	6,617	11	2.16	0.30	6.99	2.36
2	$0.75 < x \leq 4.0$	23,013	11	0.91	0.30	3.12	1.05
3	$4.0 < x \leq 125$	256,579	33	-0.40	0.17	-6.37	-1.75

Table 3.4: Faults 2.4 ('latest Quaternary' and younger, all slip rates) categorical weights: From left to right, columns represent for each category: a weight ID number, the range of native units represented, the area occupied in km², the number of training points, W+, standard deviation of W+, and studentized contrast. Statistics are presented for the binary binning threshold with maximum contrast, the binary binning threshold with maximum studentized contrast, and the ternary binning threshold.

Binary (Max Contrast)	Distance Range (km)	Area (km ²)	# Training Points	Weigh t	SD Weigh t	Stud. Contras t	Contras t
1	$0 < x \leq 0.25$	1,771	7	3.03	0.38	7.79	3.16
2	$0.25 < x \leq 294$	284,438	48	-0.13	0.14	-7.79	-3.16
Binary (Max Studentized)	Distance Range (km)	Area (km ²)	# Training Points	Weigh t	SD Weigh t	Stud. Contras t	Contras t
1	$0 < x \leq 1.0$	4,338	11	2.58	0.30	8.27	2.79
2	$1.0 < x \leq 294$	281,871	44	-0.21	0.15	-8.27	-2.79
Ternary	Distance Range (km)	Area (km ²)	# Training Points	Weigh t	SD Weigh t	Stud. Contras t	Contras t
1	$0 < x \leq 0.5$	2,653	8	2.76	0.35	7.58	2.90
2	$0.5 < x \leq 4.0$	4,705	4	1.49	0.50	2.98	1.55
3	$4.0 < x \leq 294$	278,851	43	-0.22	0.15	-7.22	-2.36

Table 3.5: Faults 5.3 ('undifferentiated Quaternary' and younger, slip rates ≥ 0.2 mm/yr) categorical weights: From left to right, columns represent for each category: a weight ID number, the range of native units represented, the area occupied in km², the number of training points, W_+ , standard deviation of W_+ , and studentized contrast. Statistics are presented for the binary binning threshold with maximum contrast, the binary binning threshold with maximum studentized contrast, and the ternary binning threshold.

3.3 Functions Fit by Area

All functions used to calculate gradational (smoothed) weights use cumulative area as the independent variable. Cumulative area is reported in the original cumulative weight table by the ArcSDM tool.

3.3.1 Heat Flow

Figure 2.18 plots cumulative area on the x-axis and shows a linear function (red points and line) fit through categorical $W+$ values plotted by their 'area midpoint' (green points). This function over-predicted the number of training sites by 0.7 systems. The equation calculated was:

$$\begin{aligned} Weight &= (-12604.2636246792 * Area) + 1.35529093731054; r^2 \\ &= 0.9957 \quad (3 - 1) \end{aligned}$$

The following modified function predicts the correct number of training sites:

$$W+ = (-12604.2636246792 * Area) + 1.3420 \quad (3 - 2)$$

In preceding equations, Area refers to cumulative area divided by 10^9

To use these functions in a different geographic region, heat flow would need to be used as the independent variable. To provide a way to use heat flow to predict weights, a function was fit between heat flow and cumulative area. These equations were generated using heat flow values that ranged approximately between 40 – 120 mW/m²; they are therefore only valid for converting heat flow values within that range. The following fifth

order polynomial function did well providing a conversion between native units and cumulative area:

$$\begin{aligned} \text{Area} &= (-0.000693899588288 * HF^5) + (0.294208771652126 * HF^4) \\ &\quad - (46.8680126599787 * HF^3) + (3,438.58527075588 * HF^2) \\ &\quad - (116991.862789404 * HF) + 1,777,327.48529318; r^2 \\ &= 0.9992 \quad (3 - 3) \end{aligned}$$

*In preceding equation, Area refers to actual cumulative area ;
HF refers to the minimum value of an interval of heat flow in mW/m²*

3.3.2 Strain Rate

Figure 2.20 plots cumulative area on the x-axis and shows a third-order polynomial function (red points and line) fit through categorical weight values plotted by their ‘area midpoint’ (green points). This function over-predicted the number of training sites by 0.1 systems. The equation calculated was:

$$\begin{aligned} \text{Weight} &= (-0.118435239069701 * \text{Area}^3) + (0.784909048939455 * \text{Area}^2) \\ &\quad - (2.113741868168450 * \text{Area}) + 1.374329871373890; r^2 \\ &= 0.9824 \quad (3 - 4) \end{aligned}$$

The following modified function predicts the correct number of training sites:

$$\begin{aligned} \text{Weight} &= (-0.118435239069701 * \text{Area}^3) + (0.784909048939455 * \text{Area}^2) \\ &\quad - (2.113741868168450 * \text{Area}) + 1.3725 \quad (3 - 5) \end{aligned}$$

In preceding equations, Area refers to cumulative area divided by 10⁵

To use these functions in a different geographic region, strain rate would need to be used as the independent variable. To provide a way to use strain rate to predict weights, a function was fit between strain rate and cumulative area. These equations were generated using strain rate values that ranged approximately between $0 - 212 \cdot 10^{-9}$ /yr; they are therefore only valid for converting strain rate values within that range. The following exponential function did well providing a conversion between native units and cumulative area:

$$Area = 136419.491338333 * e^{-0.043507263595984 * Strain}; r^2 = 0.9886 \quad (3 - 6)$$

*In preceding equation, Area refers to actual cumulative area ;
Strain refers to the minimum value of an interval of strain rate in
2nd invariant strain rate tensor (10 – 9/yr)*

3.3.3 Fault Subset 2.4 ('Latest Quaternary' and Younger of All Slip Rates)

Figure 2.23 plots cumulative area on the x-axis and shows a logarithmic function (red points and line) fit through ternary categorical weight values plotted by their 'area midpoint' (green points). This function overpredicted the number of training sites by 4.4 systems. The equation calculated was:

$$\begin{aligned} W+ &= (-0.659945933421018 * \ln (Area)) - 0.135379493730506; r^2 \\ &= 0.997 \quad (3 - 7) \end{aligned}$$

The following modified function predicts the correct number of training sites:

$$W+ = (-0.659945933421018 * \ln (Area)) - 0.212 \quad (3 - 8)$$

In preceding equations, Area refers to cumulative area divided by 10⁵

To use these functions in a different geographic region, distance to the fault would need to be used as the independent variable. To provide a way to use distance to the fault to predict weights, a function was fit between distance to the fault and cumulative area. These equations were generated using distance to the fault values that ranged approximately between 0 - 240 km; they are therefore only valid for converting distance to the fault values within that range. The following sixth order polynomial function seemed to do well providing a conversion between native units and cumulative area:

$$\begin{aligned} Area = & (0.000000790047029 * Dist^6) - (0.000326639118518 * Dist^5) \\ & + (0.051030997043967 * Dist^4) - (3.428770898797550 * Dist^3) \\ & + (38.555560768598000 * Dist^2) + (7012.46373696272 * Dist) \\ & + 1,033.52639986356; r^2 = 1.0 \quad (3 - 9) \end{aligned}$$

In preceding equation, Area refers to actual cumulative area ;

Dist refers to the distance from a fault in km

3.3.4 Fault Subset 5.3 ('Undifferentiated Quaternary' and Younger with Slip Rates Equal to or Greater Than 0.2 mm/yr)

Figure 2.24 plots cumulative area on the x-axis and shows a logarithmic function (red points and line) fit through ternary categorical weight values plotted by their 'area midpoint' (green points). This function overpredicted the number of training sites by 4.4 systems. The equation calculated was:

$$W+ = (-0.607483309885314 * \ln (Area)) + 6.931121975694720; r^2 = 0.9742 \quad (3 - 10)$$

The following modified function predicts the correct number of training sites:

$$W+ = (-0.607483309885314 * \ln (Area)) + 6.79 \quad (3 - 11)$$

In preceding equations, Area refers to actual cumulative area

To use these functions in a different geographic region, distance to the fault would need to be used as the independent variable. To provide a way to use distance to the fault to predict weights, a function was fit between distance to the fault and cumulative area. These equations were generated using distance to the fault values that ranged approximately between 0 - 240 km; they are therefore only valid for converting distance to the fault values within that range. The following fourth order polynomial function seemed to do well providing a conversion between native units and cumulative area:

$$Area = (-0.00007591509007 * Dist^4) + (0.055895867869941 * Dist^3) - (18.244881994546700 * Dist^2) + (3393.93506971629 * Dist) - 1342.97973891707; r^2 = 0.9999 \quad (3 - 12)$$

In preceding equation, Area refers to actual cumulative area ;

Dist refers to the distance from a fault in km

3.4 Review of Fitting Individual Layers by Area

The 'fit by area' approach appeared to work very well with heat flow (overprediction of 0.7 systems) and strain rate (overprediction of 0.1 systems) but not as well with faults

(overprediction of 4.4 systems with 2.4 subset, overprediction of 8.3 systems with 5.3 subset). For continuously varying phenomena such as heat flow and strain rate data, the ‘fit by area’ approach was able to generate gradational weight values that closely predicted the number of training sites, indicating that the technique can distribute weights in a way that does not overpredict within a layer.

The fit by area approach however did not work as well examining distance from fault layers, which unlike heat flow and strain rate is non-continuous. All attempts to fit distance from faults by area resulted in modest overpredictions in training site count (by approximately 8 to 15%). Only three categorical weights could be generated for a distance-based layer because only very local distance ranges correlated with geothermal systems. One weight could be generated from distances within 1 km. A second threshold was obtainable within the 2.5 – 4 km range. No additional positive weight categories could be produced, apparently because faults do not contribute to permeability beyond some critical distance, most likely less than 5 km. The third weight in any ternary binning would therefore represent a very large portion of the total area, over 90% of the total area for both the 2.4 and 5.3 subset. This likely causes any fit line to be sensitive to the third weight, magnifying the impact of its associated uncertainty.

3.5 Multilayer Analysis Conditional Independence Testing

Conditional dependencies between layers typically cause weights-of-evidence-derived posterior probability maps to overpredict the number of training sites (Bonham-Carter, 1994). Table 3.6 shows the number of training sites over-predicted by a series of posterior probability models (maps). Each of these maps are based on a unique combination of the above described evidence layers in either categorical weight format or smoothed weight format.

Fault Method	Strain & Heat: Multiclass Categorical	Heat: Multiclass Categorical (No Strain)	Strain: Multiclass Categorical (No Heat)	Strain & Heat: Smoothed By Area	Heat: Smoothed By Area (No Strain)	Strain: Smoothed By Area (No Heat)
2.4 Faults Binary 250m	1.6	1	3	1.4	1	3.3
2.4 Faults Binary 1 km	5.2	1.9	5.5	5.2		
2.4 Faults Ternary Categorical	9.1	2.7	8.2	9.3		
2.4 Smoothed By Area (Ternary)				12.5	3	11.2
5.3 Faults Binary 250m	5.2			4.7		
5.3 Faults Binary 1 km	7.6			7.4		
5.3 Faults Ternary Categorical	8.7			8		
5.3 Smoothed By Area (Ternary)				14.3		
No Faults	-2.7			-3		

Table 3.6: Conditional independence overprediction results table: The table reports the number of training sites each multilayer posterior probability model overpredicted by. Fifty-five training sites were used in the model. Rows represent different fault subsets or techniques, blue cells represent categorical models, and green cells represent smoothed models. Three-layer models using categorical continuous data are depicted with red text. Three-layer models using smoothed continuous data are depicted with purple text.

The rows in Table 3.6 represent different subsets of the normal faults layer. The first group (2.4) is the fault subset seen outlined in blue in Figure 2.2 on the lower left side and in the map Figure 1.3. They represent the two youngest groups of normal faults ('Historic' and 'Latest Quaternary') with no consideration of their slip rate. The second group of rows in Table 3.6 show the 5.3 subset, seen outlined in blue in Figure 2.2 on the upper right side and in the map Figure 1.4. They represent all normal faults of known Quaternary ages with slip rates equal to or greater than 0.2 mm/yr. The bottom row shows maps produced without faults.

The columns in Table 3.6 show whether strain rate or heat flow data were included in a map and whether the weights were derived categorically (blue) or smoothed (fit by area (green)). Weights derived by area (green) used functions that were manually adjusted to predict the exact number of training sites to avoid overpredictions from propagating through a multilayer model. The columns with darker shading use both heat flow and strain rate, the columns with lighter shading use only one layer.

A basic check for whether overpredictions are significant is a simple ratio of actual divided by predicted number of training sites (Bonham-Carter, 1994). Table 3.7 shows the conditional independence ratio for each model. The conditional independence ratio is a simple guide to assess conditional independence. The test used to calculate these values, the ArcSDM ACCI test states:

Fault Method	Strain & Heat: Multiclass Categorical	Heat: Multiclass Categorical (No Strain)	Strain: Multiclass Categorical (No Heat)	Strain & Heat: Smoothed By Area	Heat: Smoothed By Area (No Strain)	Strain: Smoothed By Area (No Heat)
2.4 Faults Binary 250m	0.972	0.982	0.948	0.975	0.982	0.943
2.4 Faults Binary 1 km	0.914	0.967	0.909	0.914		
2.4 Faults Ternary Categorical	0.858	0.953	0.870	0.855		
2.4 Smoothed By Area (Ternary)				0.815	0.948	0.831
5.3 Faults Binary 250m	0.914			0.921		
5.3 Faults Binary 1 km	0.879			0.881		
5.3 Faults Ternary Categorical	0.863			0.873		
5.3 Smoothed By Area (Ternary)				0.794		
No Faults	1.052			1.058		

Table 3.7: Conditional independence ratio table: The table reports the number of training sites each multilayer posterior probability model predicted divided by the actual number of training sites. Fifty-five training sites were used in the model. Rows represent different fault subsets or techniques, blue cells represent categorical models, and green cells represent smoothed models. Three-layer models using categorical continuous data are depicted with red text. Three-layer models using smoothed continuous data are depicted with purple text.

'Values below 1.00 may indicate conditional dependence among two or more of your data sets. Bonham-Carter, 1994 suggest that values < 0.85 may indicate a problem.'

Nearly all the tests in Table 3.7 have ratios greater than 0.85. The only tests that do not meet that standard use a faults layer that was fit by area. For this reason, it was decided that the fit by area approach did not as work well with the fault layers but could still be useful for demonstrating relative favorability.

The ACCI tool also runs the 'Agterberg & Cheng Conditional Independence Test.' This uses a 1-tailed test to calculate the probability that the inaccuracy in prediction of number of training sites is not due to chance alone. Table 3.8 shows those values for some models. Any ACCI test result below 95% is considered acceptable. The test never returns a result below 50%. Most of the calculated values are in the 60 – 85 % range and are considered good.

Fault Method	Strain & Heat: Multiclass Categorical	Heat: Multiclass Categorical (No Strain)	Strain: Multiclass Categorical (No Heat)	Strain & Heat: Smoothed By Area	Heat: Smoothed By Area (No Strain)	Strain: Smoothed By Area (No Heat)
2.4 Faults Binary 250m	62.6%	63.9%	64.9%	60.9%		
2.4 Faults Binary 1 km	85.3%	59.4%	76.4%	85.0%		
2.4 Faults Ternary Categorical	97.7%	64.8%	88.1%	97.9%		
2.4 Smoothed By Area (Ternary)						
5.3 Faults Binary 250m	81.5%			72.3%		
5.3 Faults Binary 1 km	90.6%			83.2%		
5.3 Faults Ternary Categorical	94.3%			87.5%		
5.3 Smoothed By Area (Ternary)						
No Faults	30.5%			0.0%		

Table 3.8: Agterberg-Cheng Conditional Independence Test results table: The table reports the ACCI, which uses a 1-tailed test to calculate the probability that the inaccuracy in prediction of number of training sites is not due to chance alone for each multilayer model. Rows represent different fault subsets or techniques, blue cells represent categorical models, and green cells represent smoothed models. Three-layer models using categorical continuous data are depicted with red text. Three-layer models using smoothed continuous data are depicted with purple text.

3.5.1 Conditional Independence Using Different Fault Layers

A basic trend was observed in Table 3.6 and in all the other conditional independence tables. Models using faults consistently overpredicted the least when using the smallest distance threshold, 250 m. The 1 km model overpredicted more than the 250 m model. The ternary model always predicted more than the 1 km model. The fit by area always predicted more than the ternary. This appears to be because the smaller areas covered in the models with the smaller thresholds caused less conditional dependence with other layers (strain rate mainly) despite having higher weight values.

3.5.2 Conditional Independence Between Layer Pairs

Conditional dependencies between strain rate and faults are the cause for most of the overpredictions. In Table 3.6, as larger thresholds are used with faults, models only using strain rate overpredicted more than models that only used heat flow. For example, a model overpredicted by 9.1 systems that used ternary 2.4 faults with categorical strain rate and heat flow. Removing heat flow and only using faults and strain led to overpredictions of 8.2, whereas removing strain rate and only using faults and heat flow the model overpredicted by 2.7 systems.

The bottom row of Table 3.6 shows models generated without faults, using only strain rate and heat flow. These models slightly underpredicted the number of training sites. Table 3.6 shows that heat flow and faults have low conditional dependencies. In models without strain, overpredictions are low between heat flow and all categorical fault layers.

3.5.3 Conditional Independence Between Categorical & Smooth Models

The models that use strain rate and heat flow fit by area predict almost exactly the same number of systems predicted in categorical tests. This can be seen in Table 3.6; as the row changes (different fault technique), the red numbers (categorical heat flow and strain rate) and purple numbers (smoothed heat flow and strain rate) are nearly identical. The layers that were individually fit by area perform nearly identically to categorical weights in multilayer analyses. This indicates that evidence layers created using the fit by area approach can be used in place of categorical layers without significantly altering overall conditional independence within a model.

3.6 Maps

A map was produced for each probability model that utilized faults for both categorical and smoothed depictions of heat flow and strain rate (Figure 3.1 to Figure 3.14). Maps display the posterior probability divided by the prior probability and show the number of times more or less likely of finding a geothermal system based on chance alone. Warmer colors indicate ‘more likely’ relative to the cooler colors that represent ‘less likely.’

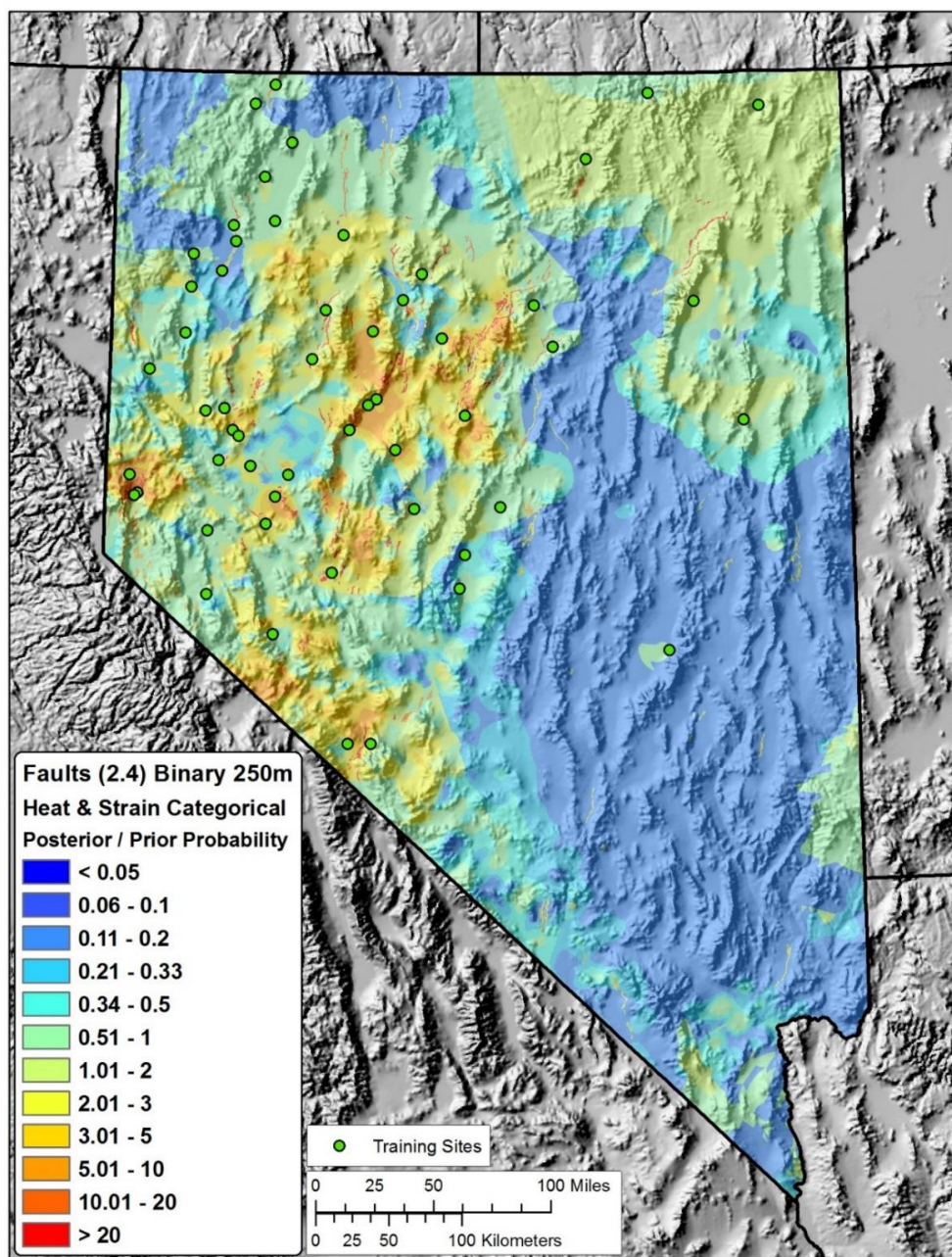


Figure 3.1: Geothermal favorability map using categorical weights for heat flow, strain rate, and a binary 250-meter buffer on the 2.4 fault subset (Age equal to or younger than 'Latest Quaternary', all slip rates). The map surface shows the posterior probability divided by the prior probability and can thus be interpreted as 'the number of times more likely one would encounter a geothermal system than due to chance alone.' Warmer colors depict higher likelihoods, cooler colors depict lower likelihoods. Layers used in this map include: categorical weights for heat flow, strain rate, and a binary 250-meter buffer on the 2.4 fault subset (Age equal to or younger than 'Latest Quaternary', all slip rates). Identified moderate and high temperature geothermal systems used as training sites are depicted as green circles.

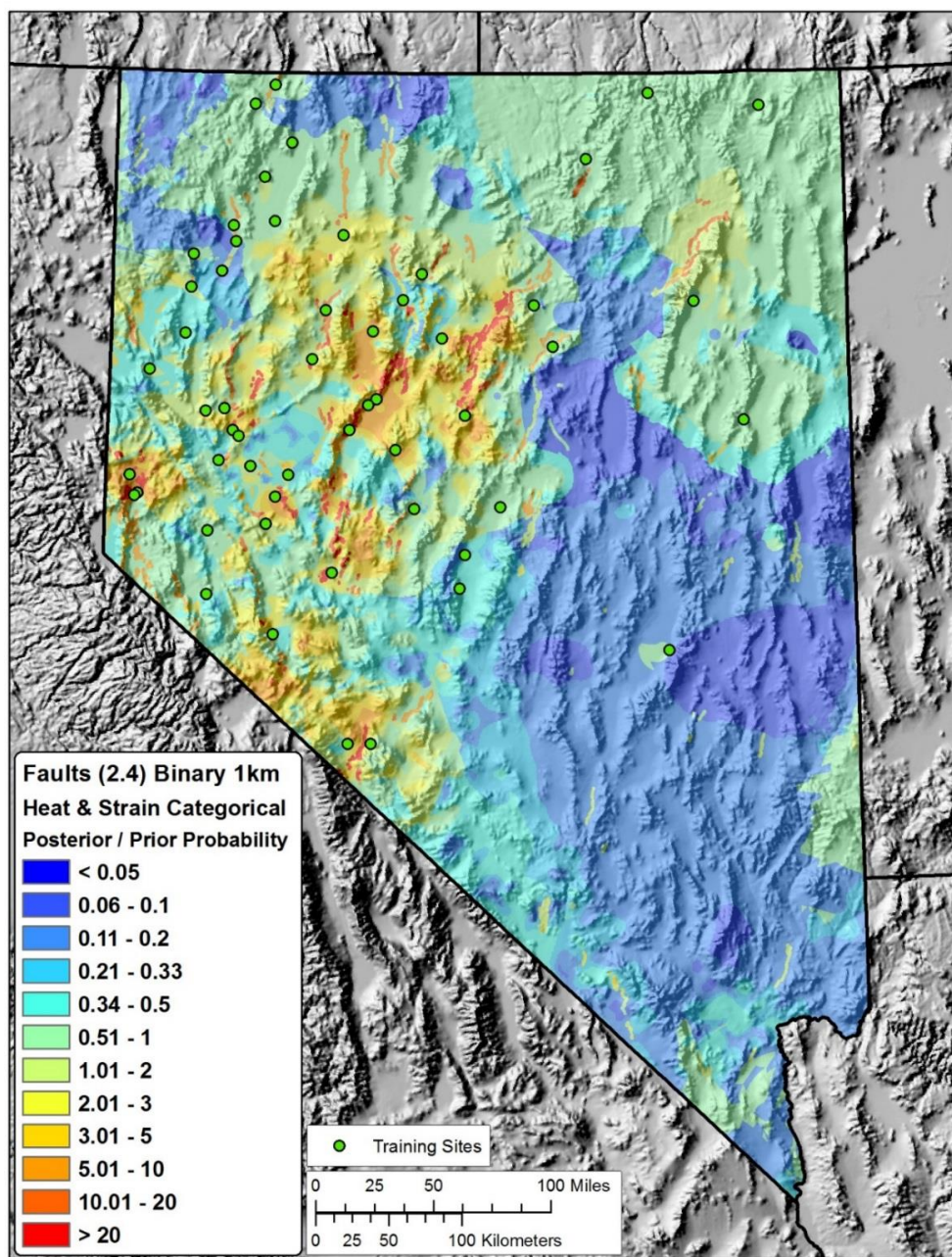


Figure 3.2: Geothermal favorability map using categorical weights for heat flow, strain rate, and a binary 1-km buffer on the 2.4 fault subset (Age equal to or younger than 'Latest Quaternary', all slip rates). The map surface shows the posterior probability divided by the prior probability and can thus be interpreted as 'the number of times more likely one would encounter a geothermal system than due to chance alone.' Warmer colors depict higher likelihoods, cooler colors depict lower likelihoods. Layers used in this map include: categorical weights for heat flow, strain rate, and a binary 1-km buffer on the 2.4 fault subset (Age equal to or younger than 'Latest Quaternary', all slip rates). Identified moderate and high temperature geothermal systems used as training sites are depicted as green circles.

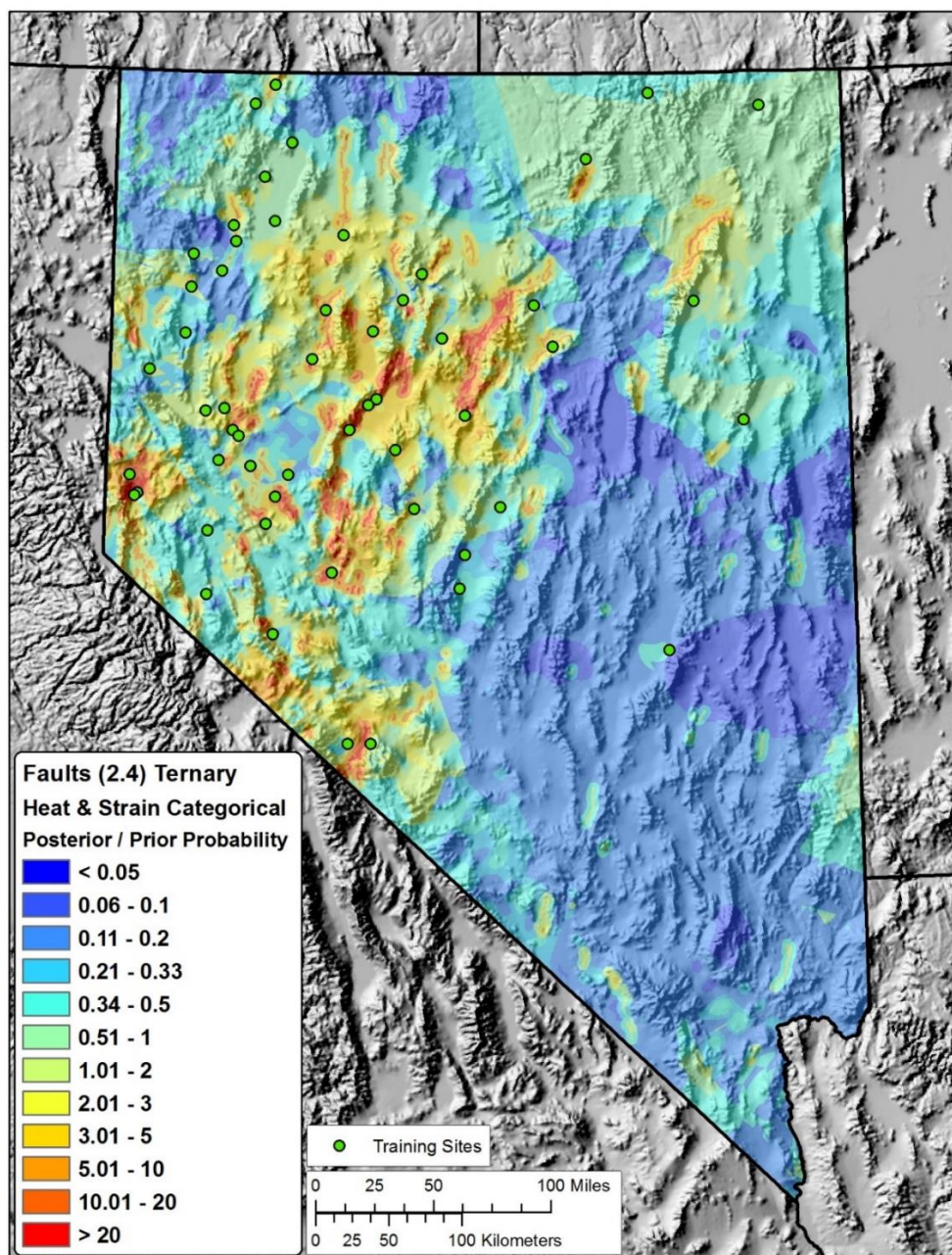


Figure 3.3: Geothermal favorability map using categorical weights for heat flow, strain rate, and ternary buffers on the 2.4 fault subset (Age equal to or younger than 'Latest Quaternary', all slip rates). The map surface shows the posterior probability divided by the prior probability and can thus be interpreted as 'the number of times more likely one would encounter a geothermal system than due to chance alone.' Warmer colors depict higher likelihoods, cooler colors depict lower likelihoods. Layers used in this map include: categorical weights for heat flow, strain rate, and ternary buffers on the 2.4 fault subset (Age equal to or younger than 'Latest Quaternary', all slip rates). Identified moderate and high temperature geothermal systems used as training sites are depicted as green circles.

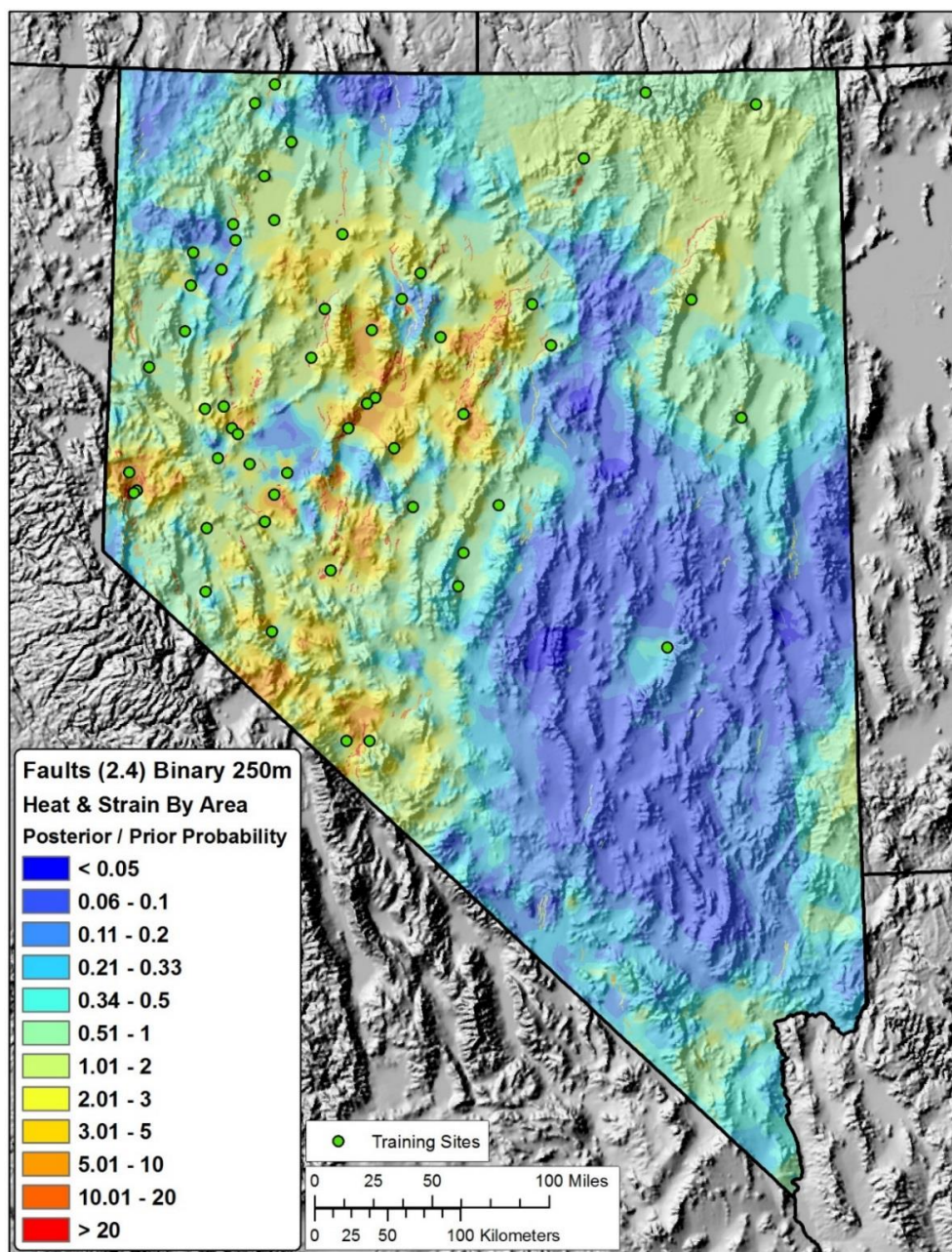


Figure 3.4: Geothermal favorability map using weights fit ‘by area’ for heat flow, strain rate, and a binary 250-meter buffer on the 2.4 fault subset (Age equal to or younger than ‘Latest Quaternary’, all slip rates). The map surface shows the posterior probability divided by the prior probability and can thus be interpreted as ‘the number of times more likely one would encounter a geothermal system than due to chance alone.’ Warmer colors depict higher likelihoods, cooler colors depict lower likelihoods. Layers used in this map include: weights fit ‘by area’ for heat flow, strain rate, and a binary 250-meter buffer on the 2.4 fault subset (Age equal to or younger than ‘Latest Quaternary’, all slip rates). Identified moderate and high temperature geothermal systems used as training sites are depicted as green circles.

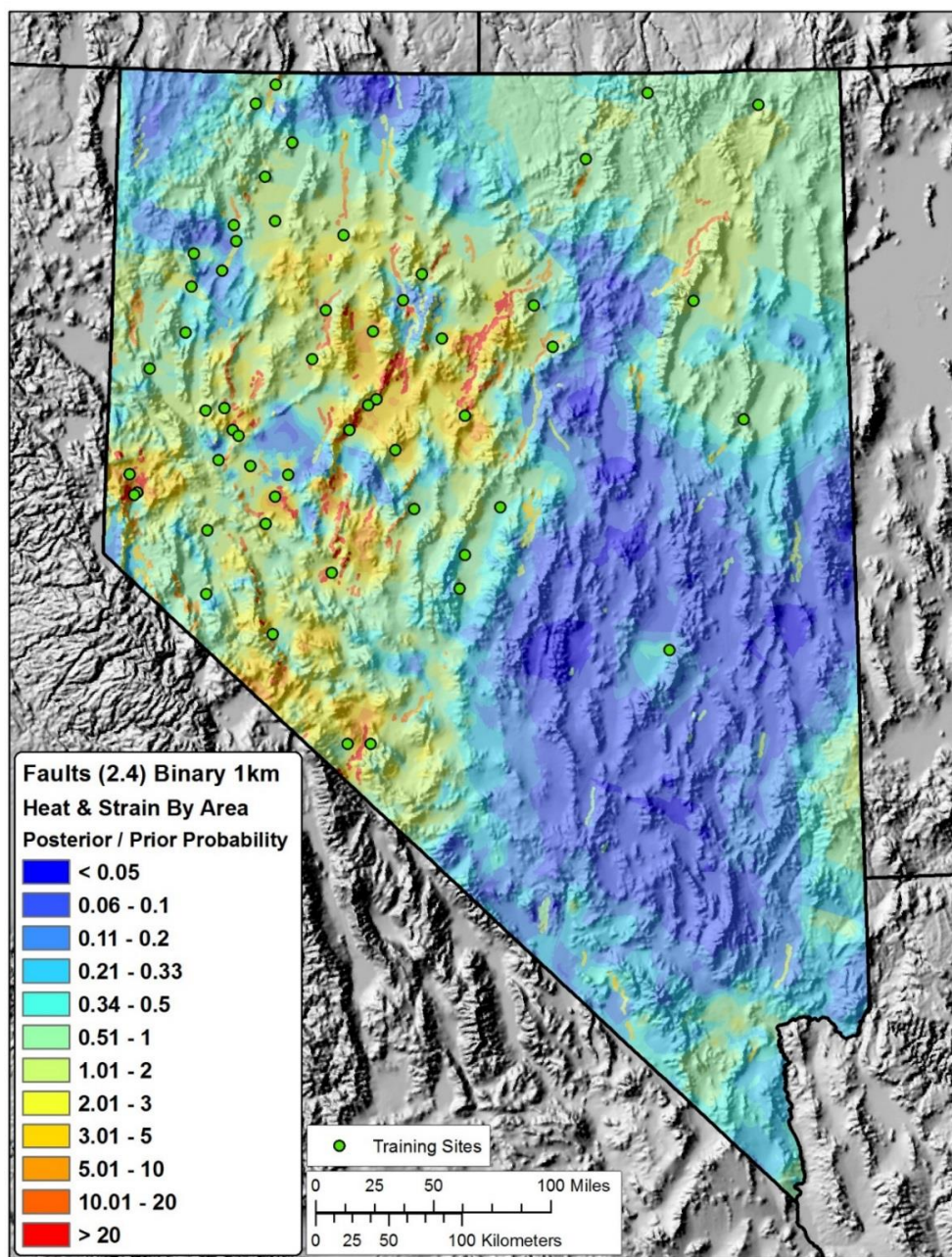


Figure 3.5: Geothermal favorability map using weights fit ‘by area’ for heat flow, strain rate, and a binary 1-km buffer on the 2.4 fault subset (Age equal to or younger than ‘Latest Quaternary’, all slip rates). The map surface shows the posterior probability divided by the prior probability and can thus be interpreted as ‘the number of times more likely one would encounter a geothermal system than due to chance alone.’ Warmer colors depict higher likelihoods, cooler colors depict lower likelihoods. Layers used in this map include: weights fit ‘by area’ for heat flow, strain rate, and a binary 1km buffer on the 2.4 fault subset (Age equal to or younger than ‘Latest Quaternary’, all slip rates). Identified moderate and high temperature geothermal systems used as training sites are depicted as green circles.

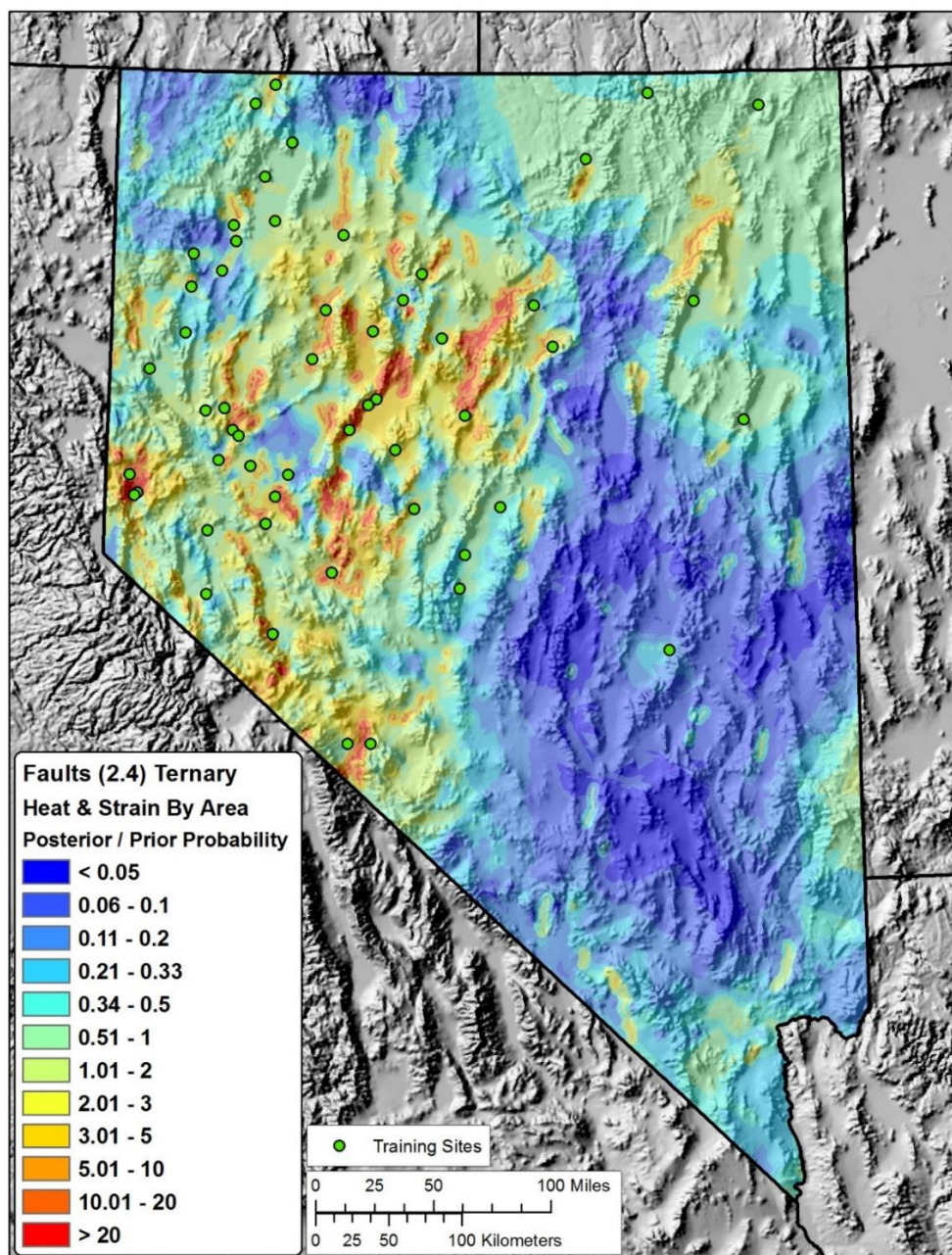


Figure 3.6: Geothermal favorability map using weights fit ‘by area’ for heat flow, strain rate, and ternary buffers on the 2.4 fault subset (Age equal to or younger than ‘Latest Quaternary’, all slip rates). The map surface shows the posterior probability divided by the prior probability and can thus be interpreted as ‘the number of times more likely one would encounter a geothermal system than due to chance alone.’ Warmer colors depict higher likelihoods, cooler colors depict lower likelihoods. Layers used in this map include: weights fit ‘by area’ for heat flow, strain rate, and ternary buffers on the 2.4 fault subset (Age equal to or younger than ‘Latest Quaternary’, all slip rates). Identified moderate and high temperature geothermal systems used as training sites are depicted as green circles.

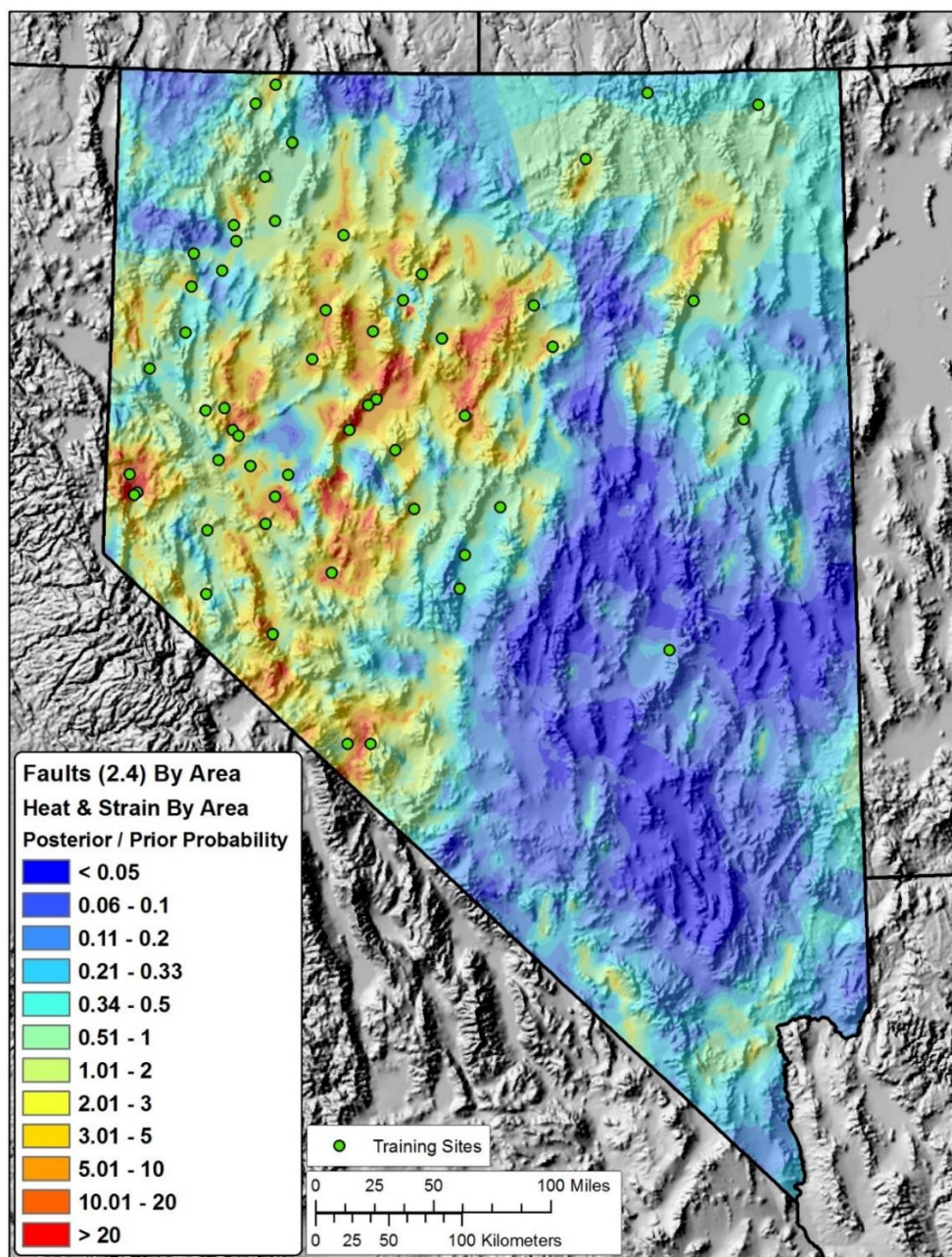


Figure 3.7: Geothermal favorability map using weights fit 'by area' for heat flow, strain rate, the 2.4 fault subset (Age equal to or younger than 'Latest Quaternary', all slip rates). The map surface shows the posterior probability divided by the prior probability and can thus be interpreted as 'the number of times more likely one would encounter a geothermal system than due to chance alone.' Warmer colors depict higher likelihoods, cooler colors depict lower likelihoods. Layers used in this map include: weights fit 'by area' for heat flow, strain rate, and the 2.4 fault subset (Age equal to or younger than 'Latest Quaternary', all slip rates). Identified moderate and high temperature geothermal systems used as training sites are depicted as green circles.

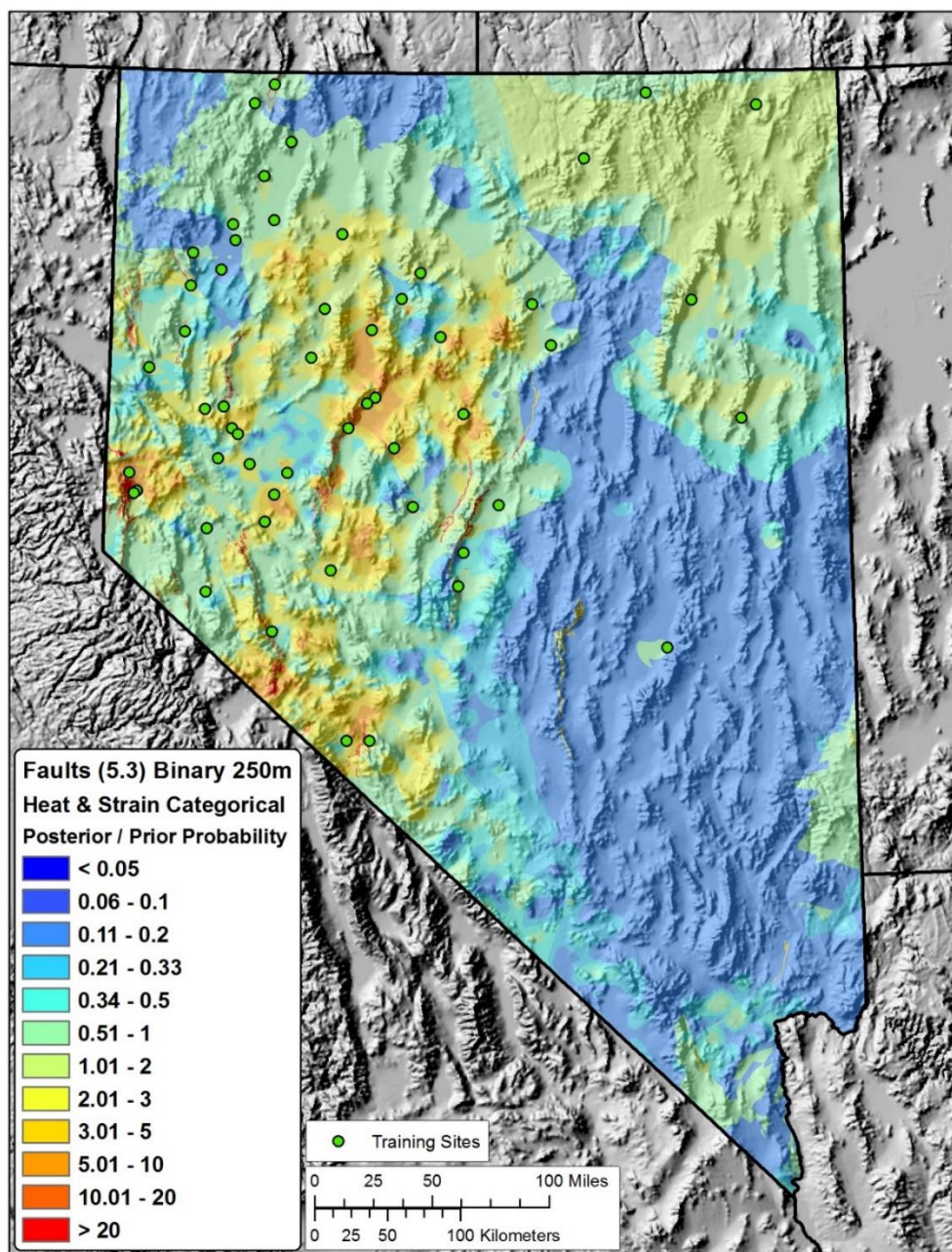


Figure 3.8: Geothermal favorability map using categorical weights for heat flow, strain rate, and a binary 250-meter buffer on the 5.3 fault subset (Age equal to or younger than ‘undifferentiated Quaternary’ and slip rate equal to or younger than 1.0 mm/yr). The map surface shows the posterior probability divided by the prior probability and can thus be interpreted as ‘the number of times more likely one would encounter a geothermal system than due to chance alone.’ Warmer colors depict higher likelihoods, cooler colors depict lower likelihoods. Layers used in this map include: categorical weights for heat flow, strain rate, and a binary 250-meter buffer on the 5.3 fault subset (Age equal to or younger than ‘undifferentiated Quaternary’ and slip rate equal to or younger than 1.0 mm/yr). Identified moderate and high temperature geothermal systems used as training sites are depicted as green circles.

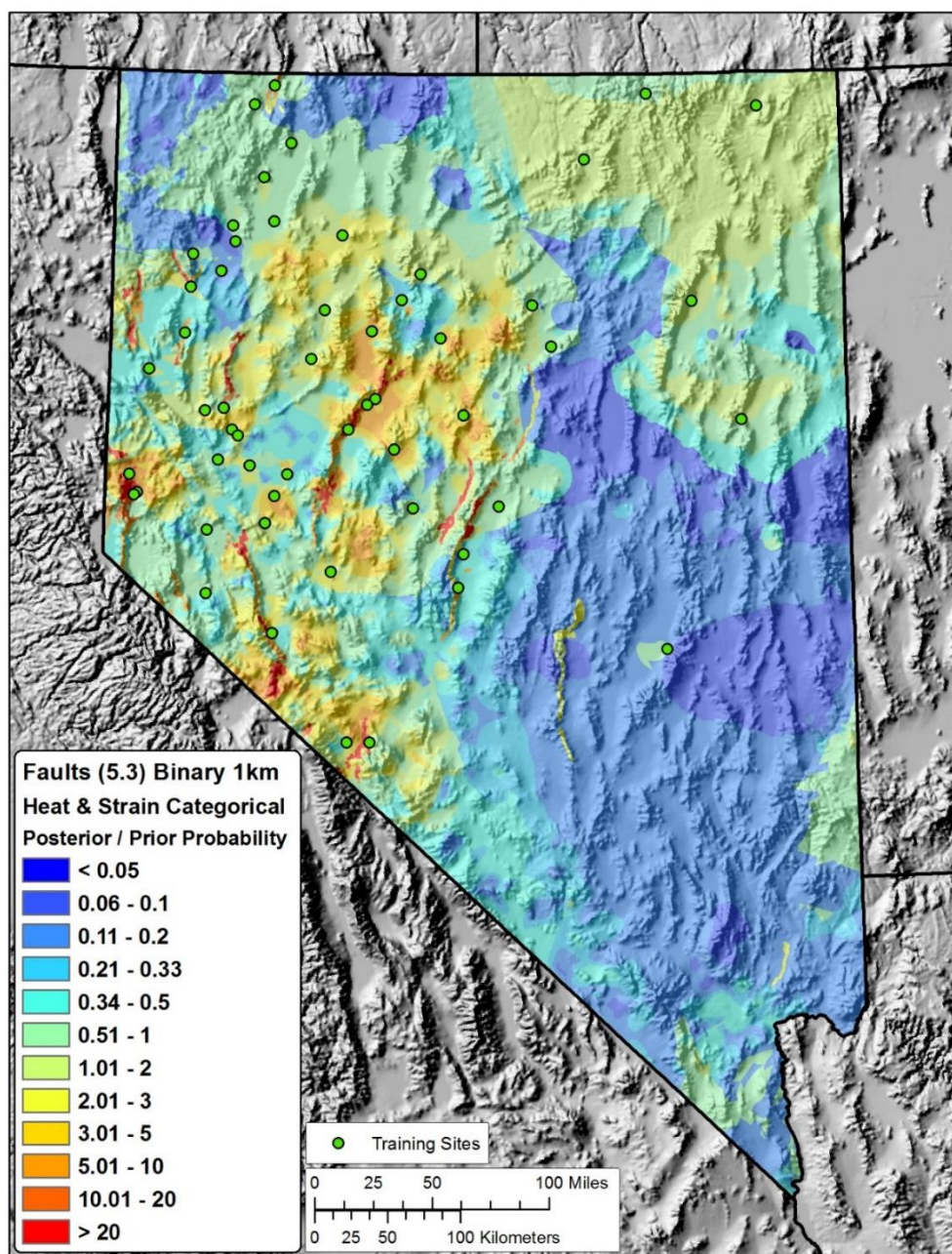


Figure 3.9: Geothermal favorability map using categorical weights for heat flow, strain rate, and a binary 1-km buffer on the 5.3 fault subset (Age equal to or younger than ‘undifferentiated Quaternary’ and slip rate equal to or younger than 1.0 mm/yr). The map surface shows the posterior probability divided by the prior probability and can thus be interpreted as ‘the number of times more likely one would encounter a geothermal system than due to chance alone.’ Warmer colors depict higher likelihoods, cooler colors depict lower likelihoods. Layers used in this map include: categorical weights for heat flow, strain rate, and a binary 1-km buffer on the 5.3 fault subset (Age equal to or younger than ‘undifferentiated Quaternary’ and slip rate equal to or younger than 1.0 mm/yr). Identified moderate and high temperature geothermal systems used as training sites are depicted as green circles.

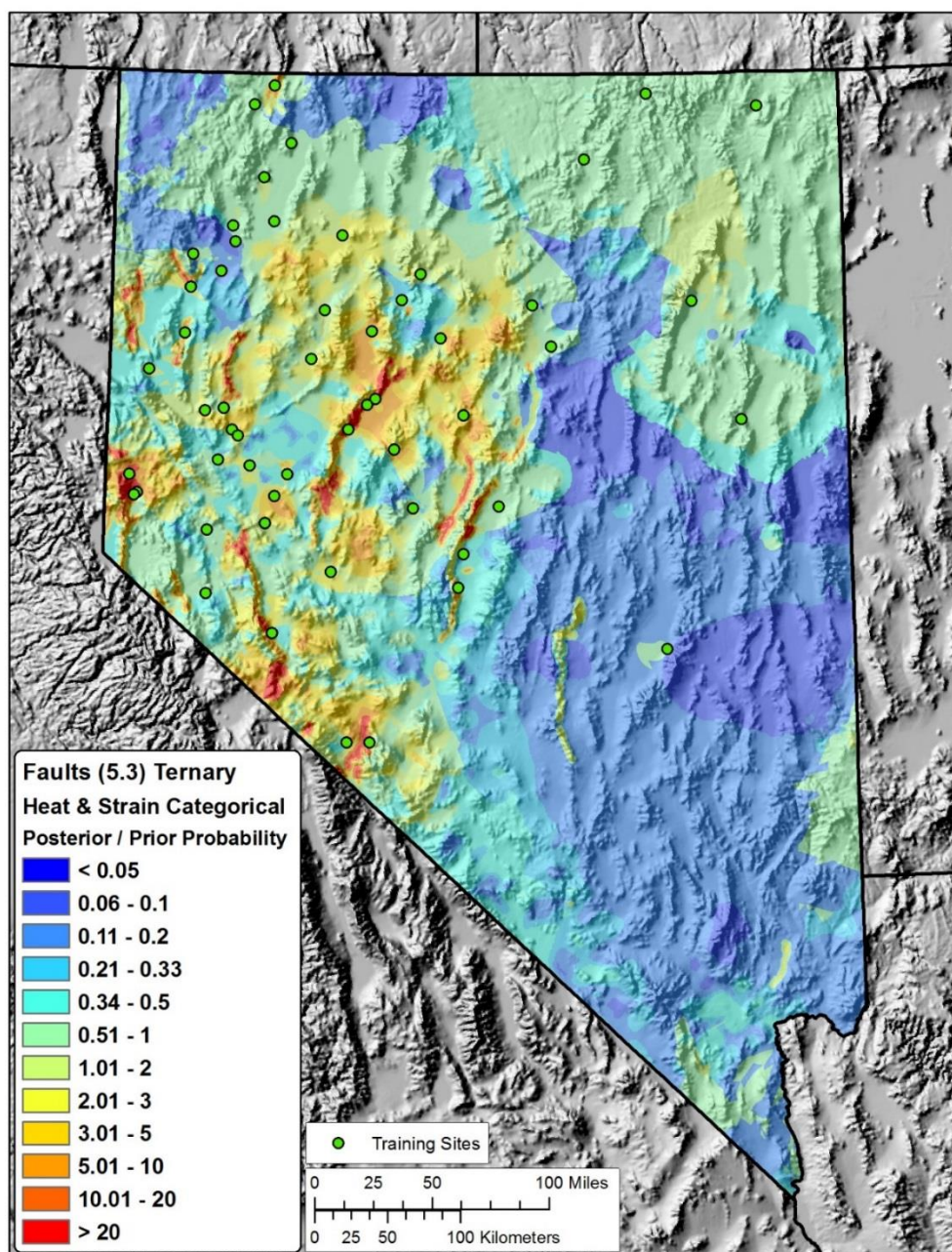


Figure 3.10: Geothermal favorability map using categorical weights for heat flow, strain rate, and ternary buffers on the 5.3 fault subset (Age equal to or younger than 'undifferentiated Quaternary' and slip rate equal to or younger than 1.0 mm/yr). The map surface shows the posterior probability divided by the prior probability and can thus be interpreted as 'the number of times more likely one would encounter a geothermal system than due to chance alone.' Warmer colors depict higher likelihoods, cooler colors depict lower likelihoods. Layers used in this map include: categorical weights for heat flow, strain rate, and ternary buffers on the 5.3 fault subset (Age equal to or younger than 'undifferentiated Quaternary' and slip rate equal to or younger than 1.0 mm/yr). Identified moderate and high temperature geothermal systems used as training sites are depicted as green circles.

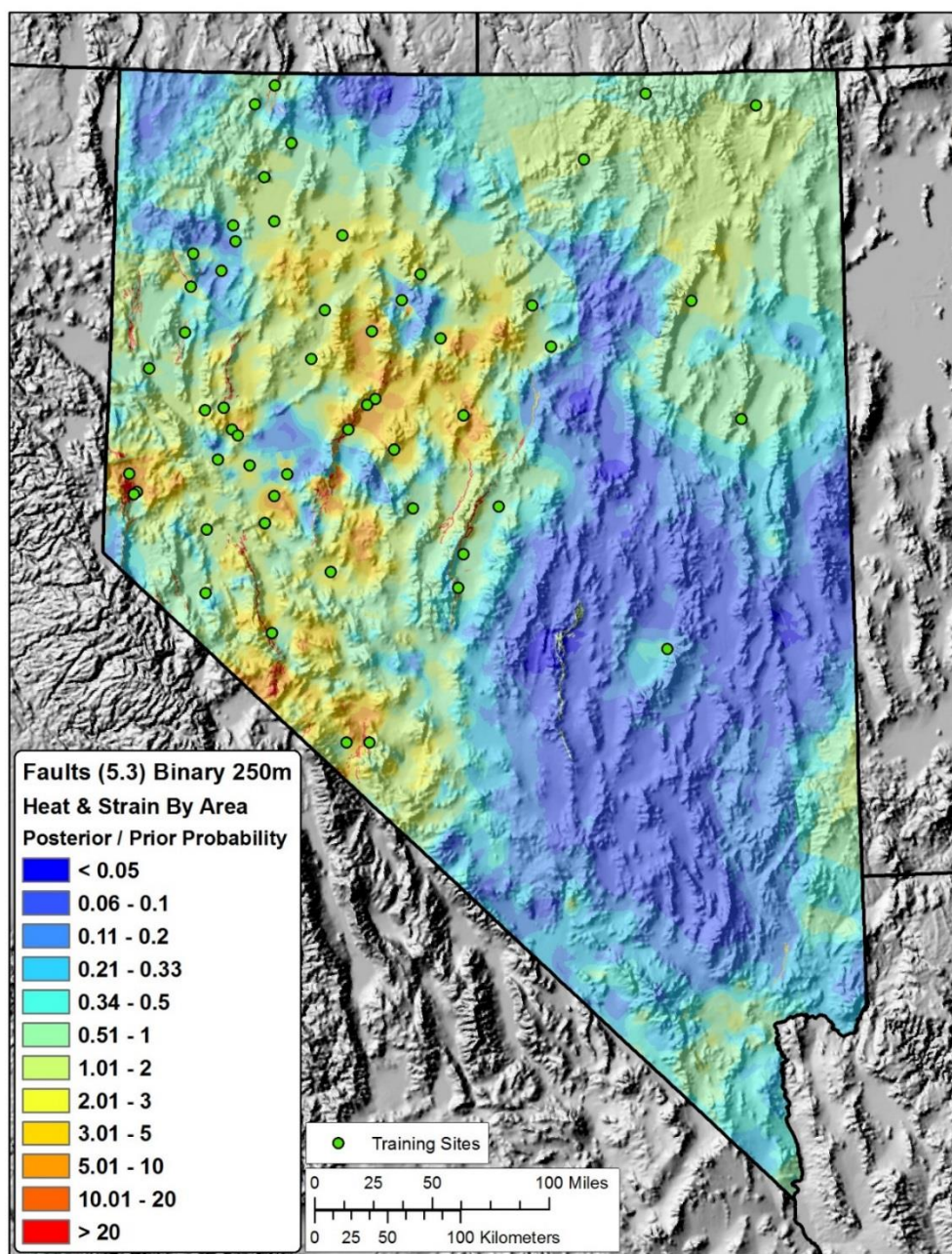


Figure 3.11: Geothermal favorability map using weights fit 'by area' for heat flow, strain rate, and a binary 250-meter buffer on the 5.3 fault subset (Age equal to or younger than 'undifferentiated Quaternary' and slip rate equal to or younger than 1.0 mm/yr). The map surface shows the posterior probability divided by the prior probability and can thus be interpreted as 'the number of times more likely one would encounter a geothermal system than due to chance alone.' Warmer colors depict higher likelihoods, cooler colors depict lower likelihoods. Layers used in this map include: weights fit 'by area' for heat flow, strain rate, and a binary 250-meter buffer on the 5.3 fault subset (Age equal to or younger than 'undifferentiated Quaternary' and slip rate equal to or younger than 1.0 mm/yr). Identified moderate and high temperature geothermal systems used as training sites are depicted as green circles.

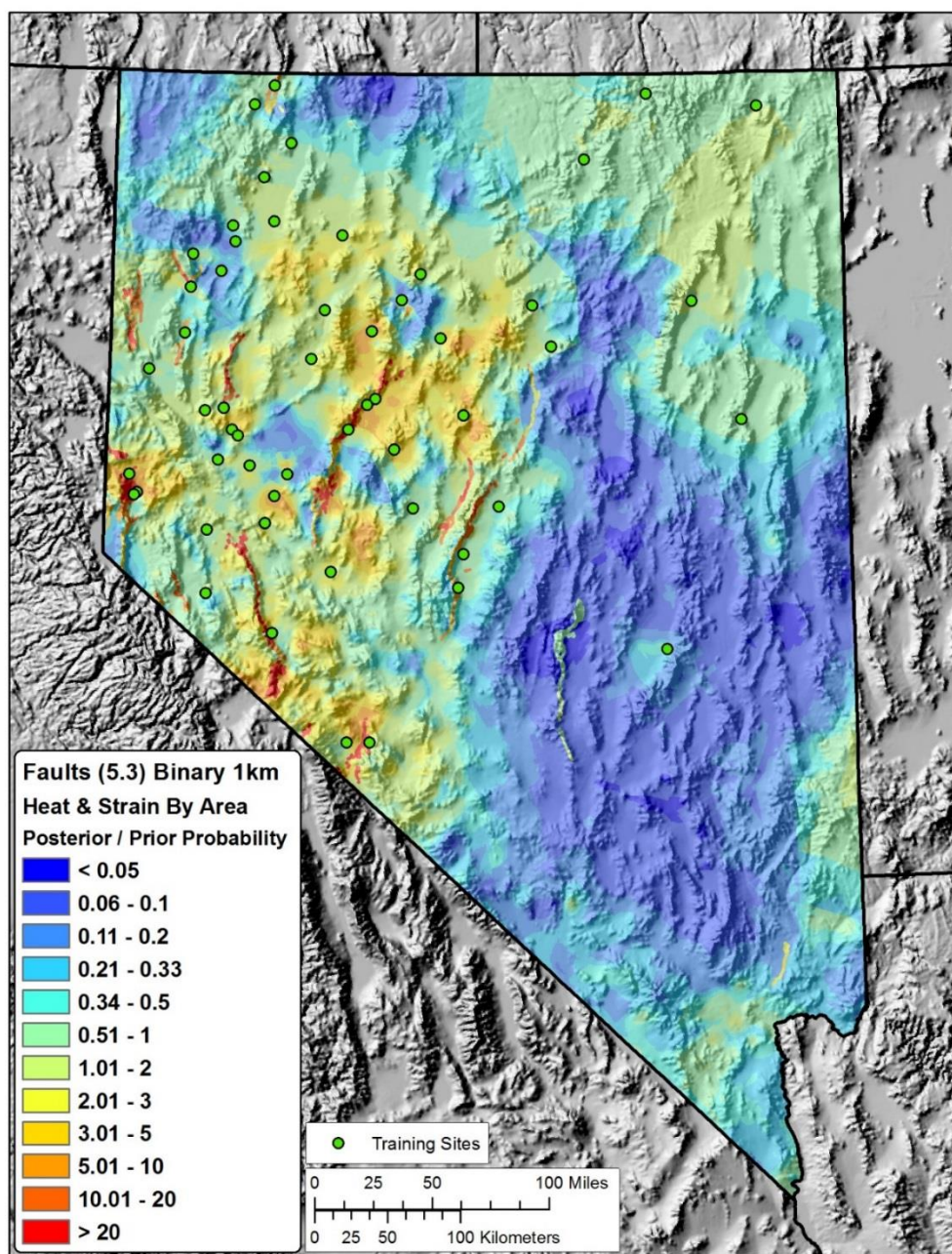


Figure 3.12: Geothermal favorability map using weights fit ‘by area’ for heat flow, strain rate, and a binary 1-km buffer on the 5.3 fault subset (Age equal to or younger than ‘undifferentiated Quaternary’ and slip rate equal to or younger than 1.0 mm/yr). The map surface shows the posterior probability divided by the prior probability and can thus be interpreted as ‘the number of times more likely one would encounter a geothermal system than due to chance alone.’ Warmer colors depict higher likelihoods, cooler colors depict lower likelihoods. Layers used in this map include: weights fit ‘by area’ for heat flow, strain rate, and a binary 1 km buffer on the 5.3 fault subset (Age equal to or younger than ‘undifferentiated Quaternary’ and slip rate equal to or younger than 1.0 mm/yr). Identified moderate and high temperature geothermal systems used as training sites are depicted as green circles.

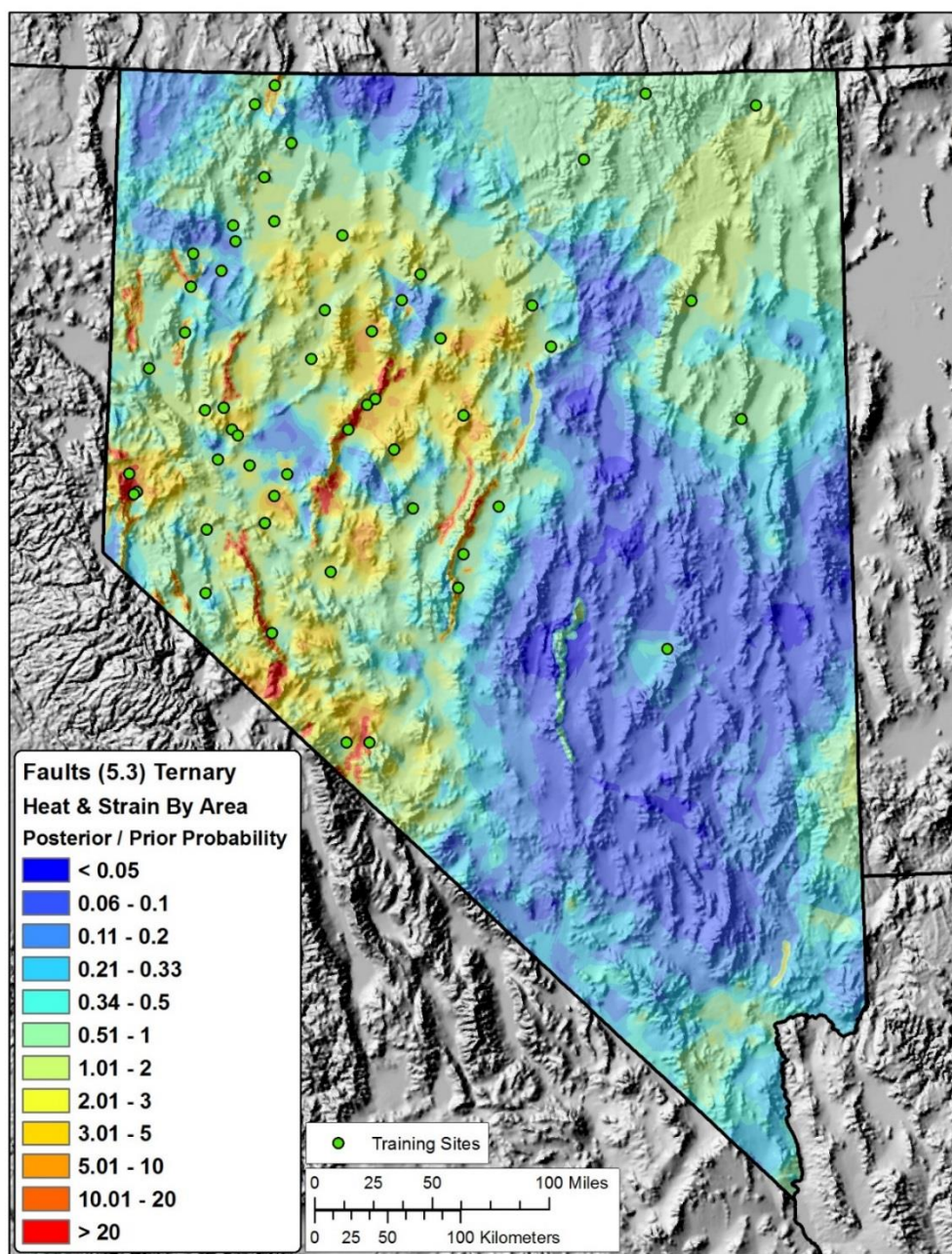


Figure 3.13: Geothermal favorability map using weights fit 'by area' for heat flow, strain rate, and ternary buffers on the 5.3 fault subset (Age equal to or younger than 'undifferentiated Quaternary' and slip rate equal to or younger than 1.0 mm/yr). The map surface shows the posterior probability divided by the prior probability and can thus be interpreted as 'the number of times more likely one would encounter a geothermal system than due to chance alone.' Warmer colors depict higher likelihoods, cooler colors depict lower likelihoods. Layers used in this map include: weights fit 'by area' for heat flow, strain rate, and ternary buffers on the 5.3 fault subset (Age equal to or younger than 'undifferentiated Quaternary' and slip rate equal to or younger than 1.0 mm/yr). Identified moderate and high temperature geothermal systems used as training sites are depicted as green circles.

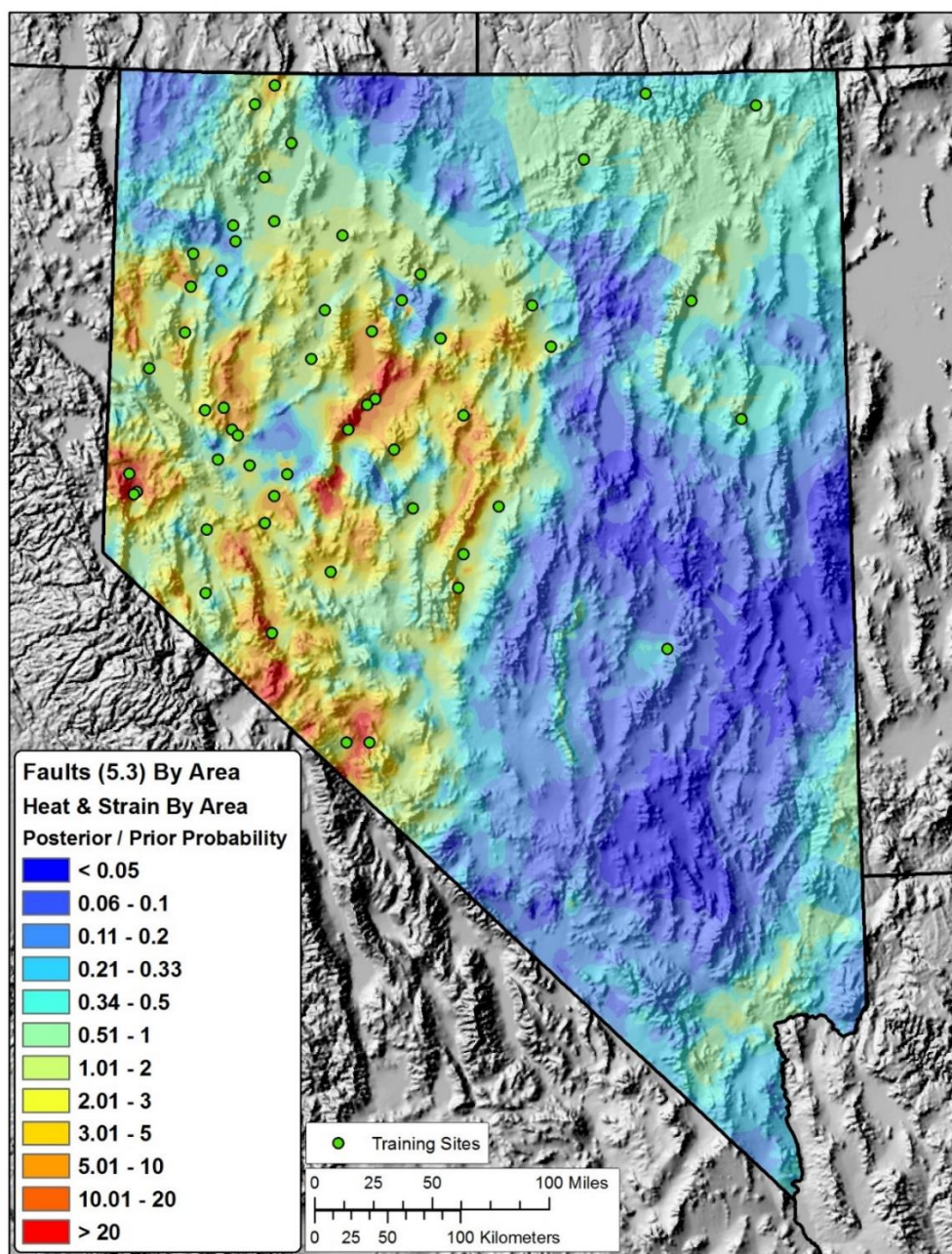


Figure 3.14: Geothermal favorability map using weights fit ‘by area’ for heat flow, strain rate, the 5.3 fault subset (Age equal to or younger than ‘undifferentiated Quaternary’ and slip rate equal to or younger than 1.0 mm/yr). The map surface shows the posterior probability divided by the prior probability and can thus be interpreted as ‘the number of times more likely one would encounter a geothermal system than due to chance alone.’ Warmer colors depict higher likelihoods, cooler colors depict lower likelihoods. Layers used in this map include: weights fit ‘by area’ for heat flow, strain rate, and the 5.3 fault subset (Age equal to or younger than ‘undifferentiated Quaternary’ and slip rate equal to or younger than 1.0 mm/yr). Identified moderate and high temperature geothermal systems used as training sites are depicted as green circles.

4.0 Discussion

The present study sought to estimate geothermal potential in Nevada by applying geographic and mathematical techniques informed by prior geothermal assessments. Geologic processes that drive hydrothermal systems were modeled by systematically transforming raw geologic data into layers that best represent their contributions to geothermal activity. Potentially relevant data were examined, sometimes using multiple processing techniques. Evidence data and processing approaches with the most useful correlations were used to create maps depicting favorability. Automated programming techniques were developed and applied to assist in isolating data subsets, execute geoprocessing tools and weight tests, and to compare weight test results. Techniques were developed and applied to fit smooth functions to weights derived via WofE.

The Discussion section begins by comparing the approaches used in the present study with approaches used in prior studies for context. Next, the best performing geothermal favorability maps from the present study are presented and examined to understand locations of and driving forces behind high favorability areas. Then, results from the present study are overlain on results from prior studies for direct comparison. Finally, summaries of additional findings are presented along with future work topics generated over the course of the present study.

4.1 Comparing Approach with Prior Works

The different reviewed studies used different evidence data, different techniques to measure correlations, and different geographic processing tools to arrive at favorability estimates. Table 4.1 summarizes evidence layers used in each study. Each study uses one layer to characterize heat (shaded red), except Williams and DeAngelo (2008), which also uses Quaternary magmatism. Each study had multiple layers related to permeability.

One of those layers always included something related to Quaternary faults (shaded purple). All studies incorporated seismicity (shaded green) except the current thesis. All studies used a map depicting something related to deformation, or strain (shaded tan) except Williams and DeAngelo (2008), though a layer estimating the stress regime was used in models not reviewed in the present study. Faulds et al. (2015) used many additional layers to characterize permeability. Notwithstanding these differences, all these studies use very similar types of data.

Layer	Coolbaugh et al., 2005	Williams and DeAngelo, 2008	Faulds et al., 2015	This Study
Heat	Thermal Gradient	Heat Flow	Temp at 3 km	Heat Flow
Faults	Gravity/Topography	Fault Distance	Faults (Many)	Fault Distance
Seismicity	Earthquakes	Earthquakes	Earthquakes	
Strain	Crustal Dilation & Slip Rate		Strain Rate	Strain Rate
Other		Magmatism	Many Permeability Layers	

Table 4.1: Prior works evidence layer table: This table shows evidence layers used in the reviewed studies. Columns depict the different studies. Rows depict types of evidence layers. Colors denote the type of evidence layer with red representing heat, purple representing Quaternary faults, green representing seismicity, and tan representing strain or deformation. Each cell denotes the actual type of data used.

Notable differences between the present study and prior studies include weight smoothing, the use of a fine study grid to verify and exploit local scale weight variations, the use of a newer strain rate map, the use of additional exploratory geographic processing techniques, a refined characterization of heat, the use of newly available QFFDB attribute information, and good conditional independence results.

4.1.1 Coolbaugh et al., 2005

Though Coolbaugh et al. (2005) used a logistic regression tool instead of WofE to generate weights, similar techniques were used to interpret and classify ranges of data into categories as were employed in the present study, and a similar looking map was produced (Figure 1.10). Categories needed to contain enough training sites to generate significant weights, just as in a WofE analysis. This resulted in evidence layers that were broken into multiple independently weighted categories. The present study used similar data to that used in Coolbaugh et al. (2005), but there are notable differences.

The ‘combined gravity and topographic gradient’ map in Coolbaugh et al. (2005) represented effective vertical displacement along faults. The present study’s use of Quaternary faults addresses the same geologic process.

The fault dilation map used in Coolbaugh et al. (2005) is a precursor to the strain rate map used in the present study, Coolbaugh et al. (2005) foresee the development of newer maps saying, ‘*Significant improvements are expected in the future as GPS station network expands and measurement accuracies improve.*’ This layer also included fault slip rates as an important component.

The seismicity map used in Coolbaugh et al. (2005) employed the general technique adopted in the present study for characterizing the possible geothermal contribution from

seismicity and broke the evidence layer into two categories. The present study experimented with different search radii and used seismic moment instead of earthquake magnitudes, as in Williams and DeAngelo (2008) but ultimately found correlations with seismic data to be weaker than with other evidence data, leading to the decision to not use seismicity in the present study.

The present study used similar data and techniques to that used in Coolbaugh et al. (2005) to represent heat. Both studies interpolated a heat flow map. Coolbaugh et al. (2005) transformed that map into a thermal gradient map by assigning thermal conductive values to lithologic units in a geologic map.

4.1.2 Williams and DeAngelo, 2008

Williams and DeAngelo (2008) directly informed the present study's approach for assessing Quaternary faults and heat flow. Williams and DeAngelo (2008) used the traditional distance-based binary weighting approach with faults as did the present study. The present study expanded on the standard technique by generating multiple binary thresholds, a ternary threshold set, and a smoothed function. The present study's use of heat flow data to represent heat was adopted directly from Williams and DeAngelo (2008). The present study only differed in this sense from Williams and DeAngelo (2008) by experimenting with temperature at depth data and different interpolation methods.

Williams and DeAngelo (2008) looks at the entire western US (Figure 1.11). Weights derived across such a large area cannot consider regional variability between the different tectonic environments present across the entire Western US but instead averages those affects out over the different environments. This may have resulted in a diminished contribution to favorability from faults (disproportionately present within the Great Basin) compared with high heat flow (present within and outside Great Basin). More

importantly, the Williams and DeAngelo (2008) assessment makes estimates about Nevada using data from the entire West while the present study is more calibrated for the extensional & transtensional tectonic conditions present in Nevada.

The large study area of Williams and DeAngelo (2008) demanded that a coarse grid be used for the analysis (pixels of 2x2 km). Fracture permeability is understood to operate at very local scales (Gleeson and Ingebritsen, 2016). The present study uses a 250 m grid. Major changes in correlation were observed at sub-kilometer scales when looking at distance from faults in the present study (Figure 2.2).

In Williams and DeAngelo (2008), fault distance had to be evaluated in increments no finer than 2 km (the grid size), and a 4 km binary buffer was used. The present study was able to find more precise binary thresholds, generate ternary thresholds, and smooth the transition from positive to negative weights.

The QFFDB did not have complete information on slip sense, recency, and slip rate at the time of Williams and DeAngelo (2008). QFFDB now has that information for all faults in the study area. The present study uses those attributes in detail, eliminating many faults used in the Williams and DeAngelo (2008) analysis. As noted earlier, 54% of Nevada is within 4 km (the search distance used in Williams and DeAngelo, 2008) of a Quaternary fault from the QFFDB. Finding the highest correlating subsets of the QFFDB resulted in stronger W+ from fewer faults, raising the favorability in more promising areas and preventing less-promising areas from appearing overly favorable. Figure 1.11 shows elevated posterior probability values in eastern Nevada, driven largely by faults that were excluded from the present study's analysis.

Williams and DeAngelo (2008) estimated undiscovered resources quantitatively by extrapolating relationships discovered in well-explored subregions of the study area

(Williams and DeAngelo, 2008). The present study did not attempt to make any quantitative estimates of undiscovered resource.

High conditional dependence between evidence layers in Williams and DeAngelo (2008) study only allowed for posterior probability maps to be used to depict relative favorability.

Williams and DeAngelo (2008) uses an RBF map for interpolating heat flow, while the present study's EBK showed a much stronger correlation in Nevada. However, the Williams and DeAngelo (2008) RBF is very similar to the RBF used in the present study.

Williams and DeAngelo (2008) didn't use strain rate data, which appear to be a useful proxy for potentially elevated rates of extensional and transtensional strain related to active permeability generation.

Williams and DeAngelo's (2008) use of seismicity generated low weights relative to the other evidence layers. The attempt to use the same approach to assess seismicity in the present study generated relatively low weight values and was therefore not used to generate posterior probability maps. Williams and DeAngelo (2008) used weighted earthquakes based on seismic moment. This approach may have not been best for characterizing sustained seismicity because of the strong focus on event size.

Williams and DeAngelo (2008) uses categorical weightings to model continuous phenomena like heat flow and seismicity, resulting in abrupt changes in posterior probability when binning thresholds are passed. The present study was able to successfully smooth weights for continuous phenomenon.

4.1.3 Faulds et al., 2015

Faulds et al. (2015) used processing techniques and weightings that benefited from having a diverse team providing multidisciplinary expert guidance. Evidence data were first explored using WofE and logistic regression testing, then weighting relationships were determined by expert consensus after considering data-driven correlations as well as expert geologic knowledge. Faulds et al. (2015) characterized geothermal favorability by presenting three maps: 'The Fairway', an 'overall favorability model' and 'exploration opportunities' (Figure 1.14). The Fairway model is the most similar to a WofE posterior probability map in the sense that it is comprised of evidence data relating to permeability and heat. The overall favorability model incorporates direct evidence, and the exploration opportunities map incorporated information about exploration history into the overall favorability model to highlight areas with high favorability that are not well explored.

The evidence data and geographic techniques used in Faulds et al. (2015) are very different than those used in the present study, making any direct comparison difficult. Faulds et al. (2015) uses many more datasets to characterize permeability. Faulds et al. (2015) characterize local, intermediate, and regional scale permeability layers from data that were not assessed in the present study. More importantly, Faulds et al. (2015) built many of the data sets used in their study while completing the project, producing local-scale high-quality data that is not generally be available for a geothermal assessment covering a larger area such as the state of Nevada. In particular, Faulds et al., 2015 identified favorable structural settings and worked to assign detailed slip rates to Quaternary faults in their study area. Faulds et al. (2015) also show different measures of favorability using colors that are scaled to show different ranges of data than colors used in the present study. For all these reasons any direct comparisons between the present study and Faulds et al. (2015) can only be done qualitatively and with an understanding of the many differences between the models.

4.1.4 Coolbaugh and Bedell, 2006

Coolbaugh and Bedell (2006) was the only study discovered in a literature review that smoothed functions related to weight values derived through WofE and is therefore is especially useful for comparison to the current study. The upper figure in Figure 1.16 shows one example of a smoothed function fit through ‘density function’ values of Coolbaugh and Bedell, which are shown to be nearly equivalent to weights of evidence in the lower Figure 1.16 figure. Values are plotted at their native unit midpoint and the smoothing functions were fit using native units as the independent variable.

Fitted values for the evidence layer seen in Figure 1.16 and for other evidence layers allowed for smoothly varying posterior probability maps. The version on the left of Figure 1.15 was derived through categorical weights, the figure on the right was derived using smoothed weights, resulting in fewer abrupt contrasts and improved favorability modeling in some regions.

Coolbaugh and Bedell (2006) directly informed the present study’s approach to fitting smoothed functions to categorically derived weight values. The present study’s recommended approach to investigate how to best bin a continuous evidence layer included the methodology seen in Figure 1.16 of using manually determined binning increments, equally spaced binning increments, and experimenting with logarithmic and polynomial transformations when fitting.

Coolbaugh and Bedell (2006) was successful in eliminating geologically artificial changes in favorability by generating smoothly varying weights but often had to fit functions through noisy data sets because of the nature of the distribution of training sites relative to ranges of the evidence data.

The present study was able to reduce noise in data when fitting by area and used an iterative approach in discovering bin ranges that promoted gradual declines in weight while maintaining important statistical considerations. The present study also went beyond the work of Coolbaugh and Bedell by demonstrating the ability to smooth weights without significantly altering conditional independence by using cumulative area as the independent variable when fitting and transforming the independent variable when appropriate.

4.2 Geothermal Favorability Maps

The geothermal favorability maps created in the present study vary based on whether smooth weights were applied, which fault subset was used, and whether one of the layers was removed resulting in a two-layer favorability map. Conditional independence tests produced values used to highlight the best-performing combinations of evidence layers. Once the best models were identified, prospective areas in those maps could be identified and examined further to see why the model identified them and whether the region has already been extensively explored.

4.2.1 Best Favorability Maps

One way to understand which models perform best and why is by understanding the results of conditional independence tests that show the conditional independence ratio and the ACCI. Table 3.7 shows the conditional independence ratio, the ratio of actual to predicted training sites where values below 0.85 '*may indicate a problem.*' This test was used to disqualify models with values below 0.85.

A few general patterns can be observed in Table 3.7. All models that used three layers have values above 0.85 except for those that use smoothed weights for fault layers. Better values were seen when shorter buffers were applied to faults. Better values were seen using the 2.4 fault subset rather than the 5.3 subset. When smoothed weights were used for strain rate and heat flow, values were very close to those from categorical models, leading to the preference for models that use smoothed heat flow and strain rate.

Table 3.8 shows the results of the ACCI test which calculates the probability that the difference between actual and expected was not due solely to chance using a 1-tailed test. This test was used to highlight models that performed well. Values below 95% are acceptable. Again, better values were seen when shorter buffers were applied to faults and when using the 2.4 fault subset rather than the 5.3 subset.

Choosing a ‘best’ performing model requires balancing the pros and cons of each option. The best performers in terms solely of conditional independence test values would always contain the shortest search radius to faults, the binary 250 m models. But these models present a limited view of Quaternary faults. Looking only within 250 m may not consider fault dip or unmapped related structures and may be too granular a view given the 250 m cell size of the study. Models using a 1 km fault radius (Figure 3.5 and Figure 3.12) also pass minimal statistical thresholds for the conditional independence ratio and ACCI tests, and therefore they may be a preferred choice for the ‘best’ model that maintains strong measures for conditional independence.

Models that do not possess strong measures for conditional independence can still be used to display relative favorability (Coolbaugh et al., 2005). This makes the ternary models appealing because they add more detail than the binary models and sometimes meet minimal conditional independence criteria even though they do not perform as well on conditional independence tests as binary models. The maps that used smoothed fault

weights in multilayer models always performed more poorly on conditional independence tests, at least partially because of the inability to model an accurate fit to a distance-based evidence layer. Models using smoothed faults could therefore best be used to show relative favorability, but they have the advantage of generating more continuously variable predictive statistics. The models that smoothed all layers (Figure 3.7 and Figure 3.14) were chosen as the ‘best’ model to display relative favorability despite their poor performance on conditional independence tests because of the purpose for which they will be used. Because they show relative favorability, they can be used as a visual tool to get an intuitive sense of the distribution of geothermal favorability as estimated by the present study and to compare qualitatively against other maps that depict relative favorability (such as those produced in Williams and DeAngelo 2008).

A total of four ‘best’ models (maps) were chosen. All used smoothed weights for heat flow and strain rate because smoothed layers for these evidence layers did not negatively affect accurate prediction of the number of training sites. Two ‘best’ models used the 2.4 subset and two used the 5.3 subset. For each subset, one model used a binary faults layer (producing a model with strong conditional independence results) and the other model used a smoothed faults layer (to display relative favorability) (Figure 4.1). Using smoothed fault data introduces uncertainties but may help to account for potentially unmapped Quaternary faults which tend to occur in clusters.

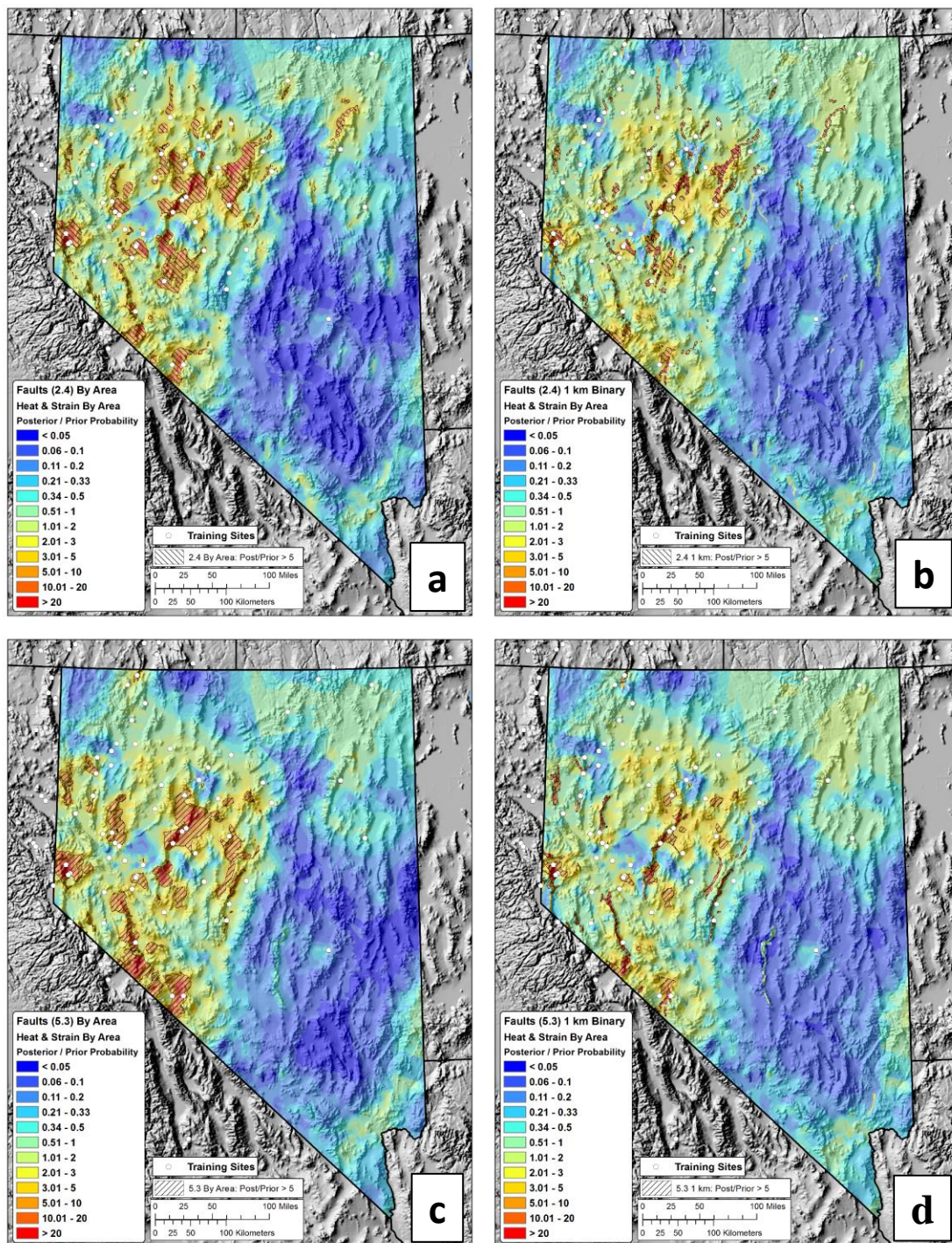


Figure 4.1: Comparison of best performing models: The four models identified as best are displayed to allow for easy comparison. The upper two figures (a and b) use the 2.4 fault subset, the lower two figures (c and d) use the 5.3 subset. The figures on the left (a and c) smooth all layers by area, the figures on the right (b and d) use a 1 km binary layer for faults. Hashed polygons were overlain to highlight areas where the ratio of poster to prior probability is greater than 5.

4.2.2 Areas of High Favorability

Figure 4.2 shows geographic maps for the 2.4 fault subset on the top row and for the 5.3 subset on the bottom row. Plots on the left and right show the same underlying relative favorability map; plots on the left show hatch patterns where the ratio of posterior to prior probability exceeded 5 in the relative favorability surfaces, plots on the right show arbitrarily defined regions of high favorability identified with names to allow for discussion of individual favorable areas. Showing the same underlying data on left and right plots was done to illustrate how favorable regions were identified. Most of the same regions appeared in maps for both fault subsets. The maps that show favorable zones also show heat flow and thermal gradient well locations to give an indication of the exploration history in different areas. Many of the zones identified as having high favorability are already known to host geothermal resources.

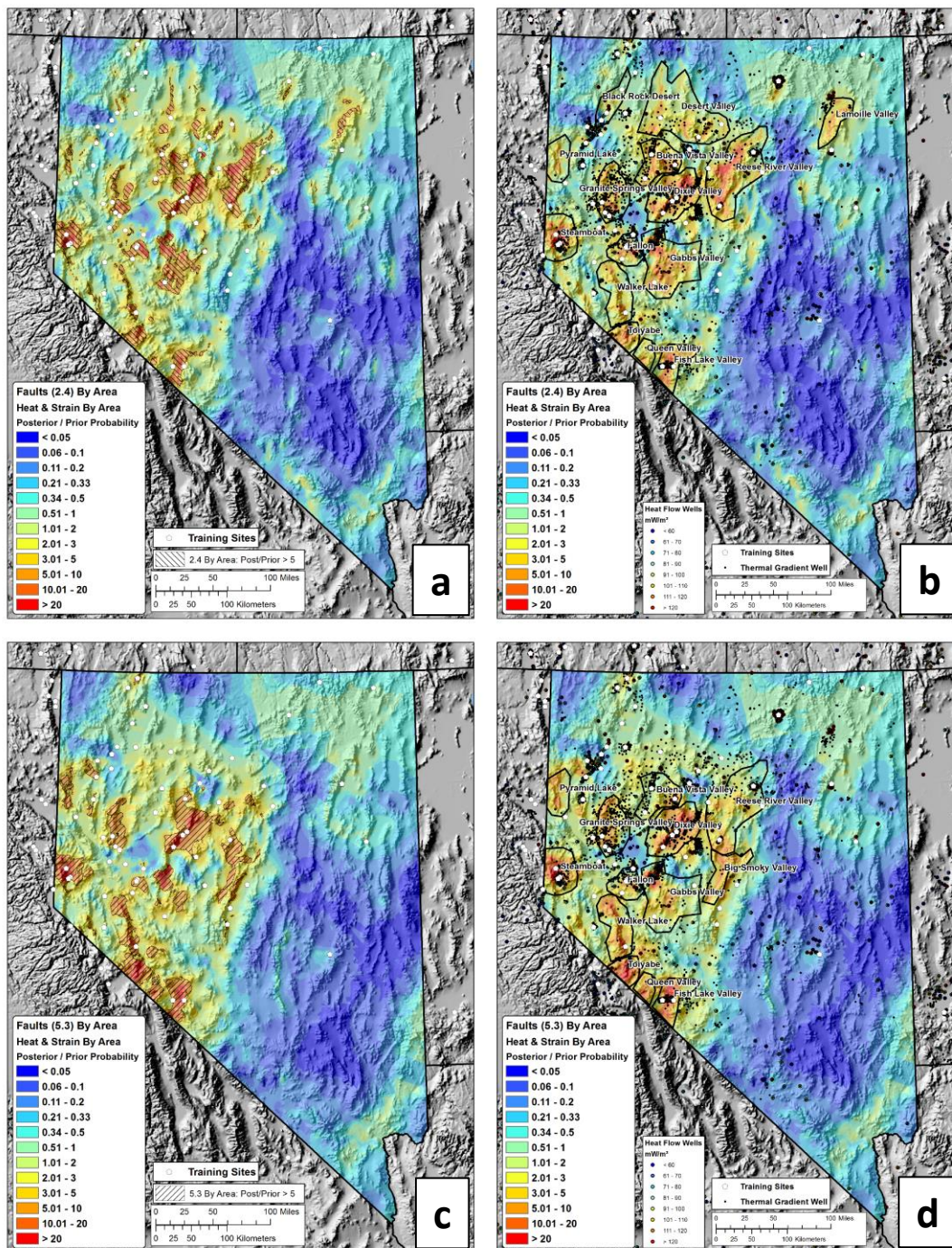


Figure 4.2: Identification of high favorability regions: These maps show regions identified by models as having high favorability. Names were assigned to broad geographic regions to allow for discussion of actual locations. Upper figures (a and b) show relative favorability surfaces generated using the 2.4 fault subsets, lower figures (c and d) show relative favorability surfaces generated using the 5.3 fault subsets. Plots on the left (a and c) show the same underlying relative favorability surface as plots on the right (b and d). Plots on the left (a and c) show hatch marks where the ratio of prior to posterior probability exceeds 5, plots on the right (b and d) show names regions identified using plots on the left.

Maps generated using the 2.4 fault subset in Figure 4.2 show high favorability and potentially limited exploration in zones referred to in the figure as Reese River Valley, Gabbs Valley, Pyramid Lake, Walker Lake, Toiyabe, Queen Valley, and Lamoille Valley. Many of these areas have high estimates for heat flow, young faults, and in some cases, high strain rates.

The region referred to as the “Reese River Valley” appears to be especially favorable and underexplored. The elevated strain rates appear very likely to induce enhanced transtension in this particular area under the Faulds et al., (2012) premise that elevated strain rates northeast of the Walker Lane drive enhanced transtension. This could be driving potentially unknown hydrothermally active structures. Similar factors drive the high favorability estimates in the Desert Valley and Black Rock Desert regions. The region referred to as the “Lamoille Valley” may also present an interesting opportunity to explore near a young fault and potentially elevated heat flow.

Maps generated using the 5.3 fault in Figure 4.2 show high favorability and potentially limited exploration in zones referred to in the figure as Big Smoky Valley, Toiyabe, Walker Lake, Queen Valley, and Fish Lake Valley. Many of these areas have high estimates for heat flow and strain rate as well as faults with relatively high designations for slip rate. Regions in and near the Walker Lane are highlighted in these maps because they tend to possess faults with elevated slip rates and also tend to have high estimated strain rates. Regions highlighted by this process may be less reliable than regions highlighted examining the 2.4 fault subset for two reasons: high strain rates in the Walker Lane likely do not lead to elevated transtension in normal structures unless as part of a pull-apart basin complex, also the slip rate designations used to generate the 5.3 subset may be biased toward better-studied areas. Results from these maps may provide unique insights but must be viewed understanding the potential limitations.

4.3 Comparing Results with Prior Works

It can be difficult to directly compare results from different geothermal assessments. Across different studies, digital data depicting results may not be available, favorability may be calculated using different evidence data and approaches, and available representations of results may depict different measures of favorability.

Areas of high favorability identified in the present study were overlain on maps from Williams and DeAngelo (2008) and Faulds et al. (2015) to better understand similarities and differences. These were the only similar studies for which digital data could be obtained that could be visualized alongside results from the present study. Williams and DeAngelo (2008) was the only reviewed study that displays the same property used in the present study (ratio of posterior and prior probability). This allowed for direct comparisons to be made and for a visual comparison to show identical symbology. Qualitative comparisons were made with a favorability map from Faulds et al. (2015) by overlaying outlines of high favorability areas identified by the present study.

4.3.1 Williams and DeAngelo, 2008

Figure 4.3 highlights how Williams and DeAngelo (2008) calculated high favorability across much of northern Nevada and how the present study was able to geographically constrain the distribution of high favorability areas. Figure 4.3 shows two models from the present study on the top row and two models from Williams and DeAngelo (2008) on the bottom row. The maps in the top row depict results from the present study with all layers smoothed by area and respectively using the 2.4 and 5.3 fault subsets; hatch marks indicate areas where the ratio of posterior to prior probability exceeded 5. Maps on the bottom row data use data from Williams and DeAngelo (2008) and show results of the overall geothermal model, named 'Model 1,' (Figure 4.3c) and the model showing

amagmatic geothermal potential named 'Model 13.' (Figure 4.3d). Hatch marks from the maps on the top row are overlain to highlight how the present study was able to more specifically target highly favorable areas within a region of relatively high favorability identified in Williams and DeAngelo (2008). All maps in Figure 4.3 use the same colors to represent the same property, the ratio of posterior probability to prior probability from a relative favorability surface, so a direct visual comparison shows similar information.

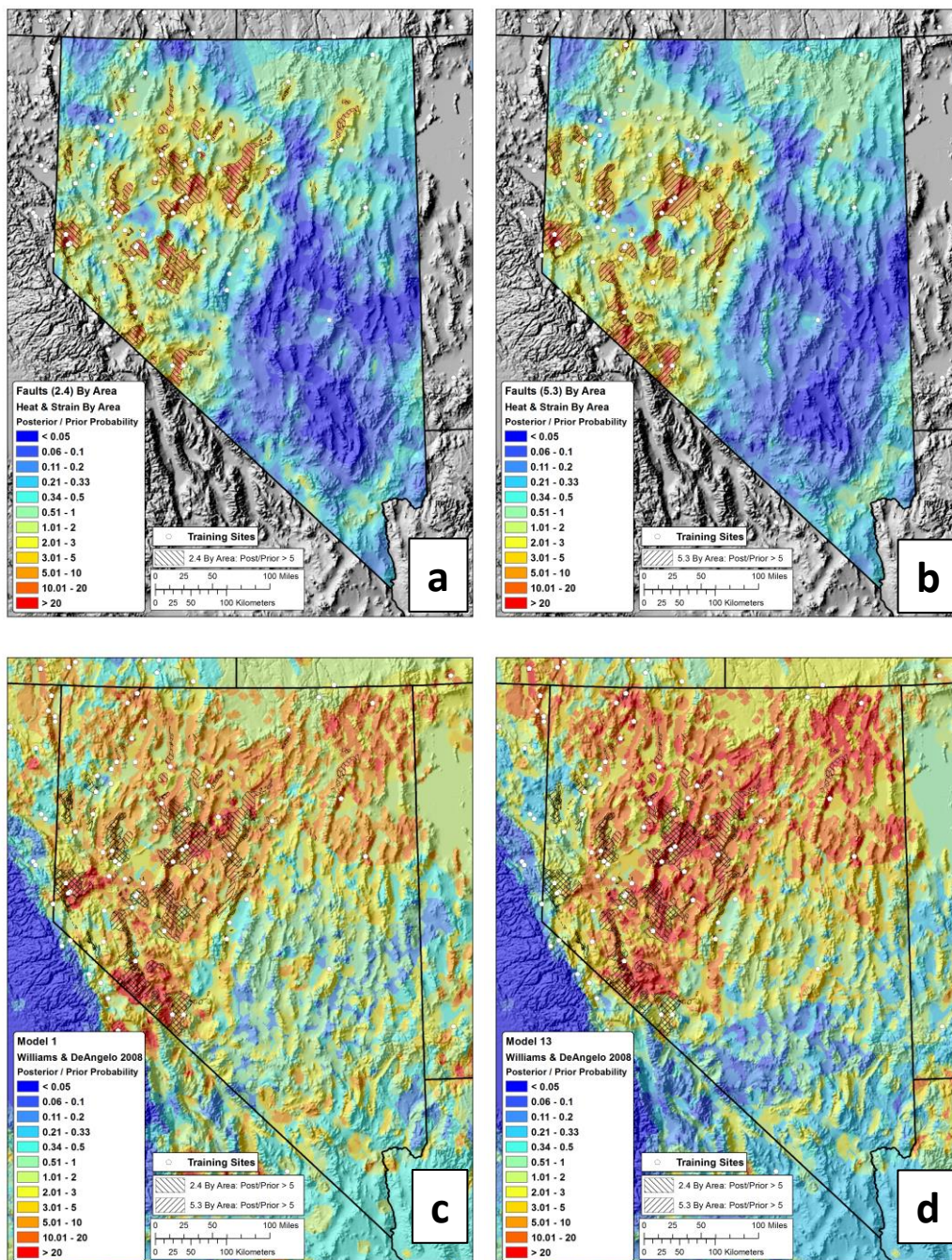


Figure 4.3: Comparison maps with Williams and DeAngelo, 2008: These maps were arranged to compare the results from the present study and Williams and DeAngelo, 2008. Hatched polygons were placed where the ratio of posterior to prior probability is greater than 5 in the present study in the upper figures (a and b). In the lower figures (c and d), the same hatched polygons were overlain on results of Williams and DeAngelo, 2008, which were symbolized using the same colors from the present study. Both studies represented displayed the same units with the same symbology and can therefore be directly compared quantitatively.

Figure 4.4 is identical to Figure 4.3 except that it includes locations of Quaternary faults and heat flow wells. Figure 4.4 helps to illustrate how high favorability estimates in Nevada by Williams and DeAngelo (2008) are driven mainly by uniformly high estimated heat flow in northern Nevada and large fault buffers across the entire state.

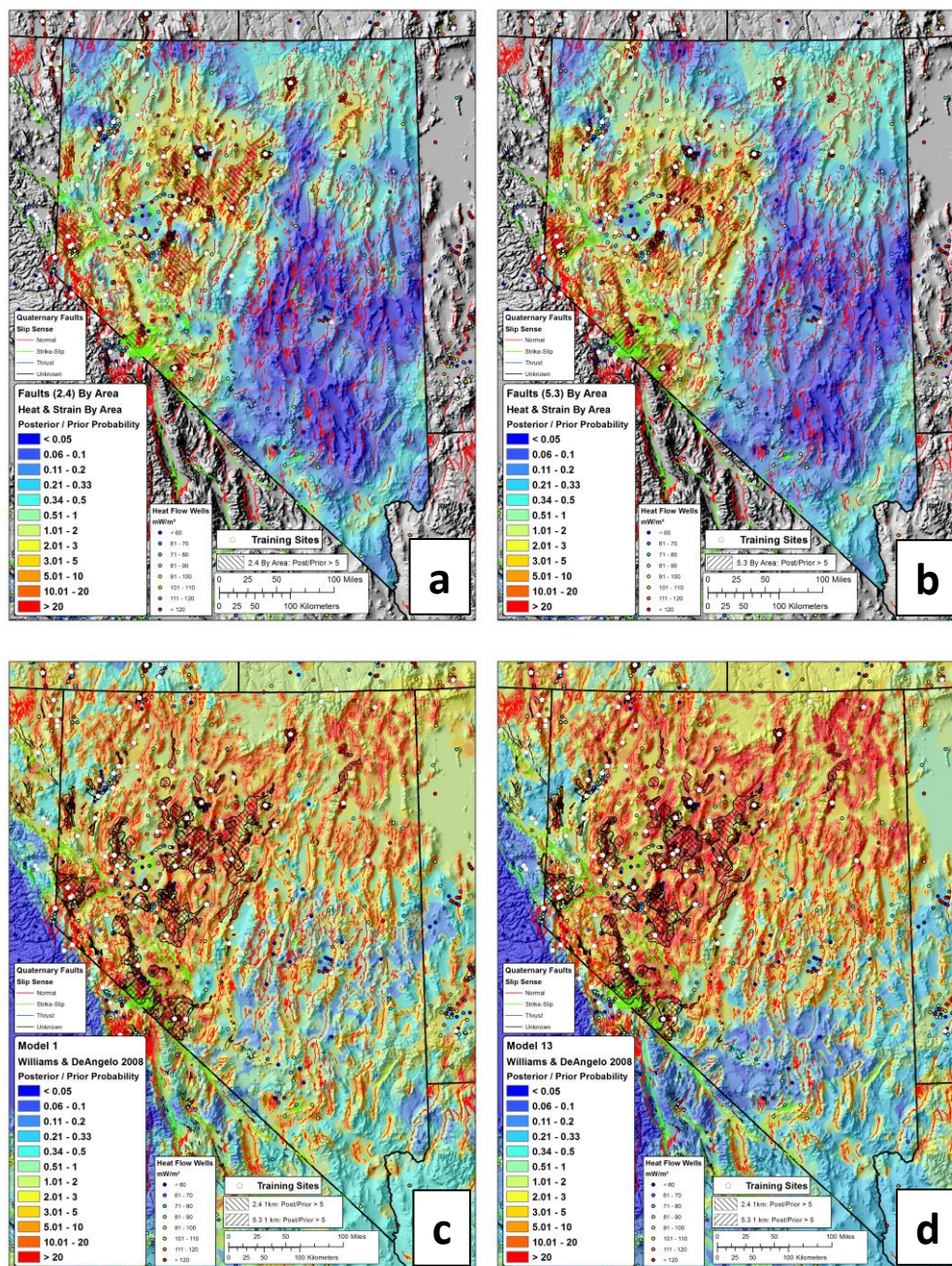


Figure 4.4: Comparison maps with Williams and DeAngelo, 2008 showing faults and heat flow wells: These maps were arranged to compare the results from the present study (a, b) and Williams and DeAngelo, 2008 (c, d). Hatched polygons were placed where the ratio of posterior to prior probability is greater than 5 in the present study in the upper figures (a, b). In the lower figures (c, d), the same hatched polygons were overlain on results of Williams and DeAngelo, 2008, which were symbolized using the same colors from the present study. Both studies represented displayed the same units with the same symbology and can therefore be directly compared quantitatively. All maps show Quaternary faults symbolized by their slip sense and heat flow wells symbolized by their heat flow in mW/m^2 .

Figure 4.4 helps to illustrate how the present study's elimination of many faults based on their slip sense, recency, and/or slip rate significantly contributed to the differences observed between the present study and Williams and DeAngelo (2008). Williams and DeAngelo (2008) did not have access to comprehensive information about slip sense, recency, and slip rate. The 4 km buffer used around all Quaternary faults in Williams and DeAngelo (2008) can be observed in the lower figures of Figure 4.4, elevating favorability across most of Nevada. Selecting the highest correlating subsets and finding more precise distance thresholds may have helped to increase measured weights with more prospective faults and reduce false positives by not weighting other faults.

The present study's EBK heat flow map appeared to capture more local variation in heat flow data compared with the heat flow estimated from Williams and DeAngelo (2008), which had high values uniformly across much of northern Nevada. Modeling this variation more precisely could help to reduce the areas identified as highly prospective. The maps from the present study provide fewer highly prospective targets than the maps from Williams and DeAngelo (2008).

Major differences exist due to the use of different evidence data. The use of strain rate to highlight areas with potentially elevated permeability in the present study would also lead to differences, as would the use of Quaternary magmatism and seismicity in Williams and DeAngelo (2008).

Most of the favorable areas identified in the present study are regions of very high favorability in Williams and DeAngelo (2008) (Figure 4.4). Notable large areas of high favorability predicted by Williams and DeAngelo (2008) do not appear in maps from the present study in the fault systems that were excluded from the present study in and near the Walker Lane (strike-slip) and in northeastern Nevada (not recently active).

The present study uses similar approaches to Williams and DeAngelo (2008) when modeling data related to Quaternary faults and heat flow, the main drivers of high favorability seen in Williams and DeAngelo (2008). Despite using similar data and techniques, the present study was able to significantly reduce the distribution of high favorability areas by more narrowly isolating geographic areas associated with favorable faults and high heat flow, targeting distinct regions of Nevada as potential future exploration targets (Figure 4.2).

4.3.2 Faulds et al., 2015

Figure 4.5 shows two models from the present study on the top row and two models from Faulds et al. (2015) on the bottom row. The maps from the present study fit continuous layers by area and use 1 km binary weights for both the 2.4 and 5.3 subset. Figure 4.5 shows the fairway map and the overall favorability model from Faulds et al. (2015) in the lower figures and uses the symbology the authors provided publicly. Only a qualitative comparison of these studies can be made because they depict favorability using different units and use different symbology.

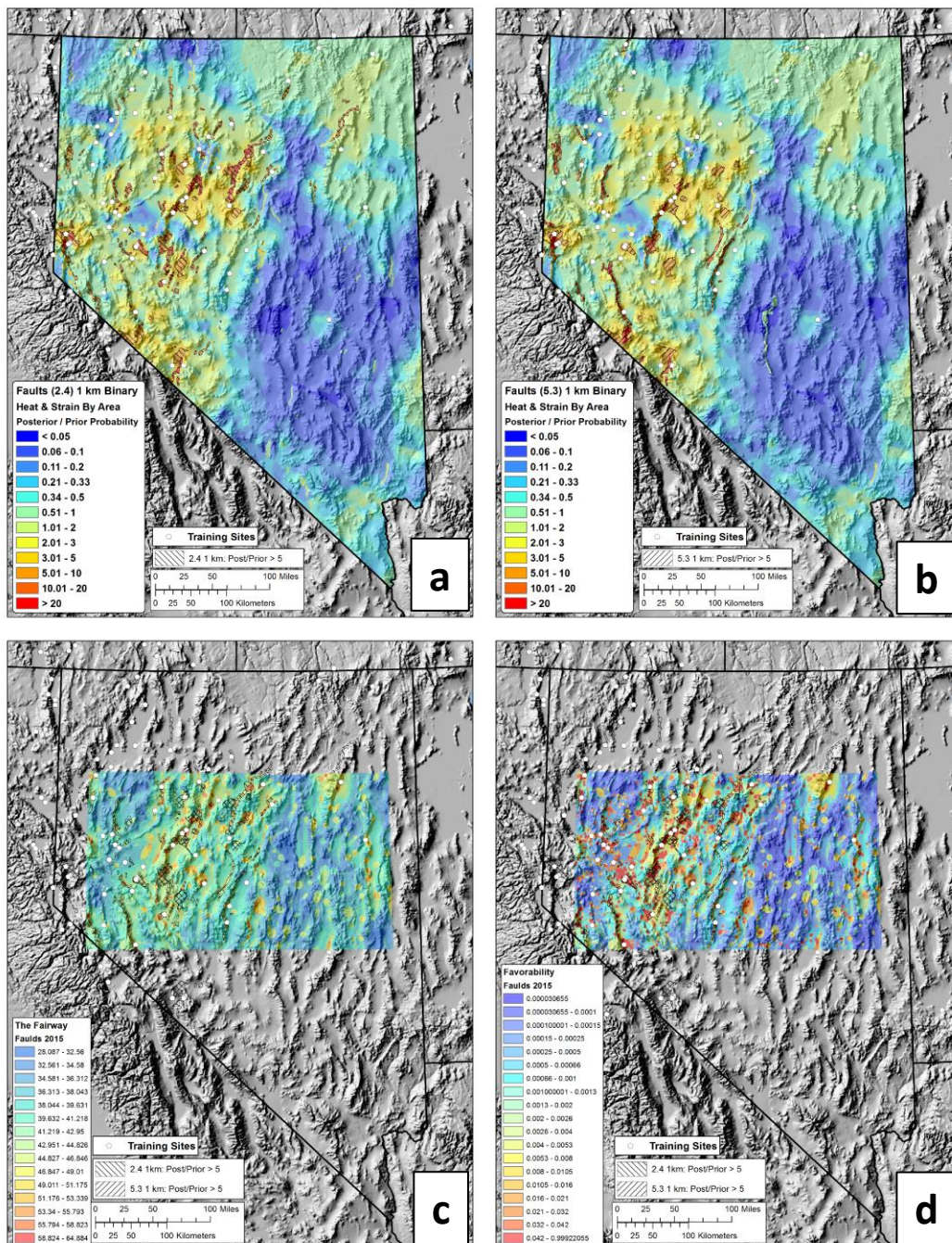


Figure 4.5: Favorability maps compared with those of Faults et al., 2015: These maps were arranged to compare the results from the present study and Faults et al., 2015. Hatched polygons were placed where the ratio of posterior to prior probability is greater than 5 in the present study in the upper figures. In the lower figures, the same hatched polygons were overlain on results of Faults et al., 2015, which used different units than the present study and were symbolized using the symbology in the publicly available data. Because different units were used, and a different symbology was applied, only qualitative comparisons can be made between maps from the two studies.

The hatch marks used in the upper figures in Figure 4.5 show areas where the ratio of posterior to prior probability exceeded 5. These same hatch marks are overlain on the Faulds et al. (2015) data in the maps on the bottom row. The bottom-left figure shows ‘The Fairway,’ the more directly comparable map to the maps from the present study. In this figure, hatch marks tend to occur in areas with relatively high values in The Fairway map, meaning that the present study is highlighting places that were also identified as favorable in Faulds et al. (2015).

Several regions show very similar distributions of high favorability, particularly in the regions identified in the Fairway map in Figure 4.2 as Reese River Valley and Gabbs Valley, which both have high estimates for heat flow and strain rate as well as young faults. Areas of high favorability in both studies also include areas referred to as Big Smoky Valley, Buena Vista Valley, and Walker Lake.

Figure 4.6 is identical to Figure 4.5, but it shows Quaternary faults and heat flow data and zooms into the figures with favorability maps from Faulds et al. (2015). Much of the similarity observed between the two studies is driven by the fact that both studies were heavily influenced by the QFFDB faults. Hatch marks can be seen closely following patterns of high favorability in the Fairway map. The hatch marks show a conservative view of the present study’s results because they depict binary fault models at a high posterior to prior probability ratio. This results in many small areas being outlined. Many of these areas likely contain the presence of normal faults and relatively high estimates for heat flow and strain rate.

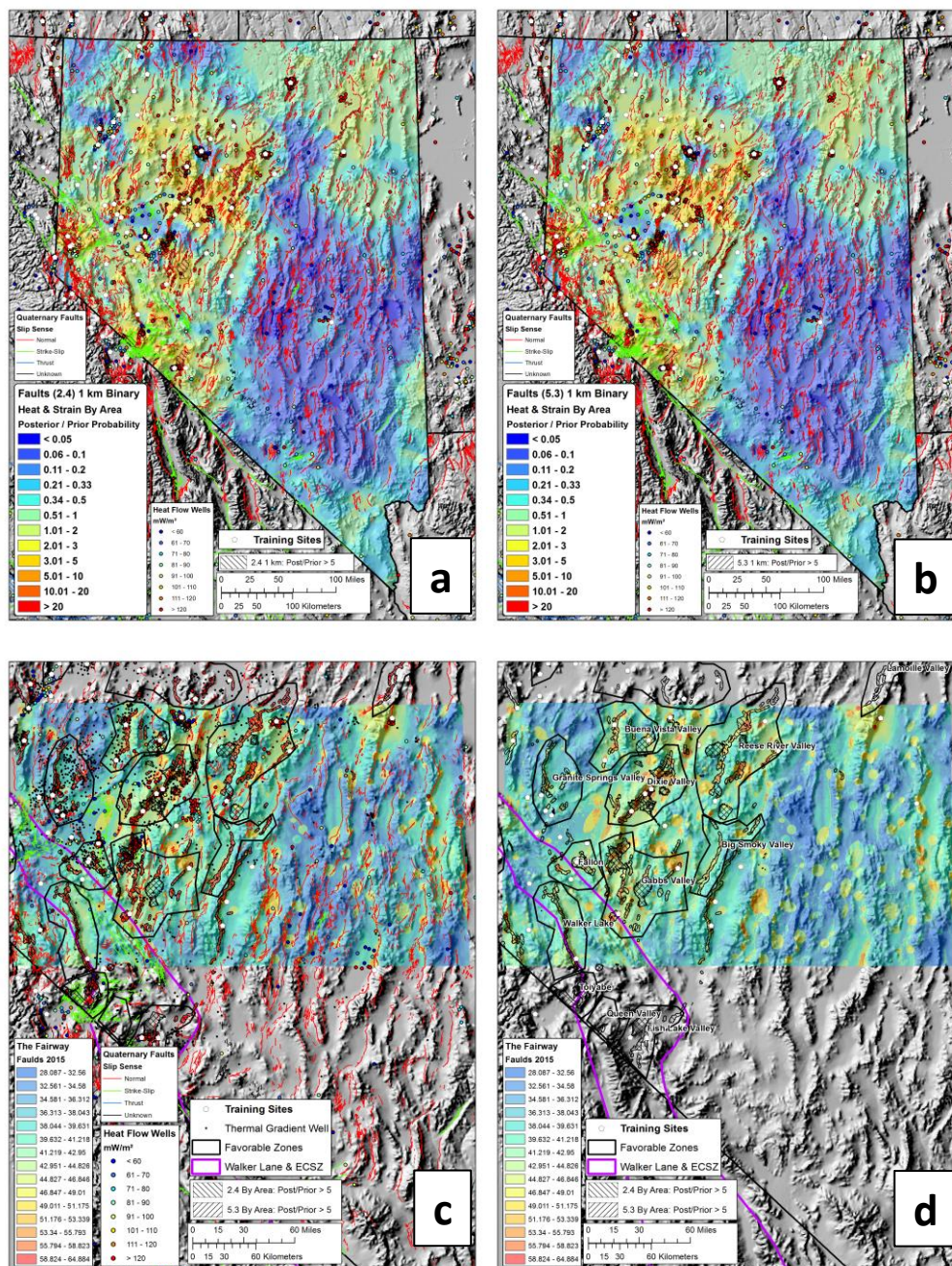


Figure 4.6: Favorability maps compared with those of Faulds et al. (2015) Fairway map: These maps were arranged to compare the results from the present study and the Fairway map from Faulds et al. (2015). Hatched polygons were placed where the ratio of posterior to prior probability is greater than 5 in the present study in the upper figures (a and b). In the lower figures (c and d), the same hatched polygons were overlain on results of Faulds et al. (2015), which used different units than the present study and were symbolized using the symbology in the publicly available data. Because different units were used, and a different symbology was applied, only qualitative comparisons can be made between maps from the two studies. All figures besides figure d show heat flow well locations and faults. Lower figures (c and d) also show outlines of favorable zones identified in Figure 4.2 and the outline of the Walker Lane seen in Figure 1.1.

Faulds et al., 2015 created specialized local-scale data, including information related to favorable structural settings and precise slip rates on faults, to calculate favorability at a fine scale resulting in a map that shows significant variations at the sub-kilometer level. The high spatial overlap seen in high favorability patterns between the two studies may help validate that the present study's predictions appear reasonable in many areas and was able to highlight local targets by focusing in on regional evidence data (Figure 4.6).

The present study is limited because it only uses three regional and publicly available evidence data sets, and therefore may not be able to identify local favorability in all the same areas identified by Faulds et al. (2015), who used high quality local-scale data and specialized experts. Many areas identified as favorable by Faulds et al. (2015) were not identified as such by the present study. Many of these areas appear to be driven by local-scale data representing permeable structural settings (ovals of higher favorability) and sometimes other evidence data not used in the present study (Figure 4.6).

The present study may however identify places that were not highly favorable in Faulds et al. (2015). Faulds et al. (2015) uses an intermediate permeability layer where they apply a 500m buffer to all Quaternary faults; this can be observed by comparing the lower left and right figures in Figure 4.6 and noticing that every fault trace seen in the left figure has a corresponding increase in favorability in the right figure. Some of these patterns were also highlighted by the present study as represented by the hatch marks but many are not. Those that are also identified by the present study may be good local targets for future exploration efforts. Examples may include areas identified in the lower right figure of Figure 4.6 as being in or near the 'Big Smoky Valley,' 'Reese River,' 'Granite Springs,' and the eastern 'Gabbs Valley' zones. Favorable areas in the 'Walker Lake' zone may be less reliable because they fall within the estimated extent of the Walker Lane.

The present study's use of data-driven weight relationships and smoothing of continuous evidence data may help to more accurately apply the contribution of regional scale evidence data to geothermal prospectivity regionally and locally where high-quality local-scale data are not available.

4.4 Additional Findings

4.4.1 Fit by Area Approach

The 'fit by area' approach worked well as an 'individual layer smoothing technique' with heat flow and strain rate but not as well with faults. The layers individually smoothed by area also performed well in multilayer analyses, calculating nearly identical values to the categorical models. Performing well in both regards indicates that this technique may be able to correctly characterize the relationship between weights and the cumulative area of an evidence layer as a mathematical function. Being able to fit a function to estimate cumulative area from native units could allow for the functions derived in the present study to be applied to identical evidence layers for other geographic areas.

Generating smoothed weights has several advantages over the categorical approach. The most salient improvement is the elimination of abrupt changes of favorability driven by bin boundaries of categorical evidence layers. To generate a single weight for a range of values in an evidence layer, that range must be isolated from all other ranges and assessed independently. A single weight value calculated for that range in a categorical analysis applies to the entire range, resulting in a situation where abrupt changes in weight occur at the bin boundaries in traditional WofE studies.

Eliminating abrupt changes in weightings for continuous phenomena like heat flow and strain rate may help to more accurately reflect each layer individually by reducing

overpredictions and underpredictions, perhaps with fewer errors to propagate through a multilayer model. If so, multilayer models that use more than one evidence layer with smoothed weights may be more accurate than the equivalent categorical model.

Despite the apparent success of this technique, it is limited. The fit by area approach requires using a function, which will inevitably have errors unless a perfect goodness of fit measure is achieved. That function is limited by the ability for a dataset to generate bins that result in categorical weights that will fit a function. Without the ability to know which type of function will be used (heat flow used linear, strain rate used polynomial, faults used logarithmic), the best approach appears to be to find gradual declines in weight while maintaining gradual increases in area and sufficient training sites. This hopefully leads each categorical weight value to be as unbiased as possible, allowing for many functions to be tested when fitting.

4.4.2 Geographic Processing Techniques

Performing a geothermal assessment involves many uncertainties. Each raw data source has issues relating to quality and completeness. Different approaches could be used to interpret raw geologic information. Those interpreted data can be subject to different techniques to assign weights. The middle step, of trying to best characterize raw geologic data into a mathematical setting, is very important.

Faults were assessed by looking at their slip sense, recency, strain rate, and dilation and slip tendencies using distance and density-based approaches. Selecting subsets based on slip sense, recency, and slip rate was effective at increasing the strength of weights while reducing the spatial area being assigned positive weights. Automated Python tools greatly assisted by quickly generating cumulative fault subsets, preparing data for weight testing, running weight tests, and summarizing WofE statistics for comparison.

Heat was assessed using an approach similar to Williams & DeAngelo (2008), though a different interpolation method was explored as well as the possibility of using temperature at depth maps that incorporated thermal affects from sediments. Exploring other surfaces depicting heat was a useful demonstration of the effectiveness of the approach ultimately adopted. Strain rate data were obtained as an interpolated map, so it was sampled to the study grid. Automated python plotting tools were helpful for exploring heat flow and strain rate data by generating cumulative and categorical weighting tests, and summarizing WofE statistics for comparison.

Earthquakes were assessed using approaches from Williams & DeAngelo (2008). Automated Python tools greatly assisted by quickly generating different density surfaces with different search radii, preparing data for weight testing, running weight tests, and summarizing WofE statistics for comparison. The lack of useful correlations indicates that the geographic processing techniques used in this analysis may not have properly characterized the effects of seismicity on permeability or that it may not be possible to do so. The technique explored in the present study essentially showed cumulative energy release from earthquakes within a set of chosen distances. High values of cumulative energy release are usually driven by large events that do not necessarily sustain permeability. Permeability in hydrothermal systems may be best sustained in settings that experience relatively continuous seismicity over time.

4.4.3 Evidence Data

The present study used three evidence layers to assess geothermal favorability. Using few evidence layers risks producing too simplistic a range of favorable scenarios but benefits from being able to use data that correlate strongly, extend regionally, and are less likely to portray the same process. Many of the other studies examined use four or more

evidence layers (Table 4.1). The present study considered evidence layers and techniques used in prior analyses and adopted those that best appeared to fit the data.

All studies used evidence layers that represented heat and contributions from faults; the present study adopted approaches similar to Williams and DeAngelo (2008) using interpolated heat flow and distance from faults (Table 4.1). With heat flow, the present study used a different interpolator (EBK) and explored temperature at depth conversions but otherwise used the same technique to generate categorical weights. The present study used the same distance-based approach for faults as Williams and DeAngelo (2008) but was able to exclude many faults based on attributes and use more precise distance thresholds. The present study's use of strain rate data was informed by prior assessments (Coolbaugh et al., 2005, Faulds et al., 2015) and other research that point to its relevance for geothermal exploration (Faulds et al., 2012, Kreemer et al., 2009). The present study derived weights for multiple categories spanning the range of strain rate values in Nevada.

Many evidence layers and techniques used in prior assessments were not adopted for the present study. Seismicity showed weak correlations that may not be characterizing sustained seismicity well. Magmatism was not used because it is not considered the likely heat source in most of Nevada. Potential field geophysics data such as gravity and magnetic field maps were not used because available approaches did not characterize structural controls well consistently across Nevada. Structural setting information and magnetotelluric data were not available statewide. Dilation and slip tendency calculations did not correlate well at the scale of the present study.

In the present study, interpolated heat flow represents heat, faults represent known locations of potentially elevated permeability, and areas of elevated strain rate represent

potentially elevated permeability in known structures as well as potentially unknown structures.

4.4.4 Cell Size

The present study used a very fine grid size compared to prior assessments. Using a 250m grid to model faults was probably helpful because large changes in $W+$ were seen in nearly every fault subset at sub-kilometer scales.

4.4.5 Two Layer Models

Conditional independence results show that most of the conditional dependence between layers exists between fault and strain rate layers, which makes sense because both represent similar forces and are being used to model permeability. Table 3.7 shows good conditional independence results when the 2.4 fault subset is paired with heat flow. Pairing faults with strain rate often resulted in weaker (higher conditional independence) values than the equivalent three-layer model. Models using two layers were produced during the present study but were not presented as maps.

4.4.6 Strain Rate Weighting

Faulds et al. (2012) argue that it would be beneficial to measure ‘*empirical relationships between strain rate and geothermal potential.*’ The present study attempts to do this. Faulds et al. (2012) also argue that elevated strain rates drive conditions that produce hydrothermal systems particularly in extensional areas of Nevada northeast of the Walker Lane (Figure 1.1). These authors warn about assigning high weights to areas of high strain rate within the Walker Lane where strike-slip faulting, not normal faulting dominates:

'The correlation between strain rates and capacity of existing geothermal power plants in the western USA suggests that it may be possible to develop empirical relationships relating strain to geothermal potential, which could ultimately guide resource assessments and exploration strategies. However, higher strain rates alone do not equate with resource potential. For example, higher strain rates along the San Andreas fault system and Walker Lane-eastern California shear zone would seemingly favor geothermal activity, but strike-slip faulting includes a component of shortening, which tends to restrict fluid flow. Accordingly, robust geothermal systems in these zones of dextral shear only occur in transtensional pull-apart basins and/or in areas of recent volcanism (e.g., Salton Trough, The Geysers, and Coso). It would appear that without recent magmatism, extensional or transtensional deformation is a necessary ingredient in generating most viable geothermal systems.'

Faulds et al. (2015) used WofE to measure '*maximum $W+ = 0.96 \pm 0.27$ with 16% of study area using the 34 high enthalpy benchmarks*' using the same strain rate map used in the present study (Kremer et al., 2012). This discovery helped guide weightings developed to model regional scale permeability (Figure 1.12). No other attempts to correlate this strain rate map with geothermal were discovered in a literature review, though other versions of strain rate maps, including earlier versions, have been shown to correlate with geothermal activity.

High strain rates in the Walker Lane represent a different set of processes than the elevated strain rates northeast of the Walker Lane, though either could lead to the development of a hydrothermal system through its respective processes. The intent of the present study and prior studies was to weight a strain rate map for its contribution to enhanced transtension in normal faults. Though elevated strain rates could lead to the development of hydrothermal systems in pull-apart basins or other structures related to

dextral shear (known examples include Walker Lake, Lee Hot Springs, Teels Marsh, Rhodes Marsh, and Columbus Marsh), weights developed in the present study sought to characterize different processes and therefore may not accurately depict contributions from strain rate within the Walker Lane.

4.5 Future Work

4.5.1 Additional Evidence Layers

Additional evidence layers could be explored and potentially incorporated. A combined structural database could be developed to include faults as well as lineations of deep structures derived through regional-scale potential geophysics, particularly gravity and magnetics. Favorable structural setting information could be explored as a potential evidence layer to be used in future studies relating to permeability. The kernel density approach with earthquakes showed correlation with geothermal training sites and may be useful for mapping permeability.

4.5.2 Other Possible Uses of Dilation and Slip Tendency

Dr. Drew Siler hypothesized that approaches that use dilation tendency might reveal stronger results on a local scale than on a regional scale (Dr. Drew Siler, personal communication, 2018). He notes that higher certainty in the direction of the stress field at local scales along with detailed fault mapping would provide better environments to pursue either distance or density-based approaches. A completely different use for dilation and slip tendency calculations could include isolating fault segments with relatively high values as precise exploration targets within favorable regions.

4.5.3 Other Possible Uses of Earthquake Data

Earthquake data could potentially be used differently. The QFFDB is probably conservative when attributing recency to a fault's age without proof, therefore many of the faults in the QFFDB assigned with an older age might be active. Perhaps seismicity could be used to better understand recency of fault activity as well as whether the fault experiences sustained seismicity. This may need to consider, for example, for every fault segment: the distance to an earthquake, the direction to an earthquake, and the fault's dip to understand whether earthquakes from the historic catalog can be attributed to fault segments.

Techniques could potentially be developed to recognize sustained seismicity over time as a proxy for dynamic permeability generation. Defining a signature for sustained seismicity would be difficult, but if possible, it may be a useful way to optimize earthquake data. Some earthquake forecasting tools use only seismicity data (ignoring fault data) to generate predictions; Dr. Tom Parsons suggests it may be possible to adapt earthquake forecasting tools to forecast ongoing permeability generation by searching for a sustained seismicity signal (Dr. Tom Parsons, personal communication, 2019).

4.5.4 Using Density Functions on Fault Subsets

The exploratory work that was not pursued using density functions with faults may have had more potential than previously noticed. For example, Figure 2.3 shows plots where it may be possible to categorize the small class range where all the systems get picked up (the class range where blue dots rise quickly) by isolating it, applying bins that distribute area evenly and fitting a function. Further refining an optimal radius may also be useful, since 1 km and 2 km distances performed better than 5 km and 10 km distances.

Density approaches may have two advantages: fault density could serve as a proxy for fault complexity (although better mapped areas get favorably biased) and it might be possible to generate more weightable categories than with distance (distance ranges are limited by actual distance). Perhaps the continuous nature of a density function would lead to results similar to those encountered when fitting continuous phenomena such as heat flow and strain rate. Using a distance function for modeling faults was found to be constraining because no more than three categorical weights could be generated (ternary) and it forces a function to be fit using one point to represent a large majority of the area. Perhaps simple or kernel density functions could be applied to faults or fault subsets (possibly selected by slip sense and recency, possibly weighted by dilation or slip tendency or another parameter), with testing for an optimal search radius. Then a fit could be applied by area to the entire range of density values without the constraints from a ternary binned distance-based surface. Alternatively, one could pursue density functions on fault subsets that are weighted based on a 'combined' indication derived from multiple indicators of fault activity such as seismicity and dilation tendency.

5.0 Conclusions

The present study develops new methodologies to assess geothermal resource favorability and applies them to arrive at a new assessment to predict where best to explore for active hydrothermal systems in the state of Nevada. The developed methods adopt best practices from prior assessments and refine prior approaches when possible. Nevada has high potential for containing undiscovered geothermal resources. The relatively comprehensive publicly available regional data coverage makes it possible to build good predictive maps and provides a good proving ground for refining methodologies. While the general framework was adopted directly from prior WofE-based geothermal assessments, new techniques were put forward to: optimally transform ‘raw’ geologic and geophysical data, automate processing and visualization, generate robust categorical weights, and calculate smoothed weights from categorical weights. Python-based tools developed in the present study greatly enhanced the efficiency of evaluating multiple processing scenarios. The improved methodology of smoothing weights minimizes potential over-prediction issues and eliminates geologically irrelevant artifacts of the modeling process.

The present study sought to create a simple representation of geothermal favorability by using the best regionally-available versions of data commonly used in geothermal assessments. The predictions in the present study may offer a somewhat conservative view of geothermal favorability by only taking three evidence data types into account, but each layer represents a major predictive factor. No other evidence data used in other studies with regional coverage appeared to represent similar significance. The final predictive maps therefore account for the relative contributions of the most reliable evidence data and do so impartially by using data-driven weights.

Approaches and results of the present study were compared with the most similar prior geothermal assessments of the region to contextualize why decisions were made and how the results compare with other estimates of geothermal favorability. The present study predicted regional and local zones of high favorability in Nevada. These results were then presented alongside results from prior assessments for context, identifying many known geothermal areas, but in some cases highlighting areas that were not identified by other assessments.

Williams and DeAngelo (2008) assessed geothermal potential of the entire western United States and therefore produced high favorability over most of Nevada with little local variation between areas of relatively higher or lower favorability. The present study aimed to: narrow the size of the geographic area highlighted as very favorable by Williams and DeAngelo (2008), identify regions that were identified differently in the models, and assess which evidence data were driving the differences. Williams and DeAngelo (2008) displayed favorability as the ratio of posterior to prior probability using a relative favorability surface; the present study displayed the same parameters and symbology allowing for a similar comparison. The present study was effective at highlighting distinct regions from within favorable areas identified in Williams and DeAngelo (2008).

Faulds et al. (2015) assessed geothermal favorability over a large portion of Nevada and produced a fine scale map using regional and local scale data. Because Faulds et al. (2015) produced a local-scale map that portrayed large changes in favorability over small distances, comparisons were made with models from the present study that highlighted local to regional-scale patterns of elevated permeability. This was done using models that performed well on conditional independence tests and showed a geographically constrained pattern of elevated favorability. Though the two studies displayed different measures of favorability and used different symbologies, many favorable areas

highlighted in the present study were also identified by Faulds et al. (2015), showing that the techniques used in the present study were effective at using regional-scale data to make reasonable regional to local-scale predictions. Many areas of elevated favorability identified by Faulds et al. (2015) fell within favorable zones identified in the present study. The present study identifies several areas with relatively high favorability and low exploration, some of which were not identified as such by Faulds et al. (2015). These areas represent promising locations to target future exploration and may potentially be used to validate predictions made in the present study.

Techniques and findings from the present study can be applied in future resource investigations. The quantitative measures relating evidence layers such as Quaternary faults, strain rate, and heat flow to geothermal resource potential could be used directly in future geothermal resource investigations exploring areas sharing a similar geologic setting. However, the analysis techniques developed in the present study, such as smoothed weights, optimal evidence layer characterization via systematic exploration, and Python tools can be applied more broadly to a wide range of other resource investigations.

References Cited

Agterberg, F.P., and Cheng, Q., 2002. Conditional Independence Test for Weights-of-Evidence Modeling. *Natural Resources Research*, v. 11, no. 4, p. 249-255.

Bennett, R.A., Wernicke, B.P., Niemi, N.A., Friedrich, A.M., and Davis, J.L., 2003, Contemporary Strain Rates in the Northern Basin and Range Province from GPS data. *Tectonics*, v. 22, no. 2, p. 3-1 – 3-31.

Blackwell, D.D., 1989. Regional Implications of Heat Flow of the Snake River Plain, Northwestern United States: *Tectonophysics*, v. 164, p. 323-343.

Blackwell, D.D., Richards, M., 2004. Geothermal Map of North America. American Association of Petroleum Geologists, Tulsa, Oklahoma, 1 sheet, scale 1:6,500,000.

Blackwell, D., Waibel, A. F., and Richards, M., 2012. Why Basin and Range Systems Are Hard to Find: The Moral of the Story is They Get Smaller with Depth. *Transactions, Geothermal Resources Council*, 36, 1321-1326.

Blewitt, G., Coolbaugh, M.F., Holt, W., Kreemer, C., Davis, J.L., and Bennett, R.A., 2002. Targeting of Potential Geothermal Resources in the Great Basin from Regional Relationships Between Geodetic Strain and Geological Structures. *Geothermal Resources Council Transactions*, v. 26, p. 523-525.

Bonham-Carter, G.F., 1994, *Geographic Information Systems for Geoscientists: Modelling with GIS (Computer Methods in the Geosciences Volume 13)*: Tarrytown, New York, Pergamon Press/Elsevier Science Publications, 398 p.

Coolbaugh, M.F. and Bedell, R., 2006, A Simplification of Weights of Evidence Using a Density Function, Fuzzy Distributions, and Geothermal Systems. GIS for the Earth Sciences: Geological Association of Canada, Special Publication 44, p. 115-130.

Coolbaugh, M.F., Raines, G.L., and Zehner, R.E., 2007. Assessment of Exploration Bias in Data-Driven Predictive Models and the Estimation of Undiscovered Resources. Natural Resources Research, v. 16, n. 2, p199-207.

Coolbaugh, M.F., Raines, G.L., Zehner, R.E., Shevenell, L.A., Williams, C.F., 2006. Prediction and Discovery of New Geothermal Resources in the Great Basin: Multiple Evidence of a Large Undiscovered Resource Base. Geothermal Resources Council Transactions, v. 30, p. 867-874.

Coolbaugh, M., Zehner, R., Kreemer, C., Blackwell, D., Oppliger, G., Sawatzky, D., Blewitt, G., Pancha, A., Richards, M., Helm-Clark, C., Shevenell, L., Raines, G., Johnson, G., Minor, T., and Boyd, T., 2005. Geothermal Potential Map of the Great Basin, Western United States: Nevada Bureau of Mines and Geology Map 151.

Coolbaugh, M., Zehner, R., Kreemer, C., Blackwell, D., and Oppliger, G., 2005b. A Map of Geothermal Potential for the Great Basin, U.S.A: Recognition of Multiple Geothermal Environments. Geothermal Resources Council Transactions, v. 29, p. 223–228.

Dobson, P. F. 2016, A Review of Exploration Methods for Discovering Hidden Geothermal Systems. Geothermal Resources Council Transactions v. 40, 695–706.

ESRI, 2017. ArcGIS Desktop: Release 10.4. Redlands, CA: Environmental Systems Research Institute.

Faulds, J.E., Henry, C.D., and Hinz, N.H., 2005. Kinematics of the Northern Walker Lane: An Incipient Transform Fault Along the Pacific – North American Plate Boundary. *Geology*, v. 33, no. 6, p. 505-508.

Faulds, J.E., and Henry, C.D., 2008. Tectonic Influences on the Spatial and Temporal Evolution of the Walker Lane: An Incipient Transform Fault Along the Evolving Pacific – North American Plate Boundary. *Circum-Pacific Tectonics, Geologic Evolution, and Ore Deposits*: Tucson, Arizona Geological Society, Digest 22, p. 437-470.

Faulds, J.E., and Hinz, N.H., 2015. Favorable Tectonic and Structural Settings of Geothermal Systems in the Great Basin Region, Western USA: Proxies for Discovering Blind Geothermal Systems. *Proceedings World Geothermal Congress, Melbourne, Australia, 19-25 April 2015*, 6 p.

Faulds, J., Hinz, N., dePolo, C., Hammond, W., Kreemer, C., Shevenell, L., Coolbaugh, M., Queen, J., Siler, D., Visser, C., Wannamaker, P., 2015. Discovering Blind Geothermal Systems in the Great Basin Region: An Integrated Geologic and Geophysical Approach for Establishing Geothermal Play Fairways. *Federal Agency and Organization: DOE EERE – Geothermal Technologies Program. Award Number: DE-EE0006731*.

Faulds, J.E., Hinz, N., Kreemer, C., Coolbaugh, M.F., 2012. Regional Patterns of Geothermal Activity in the Great Basin Region, Western USA: Correlation with Strain Rates. *Geothermal Resources Council Transactions*, v. 36, p. 897–902.

Ferrill, D. A., Winterle, J., Wittmeyer, G., Sims, D., Colton, S., Armstrong, A., Horowitz, S., Meyers, W. B., and Simons, F. F., 1999. Stressed Rock Strains Groundwater at Yucca Mountain, Nevada. *GSA Today*, 9(5), 2–9.

Geological Survey of Finland (GSF), 2018. Spatial Data Modeler 5 for ArcGIS Pro, <https://github.com/gtkfi/ArcSDM>.

Gleeson T, Ingebritsen S, 2016, Crustal permeability. Wiley, New York. DOI: 10.1002/9781119166573. p. 4-5.

Hammond, W.C., and Thatcher, W., 2004. Contemporary Tectonic Deformation of the Basin and Range Province, Western United States: 10 Years of Observation with the Global Positioning System. *Journal of Geophysical Research*, v. 109, B08403.

Koenig, J.B. and McNitt, J.R., 1983. Controls on the Location and Intensity of Magmatic and Nonmagmatic Geothermal Systems in the Basin and Range Province. *Geothermal Resources Council Special Report No. 13*, p. 93.

Kreemer, C., Blewitt, G., and Hammond, W.C., 2009. Geodetic Constraints on Contemporary Deformation in the Northern Walker Lane: 2. Velocity and Strain Rate Tensor Analysis, in *Late Cenozoic Structure and Evolution of the Great Basin-Sierra Nevada Transition*. *Geological Society of America Special Volume 447*, p. 17-31.

Kreemer, C., Hammond, W.C., Blewitt, G., Austin, A.A., and Bennett, R.A., 2012. A Geodetic Strain Rate Model for the Pacific-North American Plate Boundary, Western United States. *Nevada Bureau of Mines and Geology Map 178*, scale 1:1,500,000.

Krivoruchko K. and Gribov A., 2014. Pragmatic Bayesian Kriging for Non-Stationary and Moderately Non-Gaussian data. *Mathematics of Planet Earth. Proceedings of the 15th Annual Conference of the International Association for Mathematical Geosciences*. Springer 2014, pp. 61-64.

Morris, A., Ferrill, D., A., and Henderson, D., B., 1996. Slip-Tendency Analysis and Fault Reactivation. *Geology* 24, no. 3: 275–78.

NCEDC, 2016, Northern California Earthquake Data Center. UC Berkeley Seismological Laboratory. Dataset. doi:10.7932/NCEDC.

Pérouse, E., and Wernicke, B., 2017. Spatiotemporal Evolution of Fault Slip Rates in Deforming Continents: The Case of the Great Basin Region, Northern Basin and Range Province. Vol. 13, 2017. <https://doi.org/10.1130/GES01295.1>.

Saltus, R.W., and Jachens, R.C., 1995. Gravity and Basin-Depth Maps of the Basin and Range Province, Western United States. Geophysical Investigation Map, 1995. USGS Publications Warehouse.

<http://pubs.er.usgs.gov/publication/gp1012>.

Sass, J.H., A.H. Lachenbruch, R.J. Munroe, G.W. Greene, and T.H. Moses, Jr., 1971. Heat flow in the Western United States. *Journal of Geophysical Research*, v. 76, n. 26, p. 6376-6413.

Siler, D.L., Faulds, J.E., Mayhew, B., Mcnamara, D.D., 2016. Analysis of the Favorability for Geothermal Fluid Flow in 3D: Astor Pass Geothermal Prospect, Great Basin, Northwestern Nevada, USA. *Geothermics* 60, 1–12.

<https://doi.org/10.1016/j.geothermics.2015.11.002>

Siler, D.L., Zhang, Y., Spycher, N.F., Dobson, P.F., McClain, J.S., Gasperikova, E., Zierenberg, R.A., Schiffman, P., Ferguson, C., Fowler, A., Cantwell, C., 2017. Play-

fairway Analysis for Geothermal Resources and Exploration Risk in the Modoc Plateau Region. *Geothermics* 69. <https://doi.org/10.1016/j.geothermics.2017.04.003>

Raines, G.L., Bonham-Carter, G.F. and Kemp, L., 2000, Predictive Probabilistic Modelling Using ArcView GIS: *ArcUser*, v. 3, n. 2, p. 45-48.

U.S. Geological Survey (USGS), 2006. Quaternary Fault and Fold Database for the United States. Accessed 2018, from US Geological Survey web site: <http://earthquake.usgs.gov/hazards/qfaults/>.

Williams, C.F., 2004. Development of Revised Techniques for Assessing Geothermal Resources. Proceedings, 29th Workshop on Geothermal Reservoir Engineering, Stanford University, Stanford, California.

Williams, C.F., 2007. Updated Methods for Estimating Recovery Factors for Geothermal Resources. Proceedings, 32nd Workshop on Geothermal Reservoir Engineering, Stanford University, Stanford, California.

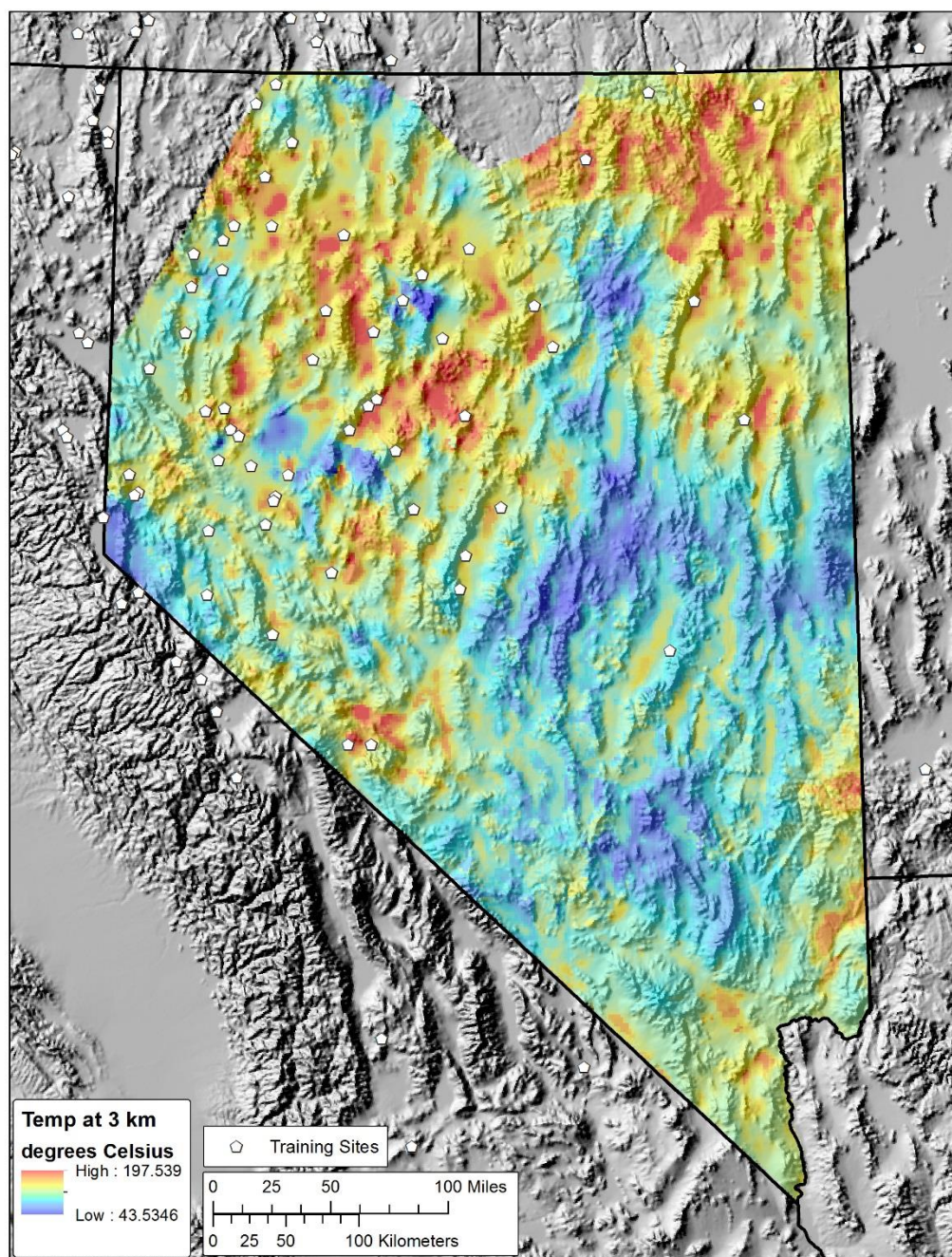
Williams, C.F., DeAngelo, J., 2008. Mapping Geothermal Potential in the Western United States. *Geothermal Resources Council Transactions* v. 32, 181-188.

Williams, C.F., DeAngelo, J., 2011. Evaluation of Approaches and Associated Uncertainties in the Estimation of Temperatures in the Upper Crust of the Western United States. *Geothermal Resources Council Transactions*, v. 35, 1599-1605.

Williams, C.F., Reed, M.J., Mariner, R.H., DeAngelo, J., and Galanis, S.P.J., 2008. Assessment of Moderate- and High-Temperature Geothermal Resources of the United States: US Geological Survey Fact Sheet 2008–3082, p. 4.

Appendices

Appendix 1: Temperature at Depth Map



Appendix 1: Estimated Temperature at 3 km depth using sediment thickness: The background colors show estimated temperature (degrees Celsius) at 3 km depth. Training sites are depicted as white pentagons.

Appendix 2: EBK Statistics

Model	RMSE	rmsStd	model	transformation	time(s)	subsetSize	overlap
1	18.329	1.#QNAN	POWER	NONE	6	100	3
2	18.334	0.980	POWER	NONE	10	100	5
3	18.413	0.995	POWER	NONE	3	100	1
4	18.424	1.#QNAN	WHITTLE_DETRENDED	EMPIRICAL	30	100	3
5	18.430	1.#QNAN	EXPONENTIAL_DETRENDED	EMPIRICAL	30	100	3
6	18.439	1.#QNAN	K_BESSEL_DETRENDED	EMPIRICAL	139	100	3
7	18.440	1.#QNAN	WHITTLE	EMPIRICAL	33	100	3
8	18.442	1.#QNAN	K_BESSEL	EMPIRICAL	141	100	3
9	18.448	1.008	POWER	NONE	9	500	1
10	18.450	0.995	POWER	NONE	30	500	5
11	18.457	0.991	POWER	NONE	4	250	1
12	18.465	1.016	POWER	NONE	14	250	5
13	18.470	0.996	POWER	NONE	18	500	3
14	18.473	1.021	POWER	NONE	9	250	3
15	18.473	1.#QNAN	EXPONENTIAL	EMPIRICAL	33	100	3
16	18.517	1.539	EXPONENTIAL_DETRENDED	EMPIRICAL	12	100	1
17	18.558	1.438	EXPONENTIAL	EMPIRICAL	53	100	5
18	18.566	1.542	K_BESSEL_DETRENDED	EMPIRICAL	52	100	1
19	18.575	1.445	K_BESSEL	EMPIRICAL	248	100	5
20	18.603	1.445	K_BESSEL_DETRENDED	EMPIRICAL	495	500	5
21	18.626	1.#QNAN	LINEAR	NONE	2	100	3
22	18.632	1.452	WHITTLE_DETRENDED	EMPIRICAL	12	100	1
23	18.636	1.427	K_BESSEL_DETRENDED	EMPIRICAL	247	100	5
24	18.641	1.405	WHITTLE	EMPIRICAL	57	100	5
25	18.646	0.978	LINEAR	NONE	3	100	5
26	18.646	1.441	WHITTLE_DETRENDED	EMPIRICAL	55	100	5
27	18.664	1.356	K_BESSEL_DETRENDED	EMPIRICAL	87	250	1
28	18.667	1.397	EXPONENTIAL_DETRENDED	EMPIRICAL	53	100	5
29	18.669	1.536	EXPONENTIAL	EMPIRICAL	13	100	1
30	18.686	1.607	K_BESSEL	EMPIRICAL	52	100	1
31	18.687	1.413	K_BESSEL	EMPIRICAL	155	500	1
32	18.688	1.623	K_BESSEL_DETRENDED	EMPIRICAL	318	250	5
33	18.704	1.370	K_BESSEL	EMPIRICAL	485	500	5
34	18.710	1.554	K_BESSEL_DETRENDED	EMPIRICAL	215	250	3
35	18.714	1.548	K_BESSEL	EMPIRICAL	308	250	5
36	18.727	1.386	K_BESSEL	EMPIRICAL	83	250	1

37	18.741	0.992	LINEAR	NONE	1	100	1
38	18.761	1.582	EXPONENTIAL_DETRENDED	EMPIRICAL	62	500	3
39	18.763	1.588	EXPONENTIAL_DETRENDED	EMPIRICAL	61	250	5
40	18.777	1.595	K_BESSEL_DETRENDED	EMPIRICAL	166	500	1
41	18.780	1.427	EXPONENTIAL_DETRENDED	EMPIRICAL	18	250	1
42	18.790	1.486	K_BESSEL_DETRENDED	EMPIRICAL	340	500	3
43	18.796	1.732	EXPONENTIAL_DETRENDED	EMPIRICAL	40	250	3
44	18.800	0.990	LINEAR	NONE	3	500	5
45	18.828	0.994	LINEAR	NONE	2	500	3
46	18.829	1.399	WHITTLE	EMPIRICAL	13	100	1
47	18.848	1.018	LINEAR	NONE	2	250	3
48	18.850	1.556	K_BESSEL	EMPIRICAL	207	250	3
49	18.857	1.004	LINEAR	NONE	1	500	1
50	18.858	1.455	EXPONENTIAL	EMPIRICAL	15	250	1
51	18.883	1.013	LINEAR	NONE	2	250	5
52	18.886	0.992	LINEAR	NONE	1	250	1
53	18.892	1.641	WHITTLE_DETRENDED	EMPIRICAL	60	250	5
54	18.896	1.542	K_BESSEL	EMPIRICAL	338	500	3
55	18.919	1.537	EXPONENTIAL	EMPIRICAL	57	250	5
56	18.938	1.428	WHITTLE_DETRENDED	EMPIRICAL	58	500	3
57	18.939	1.495	EXPONENTIAL_DETRENDED	EMPIRICAL	88	500	5
58	18.945	1.343	WHITTLE_DETRENDED	EMPIRICAL	87	500	5
59	18.970	1.548	EXPONENTIAL_DETRENDED	EMPIRICAL	26	500	1
60	18.979	1.457	WHITTLE_DETRENDED	EMPIRICAL	16	250	1
61	19.007	1.568	EXPONENTIAL	EMPIRICAL	38	250	3
62	19.072	1.512	EXPONENTIAL	EMPIRICAL	85	500	5
63	19.100	1.456	EXPONENTIAL	EMPIRICAL	25	500	1
64	19.118	1.716	WHITTLE_DETRENDED	EMPIRICAL	39	250	3
65	19.150	1.441	WHITTLE	EMPIRICAL	61	250	5
66	19.183	1.571	WHITTLE_DETRENDED	EMPIRICAL	24	500	1
67	19.183	1.397	WHITTLE	EMPIRICAL	53	500	3
68	19.197	1.420	WHITTLE	EMPIRICAL	78	500	5
69	19.222	1.336	WHITTLE	EMPIRICAL	16	250	1
70	19.239	1.467	EXPONENTIAL	EMPIRICAL	56	500	3
71	19.345	1.648	WHITTLE	EMPIRICAL	40	250	3
72	19.362	1.408	WHITTLE	EMPIRICAL	24	500	1
73	20.436	1.#QNAN	THIN_PLATE_SPLINE	NONE	2	100	3
74	20.436	0.959	THIN_PLATE_SPLINE	NONE	3	100	5
75	20.553	0.968	THIN_PLATE_SPLINE	NONE	1	100	1

76	20.595	0.977	THIN_PLATE_SPLINE	NONE	1	250	3
77	20.682	0.959	THIN_PLATE_SPLINE	NONE	1	500	1
78	20.690	0.959	THIN_PLATE_SPLINE	NONE	2	500	3
79	20.690	0.976	THIN_PLATE_SPLINE	NONE	2	250	5
80	20.708	0.954	THIN_PLATE_SPLINE	NONE	1	250	1
81	20.717	0.958	THIN_PLATE_SPLINE	NONE	2	500	5

Appendix 2: Kriging parameters and cross-validation statistics used to select a best performing EBK model.

Appendix 3: Python Code

The code included below should work with a standard installation of ArcGIS. Modules used in the scripts are all part of the standard installation of ArcGIS.

Processing Tools

'''

Python Processing Tools: 4 tools.

- 1) Subset-Distance Cumulative Weight Test Tool
- 2) Density Function and Cumulative Weight Tool
- 3) Continuous Layer Reclassify and Cumulative Weight Test Tool
- 4) Categorical Weight Test Tool

To use tools, set toolbox locations, folder locations, and tool parameters.
Then uncomment code in the 'Tools' section

Jacob DeAngelo

'''

Import modules

import sys, string, os, time, csv

import numpy as np

import arcpy

import ntpath

from arcpy import env

Clock

starttime = time.clock()

print "Starting " + time.strftime("%I:%M:%S", time.localtime())

Set toolbox location(s): Xtools and ArcSDM toolboxes must be referenced

arcpy.ImportToolbox(r'C:\Program Files (x86)\DataEast\XTools Pro\Toolbox\XTools
Pro.tbx') # This filepath must point to the xTools toolbox

arcpy.ImportToolbox('C:\ArcProjects\Workspace\ArcSDM2018\ArcSDM-
master\ArcSDM-master\Toolbox\ArcSDM.pyt') # This filepath must point to the
ArcSDM toolbox

'''

Folders: Input, output, workspace

'''

inPathName =

r'C:\ArcProjects\Datasets\PlayFairway\NevadaPFA\layers\NevadaState1\sdmIn7' #

Folder containing input data

```

# 'Categorical Weight Test Tool' outPath
#outPathName =
r'C:\ArcProjects\Datasets\PlayFairway\NevadaPFA\layers\NevadaState2\calcWofE\inLa
yers\flt_r3Aug2018\mess' # Folder to contain output data
# 'Continuous Layer Reclassify and Cumulative Weight Test Tool' outPath
#outPathName =
r'C:\ArcProjects\Datasets\PlayFairway\NevadaPFA\layers\NevadaState2\heat_250m_v3\
mess' # Folder to contain output data
# 'Density Function and Cumulative Weight Tool, calculate weights tools' outPath
#outPathName =
r'C:\ArcProjects\Datasets\PlayFairway\NevadaPFA\layers\NevadaState2\eq1\ptDensLog
NotWeighted\replicationVerification' # Folder to contain output data
# 'Subset-Distance Cumulative Weight Test Tool' outPath
outPathName =
r'C:\ArcProjects\Datasets\PlayFairway\NevadaPFA\layers\NevadaState2\fault_subsets_A
ug2018\replicateVerify' # Folder to contain output data
outWorkspaceName =
r'C:\ArcProjects\Datasets\PlayFairway\NevadaPFA\layers\initialAttempts\junkToDelete'
# Workspace folder, to contain junk files

'''
Tool User Settings
'''

# Parameters for all tools: List of training sites, name of study area raster
trainingSets = ["gs.shp"] # List of training point shapefiles to be analyzed
studyAreaRasterName = "nev250m" # Name of study area raster in inPathName folder

# Parameters for 'Subset-Distance Cumulative Weight Test Tool': Attributes must be
present in all evidence data
evidenceSets = ["fdn.shp", "fds.shp"] # Evidence data sets
attribute1 = 'agecode' # Attribute 1
attribute2 = 'slipcode' # Attribute 2

# Parameters for 'Continuous Layer Reclassify and Cumulative Weight Test Tool'
contLayers = ["hf_ebk250"] # Name of the raster file to be reclassified & weight tested.
These must be placed in the output folder.
numberOfIntervals = '50' # Number of intervals used for reclassification
reclassInterval = "1" # Size of each interval (in units

# Parameters for 'Density Function and Cumulative Weight Tool, Calculate Weights
Tool'

```

```

shpList = ['e15.shp'] # List of evidence data sets to be analyzed
radiusList = [1000,2000] # List of radii used in density functions
fieldList = [] # If user wants to weight based on an attribute, enter attribute name(s) in
this list

# Parameters for 'Categorical Weight Test Tool'
catList = ["fn24r_t4", "fn24r_t5"] # Name(s) of categorical rasters for which weights will
be calculated. These must be placed in the output folder.

'''
Set Geoprocessing environments, other settings: no not modify these
'''

inPath = inPathName + '\\'
outPath = outPathName + '\\'
outWorkspace = outWorkspaceName + '\\'
arcpy.gp.overwriteOutput = True
arcpy.CheckOutExtension("spatial")
studyAreaRaster = inPath + studyAreaRasterName # Do not change this
cellSize = int(str(arcpy.GetRasterProperties_management(studyAreaRaster,
"CELLSIZEX"))) # Do not change this
prjFileName = evidenceSets[0].replace(".shp", ".prj")
prjFile = inPath + prjFileName
prjString = open(prjFile, 'r').read()
rastExtent = arcpy.sa.Raster(studyAreaRaster).extent
arcpy.env.extent = rastExtent
arcpy.env.snapRaster = studyAreaRaster
arcpy.env.mask = studyAreaRaster
arcpy.env.workspace = outWorkspace
arcpy.env.scratchWorkspace = outWorkspace
arcpy.env.outputCoordinateSystem = prjString
arcpy.env.cellSize = cellSize

'''
Internal modules: no not modify these
'''

def eucDist(evidenceIn, distRast, cellSize):
    arcpy.gp.EucDistance_sa(evidenceIn, distRast, "", cellSize, "")

```

```

def reclassByIntFlipAndMax(unclassRast, rInterval):

    # Reclassification Prep
    rasterMinx = arcpy.GetRasterProperties_management(unclassRast, "MINIMUM")
    rasterMin = rasterMinx.getOutput(0)
    rasterMaxx = arcpy.GetRasterProperties_management(unclassRast, "MAXIMUM")
    rasterMax = rasterMaxx.getOutput(0)
    print "Raster min :" + rasterMin
    print "Raster max :" + rasterMax

    # New modified minimum value
    ratioMinInt = int(float(rasterMin)/float(rInterval))
    rastMinMod = ratioMinInt * float(rInterval)

    # Create class numbers
    rastRange = float(rasterMax)-float(rasterMin)
    ## numIntervals = math.ceil(rastRange/float(rInterval))
    numIntervals = 40
    blankRange = range(int(numIntervals))
    reclassInt = [(x+1) for x in blankRange]
    revArray = reclassInt[::-1]

    # Min reclass value calc
    def minReclassValue(reclassInt):
        ratioMinInt = int(float(rasterMin)/float(rInterval))
        minimumValueRange = [(x+ratioMinInt)*float(rInterval) for x in blankRange]
        minimumValueRange.remove(minimumValueRange[0])
        joj = math.ceil(float(rasterMin))-1
        newMin = (float(rasterMin))-(float(rInterval))
        minimumValueRange.insert(0, newMin)
        if minimumValueRange[0] == -1:
            minimumValueRange.remove(minimumValueRange[0])
            minimumValueRange.insert(0, 0.0)
        else:
            pass
        return minimumValueRange

    # Max reclass value calc
    def maxReclassValue(reclassInt):
        ratioMinInt = int(float(rasterMin)/float(rInterval))
        maximumValueRange = [(((x+ratioMinInt)*float(rInterval))+float(rInterval)) for x
in blankRange]

```

```

    maximumValueRange.remove(maximumValueRange[len(maximumValueRange)-
1])
    maximumValueRange.insert(len(maximumValueRange),
math.ceil(float(rasterMax)))
    return maximumValueRange

minValueRange = minReclassValue(reclassInt)
maxValueRange = maxReclassValue(reclassInt)

# Make 1 string
kk = ".join('{} {} {}';'.format(v[0], v[1], k+1) for k,v in
enumerate(zip(minValueRange, maxValueRange)))
fullString = kk[:-1]
quoteString = "" + fullString + ""
print fullString
return fullString

# Toggle code under & over this message to flip reclass
##  minValueRange = minReclassValue(reclassInt)
##  maxValueRange = maxReclassValue(reclassInt)
##  revMinRange = minValueRange[::-1]
##  revMaxRange = maxValueRange[::-1]
##
##  # Make 1 string
##  kk = ".join('{} {} {}';'.format(v[0], v[1], k+1) for k,v in
enumerate(zip(revMinRange, revMaxRange)))
##  pString = kk[:-1]
##  fullString = pString + ';NODATA ' + str((reclassInt[len(reclassInt)-1])+1)
##  return fullString

def reclassByInt(unclassRast, rInterval):

    # Reclassification Prep
    rasterMinx = arcpy.GetRasterProperties_management(unclassRast, "MINIMUM")
    rasterMin = rasterMinx.getOutput(0)
    rasterMaxx = arcpy.GetRasterProperties_management(unclassRast, "MAXIMUM")
    rasterMax = rasterMaxx.getOutput(0)
    print "Raster min :" + rasterMin
    print "Raster max :" + rasterMax

    # New modified minimum value

```

```

ratioMinInt = int(float(rasterMin)/float(rInterval))
rastMinMod = ratioMinInt * float(rInterval)

# Create class numbers
rastRange = float(rasterMax)-float(rasterMin)
numIntervals = math.ceil(rastRange/float(rInterval))
## numIntervals = 50
blankRange = range(int(numIntervals))
reclassInt = [(x+1) for x in blankRange]
revArray = reclassInt[::-1]

# Min reclass value calc
def minReclassValue(reclassInt):
    ratioMinInt = int(float(rasterMin)/float(rInterval))
    minimumValueRange = [(x+ratioMinInt)*float(rInterval)) for x in blankRange]
    minimumValueRange.remove(minimumValueRange[0])
    joj = math.ceil(float(rasterMin))-1
    newMin = (float(rasterMin))-(float(rInterval))
    minimumValueRange.insert(0, newMin)
    if minimumValueRange[0] == -1:
        minimumValueRange.remove(minimumValueRange[0])
        minimumValueRange.insert(0, 0.0)
    else:
        pass
    return minimumValueRange

# Max reclass value calc
def maxReclassValue(reclassInt):
    ratioMinInt = int(float(rasterMin)/float(rInterval))
    maximumValueRange = [(((x+ratioMinInt)*float(rInterval))+float(rInterval)) for x
in blankRange]
    maximumValueRange.remove(maximumValueRange[len(maximumValueRange)-
1])
    maximumValueRange.insert(len(maximumValueRange),
math.ceil(float(rasterMax)))
    return maximumValueRange

## minValueRange = minReclassValue(reclassInt)
## maxValueRange = maxReclassValue(reclassInt)
##
## # Make 1 string

```

```

##  kk = ".join('{} {} {}';'.format(v[0], v[1], k+1) for k,v in
enumerate(zip(minValueRange, maxValueRange)))
##  fullString = kk[:-1]
##  quoteString = "" + fullString + ""
##  print fullString
##  return fullString

# Toggle code under & over this message to flip reclass
minValueRange = minReclassValue(reclassInt)
maxValueRange = maxReclassValue(reclassInt)
revMinRange = minValueRange[::-1]
revMaxRange = maxValueRange[::-1]

# Make 1 string
kk = ".join('{} {} {}';'.format(v[0], v[1], k+1) for k,v in enumerate(zip(revMinRange,
revMaxRange)))
fullString = pString + ';NODATA ' + str((reclassInt[len(reclassInt)-1])+1)
return fullString

def reclassEqInt(unclassRast, numInterval):

# Reclassification Prep
rasterMinx = arcpy.GetRasterProperties_management(unclassRast, "MINIMUM")
rasterMin = rasterMinx.getOutput(0)
rasterMaxx = arcpy.GetRasterProperties_management(unclassRast, "MAXIMUM")
rasterMax = rasterMaxx.getOutput(0)
print "Raster min :" + rasterMin
print "Raster max :" + rasterMax

# Calcluate reclass interval value
rInterval = str((float(rasterMax) - float(rasterMin))/float(numInterval))

# New modified minimum value
ratioMinInt = int(float(rasterMin)/float(rInterval))

# Create class numbers
rastRange = float(rasterMax)-float(rasterMin)
numIntervals = math.ceil(rastRange/float(rInterval))
blankRange = range(int(numIntervals))
reclassInt = [(x+1) for x in blankRange]

# Min reclass value calc

```

```

def minReclassValue(reclassInt):
    ratioMinInt = int(float(rasterMin)/float(rInterval))
    minimumValueRange = [(float(rasterMin)+(float(rInterval)*intNum)) for intNum in
blankRange]
    minimumValueRange.remove(minimumValueRange[0])
    newMin = (float(rasterMin))-(float(rInterval))
    minimumValueRange.insert(0, newMin)
    if minimumValueRange[0] == -1:
        minimumValueRange.remove(minimumValueRange[0])
        minimumValueRange.insert(0, 0.0)
    else:
        pass
    return minimumValueRange

# Max reclass value calc
def maxReclassValue(reclassInt):
    maximumValueRange = [(float(rasterMin)+(float(rInterval)*intNum)) for intNum in
reclassInt]
    maximumValueRange.remove(maximumValueRange[len(maximumValueRange)-
1])
    maximumValueRange.insert(len(maximumValueRange),
math.ceil(float(rasterMax)))
    return maximumValueRange

minValueRange = minReclassValue(reclassInt)
maxValueRange = maxReclassValue(reclassInt)
revMinRange = minValueRange[::-1]
revMaxRange = maxValueRange[::-1]

# Make 1 string
kk = ".join('{} {} {}';'.format(v[0], v[1], k+1) for k,v in enumerate(zip(revMinRange,
revMaxRange)))
pString = kk[:-1]
fullString = pString + ';NODATA ' + str((reclassInt[len(reclassInt)-1])+1)
return fullString

def reclassRaster(distRaster, reclassString):
    # Process: Reclassify
    euclidDistReclass = distRaster + "r"
    arcpy.gp.Reclassify_sa(distRaster, "Value", reclassString, euclidDistReclass,
"DATA")

```

```

def calcWts(trainPts, inRaster, outTable):
    # Process: Calculate Weights
    arcpy.CalculateWeightsTool_ArcSDM(inRaster, "", trainPts, "Ascending", outTable,
    "2", "1", "-99", "1")

def catWts(trainPts, inRaster, outTable):
    # Process: Calculate Weights
    arcpy.CalculateWeightsTool_ArcSDM(inRaster, "", trainPts, "Categorical", outTable,
    "2", "1", "-99", "1")

def nhLog(eqIn, nhField, radius, nhRaster):
    # Process: Point Statistics
    arcpy.gp.PointStatistics_sa(eqIn, nhField, nhRaster, cellSize, "Circle " + str(radius) + "
    MAP", "SUM")

    # Process: Log10
    arcpy.gp.Log10_sa(nhRaster, nhRaster + '1')

def nhSum(eqIn, nhField, radius, nhRaster):
    # Process: Point Statistics
    arcpy.gp.PointStatistics_sa(eqIn, nhField, nhRaster, cellSize, "Circle " + str(radius) + "
    MAP", "SUM")

def logTenRast(rastIn):
    # Process: Log10
    arcpy.gp.Log10_sa(rastIn, rastIn + '1')

def kernelDensity(evidenceIn, nhField, radius, kdRast):
    arcpy.gp.KernelDensity_sa(evidenceIn, nhField, kdRast, cellSize, str(radius),
    "SQUARE_KILOMETERS")

def simpleDensity(evidenceIn, nhField, radius, sdRast):
    arcpy.gp.PointDensity_sa(evidenceIn, nhField, sdRast, cellSize, "Circle " + str(radius)
    + " MAP", "SQUARE_KILOMETERS")

def lineDensity(evidenceIn, nhField, radius, ldRast):
    arcpy.gp.LineDensity_sa(evidenceIn, nhField, ldRast, cellSize, str(radius),
    "SQUARE_KILOMETERS")

def unique_values(table , field):
    with arcpy.da.SearchCursor(table, [field]) as cursor:
        return sorted({row[0] for row in cursor})

```

```

def selAttrib(inputFaults, ageWtsList, slipWtsList):
    ageCodes = unique_values(inputFaults, attribute1)
    slipCodes = unique_values(inputFaults, attribute2)
    print (ageCodes)
    print (slipCodes)
    arcpy.MakeFeatureLayer_management(inputFaults, "fltlyr")
    for aCat in ageCodes:
        print aCat
        for sCat in slipCodes:
            selStr = "" + attribute1 + "" + " <= " + str(aCat) + " AND " + "" + attribute2 + "" +
" <= " + str(sCat)
            print 'selStr = ' + selStr
            arcpy.SelectLayerByAttribute_management("fltlyr", "NEW_SELECTION",
selStr)
            fltName = (ntpath.basename(inputFaults))[:-4]
            faultSubset = outputPath + fltName + '_' + str(aCat) + '_' + str(sCat) + '.shp'
            print faultSubset
            arcpy.CopyFeatures_management("fltlyr", faultSubset, "", "0", "0", "0")
            if arcpy.management.GetCount(faultSubset)[0] == "0":
                print 'no data in: ' + faultSubset
            else:
                distRaster = faultSubset[:-4]
                eucDist(faultSubset, distRaster, cellSize)
                fullRcString = reclassByIntFlipAndMax(distRaster, reclassInterval)
                reclassRaster(distRaster, fullRcString)
                for trSet in trainingSets:
                    print 'Evidence: ' + (ntpath.basename(faultSubset))[:-4] + '. Training:' + trSet
                    wtsTable = outputPath + trSet[:-4] + '_' + str(aCat) + '_' + str(sCat) + '_' +
(ntpath.basename(faultSubset))[:-4]
                    calcWts(inPath + trSet, distRaster + "r", wtsTable)
                    print "Table created: " + wtsTable

                #CleanUp
                # Delete xml if it exists
                xmlJunk1 = wtsTable + ".dbf.xml"
                try:
                    os.remove(xmlJunk1)
                except OSError:
                    pass

```

```

'''
Tools: There are 4 tools below- to use any of them, uncomment the text
'''

# Density Function and Cumulative Weight Tool, Calculate Weights Tool: (Uncomment
next 40 lines to run this)
##
###for nameField in fieldList:
##  for shpName in shpList:
##    print 'Running on point file: ' + shpName
##    shpPath = inPath + shpName
##    for nhRadius in radiusList:
##      print 'Running on radius: ' + str(nhRadius)
##      nhRast = outputPath + shpName[:-4] + nameField[:1] + str(nhRadius)
##
##      #nhSum(shpPath, nameField, nhRadius, nhRast)
##      simpleDensity(shpPath, nameField, nhRadius, nhRast)
##      #lineDensity(shpPath, nameField, nhRadius, nhRast)
##      #kernelDensity(shpPath, nameField, nhRadius, nhRast)
##
##      logRaster = 'log'
##      if logRaster == 'log':
##          logTenRast(nhRast)
##          logRast = nhRast + 'l'
##          fullRcString = reclassEqInt(logRast, numberOfIntervals)
##          reclassRaster(logRast, fullRcString)
##      elif logRaster == 'notlog':
##          fullRcString = reclassEqInt(nhRast, numberOfIntervals)
##          reclassRaster(nhRast, fullRcString)
##
##      for trSet in trainingSets:
##          print 'Evidence: ' + shpName + '. Training:' + trSet
##          wtsTable = outputPath + shpName[:-4] + nameField + '_' + str(nhRadius) + '_' +
trSet[:-4]
##          if logRaster == 'log':
##              calcWts(inPath + trSet, nhRast + "lr", wtsTable)
##          elif logRaster == 'notlog':
##              calcWts(inPath + trSet, nhRast + "r", wtsTable)
##          print "Table created: " + wtsTable
##
##      #CleanUp

```

```

##          # Delete xml if it exists
##          xmlJunk1 = wtsTable + ".dbf.xml"
##          try:
##              os.remove(xmlJunk1)
##          except OSError:
##              pass

# Continuous Layer Reclassify and Cumulative Weight Test Tool: (Uncomment next 17
lines to run this)
##
##for evSet in contLayers:
##    fullRcString = reclassByInt(outPath + evSet, reclassInterval)
##    reclassRaster(outPath + evSet, fullRcString)
##    for trSet in trainingSets:
##        print 'Evidence: ' + evSet + '. Training:' + trSet
##        wtsTable = outPath + evSet + '_' + trSet[:-4]
##        calcWts(inPath + trSet, outPath + evSet + "r", wtsTable)
##        print "Table created: " + wtsTable
##
##    #CleanUp
##    # Delete xml if it exists
##    xmlJunk1 = wtsTable + ".dbf.xml"
##    try:
##        os.remove(xmlJunk1)
##    except OSError:
##        pass

# Categorical Weight Test Tool: (Uncomment next 14 lines to run this)
##
##for trSet in trainingSets:
##    for cat in catList:
##        print 'Evidence: ' + cat + '. Training:' + trSet
##        wtsTable = outPath + cat + '_' + trSet[:-4]
##        catWts(inPath + trSet, outPath + cat, wtsTable)
##
##    #CleanUp
##    # Delete xml if it exists
##    xmlJunk1 = wtsTable + ".dbf.xml"
##    try:
##        os.remove(xmlJunk1)

```

```
##     except OSError:
##         pass

# Subset-Distance Cumulative Weight Test Tool: (Uncomment next 9 lines to run this)
##
#### Fault selection
##ageWts = []
##slipWts = []
##
##for evSet in evidenceSets:
##
##    print 'Evidence:' + evSet
##    selAttrib(inPath + evSet, ageWts, slipWts)

'''
Clock
'''

stoptime = time.clock()
print "Done " + time.strftime("%I:%M:%S", time.localtime())
elapsed = stoptime-starttime
print "Elapsed time in seconds "
print str(elapsed) + " for them to go"
```

Cumulative Plotting Tool

```

'''
Cumulative Plotting Tool

Jacob DeAngelo
'''

# Import modules
import sys, string, os, time
import numpy as np
import matplotlib
from matplotlib.backends.backend_agg import FigureCanvasAgg as FigureCanvas
from matplotlib.figure import Figure
import matplotlib.mlab as mlab
import matplotlib.pyplot as plt
import matplotlib.gridspec as gridspec
import glob
import arcpy
import ntpath
from pylab import figure, show, legend, ylabel

# Clock
starttime = time.clock()
print "Starting " + time.strftime("%I:%M:%S", time.localtime())

# Initial User Settings
gs = gridspec.GridSpec(1, 2, width_ratios=[3, 2]) # figure size ratio (No need to modify
this)
arcpy.ImportToolbox(r'C:\Program Files (x86)\DataEast\XTools Pro\Toolbox\XTools
Pro.tbx') # This filepath must point to the xTools toolbox

# Important User Settings

# Data folder: The following folder must point to the folder with .dbf files that will be
plotted
dataFolderName =
r'C:\ArcProjects\Datasets\PlayFairway\NevadaPFA\layers\NevadaState2\fault_subsets4\2
019_faultPlot\devVerify1'
dataFolder = dataFolderName + '\\' # Do not change this

# Set Invert of x-axis: 'invert' to invert x-axis, otherwise leave blank

```

```

invert = "
#invert = 'invert' # To invert x-axis, uncomment this line

# If user is plotting distance, set to 'distance' to correctly plot data and labels, otherwise
leave as 'nonDist' for other surfaces (HF, density, etc)
usage = 'nonDist'
#usage = 'distance' # To use distance mode, uncomment this line
distFactor = 4 # Conversion from 'Class' to 'km' For example, if class represents 250m,
use '4' (250m = 1km/4)

# Cut the Studentized Contrast in half if nessicary- to do so set to 'scHalf'
scHalf = "
#scHalf = 'scHalf' # To cut SC in half, uncomment this line

# Define internal modules

# Read .dbf file
def Excel2CSV(ExcelFile, SheetName, CSVFile):
    import xlrd
    import csv
    workbook = xlrd.open_workbook(ExcelFile)
    worksheet = workbook.sheet_by_name(SheetName)
    csvfile = open(CSVFile, 'wb')
    wr = csv.writer(csvfile, quoting=csv.QUOTE_ALL)
    for rownum in xrange(worksheet.nrows):
        wr.writerow(
            list(x.encode('utf-8') if type(x) == type(u'') else x
                for x in worksheet.row_values(rownum)))
    csvfile.close()

# Get unique values, order preserved
def uVal(seq):
    checked = []
    for e in seq:
        if e not in checked:
            checked.append(e)
    return checked

# Get lisits from .dbf

```

```

fileList = []
for files in glob.glob(dataFolder + '*.dbf'):
    fileList.append((ntpath.basename(files))[:-4])
evList = []
radList = []
trainList = []
for fileName in fileList:
    evList.append(fileName.split("_")[0])
    radList.append(fileName.split("_")[1])
    trainList.append(fileName.split("_")[2])
evUnique = uVal(evList)
radUnique = uVal(radList)
trainUnique = uVal(trainList)

# reorder y-axis
if str.isdigit(trainUnique[0]) == True:
    trainUnique.sort(key=float)
else:
    pass
print evUnique
print radUnique
print trainUnique
plotNum = int(str(len(radUnique)) + str(len(trainUnique)) + str(9))
print plotNum

# Processing
for evType in range(len(evUnique)):

    # Create a figure with size 6 x 6 inches.
    fWid = (len(radUnique) * 6) + 2
    fHei = (len(trainUnique) * 5) + 3
    fig2 = Figure(figsize=(fWid, fHei), dpi=80, facecolor='w', edgecolor='k')

    # Create a canvas and add the figure to it.
    canvas2 = FigureCanvas(fig2)

    # Processing
    for fil in range(len(fileList)):
        if fileList[fil].split("_")[0] == evUnique[evType]:
            files = dataFolder + fileList[fil] + '.dbf'
            print files

```

```

# Calculate subplot location number
numTrain = (trainUnique.index(fileList[fil].split("_")[2]))
numRad = (radUnique.index(fileList[fil].split("_")[1]))
sln = (numTrain * (len(radUnique))) + (numRad + 1)
print 'Count Training: ' + str(numTrain)
print 'Count Radius: ' + str(numRad)
print sln

# dbf to xls
xlsFile = files[:-4] + '.xls'
try:
    os.remove(xlsFile)
except OSError:
    pass
# Process: Table To Excel
arcpy.TableToExcel_conversion(files, xlsFile, "NAME", "CODE")

# xls to csv
fileName = (ntpath.basename(xlsFile))[:-4]
if len(fileName)>31:
    sheetName = (fileName)[:31]
else:
    sheetName = fileName
csvFile = xlsFile[:-4] + '.csv'
Excel2CSV(xlsFile, sheetName, csvFile)
print csvFile

# Read data from a CSV file
r = mlab.csv2rec(csvFile)

# Create a figure with size 6 x 6 inches.
fig = Figure()

# Create a canvas and add the figure to it.
canvas = FigureCanvas(fig)

# Create a subplot.
ax = fig.add_subplot(111)
ay = fig2.add_subplot(int(str(len(trainUnique))),int(str(len(radUnique))),sln)

# Invert setting

```

```

if invert == 'invert':
    ax.invert_xaxis()
    ay.invert_xaxis()

# Get data from spreadsheet
r.cols = r.dtype.names

# Distance/Non-Distance Settings
if usage == 'distance':
    xAxisData = r[r.cols[2]]/distFactor
    xAxisTrainData = (r[r.cols[2]]/4)[: -1]
elif usage == 'nonDist':
    xAxisData = r[r.cols[2]]
    xAxisTrainData = (r[r.cols[2]])[: -1]

yAxisData = r[r.cols[6]]

# Plot Training Count or Percentage
trainPlotType = 'Count'
if trainPlotType == 'Count':
    trainData = r[r.cols[5]][: -1]
elif trainPlotType == 'Percentage':
    trainData = r[r.cols[5]][: -1]/r[r.cols[3]][: -1]
else:
    print 'Training plot type was set wrong'
    pass

areaCovered = r[r.cols[3]][-25]
areaCoveredTotal = r[r.cols[3]][-1]
print 'Area Covered (km2): ' + str(areaCovered)

# Set the title.
theTitle = fileName

if usage == 'distance':
    titleString = theTitle.split("_")[0] + '!' + theTitle.split("_")[1] + '!' +
theTitle.split("_")[2] + '!' + '4km: ' + str('{:,}'.format(int(areaCovered))) + ' km2 (' +
str(int(100*(areaCovered/areaCoveredTotal))) + '%), ' + str('{:,}'.format(int(r[r.cols[5]][-
25]))) + ' TP.' + ' +W 1km: ' + str(round(yAxisData[3], 1))
    ax.set_title(titleString,fontSize=11)
    ay.set_title(titleString,fontSize=10)
elif usage == 'nonDist':

```

```

        titleString = theTitle.split("_")[0] + '.' + theTitle.split("_")[1] + '.' +
theTitle.split("_")[2]
        ax.set_title(titleString,fontsize=18)
        ay.set_title(titleString,fontsize=16)

print titleString

# Set the X Axis label.
if usage == 'distance':
    ax.set_xlabel("Kilometers",fontsize=12)
    ay.set_xlabel("Kilometers",fontsize=12)
elif usage == 'nonDist':
    if theTitle.split("_")[1] == 'hf':
        xAxisTitle = "mW/m2"
    elif theTitle.split("_")[1] == 't3':
        xAxisTitle = "Degrees Celsius"
    elif theTitle.split("_")[1] == 'str':
        xAxisTitle = "Second Invariant of Strain Rate Tensor (10^-9/yr)"
    elif theTitle.split("_")[1] == 'str8cNative':
        xAxisTitle = "Second Invariant of Strain Rate Tensor (10^-9/yr)"
    else:
        xAxisTitle = "Class"
    ax.set_xlabel(xAxisTitle,fontsize=12)
    ay.set_xlabel(xAxisTitle,fontsize=12)

# Set the Y Axis label. The limits are set to show weight values between  $W_+ = 0$ 
and  $W_+ = 4$ 
ax.set_ylabel("+ W",fontsize=12)
ax.set_ylim(0, 4)
ay.set_ylabel("+ W",fontsize=12)
ay.set_ylim(0, 4)

# Display Grid.
ax.grid(True,linestyle='-',color='0.75')
ay.grid(True,linestyle='-',color='0.75')

# Generate the Scatter Plot.
ax.plot(xAxisTrainData,yAxisData[:-1],'-r-', xAxisTrainData, yAxisData[:-1], 'r. ');
ay.plot(xAxisTrainData,yAxisData[:-1],'-r-', xAxisTrainData, yAxisData[:-1], 'r. ');

# Error bars
error = r[r.cols[7]][:-1]

```

```

    ax.fill_between(xAxisTrainData, yAxisData[:-1]-error, yAxisData[:-1]+error,
alpha=0.25)
    ay.fill_between(xAxisTrainData, yAxisData[:-1]-error, yAxisData[:-1]+error,
alpha=0.25)

# Studentized
if scHalf == 'scHalf':
    ax.plot(xAxisTrainData, r[r.cols[12]][:-1]/2, 'm. ');
    ay.plot(xAxisTrainData, r[r.cols[12]][:-1]/2, 'm. ');
else:
    ax.plot(xAxisTrainData, r[r.cols[12]][:-1], 'm. ');
    ay.plot(xAxisTrainData, r[r.cols[12]][:-1], 'm. ');

# Second plot: Training sites count plot
ax2 = fig.add_subplot(111, sharex=ax, frameon=False)
ay2 = fig.add_subplot(int(str(len(trainUnique))),int(str(len(radUnique))),sln,
sharex=ay, frameon=False)
ax2.plot(xAxisTrainData, trainData, 'b.', markersize=8)

ay2.plot(xAxisTrainData, trainData, 'b.', markersize=6)
ax2.yaxis.tick_right()
ay2.yaxis.tick_right()
ax2.yaxis.set_label_position("right")
ay2.yaxis.set_label_position("right")

# Label: Training Count or Percentage
if trainPlotType == 'Count':
    ax2.set_ylabel("Training Points Count",fontsize=12)
    ay2.set_ylabel("Training Points Count",fontsize=12)
elif trainPlotType == 'Percentage':
    ax2.set_ylabel("Training Points Per Square km",fontsize=12)
    ay2.set_ylabel("Training Points Per Square km",fontsize=12)
else:
    print 'Training plot type was set wrong'
    pass

# Third plot: Contrast
ax.plot(xAxisTrainData, r[r.cols[10]][:-1], 'g.', markersize=5)
ay.plot(xAxisTrainData, r[r.cols[10]][:-1], 'g.', markersize=5)

fig.autofmt_xdate()
fig.suptitle(theTitle,fontsize=14)

```

```
# Save the generated Scatter Plot to a PNG file.
outPNG = csvFile.replace(".csv", ".png")
#canvas.print_figure(outPNG,dpi=250)
#outPNG = csvFile.replace(".csv", ".pdf")
canvas.print_figure(outPNG)

os.remove(xlsFile)

# Plot Title
fig2.suptitle(evUnique[evType] + " + W. Totoal Area (km2): " +
str('{:,}'.format(int(areaCoveredTotal))),fontsize=20)
fig2.subplots_adjust(wspace = 0.35)

# Generate figures
canvas2.print_figure(dataFolder + '_' + evUnique[evType] + '_Summary.png')
canvas2.print_figure(dataFolder + '_' + evUnique[evType] + '_Summary.pdf')

# Clock
stoptime = time.clock()
print "Done " + time.strftime("%I:%M:%S", time.localtime())
elapsed = stoptime-starttime
print "Elapsed time in seconds "
print elapsed
```

Categorical Plotting Tool

```

'''
Categorical Plotting Tool

Jacob DeAngelo
'''

# Import modules
import sys, string, os, time
import numpy as np
import matplotlib
from matplotlib.backends.backend_agg import FigureCanvasAgg as FigureCanvas
from matplotlib.figure import Figure
import matplotlib.mlab as mlab
import matplotlib.pyplot as plt
import matplotlib.gridspec as gridspec
import glob
import arcpy
import ntpath
from pylab import figure, show, legend, ylabel

# Clock
starttime = time.clock()
print "Starting " + time.strftime("%I:%M:%S", time.localtime())

# Initial User Settings
gs = gridspec.GridSpec(1, 2, width_ratios=[3, 2]) # figure size ratio (No need to modify
this)
arcpy.ImportToolbox(r'C:\Program Files (x86)\DataEast\XTools Pro\Toolbox\XTools
Pro.tbx')# This filepath must point to the xTools toolbox

# Important User Settings

# Data folder: The following folder must point to the folder with .dbf files that will be
plotted
dataFolderName =
r'C:\ArcProjects\Datasets\PlayFairway\NevadaPFA\layers\NevadaState2\heat_250m_v3\r
eclass3\2019Plot\devVerify1'
dataFolder = dataFolderName + '/' # Do not change this

# Set Invert of x-axis: 'invert' to invert x-axis, otherwise leave blank

```

```

invert = "
#invert = 'invert' # To invert x-axis, uncomment this line

# Set either 'plotByCategory' (Uses native 'class' units from .dbf table) or 'plotByClass'
(must use corresponding lists in 'binLists' section)
plotBy = 'plotByCategory'

# If user chooses to plot studentized contrast (Set to 'studentized') or weight/standatd
deviation (Set to 'catStudentized')
scType = 'studentized'
#scType = 'catStudentized'

# binLists: 'breakList' must be set to the text after the first '_' in .dbf file name,
'breakValues' must be set to bin thresholds
breakNames = ['r1', 'r2', 'r3']
breakValues = [[163, 185, 201, 219, 231],
[163, 186, 198, 208, 216, 225, 231],
[145, 177, 192, 201, 211, 227, 231]]

breakDict = dict(zip(breakNames, breakValues))
print(breakDict)

# Do not change this
plotType = 'Categorical'
#plotType = 'Ascending'

# Define internal modules

# Read .dbf file
def Excel2CSV(ExcelFile, SheetName, CSVFile):
    import xlrd
    import csv
    workbook = xlrd.open_workbook(ExcelFile)
    worksheet = workbook.sheet_by_name(SheetName)
    csvfile = open(CSVFile, 'wb')
    wr = csv.writer(csvfile, quoting=csv.QUOTE_ALL)
    for rownum in xrange(worksheet.nrows):
        wr.writerow(
            list(x.encode('utf-8') if type(x) == type(u'') else x
                for x in worksheet.row_values(rownum)))

```

```

csvfile.close()

# Get unique values, order preserved
def uVal(seq):
    checked = []
    for e in seq:
        if e not in checked:
            checked.append(e)
    return checked

# Get lisits from .dbf
fileList = []
for files in glob.glob(dataFolder + '*.dbf'):
    fileList.append((ntpath.basename(files))[:-4])
evList = []
radList = []
trainList = []
for fileName in fileList:
    evList.append(fileName.split("_")[0])
    radList.append(fileName.split("_")[1])
    trainList.append(fileName.split("_")[2])
evUnique = uVal(evList)
radUnique = uVal(radList)
trainUnique = uVal(trainList)

# reorder y-axis
if isinstance(trainUnique[0], str) == True:
    pass
else:
    trainUnique.sort(key=float)
print evUnique
print radUnique
print trainUnique
plotNum = int(str(len(radUnique)) + str(len(trainUnique)) + str(9))
print plotNum

# Processing
for evType in range(len(evUnique)):

```

```

# Create a figure with size 6 x 6 inches.
fWid = (len(radUnique) * 6) + 2
fHei = (len(trainUnique) * 5) + 3
fig2 = Figure(figsize=(fWid, fHei), dpi=80, facecolor='w', edgecolor='k')

# Create a canvas and add the figure to it.
canvas2 = FigureCanvas(fig2)

# Processing
for fil in range(len(fileList)):
    if fileList[fil].split("_")[0] == evUnique[evType]:
        files = dataFolder + fileList[fil] + '.dbf'
        print files

        # Calculate subplot location number
        numTrain = (trainUnique.index(fileList[fil].split("_")[2]))
        numRad = (radUnique.index(fileList[fil].split("_")[1]))
        sln = (numTrain * (len(radUnique))) + (numRad + 1)
        print 'Count Training: ' + str(numTrain)
        print 'Count Radius: ' + str(numRad)
        print sln

        # dbf to xls
        xlsFile = files[:-4] + '.xls'
        try:
            os.remove(xlsFile)
        except OSError:
            pass
        # Process: Table To Excel
        arcpy.TableToExcel_conversion(files, xlsFile, "NAME", "CODE")

        # xls to csv
        fileName = (ntpath.basename(xlsFile))[:-4]
        if len(fileName)>31:
            sheetName = (fileName)[:31]
        else:
            sheetName = fileName
        csvFile = xlsFile[:-4] + '.csv'
        Excel2CSV(xlsFile, sheetName, csvFile)
        print csvFile

# Read data from a CSV file

```

```

r = mlab.csv2rec(csvFile)

# Create a figure with size 6 x 6 inches.
fig = Figure()

# Create a canvas and add the figure to it.
canvas = FigureCanvas(fig)

# Create a subplot.
ax = fig.add_subplot(111)
ay = fig2.add_subplot(int(str(len(trainUnique))),int(str(len(radUnique))),sln)

# Invert setting
if invert == 'invert':
    ax.invert_xaxis()
    ay.invert_xaxis()

# Get data from spreadsheet
r.cols = r.dtype.names

# Plot by Category or Class Settings
if plotBy == 'plotByCategory':
    ax.set_xlabel("Category",fontsize=12)
    ay.set_xlabel("Category",fontsize=12)
elif plotBy == 'plotByClass':
    ax.set_xlabel("Class",fontsize=12)
    ay.set_xlabel("Class",fontsize=12)
else:
    ax.set_xlabel("Category",fontsize=12)
    ay.set_xlabel("Category",fontsize=12)

# Dictionary lookup for category to class conversion
if plotBy == 'plotByCategory':
    pass
elif plotBy == 'plotByClass':
    # Generate category's average class values
    sas = breakDict.get(fileList[fil].split("_")[1])
    print sas
    avList = []
    for valCode in range(len(sas)):
        if sas[valCode-1] > sas[valCode]:
            avList.append((sas[valCode]+0)/2)

```

```

        else:
            avList.append((sas[valCode]+sas[valCode-1])/2)
        print avList
    else:
        pass

# Set either 'plotByCategory' or 'plotByClass'
if plotBy == 'plotByCategory':
    if plotType == 'Categorical':
        xAxisData = r[r.cols[2]]
        xAxisTrainData = (r[r.cols[2]])[-1]
    elif plotType == 'Ascending':
        xAxisData = r[r.cols[2]]/4
        xAxisTrainData = (r[r.cols[2]]/4)[-1]
    else:
        print 'Set the plotType variable to either Categorical or Ascending'
elif plotBy == 'plotByClass':
    if plotType == 'Categorical':
        xAxisData = avList
        xAxisTrainData = avList[-1]
    elif plotType == 'Ascending':
        xAxisData = r[r.cols[2]]/4
        xAxisTrainData = avList[-1]
    else:
        print 'Set the plotType variable to either Categorical or Ascending'

yAxisData = r[r.cols[6]]

# Plot Training Count or Percentage
trainPlotType = 'Count'
if trainPlotType == 'Count':
    trainData = r[r.cols[5]]
elif trainPlotType == 'Percentage':
    trainData = r[r.cols[5]]/r[r.cols[3]]
else:
    print 'Training plot type was set wrong'
    pass

areaCovered = r[r.cols[3]][-2]
areaCoveredTotal = r[r.cols[3]][-1]

# Studentized type setting

```

```

if scType == 'catStudentized':
    studCon = r[r.cols[6]]/r[r.cols[7]]
else:
    studCon = r[r.cols[12]]

print 'Area Covered (km2): ' + str(areaCovered)

# Set the title.
theTitle = fileName
titleString = theTitle + '. ' + str('{:}'.format(int(areaCovered))) + ' km2 (' +
str(int(100*(areaCovered/areaCoveredTotal))) + '%), ' + str('{:}'.format(int(r[r.cols[5]][-
2]))) + ' TP'
print titleString

if plotType == 'Categorical':
    ax.set_title(theTitle,fontsize=12)
    ay.set_title(theTitle,fontsize=12)
elif plotType == 'Ascending':
    ax.set_title(titleString,fontsize=12)
    ay.set_title(titleString,fontsize=12)
else:
    print 'Set the plotType variable to either Categorical or Ascending'

# Set the X Axis label.
# Set either 'plotByCategory' or 'plotByClass'

if plotBy == 'plotByCategory':
    ax.set_xlabel("Category",fontsize=12)
    ay.set_xlabel("Category",fontsize=12)
elif plotBy == 'plotByClass':
    if fileList[fil].split("_")[1] == 'str8cNative':
        ax.set_xlabel("Second Invariant of Strain Rate Tensor (10^-
9/yr)",fontsize=12)
        ay.set_xlabel("Second Invariant of Strain Rate Tensor (10^-
9/yr)",fontsize=12)
    else:
        ax.set_xlabel("Class",fontsize=12)
        ay.set_xlabel("Class",fontsize=12)
else:
    ax.set_xlabel("Category",fontsize=12)
    ay.set_xlabel("Category",fontsize=12)

```

```

# Set the Y Axis label. The limits are set to show weight values between  $W_+ = -1$ 
and  $W_+ = 4$ 
ax.set_ylabel("+ W",fontsize=12)
ax.set_ylim(-1, 4)
#ax.set_ylim(-2, 2)
ay.set_ylabel("+ W",fontsize=12)
ay.set_ylim(-1, 4)
#ay.set_ylim(-2, 2)

# Display Grid.
ax.grid(True,linestyle='-',color='0.75')
ay.grid(True,linestyle='-',color='0.75')

# Generate the Scatter Plot.

# Plot Zero Line
zeroPts = []
for xad in xAxisData:
    zeroPts.append(0)
print zeroPts

ax.plot(xAxisData, zeroPts, 'k-', markersize=5, linewidth=2);
ay.plot(xAxisData, zeroPts, 'k-', markersize=5, linewidth=2);

# Plot Weight Line
ax.plot(xAxisData,yAxisData,'r-', xAxisData, yAxisData, 'r.', markersize=12);
ay.plot(xAxisData,yAxisData,'r-', xAxisData, yAxisData, 'r.', markersize=15);

# Error bars
error = r[r.cols[7]]
ax.errorbar(xAxisData, yAxisData, yerr = error, linewidth = 3, color = 'red')
ay.errorbar(xAxisData, yAxisData, yerr = error, linewidth = 3, color = 'red')

# Second plot: Training sites count plot
ax2 = fig.add_subplot(111, sharex=ax, frameon=False)
ay2 = fig2.add_subplot(int(str(len(trainUnique))),int(str(len(radUnique))),sln,
sharex=ay, frameon=False)

ax2.plot(xAxisData, trainData, 'b.', markersize=12)
ay2.plot(xAxisData, trainData, 'b.', markersize=15)
print xAxisData
ax2.yaxis.tick_right()

```

```

ay2.yaxis.tick_right()
ax2.yaxis.set_label_position("right")
ay2.yaxis.set_label_position("right")

# Label: Training Count or Percentage
if trainPlotType == 'Count':
    ax2.set_ylabel("Training Points Count",fontsize=12)
    ay2.set_ylabel("Training Points Count",fontsize=12)
elif trainPlotType == 'Percentage':
    ax2.set_ylabel("Training Points Per Square km",fontsize=12)
    ay2.set_ylabel("Training Points Per Square km",fontsize=12)
else:
    print 'Training plot type was set wrong'
    pass

# Third plot: Training sites per area examined
ax3 = fig.add_subplot(111, sharex=ax2, frameon=False)
ay3 = fig2.add_subplot(int(str(len(trainUnique))),int(str(len(radUnique))),sln,
sharex=ay2, frameon=False)

# Plot either area or TpArea - (Training points over area)
greenPlot = 'area'
if greenPlot == 'TpArea':
    ax3.plot(xAxisData, r[r.cols[5]]/r[r.cols[3]], 'g.', markersize=10)
    ay3.plot(xAxisData, r[r.cols[5]]/r[r.cols[3]], 'g.', markersize=13)
elif greenPlot == 'area':
    areaList = r[r.cols[3]]
    ax3.plot(xAxisData, areaList, 'g.', markersize=10)
    ay3.plot(xAxisData, areaList, 'g.', markersize=13)
    ax3.plot(xAxisData, np.cumsum(areaList), 'g-', markersize=10)
    ay3.plot(xAxisData, np.cumsum(areaList), 'g-', markersize=13)
else:
    print 'Need to set the green point choice- Area or TP/Area'

print xAxisData

ax3.set_yticklabels([])
ay3.set_yticklabels([])

# Plot Studentized Contrast (It's turned off, uncomment the next 18 lines to
enable)
## ax.plot(xAxisData, studCon, 'm.', markersize=9);

```

```

##      ay.plot(xAxisData, studCon, 'm.', markersize=12);

##      # Plot Zero Line
##      zeroPts = []
##      for xad in xAxisData:
##          zeroPts.append(0)
##      print zeroPts
##
##      ax.plot(xAxisData, zeroPts, 'k-', markersize=5, linewidth=2);
##      ay.plot(xAxisData, zeroPts, 'k-', markersize=5, linewidth=2);

##      ax2.set_yticklabels([])
##      ay2.set_yticklabels([])
##      ax2.set_xticklabels([])
##      ay2.set_xticklabels([])

##      ax2.set_ylabel("Training Points Count",fontSize=12)
##      ay2.set_ylabel("Training Points Count",fontSize=12)

fig.autofmt_xdate()
fig.suptitle(theTitle,fontSize=14)

# Save the generated Scatter Plot to a PNG file.
outPNG = csvFile.replace(".csv", ".png")
#canvas.print_figure(outPNG,dpi=75)
#outPNG = csvFile.replace(".csv", ".pdf")
canvas.print_figure(outPNG)

os.remove(xlsFile)

# Plot Title
if plotType == 'Categorical':
    fig2.suptitle(evUnique[evType] + "+ W Categorical. Total Area (km2): " +
str('{:,.}').format(int(sum(r[r.cols[3]]))),fontSize=14)
    elif plotType == 'Ascending':
        fig2.suptitle(evUnique[evType] + "+ W Ascending. Total Area (km2): " +
str('{:,.}').format(int(areaCoveredTotal))),fontSize=14)
    else:
        print 'Set the plotType variable to either Categorical or Ascending'

fig2.subplots_adjust(wspace = 0.35)

```

```
# Generate figures
canvas2.print_figure(dataFolder + '_' + evUnique[evType] + '_Summary.png')
canvas2.print_figure(dataFolder + '_' + evUnique[evType] + '_Summary.pdf')

# Clock
stoptime = time.clock()
print "Done " + time.strftime("%I:%M:%S", time.localtime())
elapsed = stoptime-starttime
print "Elapsed time in seconds "
print elapsed
```

Appendix 4: Other Possible Future Work Topics

The heat flow database could be improved by manually re-evaluating each well to understand whether the measured heat flow value reflects crustal background heat flow or is influenced by local hydrological disturbances or errors. Every heat flow well examined in the present study has already been evaluated in such a manner, but improvements could be made to best characterize the underlying raw data systematically across the region. Although this would require an investment of time, it would undoubtedly result in a more accurate heat flow map.

The robustness of the modeling could be tested and improved by assessing different study areas that have different types of geologic terrain. If effects from anomalous geology significantly influence the assessment results, it may be best to exclude regions with distinct tectonics or hydrology that diverge from the regional character of a study area. Areas previously alluded to include the carbonate aquifer system or Walker Lane in the southern and western Great Basin, respectively. An example of such an approach is given by Coolbaugh et al. (2005) who calculated weights in areas without regional aquifers and then extrapolated those weights into areas underlain by regional aquifers. It may be useful to examine many different study areas in an analysis of a region.

It may be useful to examine many different training site sets as well. Better training site information (e.g., temperature, confidence, favorable structural settings, etc.) could also improve model performance. Multiple training site sets could be useful to pair with different study area sets. If possible, the 2-D lateral extent of training sites, defined as polygons, might provide a better representation of benchmark characteristics.

Estimations of undiscovered resource could be made quantitatively. The models that are within acceptable ranges for conditional independence could be used to estimate undiscovered resource potential in terms of systems or even electric generation capacity.

Python plotting tools could be improved to show bin boundaries, plot by area, calculate fits, and report functions. If these improvements were made, a user could experiment with a series of bin ranges and quickly see which functions provide the best fits without the need for manual statistical evaluation of each bin range and associated curve-fitting.

A map depicting 'known absence of geothermal' could be created from locations of well-understood deep holes or other indicators to rule areas out from consideration or to train different data-driven techniques.

Monte Carlo simulations could be explored with training data subsets. This could reveal more reliable weighting relationships.

The temperature at depth maps that accounted for sediment thickness did not correlate in the present study but might prove useful for other purposes or be a useful standalone product. Temperature was estimated at 1, 2, 3, 4, 5 and 6 km depth using both the EBK and RBF maps. The temperature at 3 km depth made using the EBK is shown as Appendix 1.